Charge dynamics at the interface separating two dielectric media.

Eric Giglio

Normandie Université

THESE HDR

Pour obtenir le diplôme d'Habilitation à Diriger des Recherches

Spécialité PHYSIQUE

Centre de Recherche sur les Ions, les Matériaux et la Photonique (CIMAP)

Boulevard Henri Becquerel, BP5133, 14070 Caen cedex 5

Charge dynamics at the interface of two dielectric media.
Two cases :
(i) shape deformation of droplets charged at the Rayleigh limit.
(ii) ion transport through insulating capillaries

Présentée et soutenue par
Eric GIGLIO

Thèse soutenue publiquement le 3 décembre 2019 devant le jury composé de		
Mme. Francesca GULMINELLI	Professeur de l'Université CAEN-NORMANDIE Lab. de Physique Corpusculaire (LPC)	Rapporteur
M. Christoph LEMELL	Professeur de l'Univ. of Technology of Vienna Institut for Theoretical Physics	Rapporteur
M. Bruno MANIL	Professeur de l'Université Paris 13 Laboratoire de Physique des Lasers (LPL)	Rapporteur
M. Jose Maria MONTANERO	Professeur de l'Université d'Extremadura (Espagne) Department of Mechanic Engineering, Energy and Materials,	Examinateur
M. Philippe RONCIN	Directeur de Recherche au CNRS Institut des Sciences Moléculaires d'Orsay, Paris-11, (ISMO)	Examinateur
M. Emmanuel BALANZAT	Directeur de Recherche au CNRS Centre de Rech. sur les Ions, les Matériaux et la Photonique (CIMAP)	Examinateur, Garant

Université CAEN–NORMANDIE

Centre de Rech. sur les Ions,
les Matériaux et la Photonique

Charge dynamics at the interface separating two dielectric media.

(1) Shape deformation of droplets charged at the Rayleigh limit

—

(2) Ion transport through insulating capillaries

Giglio Eric

giglio@ganil.fr

https://cv.archives-ouvertes.fr/eric-giglio

https://www.researchgate.net/profile/Eric_Giglio/research

Centre de Recherche sur les Ions, les Matériaux et la Photonique (CIMAP), Normandie Univ, ENSICAEN, UNICAEN, CEA, CNRS

Boulevard Henri Becquerel BP5133 14070 Caen cedex 5, France

Short note about of the choice of two topics presented in the manuscript

In this short note, the author wants two highlight the historical link between the seemingly independent topics presented in chapter one and chapter two. While both topics study different objects and physical phenomena, they have in common the charge dynamics of free charges at the interface separating two dielectric media. From 2007 to 2013, the author studied the spontaneous droplet deformation of critically charged droplets. During that time, the author developed, among other, a model for the surface charge dynamics at the droplet surface, i.e., at the interface separating a charged conducting liquid from a gas interface with negligible viscosity. In 2013, the author was asked for theoretical support in the transport of an ion beam through insulating capillaries. The knowledge gathered from the previous work allowed the author to imagine a (CPU efficient) approach for the charge dynamics in the capillary wall and evaluation of the electric field. The numerical model developed for the computation of the beam trajectories through the capillary in chapter two in thus based on the charge dynamics model derived from the droplet topic presented in chapter one. From 2013 up to now, the numerical model is used successfully to describe and predict experimental results in the field of beam transport through insulating capillaries.

Contents

List of Figures

Chapter 1

Shape deformation of critically charged microdroplets

Collaborations (CIMAP):   J. Rangama, A. Radcliffe*, S. Guillous, B. Manil, B.A. Huber
Centre de Recherche sur les Ions, les Matériaux et la Photonique (CIMAP)
* Post-doctoral position (12 months)

Collaborations (Ilmenau):   D. Duft, R. Müller, T. Leisner, M. Brickman, C. Wender, T. Achtzehn
Universität Ilmenau D ; Contrat : PROCOP (00353XC, 05927XC)

1.1   Introduction

If electric charges are present in liquids that are pulverized, the formed droplets may be charged. Such pulverization processes are for example found in oceans or waterfalls and are encountered in the atmosphere. Electrified droplets are also involved in metallic powder production, ink-jet printing, microspray lubrication, emulsification, spray painting and occur in a variety of industrial processes [19]. The droplets range typically from the micrometer to the millimetre. It was found advantageous to create charge droplets that can be guided by electric fields, allowing to optimize the covering of the surface of a given object. If the droplets are pulverized in the presence of an electric field, the amount of charge (and sign) carried by the droplet can by controlled by the electric field. Electroscope ionization, a technique that is revolutionizing the mass-spectrometric analysis of large biomolecules is another application of electrified droplets. Now, if a droplet is

charged to a critical value so that the repulsive electrostatic force overcomes the attractive surface tension force, the droplet breaks up, sending out more charged daughter droplets and leaving behind a stable residual drop. The charge is expected to be emitted from fine jets, triggered by the spontaneous shape deformation of the critically charged drop.

In this manuscript the author will describe the spontaneous shape deformation of critically charged droplets after the onset of the charge instability. The work will briefly introduce the notion of the Rayleigh limit of charged droplets, discuss the experimental setup and observed data sets. In the main part of this first chapter, a detailed discussion of the modelling and simulation of the droplet deformation, from the initially spherical shape to the intermediate shape just before the excess charge is ejected and back to spherical sub-critically charged drop, is proposed. We are in particular interested in the influence of the viscosity and conductivity of liquid on the shape deformation and charge break-up. The project was supported by the ANR "DYNAMIC" 2007, with the author being the project leader.

1.1.1 The Rayleigh limit of charged droplets

At equilibrium, the total charge carried by the spherical droplet is uniformly distributed at the surface (similar to a plain spherical conductor), as the ions are free to move in the liquid. This generates a force at the surface that acts outwards, counteracting the inwards force due to the surface tension. The stability of charged droplets has been studied theoretically as early as 1882 by Lord Rayleigh [2]. Considering small deformation amplitudes, he expanded the axial surface deformation $R(\theta, t)$ on Legendre polynomials P_n, where a_m is the amplitude of the surfaces mode $m \geq 2$,

$$R(\theta, t) = R_0 + a_2(t)P_2(\cos\theta) + a_4(t)P_4(\cos\theta) + \ldots \quad , \; a_m \ll R_0 \qquad (1.1)$$

and calculated the eigenfrequency f_m of each mode $m \geq 2$. He concluded that, in an incompressible charged liquid droplet of radius R, the quadupole oscillation becomes unstable against small perturbations as soon as the disruptive Coulomb pressure $P_c = \sigma^2/2\varepsilon_0$ due to the surface charges σ equals the cohesive capillary pressure $P_s = 2\gamma/R$ due to the surface tension γ of the liquid. This result is expressed by the equation of natural frequency f_m of the mth surface mode of a spherical droplet,

$$f_m = \frac{1}{2\pi}\left(\frac{\gamma m(m-1)}{\rho R^3}\left[(m+2) - 4X\right]\right)^{1/2} \qquad (1.2)$$

where ρ is the density of the liquid. The fissility parameter X stands for the ratio between the two pressures and is defined as [1],

$$X = \frac{P_c}{P_s} = \frac{\sigma^2/2\varepsilon_0}{2\gamma/R} = \frac{Q^2}{64\pi^2\gamma\varepsilon_0 R^3} \quad . \tag{1.3}$$

where we introduced the total charge $Q = 4\pi\sigma R^2$ of the droplet. The last term of (1.3) gives the explicit dependence of X on the droplet radius and shows that the fissility increases with decreasing radius R. The frequency equation (1.2) indicates that for a sub-critical fissility, $X < 1$, the modes $(m > 2)$ have all a positive frequency and the charged droplet is stable against small perturbations. At the Raygleigh limit, when the fissility becomes critical, $X \geq 1$, the frequency of the quadrupole moment $(m = 2)$ becomes imaginary and its mode is unstable against small perturbations, resulting into a droplet that deforms spontaneously. While Lord Rayleigh predicted in his paper [2] the formation of fine jets, he gave no further details about the shape deformation after the onset of the "Rayleigh instability" of a charged droplet.

Taylor Cone

By charging to several thousand Volt a drop of liquid standing at the lower end of a glass tube, Zeleny observed in 1917 for the first time the disintegration of charged drops [3]. He measured the potential at which they disintegrated owing to the formation of a pointed end from which issued a narrow jet. Working with isolated charged bubbles, Sir G. Taylor (1964) was the first to point out that the drop elongates until it quickly develops an apparently conical end and that a narrow jet appears at the vertex [8]. Moreover Taylor realized that a conical point could exist in equilibrium and gave the condition for its steady state. Namely, the exact balance of capillary pressure and electrostatic pressure on a perfectly conducting conical fluid occurs only for an opening half-angle of 49.3°. Indeed, formation of conical liquid meniscus and associated jet emission are complex fluid dynamical phenomena and received much attention in recent years. Cloupeau *et al.* [24] (1989) determined the domains of operation in this cone-jet mode, after achieving good reproducibility of phenomena. How does a cone-jet form and how does the thin jet that emanates from the cone's tip break up into small drop was theoretically (numerically) investigated among other by Pantano *et al.* [30] (1994), by Gañán [33] (1997), by Jens Egger [34] (1997), by de la Mora *et al.* [48] (2007)

---

[1]The fissility, expressed as the ratio Coulomb energy E_c over twice the surface energy E_s of the droplet, $X = E_c/2E_s$, is often used in the literature to express the Rayleigh limit of the droplet. While it is a compact notation, it is not really helpful to understand the origin of the instability and should be depreciated in favour of (1.3).
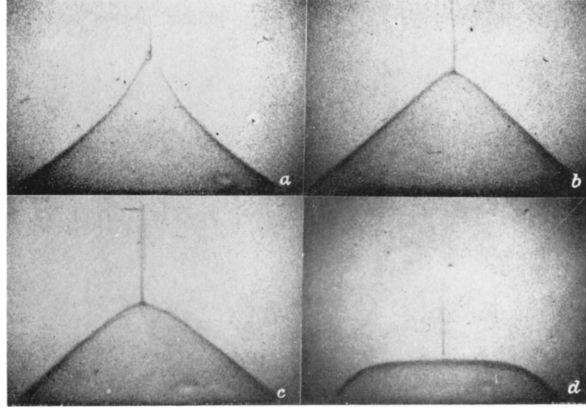
Figure 1.1: *Soap film, microsecond exposures of successive stages (a) of jet formation; (b), (c), (d) subsequent collapse (Taylor 1964).*

and by Collins *et al.* [50] (2008). The latter report simulations and experiments that enable a comprehensive picture of the mechanisms of cone formation, jet emission and break-up that occurred during electrodynamic tip streaming from a liquid film of finite conductivity. They propose a scaling law to predict the size of the daughter droplets produced from jet-break-up. More recently Collins *et al.* [57] (2013) gave universal scaling laws for the disintegration of electrified drops, that is, neutral drops in an uniform strong electric field. They used theory and simulation, to show that conductivity can be tuned to yield three scaling regimes for radius and charge of the daughter droplets. Similarly, Gañán-Calvo *et al.* (2016) proposed universal scaling laws of the first ejected daughter droplet from an electrified drop [61]. It ought to be emphasized that the interest is not purely academic as the production of microsized or nanosized jets is of present considerable importance in modern technologies that require a fine control of the size of jets and their decay droplets, including electrospray ionization mass spectrometry (ESI-MS) of large biomolecules [23] as well as printing and coating processes [47]. Electrified droplets were also found to influence the raindrops formation in thunderclouds [13].

Observation of charge emission near the Rayleigh limit

Several experimental studies have attempted to verify Lord Rayleigh's prediction. Hendricks in 1962 produced charged oil drops and accelerated them through a large potential to measure size and charge [6]. In nearly all cases, the charge on the droplet was near or below the Rayleigh limit. Observations of exploding single droplets were made by Doyle *et al.* [7] (1964) using a Millikan-type apparatus.

They examined the stability of evaporating charged Aniline and water droplets. During the evaporation, only neutral molecules are emitted[2]. As a result, the initial charge is conserved until the droplet reach a critical radius, for which the droplet becomes unstable. They reported that at breakup, the parents drop ejected a cloud of very small droplets, which carried away about 30% of its charge but relatively little mass. Schweizer and Hanson [10] (1971) experimented with a charged droplet
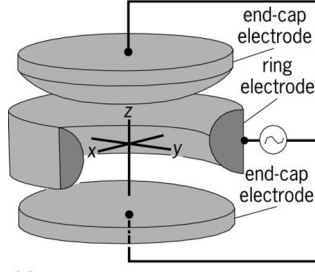
Figure 1.2: Ring electrode Paul trap

in a quadrupole trap (type Paul trap). This quadupole trap used superposed ac and dc fields to maintain the droplet at the center of the ac ring electrode. The dc field generates a vertical force on the droplet that balances its weight, allowing to extract the mass of the droplet. They reported confirmation of the Rayleigh limit (with a spread of ±4%) for droplets with a radius between 7.5 and 20 μm. The droplets lost $23 \pm 5\%$ of their initial charge but only $5 \pm 5\%$ of their mass in the explosion. Several other experimental studies reported a range of charge and mass losses. For example, using levitation techniques, Roulleau and Desbois [11] estimated a charge loss in the range of 16% - 40%, but could not detect the mass loss. Rhim and co-workers [20] (1987) at the Jet Propulsion Laboratory (JPL) used a hybrid electrostatic-acoustic technique to levitate charged droplets with diameter of the order of 1 mm. They found that water droplets burst prior to reaching the Rayleigh limit. They were not able to quantify their results, but they speculated that the drop became resonant with the quadrupole field before reaching the Rayleigh limit. Their video camera system was not sensitive enough to detect mass loss during the explosion. In the work of Taflin *et al.* [22] (1989), micro-droplets were trapped in Paul traps and the size monitored precisely with a laser and a photomultiplier tube mounted a right angle. The "optical resonance spectrum" was used to obtain the size of the droplet to within ±0.01%. They too found that droplets burst prior to reaching the Rayleigh limit with a critical charge only 0.8 times the Rayleigh charge. They investigated if the premature explosion was due

---

[2]Due to the strong image-charge interaction of charged particles with a dielectric surface, ions are tighter bound to the droplet surface than neutral molecules.
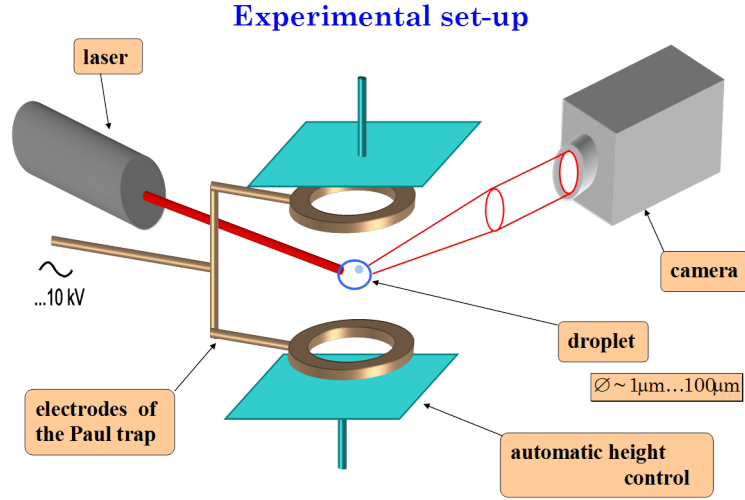
Figure 1.3: Scheme of experimental setup used by Taflin (1989) and Duft (2003). The photomultiplier at right angle with the laser is not shown.

to thermal fluctuations on the surface, but concluded otherwise. They found it also not likely that a resonance associated with the ac frequency and the droplet oscillation could lead to premature fissioning of the droplet as the eigen-frequency of the droplet with only 80% of the Rayleigh charge would be much higher than the 60 Hz of the ac trapping field. Their preferred explanation is that contamination of the surface could lead to regions of low surface tension, which would reach the Rayleigh limit before a pure component droplet would do so. They also noted that with each explosion, the mass loss was within $1\% - 2.3\%$, while the charge loss ranged between 10% and 18%. They found however no correlation between mass and charge loss in the reported data. Using electrodynamic balance for drop levitation, Richardson *et al.* [1] observed a 15% charge loss for dioctyl-phthalate droplets and around 50% for sulphuric acid drops. The mass loss observed in the case of both liquids was less than 2.5%. Gomez and Tang [29] measured the charge and size of heptane droplets generated by electrostatic sprays and observed rupture of droplets, when they had charging levels between 70% and 80% of the Rayleigh limit. On the whole, experimental results estimate the charge loss in the range of 15% - 50% with less than 5% mass loss. The discrepancy observed in different experiments may be attributed to the errors encountered in the measurements due to the very fast dynamics of the process as well as the influences of other parameters such as applied electric field, acceleration due to gravity, and aerodynamic drag. There is however an agreement that the droplets seem to burst prior to reaching the Rayleigh limit with a critical charge only 0.8 times the Rayleigh charge.

More recently, Duft *et al.* [38] (2002) report direct observation of the breakup of
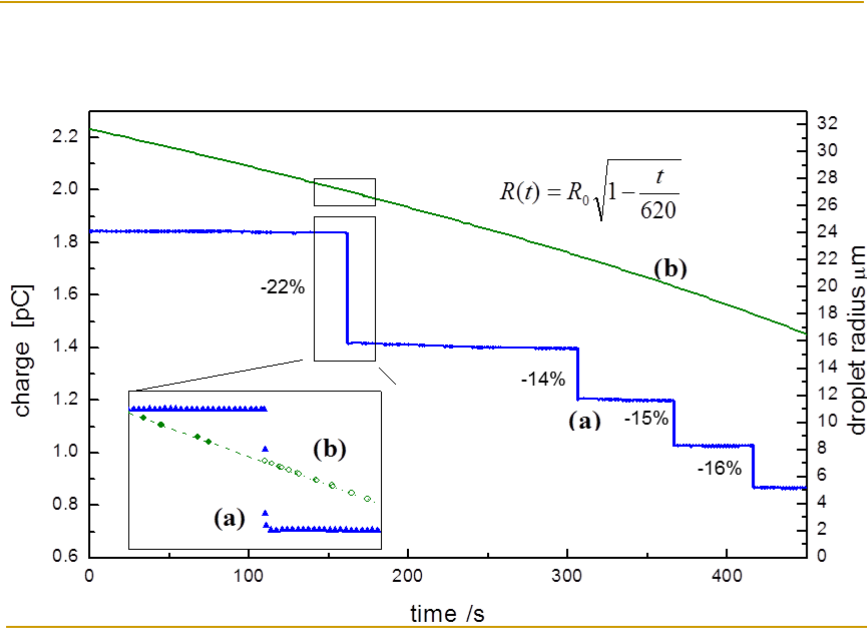
Figure 1.4: Size and charge of an evaporating glycol droplet. The dotted region around the first Coulomb instability is enlarged in the inset (Duft 2002).

charged micro-droplets where the amplitude and phase of the forced quadrupole shape oscillation of the droplets are taken as probes for their fissility. Indeed, at resonance (X=1), the phase between the droplet oscillation and the external quadupole AC field is shifted by $\phi = \pi/2$. They found that for the glycol droplet investigated, the breakup takes place for $\phi \simeq 1.0$ rad which corresponds to $X \simeq 0.97$ [14], independent of the size of the droplet at the moment of instability. This was the first clear indication that for evaporating highly charged microdroplets of glycol, the instability occurs indeed close to the Rayleigh limit, confirming Rayleigh prediction. This is in contrast to the previous investigations [6, 7, 10, 20, 22, 29] which report a critical fissility between 0.5 and 0.8, when using the tabulated surface tension of the droplet liquid. However, using the tabulated surface tension of glycol, Duft *et al.* found an apparent critical fissility of $X \simeq 0.7$ as well. They noticed that the apparent fissility decreases with subsequent instabilities of the same droplet and therefore tentatively attribute the reduced surface tension to surface active contaminants, which become more and more concentrated as the droplet shrinks[3].

This prediction is also corroborated by our simulations of a low viscous charged

---

[3]At this point, one may also ask in how far the ions that accumulate at the surface influence the surface tension of the liquid droplet.
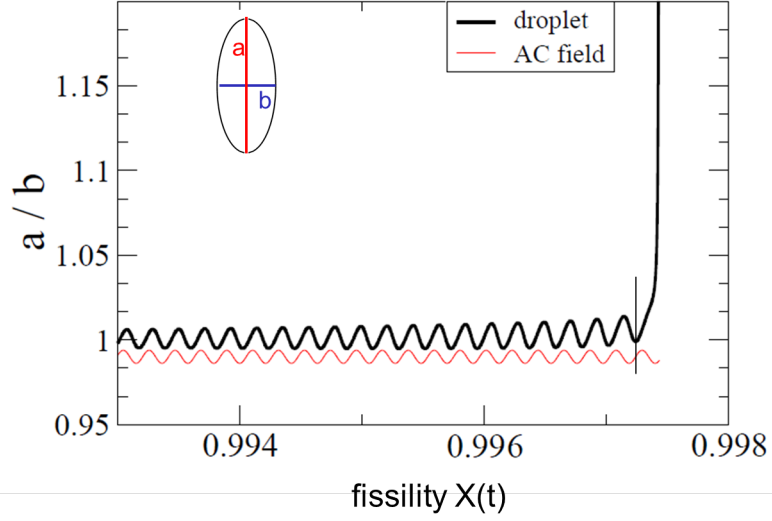
Figure 1.5: *Simulated forced oscillation of an evaporating droplet (given by the aspect ratio, major axis over minor axis, (a/b) as a function of time in a quadrupole AC field. The time-dependence of the fissility $X(t)$ is due to the decreasing droplet radius in time. The amplitude and mean value of the driving AC field are scaled and shifted for better readability of the phase. The spontaneous spheroidal deformation of the droplet takes place for $X \simeq 0.997$ with a phase shift of about $\pi/2$, as highlighted by the vertical black line. The simulation used a quadrupole AC field of 200 Hz having a potential amplitude at the droplet surface of 40 mV.*

droplets in an external oscillating quadrupole field of the Paul trap. Simulations show that the forced oscillation in a Paul trap will not trigger the spontaneous deformation until the fissility of the droplet gets close to the Rayleigh limit. In figure 1.5, we simulated the droplet oscillation in an AC quadrupole field. The frequency of the AC field and it's potential at the droplets surface were chosen to reproduce the experimental conditions of the setup used by Duft (2003). The electric potential of the external AC field drives the mobile charges at the droplet's surface, inducing a quadruple Coulomb pressure at the surface, making the quadrupole mode of the surface oscillate at the frequency of the AC field. Details about the simulations will be given in section 1.4. Due to evaporation, the radius $R(t)$ of the droplet decreases with time. As a result the fissility $X(t)$ of the droplet increases (1.3), while the eigenfrequency of the quadrupole moment $f_2(t)$ decreases. Using
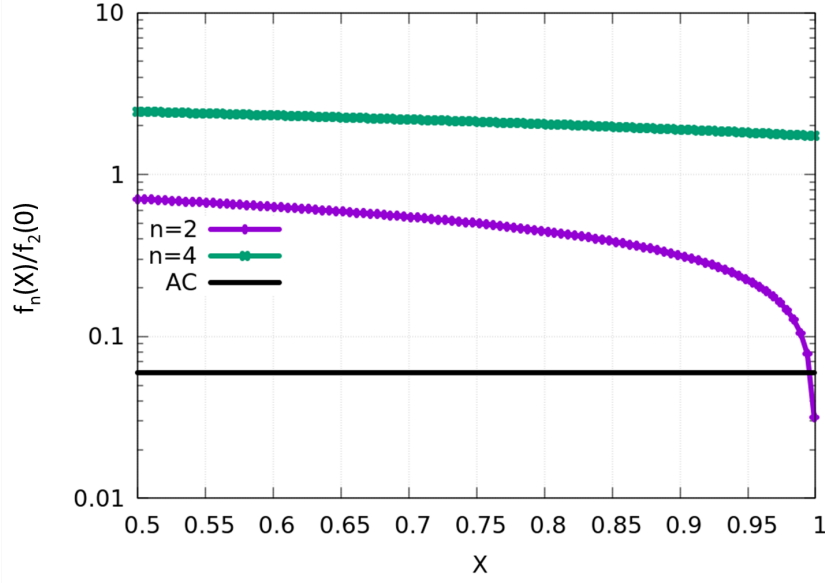
Figure 1.6: Eigenfrequencies $f_n(X)$ of the quadrupole mode (violet) and octupole mode (green) as a function of the fissility X, normalized with respect to the quadrupole frequency $f_2(0) = 8.5$ kHz of a neutral $(X = 0)$ water droplet of $R_0 = 100$ μm. The frequency of the quadrupole field of the trap is typically about 200 Hz, thus $f_{AC}/f_2(0) = 0.0176$. In this case, the quadruple eigenfrequency $f_2(X)$ of the given water droplet crosses the AC frequency at $X = 0.997$.

equation 1.2, the time-evolution of the eigen-frequency may be written,

$$f_2(t) = f_2^0(t) \left(1 - \frac{R_c^3}{R^3(t)} \right)^{1/2} = f_2^0(t) \left(1 - X(t) \right) \tag{1.4}$$

where $f_2^0(t) = \frac{1}{2\pi} \sqrt{\frac{8\gamma}{\rho R^3(t)}}$ is the quadrupole eigen-frequency of a neutral droplet of radius $R(t)$ and $R_c = (Q^2/(64\pi^2\gamma\varepsilon_0))^{(1/3)}$ the critical radius. Once the droplet radius approaches the critical radius, $f_2(t)$ decreases quickly and reaches the frequency f_{AC} of the AC field in the Paul trap (see figure 1.6). At that point, the amplitude of the quadrupole mode increases due to the resonance, triggering the spontaneous spheroidal deformation of the droplet (see figure 1.5). This also means that, out of resonance, the amplitude of the forced oscillations of the droplet in the Paul trap is so small that it cannot trigger the spontaneous deformation of a droplet. Only at resonance and only for $X \simeq 1$ can the spontaneous deformation of a droplet be triggered by the AC field of the Paul trap. In agreement with Taflin [22], this study discards thus the assumption that the AC field may trigger the spontaneous deformation of the droplet for fissilities X well below unit.

9

1.1.2   How does the deformation develops ?

While the eigenfrequency analyses of the first multipole modes of surface oscillations tells us that the quadupole mode is the first to become unstable, it does not tell us how the droplet deforms initially. Using the deformation energy for small quadrupole amplitudes [5],

$$W(a_2) = \frac{4}{5}(1 - X)a_2^2 + \frac{3}{5}(X - \frac{3}{2})a_2^3 + \dots \quad , \qquad (1.5)$$

we can discuss the initial spheroidal deformation at the Rayleigh limit. The deformation energy has been plotted in figure 1.7 as a function of the amplitude a_2 and for three different fissilities. For $a_2 > 0$, the droplet is prolate spheroidal and for $a_2 < 0$ the droplet is oblate spheroidal, with the axis symmetry as indicated. For $X < 1$, the energy potential wall is parabolic with positive curvature and the droplet shape oscillates between oblate and prolate. For $X = 1$, the quadratic term in W is zero and the cubic term dominates. As a result, for $a_2 > 0$, the barrier has been suppressed and the droplet deforms spontaneously towards prolate spheroidal shapes. As we will see, prolate shape deformations are indeed observed in the experiments. Interestingly, for $X > 1$, the oblate deformation space is now also accessible and the droplets can become oblate. The latter deformation mode can be enforced by pre-deforming the droplet into a oblate shape when reaching
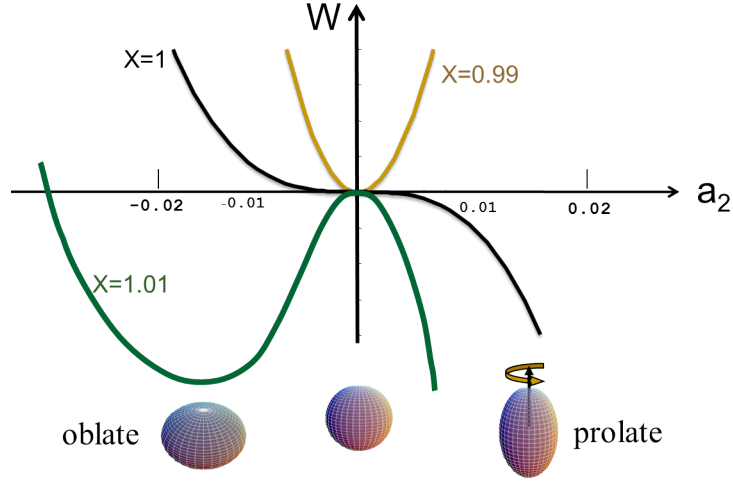
Figure 1.7: *Deformation energy of a critically charged droplet as a function of the amplitude of the quadupole mode. For a negative amplitude, the deformation is oblate, while for positive it is prolate. The deformation energy is given for subcritical ($X < 1$), critical ($X = 1$) and super-critical ($X > 1$) fissilities.*

the Rayleigh limit. However, in the Paul trap, the evaporating droplet is initially sub-critical $X < 1$ and the fissility approaches the limit from the lower end. As a result, the droplet always deforms spontaneously towards a prolate spheroidal, just before crossing the $X = 1$ limit.
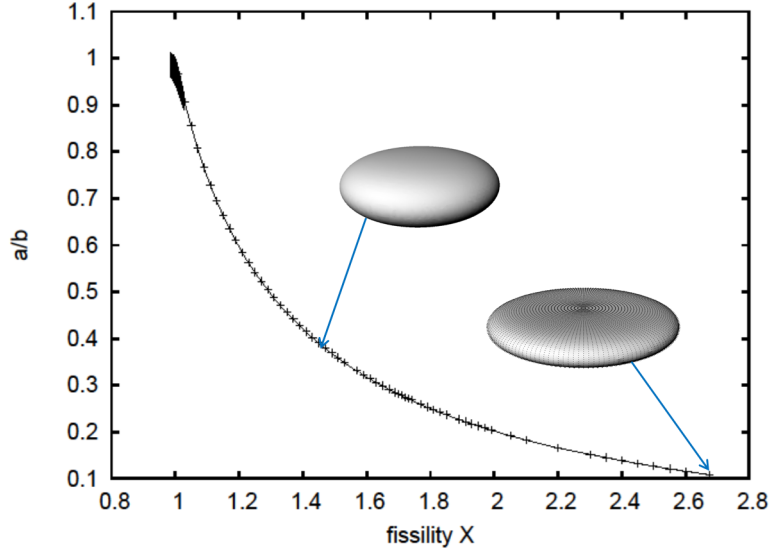
Figure 1.8: Equilibrium shape of a super-critically charged droplet as a function of the fissility. Deformation is assumed axisymmetric.

Note that in the super-critical case $(X > 1)$, the deformation energy shows a minimum for a negative amplitude. I would like to stress that in this analysis, the drop deformation is assumed axisymmetric. The existence of a minimum in the deformation energy means that one can expect the super-critical droplet to stabilize in an oblate shape and that the equilibrium shape depends only on the fissility. Simulations performed with our numerical code, based on the approach given in section 1.4.4, indeed confirmed that the droplet stabilizes in an oblate-like shape. The higher the fissility the flatter the droplet (see figure 1.8). For fissilities above 2, the shapes tends towards a disk, with the charge located at the border, where the curvature is largest. The insets of figure 1.8 shows the disk-like droplet for two different fissilities, namely $X = 1.4$ and $X = 2.7$. For larger fissilities, the simulations were not accurate enough to be predictive. Similar results, based on axisymmetric Navier-Stokes calculations, were presented in [58]. The trend suggests that, with increasing fissility, the droplet ends up in a doughnut shape,

11

as it would reduce the surface energy with respect to the disk shape. While oblate deformations can be calculated numerically for super-critical droplets by enforcing an initial oblate shape, it is much harder to observe them experimentally as the droplet is usually initially sub-critical and deforms spontaneously into the prolate domain when reaching the critical radius due to evaporation. One could however image the case where the charge of a slowly oscillating drop in a Paul trap is suddenly increased above the Rayleigh limit by an intense ion beam so that it becomes super-critically while being oblate deformed[4]. Another reason why such oblate shape may never be observed is that the droplet can deform by breaking the axial symmetry of the drop and elongate along an arbitrary direction orthogonal to the symmetry axis. As our code imposes axial symmetry, such calculations were not performed. Nevertheless, it would be interesting to calculate the stability of the equilibrium shape against small surface perturbations in a future work.

Observation of the prolate shape evolution

While the work of Duft *et al.* (2002) [38] confirmed the Rayleigh prediction of the instability of charged droplet close to the Rayleigh limit, it was still unclear how exactly the drope deforms and how exactly the charge was emitted from the droplets. In a pioneering work, Duft and coworkers [39] published in Nature (2003) the observed shape evolution of a critically charged ethylene glycol droplet, by taking snapshots of a fast deforming droplet at the Rayleigh limit (Fig. 1.9). The charged droplet was trapped in a Paul trap and the radius of the evaporating droplet was monitored. From the vertical position of the droplet in the trap, the ratio charge over mass was deduced. From the radius, the initial charge was calculated. A scheme of the setup is given in figure 1.11 and details about the experimental techniques are found in [38, 39, 42, 49]. A similar setup is further discussed in section 1.2.

The injected charged drop is stabilized in the middle of the Paul trap, while it's fissility increases with ongoing evaporation. Once the eigenfrequency of the quadrupole moment of the surface oscillation of the charge drop reached the frequency of the AC field of the Paul trap, the droplet deforms spontaneously into a prolate form. The onset of the deformation is tracked by the photo-multiplier which triggers, with a predefined delay, the flash lamp. This way the snapshots are takes at different deformation times. Putting the time origin at the moment the jet appears, the first snapshot was taken 150 μs before the time origin, when the droplet had already a clear prolate shape. The droplet deforms fast into a rugby-ball shape and then pointed ends appear at the tip. The charge concentrates at

---

[4]Note that the author has not evaluated if such a fast charge accumulation is possible with ion beams.
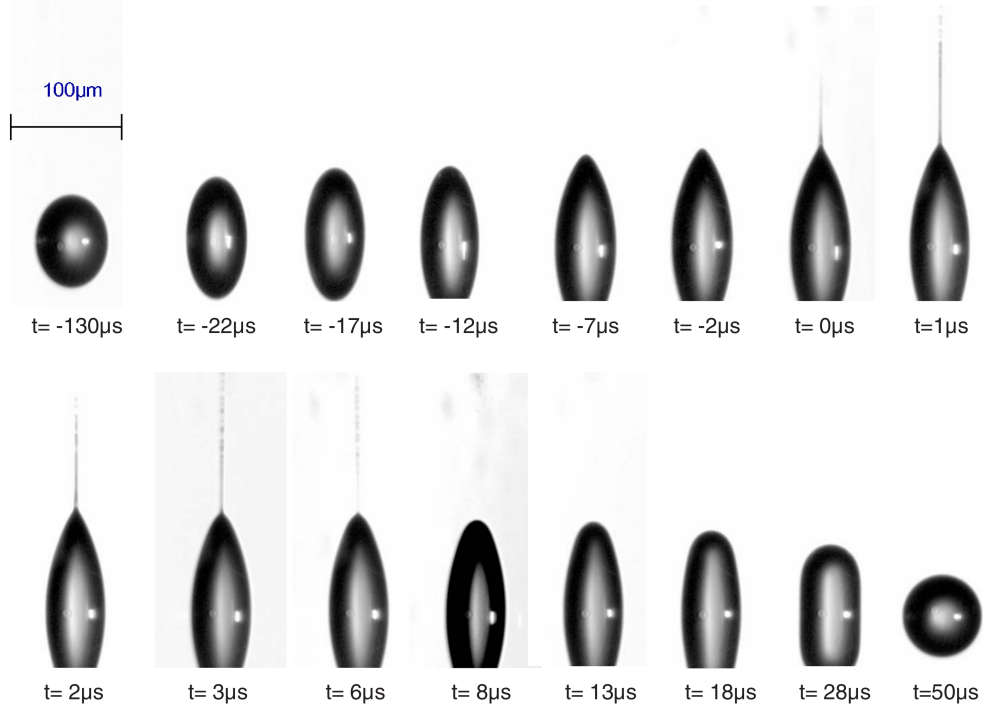
Figure 1.9: Snapshots showing the shape evolution of a glycol droplet with a radius of 24 μm after the onset of the instability. Droplet's temperature when injected was (85° C). During evaporation in an atmosphere at room temperture, the liquid cools down so that the temperature, at the moment of instability, is unknown (but estimated close to room temperature). Jet emission is chosen as origin of time. The second jet at the bottom of the droplet is not shown. Extracted from Giglio et al. (2008) [49]

the tips (because of the point effect) increasing locally the coulomb pressure. A jet is formed and charged matter is ejected from both tips. The fine jets of matter together with the concentrated charge at the tip explain intuitively the ~ 35 % charge loss and only ~ 2 % mass loss during the process. The total charge of the droplet has decreased by a certain amount and the fissility becomes again sub-critical. The jet breaks up after several microseconds and the droplet returns to its initial spherical shape. With ongoing evaporation the droplet reaches again the Rayleigh limit, trigging a new deformation and jet emission, until the drop has evaporated completely. The series of snapshots allow to realize a "film" of the charge break-up. Apart from Glycol drops, the group of T. Leisner also investigated water droplets and in particular supercooled ($-5°$ C) pure water droplets, which are found in thunderclouds. Figure 1.10 shows snapshots of the shape evolution of such a supercooled water droplet. Note that while the shape evolution is

13
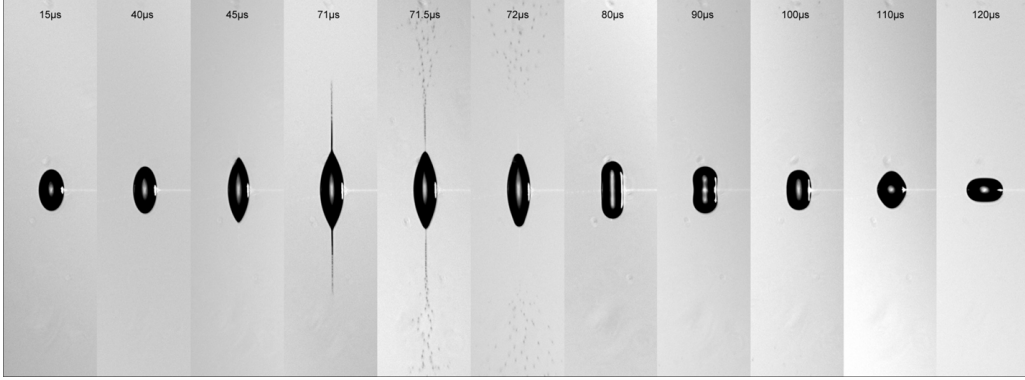
Figure 1.10: Snapshots showing the shape evolution of a supercooled water droplet (-5°C) with a radius of 35 μm after the onset of the instability. Extracted from Giglio et al. (2008) [49]

in general similar to the one for Glycol, it differs in detail, motivating thus further investigations.

1.1.3 Motivation

The aim of this work is to describe numerically and experimentally the shape evolution of a critically charged droplet. The topic arose from a collaboration of a group of CIMAP supervised by B. Huber and a group of the university of Karlsruhe supervised by T. Leisner. It was found experimentally that the deformation pathway as well as the jet emission of glycol droplets differs in detail from supercooled water droplets [49]. For example, the elongation of the glycol droplet just before jet formation was larger than for supercooled water droplets, which in turn was larger than water droplet at room temperature. In particular, for water droplets at room temperature, no jet emission was observed but charge emission of more then 20 % of the initial charge was still measured, hinting to an extremely thin jet and/or super-fast build up and relaxation of the jet during charge emission, so that the probability of getting a snapshot of the jet was too small. Also, for low viscous water droplets, the return to the initial spherical shape went through strongly deformed intermediate droplet shapes, which were not observed for glycol drops.

On the theoretical front, no reliable simulations of droplet deformations existed so far except for the work of Belelú *et al.* who presented a preliminary study of the viscous droplet deformation in the creeping flow approximation (Stokes flow). However this approximation may break down for the ultrafast low viscous droplet deformation, for which the advective inertial forces may dominate the viscous

14

forces. We propose in this work to model and simulate the droplet break-up of a critically charged droplet, from the initial spherical shape to the jet formation and back to the spherical shape. This allows to highlight the role of the different liquid parameters like density, viscosity, surface tension and conductivity of the liquid on the shape deformation and jet formation. We want a model that is able to predict with high accuracy the different shapes of the deforming droplet and explains in how far the conductivity or viscosity of the liquid affect the details of the droplet deformation and jet formation. Analysing the tip shape just before jet formation, will confirm if the jet is emitted from a Taylor cone as for electrified liquids [8]. Further it gives the intensity of the electric field at the tip at charge break-up and. Finally details about the jet formation and it's size can be studied. It ought to be emphasized that the interest in not purely academic as the production of micro-sized or nano-sized jets is of present considerable importance in modern technologies that require a fine control of the size of the jets and their decay droplets. For this purpose, we developed numerical codes able to simulate the axisymmetric deformation of a charged drop in the presence of an external field (for example the AC field of the quadrupole trap). The model is based on various approximations of the Navier-Stokes equation and will be discussed in section 1.4.

On the experimental front, we propose to build our own setup that allowed us to inject droplets of various liquids, trap them and observe their spontaneous deformation once it reached the critical fissility. The motivation is to produce new experimental results which provide guide lines (constraints) to theoretical models. A particular case represent mercury droplets which have high conductivity and high density. They represent thus model systems for theoretical study as the droplet surface is an equipotential and the dynamic viscosity of 1.5 ctP is rather low (comparable to water) so that simplified numerical models can be used to simulate the deformation of mercury droplets. Other interesting liquids are water droplets with additional salt or acid to increase their conductivity. Or a mix of glycol and water so as to modify finely the viscosity of the liquid. Finally we want to change the polarity of the charged droplets to study the effect of the conductivity on the droplet deformations and jet emission as the mobility of positive and negative charge carriers in the same liquid may differ significantly.

The topic was founded by the ANR 2007 program (ANR-07-JCJC-0062-01, label "Dynamic") for 3 years for an amount of 135 000 €, including a post-doctoral position of 12 month that was attributed to D. Allister Radcliffe. The program founded a new experimental setup for injecting, trapping and observing droplet deformations of different liquids via highly resolved snapshots.

1.2 Experimental setup

The experimental setup used for trapping and taking snapshots of the droplet is similar to the one presented in [39, 42, 49]. In a nutshell, a charged droplet is injected into a Paul trap, where it evaporates until it reaches the critical fissiliy $X = 1$. The onset of the Coulomb instability is monitored by a photo-diode which triggers the flash lamp and the CCD camera. Delaying the trigger allows taking snapshots at different times of the shape deformation. We give below some details
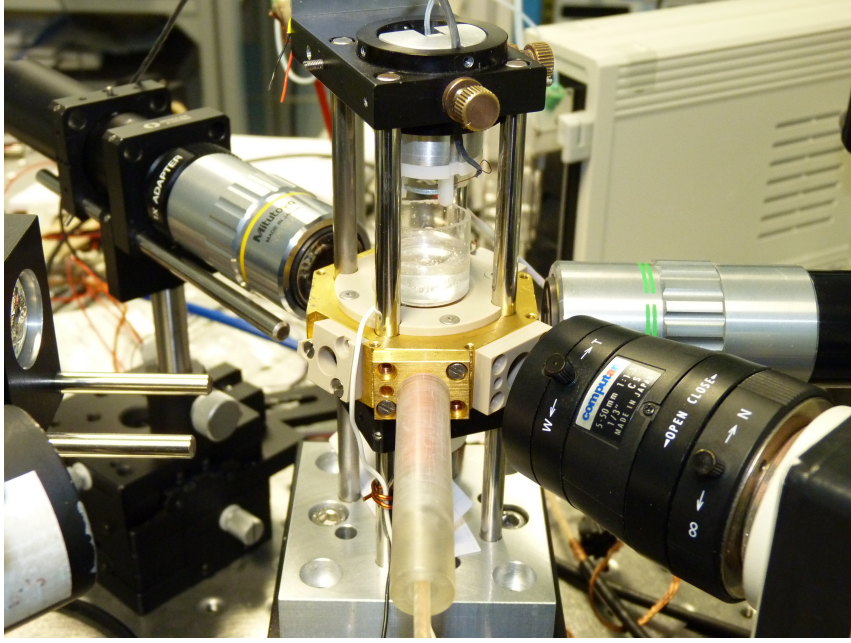
Figure 1.11: Photo of the setup in CIMAP. Vertically above the quadrupole trap is the injector for micro-drops. Flash-lamp, CCD camera photo-multiplier and optics for the laser beam are shown. Credit to Jimmy Rangama (CIMAP).

about the experimental setup.

Individual droplets are generated on demand with a piezo-driven nozzle, charged by influence from a high voltage electrode and injected into a electrodynamic balance operating at ambient pressure. The electromagnetic levitator has been generously borrowed by the group of T. Leisner of Ilmenau [38, 39, 42]. The levitator follows a well proven design [17, 21] and consists of two ring electrodes (inner diameter, 10 mm; vertical distance, 2 mm) which are encapsulated in a chamber. The chamber is machined from massive brass in a shape of an octagon and carries the necessary ports for various optical and electrical probes. In order to levitate the charged droplets, an AC voltage of about 2 kV amplitude and a frequency of

16

200 Hz is applied to both ring electrodes. The resultant electrical quadrupole field is rotationally symmetric around the vertical axis. For a charged particle with a large charge over mass ratio, the AC field would be sufficient to trap the particle in the center of the trap. For charged micro-droplets however, the ratio charge over mass is too low and a static vertical field for the compensation of the gravitational acceleration on the droplet is needed. The latter is created by superimposing a DC voltage of opposite sign to the top and bottom electrode. The droplet is illuminated by a NeHe laser beam in the horizontal plane and imaged onto a vertically oriented linear CCD array in order to determine its vertical position in the trap. The CCD array then pilots the intensity of the DC field to keep the droplet centred in the trap, via a feed-back regulator. From this voltage, the mass to ratio the of the droplets can be determined with a time resolution of 100 ms. This value serves to adjust the frequency of the AC voltage to assure stable trapping as the droplet evaporates. Under typical conditions, this frequency varies between 200 Hz and 500 Hz. The Laser light scattered from the droplet under 90° is collected
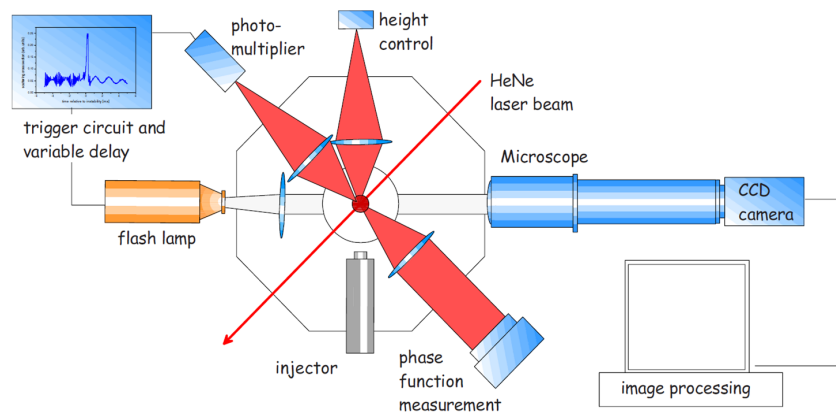
Figure 1.12: Schematic experimental setup (cross section through the levitator in the horizontal plane. Unlike the setup used by Duft et al. (2003) the injector is placed vertically above the quadrupole trap. Extracted from Giglio et al. (2008) [49]

by a second microscope objective and imaged onto a photo-multiplier tube. Its signal serves to control the amplitude of the forced quadrupole oscillation of the droplets in the field of the trap. It also serves to track the onset of the instability. Indeed, when the droplet becomes prolate spheroidal, the intensity of the reflected light increases. The fast increase of the signal provides the origin of the time at the onset of the instability which serves to trigger the flash lamp and the CCD camera after a predefined delay for the ultrafast photography of the droplet shape.
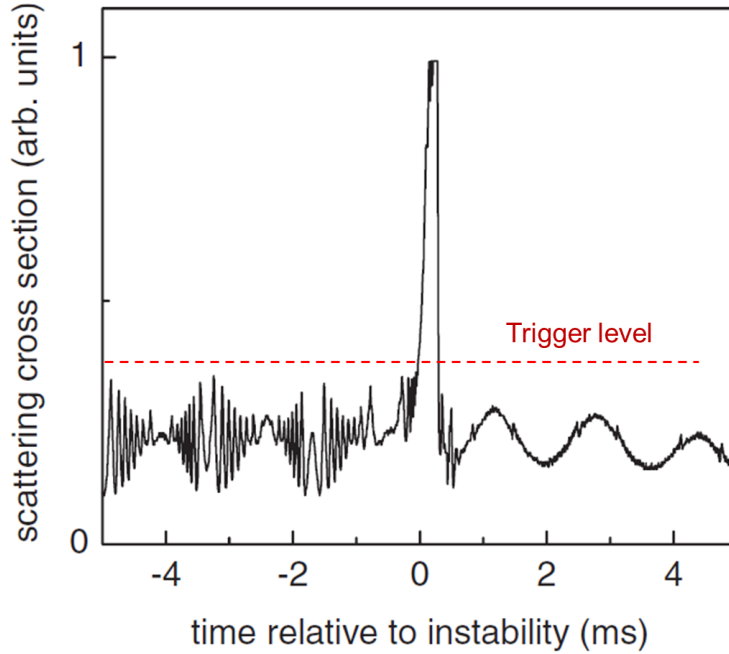
Figure 1.13: Time resolved light scattering intensity of a levitated droplet around the break-up. Red dashed line gives the trigger level for fixing the time origin. Extracted from Giglio et al. (2008) [49] and modified to include the trigger level.

Injector

The shape deformation taking place in typically less then 300 μs, the setup can take only one single snapshot of the deforming droplet. The sequence of snapshots given in figure 1.9 and 1.10 represents thus each time a different droplet. In order to have a coherent sequence, the size and charge of the injected droplet as well as its injection velocity must be perfectly reproducible. We chose therefore a piezo-electric injector like the one presented in figure 1.14. The integrated piezoelectric actuator induces a shock-wave into the fluid contained in the head, which causes a droplet to be emitted from the nozzle. The experimental results presented in section 1.3 where obtained using a piezoelectric microdispensers from GeSim. The latter was limited to liquids having a viscosity of less than 5 mPa.s and was not heatable. The liquid was grounded and the injector positioned 2 mm on top of a centred ring electrode, which is polarized so as to create an electric field of about 1 kV/mm between the electrode and the outlet of the dispenser. Under the influence of the electric field, the charges in the jet produced by the injector are separated. When the drop separates from the jet, the drop has accumulated an excess charge. With the computer controlled inject-unit, droplets of same size and

charge are produced with high reproducibility. Once produced, the droplets fall into the trap 15 mm below where they are immobilized by the electric field. It should be emphasized that compared to the setup of our colleagues in Ilmenau, we lacked the possibility to heat the injector as well as heat or cool the Paul trap.
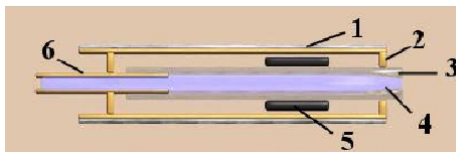
Figure 1.14: Scheme of a piezo-electric injector. (1) piezo-driven plates, putting a pressure on the liquid, injecting liquid from the nozzle; (2) Grounded electrode; (3) Glass tube, (4) liquid.

Taking Snapshots

The trapped droplets have a diameter between 20 to 80 μm. The instability lasts between 20 and 400 μs. For image acquisition, we chose therefore to use a high resolution CCD camera (PCO 2000) which has an ultra-fast shutter ($\sim$ 5 μs) equipped with an objective $\times 20$. The light source for illuminating the droplet is a flash lamp NANOLIT (High-Speed Photo-System). The lamp has the particularity of emitting a light flash which lasts about 25 ns for an energy of 9 mJ. The set, "CCD/flash" is triggered during the instability. By varying the delay time after the photo-diode has detected the onset of the instability, a series of time ordered snapshots are obtained. The size of the droplet can be determined from the microscope images within an error of ± 0.5 μm form the first prolate shaped drop or alternatively from the final spherical drop.

1.2.1 Deformation pathway

In order to compare easily the deformation pathways of different droplets, the shapes have been fitted with the mathematical expression of a superellipsoid of the form

$$\left|\frac{z}{a}\right|^n + \left|\frac{\sqrt{x^2 + y^2}}{b}\right|^n = 1 \quad . \tag{1.6}$$

The shapes have been fitted with the constraint of constant volume so that the fit had only two independent parameters, namely a/b and n. Superellipsoid can either fit capsule or spindle-like forms, depending on n. The aspect ratio a/b gives the elongation of the droplet. Adjusting $(a/b, n)$ for the droplet shape for each

19
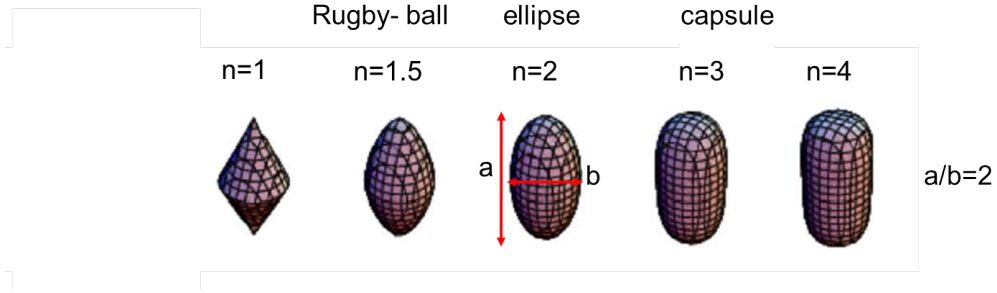
Figure 1.15: Superellipsoids have a mathematically simple expression (eq. 1.6) and can fit most of the observed droplet shapes with just two degrees of freedom, $(\frac{a}{b}, n)$, from pointed rugby-ball to spheroid to capsule with increasing n (generated with the Superellipsoid function in Mathematica (Wolfram))
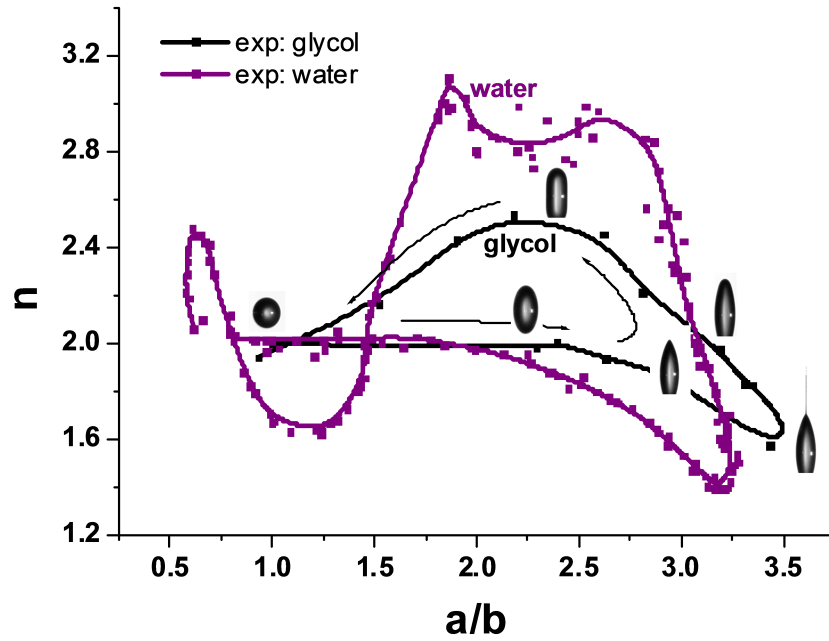
Figure 1.16: Deformation pathway for glycol (black) and supercooled water (violet) droplets. The aspect ratio a/b and exponent n correspond to a shape fitted with a superellipsoid. The arrows give the direction of the time evolution of the path. Extracted from Giglio et al. (2008) [49]

snapshot yields a number of points that can be plotted on an graph with a/b as the abscissa and n as the ordinate, so that the whole droplet deformation path can be represented reasonably well on a 2D graph. In figure 1.16, we give the deformation pathway of glycol and water droplets, where the snapshots have been shown in figure 1.9 and 1.10 respectively. Fitting the shapes by a superellipsoid allows to compare the deformation pathway of droplets having different liquid properties. First, we note that the general behavior is similar in both cases: the instability starts with increasing a/b, while n remains nearly constant at $\simeq 2$, meaning that the initial deformation remains mainly prolate spheroidal. Then n decreases and the form becomes spindle-like. The charge emission however occurs at $a/b \simeq 3.2$ and $n \simeq 1.4$ for water drops and at $a/b \simeq 3.5$ and $n \simeq 1.6$ for glycol. After emission, the tip flattens, while n increases quickly well above 2 to fit an elongated capsule, before both parameters come back to their initial values. The return can be monotone or oscillatory, depending on the viscosity of the fluid. Indeed, the water droplet exhibits a double oscillatory behaviour between an oblate and prolate ellipsoid and between sharp and flattened ends. For glycol, the amplitudes of this motion are much smaller than for water, as dissipation is much stronger. The $(a/b, n)$ representation of the droplet shapes is thus a handy tool to analyse in detail the spontaneous shape evolutions of droplets at the Rayleigh limit of liquids with different physical properties. It should be noted that the scattering in the experimental data shown in the (a/b,n) graphs results mainly from the qualitative fit of the snapshots by the superellipsoid equation. The fit was done using a software, written by Pierre Salou (at that time PhD student in CIMAP), and then the obtained values (a/b,n) were verified for consistency by the authors. Similar shapes can give some dispersion in the fitted parameters especially for $n > 2.5$ and $n < 1.7$. In the following, we will use the deformation pathway as an analysis tool to study the influence of the liquid properties on the droplet shape deformation.

1.3 Experimental Results

We wanted to explore the charge break-up of droplets for a large range of viscosity, density, surface tension and conductivity. We wanted to see the influence of those parameters on the deformation pathway and jet formation as well as charge emission. The idea was also to gather experimental data that are constraints for the numerical model presented below.

Mercury droplets

One interesting class of liquids are metallic liquid like mercury, which are electrically conducting and have a low viscosity of about 1.5 mPa.s (1.5 cP), see Table

	density (kg/m³)	surface tension (N/m)	viscosity (cP)
water (20° C)	1000	0.072	1
water (−5° C)	1000	0.076	2.2*
glycol (25° C)	1102	0.048	16
mercury (20° C)	13500	0.48	1.5

Table 1.1: Physical properties of various liquids (1 cP = 1 mPa.s).
*Viscosity of pure water at −5° C is obtained from "Viscosity of deeply supercooled water and its coupling to molecular diffusion", A. Dehaoui, B. Issenmann, and F. Caupin, PNAS September 29, (2015) 112 (39) 12020-12025; https://doi.org/10.1073/pnas.1508996112.

1.1. Mercury droplets should behave closely to perfectly conducting inviscid liquid drops, a class of ideal liquids. The emitted charge carriers in the jet of positively and negatively charged mercury droplets during charge breakup is also fundamentally different so that metallic droplets are a class of their own. We tried thus to inject and trap mercury micro-droplets in our Paul trap. Unfortunately, after several months of testing we did not succeed in trapping mercury droplets. The problem lay mainly within the injector. The meniscus of the mercury liquid at the outlet of the injector tent to oxidize quickly, blocking further injection. We
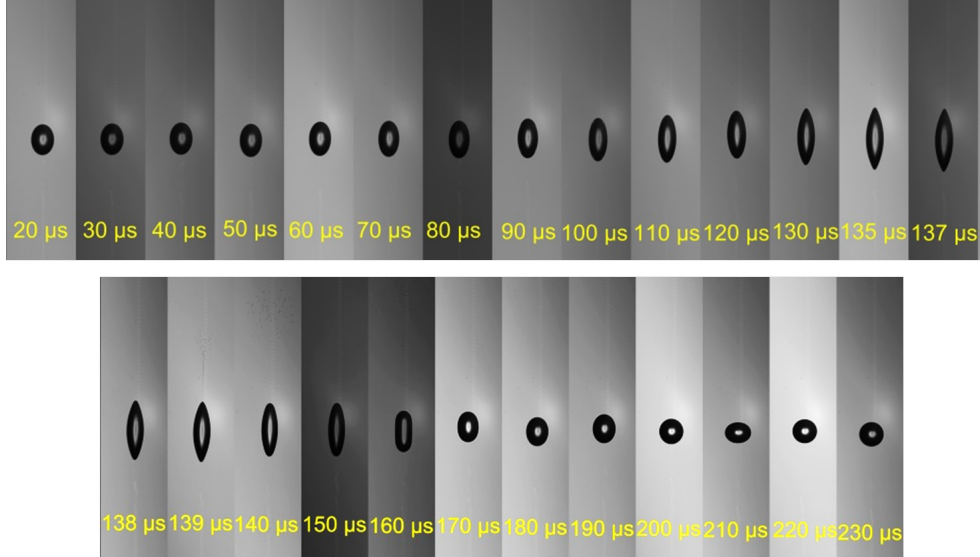
Figure 1.17: Snapshots of the deforming,droplets (⌀ = 52μm) after the onset of instability. Droplet composition was 60% water and 40% glycol, injected at room temperature.

tried two different injectors: A home-maid $\varnothing = 80\mu$m injector graciously borrowed by the group of T. Leisner and a microdrop dispenser (MD-K-130) with a non-heated $\varnothing = 70\mu$m nozzle head from microdrop. At the end, both injectors were quickly made unusable by the mercury liquid. Also, the weight of the droplets was such that they fall simply through the trap, even when a DC field was present to balance the weight of the drops. Finally, the stringent regulations and constraints associated with the manipulation of toxic mercury made the drop injection and trapping a difficult task. We had to move the whole setup under a chemical hood, adding some delay and increasing the manipulation difficulties. As we never succeeded to repetitively trap mercury droplets, we give up the study of critically charged mercury micro-droplets. Note that another non-negligible factor that makes the observation of mercury droplet a difficult task is its low vapour pressure of 0.002 mbar, reducing the evaporation rate by a factor 1000 with respect to water droplets at room temperature, meaning that a trapping time of several hours may be necessary before the droplet reaches the Rayleigh limit.

Glycol-water droplets

We then switched to glycol-water droplets. By varying the percentage of water in a glycol-water mixture, we were able to alter finely the viscosity of the droplets between 1 and 20 cP. However, here we were limited by our piezo-electric injector, which is able to work only with liquids having a viscosity lower than 5 cP. We succeeded to inject and trap droplets at room temperature, having a mixture of 60% of water and 40 % of glycol. From the data sheet Ethylene Glycol-MEGlobal [5] we get the viscosity and surface tension of the mix at 23° C, namely $\mu_{\mathrm{mix}} \simeq 2.3$ cP and $\gamma_{\mathrm{mix}} \simeq 0.058$ N/m. We show in figure 1.17 snapshots of the deforming droplet at different times after the onset of the instability. When injected, the trapped droplets have an initial radius of 34 μm. We estimate the density ρ of the mix to be well approximated by the weighted mean value of water and glycol, $\rho_{\mathrm{mix}} = 1060$ kg/m^3. At the onset of the instability, we found the radius to be about $R = 26$ μm, meaning that the droplet carried a charge of about $Q = 4\pi\sqrt{\gamma_{\mathrm{mix}}R^3\varepsilon_0} \simeq 1.2$ pC. We see that 137 μs after the onset of the instability, the droplet emits a jet of charged matter. We remind that the times below the snapshots give time intervals relative to a trigger rather than absolute times. Indeed, they are taken relative to a threshold deformation that triggers the flash lamp. As the threshold value is put manually to an arbitrary value between $1.2 < a/b < 1.5$, the times may vary from one experiment to another. At the moment of jet emission, the elongation ratio a/b is about 3.2, similar to the one found for supercooled water (Fig.1.10 and Fig.1.18). After jet emission, the droplet returns to the spherical

---

[5]https://www.meglobal.biz/products-and-applications/product-literature/
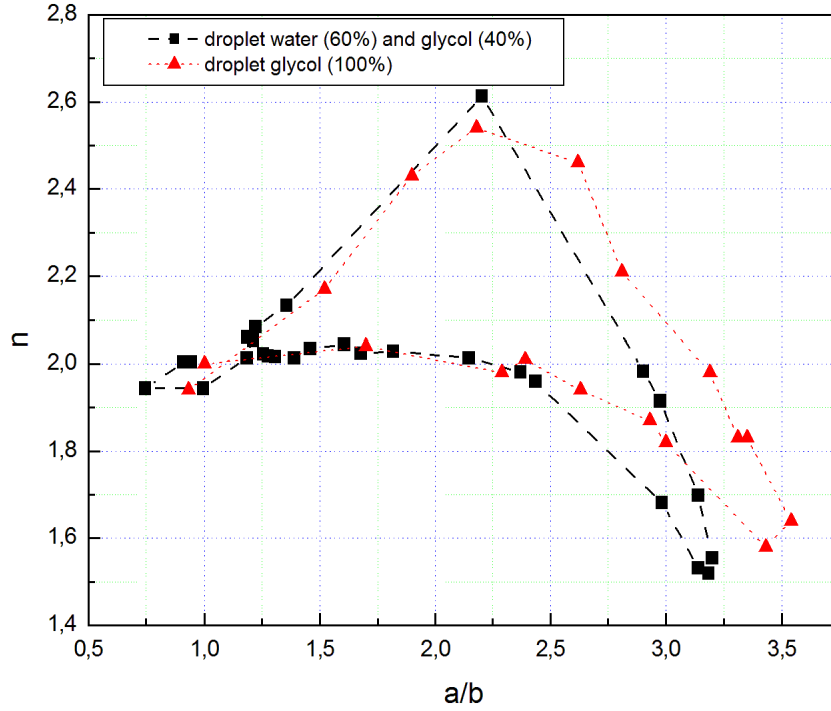
Figure 1.18: Deformation pathway for droplet of mixed liquids water 60% and glycol 40 % The aspect ratio a/b and exponent n correspond to a shape fitted with a superspheroid.

shape, with an overshooting at 200 μs into the oblate spheroidal domain. The deformation pathway of the water-glycol droplets is illustrated in figure 1.18, where is is compared to the pure glycol droplets. While the initial pathway ($a/b < 2$) are similar, they differ quickly with increasing elongation. In particular, the pointed tips form earlier, as is show by the parameter n, which decreases faster with a/b for the mixed liquid. Also, the mixed liquid droplet becomes oblate shaped, $a/b < 1$, on its "return" path, unlike the pure glycol droplet.

Pure water droplets

We also studied pure water droplets at room temperature (22° C). De-ionized water was used and graciously made available by Yvette N'Gono from CIMAP laboratory. Inverting the polarity of the polarization ring of the injector, we can inject negatively charged droplets. Of course, the DC field that balance the weight

of the drop needed to be inverted accordingly. In figure 1.32 we compare the deformation pathway of negatively and positively charged droplets. More than 200 snapshots were taken and fitted by a superellipsoid. Surprisingly no jets were detected on the snapshots, neither for positively nor for negatively charged water droplets at room temperature. We took more than 30 snapshots of the moment where the elongated droplet shapes have pointed ends, but found no trace of small daughter droplets or jets on the snapshots, unlike for glycol and supercooled water [39, 49]. We concluded that the jet was too thin to be observed and estimated that the jet radius, if any, must be smaller than the resolution of the snapshots of 0.36 µm. These observations are corroborated by the experimental results presented in the Ph.D work of R. Müller [52]. Full black squares stand
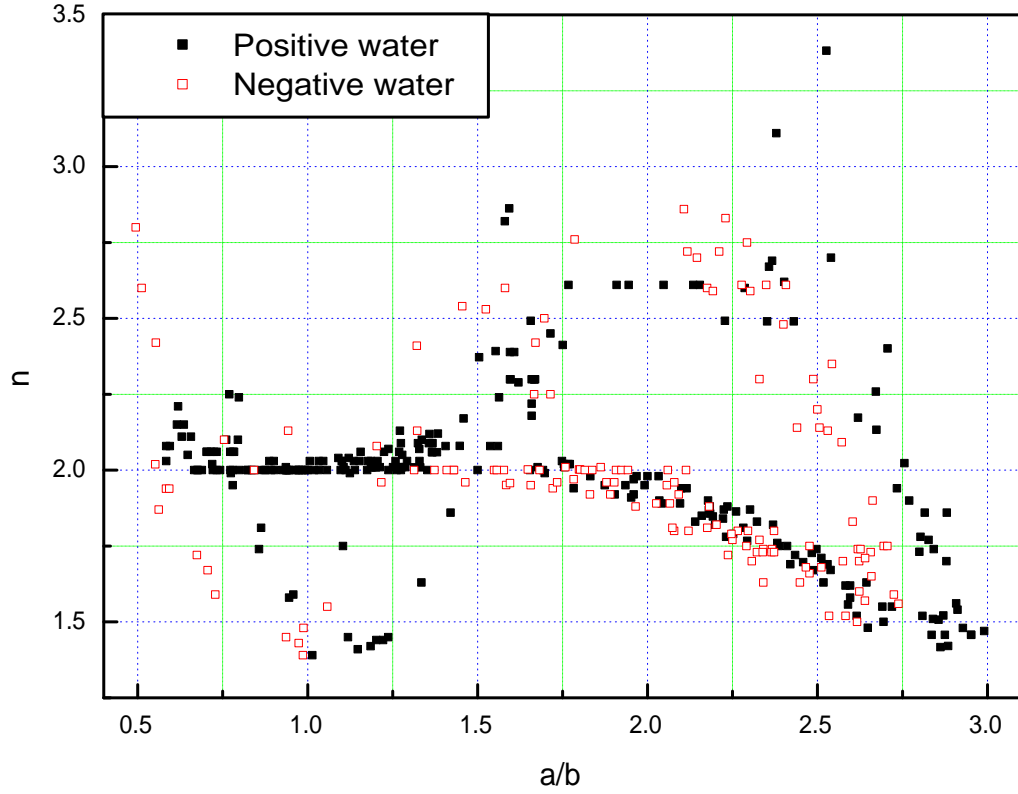
Figure 1.19: Deformation pathway for positively and negatively charged water droplets.

for positively charged while red squared stand for negatively charged pure water droplets. Both pathways are similar but differ in detail. We found that positively charged drops are more elongated (have a larger aspect ratio) at charge emission. Also, while both go through strongly deformed oblate shapes before returning the equilibrium (spherical) shape, the return path of positively and negatively charged droplets seems shifted by $\Delta a/b \simeq 0.4$. At this point we mere note that what differs positively from negatively charged droplets is the mobility of their respective excess charge carriers. For positively charged drops, the excess charge carrier is the proton or more precisely the hydronium cation H_3O^+ with a mobility of 36×10^{-8} $m^2s^{-1}V^{-1}$, while for negatively charged water drops it is the hydroxyl anion OH^-, with a mobility of 20×10^{-8} $m^2s^{-1}V^{-1}$, thus almost two times slower [53, 32]. The influence of the charge mobility will be studied in detail in section 1.5. Below, in figure 1.20, we give snapshots of positively charged pure water droplets at room temperature are shown. Having a low viscosity, water droplets show strongly deformed shapes after jet emission, with shapes ranging from "diamond" to "peanut" shapes and from oblate to prolate shapes.
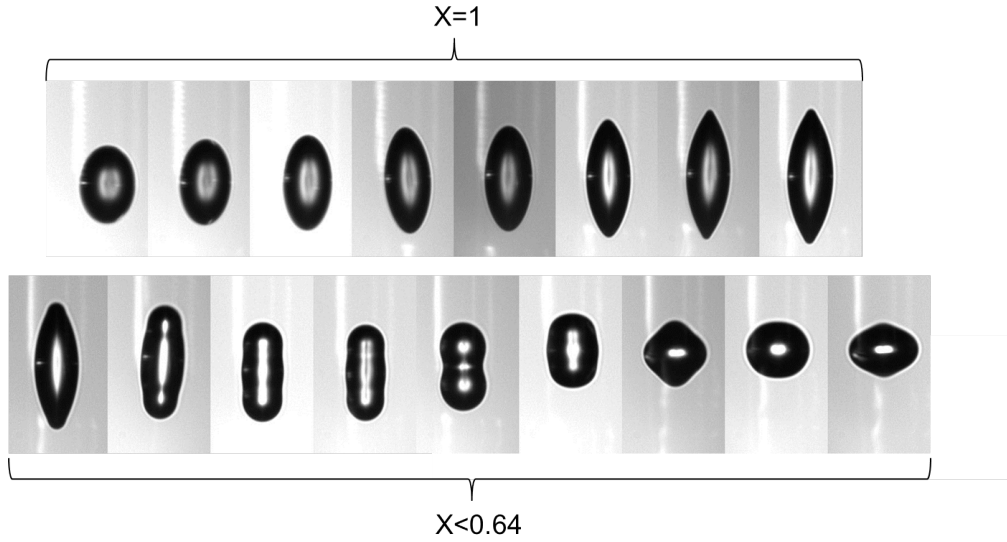
Figure 1.20: Snapshots of the instability of positively charged water droplets, injected at room temperature. Note the absence of jets and daughter droplets.

1.4 Theoretical models and simulations

Using simulations, we want to understand in more detail how the viscosity and electrical conductivity influence the shape deformation of critically charged droplets. Some simulations of critically charged droplet deformations have already be performed by several authors. We may cite the work of Belelú *et al.* [46] and Gawande *et al.* [62] who presented a study of the shape deformation of a charged viscous perfectly conducting drop suspended in air. Using the boundary-element method (BEM) to solve the Stokes flow equation (creeping flow approximation), they found that the viscous drop attains an aspect ratio of 3.86 at charge breakup, close to the observed value of 3.85 [38, 39]. However the Stokes flow approximation may break down for the ultra-fast low-viscous droplet deformation, for which the advective inertial forces may dominate the viscous forces. The case of an inviscid perfectly conducting liquid droplets was discussed by Giglio *et al.* in [49] where the simulated pathway was compared to glycol and supercooled water droplets. The authors concluded that viscous forces or finite conductivity are necessary in order to simulate accurately the different experimentally observed droplet deformations. Burton and Taborek [55] extended the study of inviscid liquid drops by considering a finite ohmic bulk and surface conductivity and showed the influence of both conductivities on the elongation of the drop and on the tip formation. Alastair Radcliffe, who occupied a post-doc position in 2010 in our group SIMUL, used the finite element methods (FEM) to solve the Navier-Stokes (NS) equation and to simulate the deformation of perfectly conducting viscous droplets. His preliminary results [58] will be discussed in section 1.5.5. He later improved the algorithms and succeded to simulate the drop deformation up to the jet formation [59]. Related to our study are also the work of Nganguia *et al.* [60], who studied the inertia effects on the electrode formation of a viscous drop under a DC electric field. Collins *et al.* [50] used FEM with elliptic mesh generation and adaptive implicit time integration to solve the NS equations that described the jet formation of electrified liquids. They discussed the profile of the jet as a function of the liquid properties and found that conical (Taylor) tips can occur with perfectly conducting fluids because charge transport by ohmic conduction is instantaneous so that the electrostatic pressure continually balances the increasing capillary pressure. However, for a leaky-dielectric (low conductivity) fluid, jets develops without going through a conical cusp. In a later work, their simulations unequivocally show that electrospray daughter droplets, that is droplets that where formed by the jet of an electrified parent droplet, are coulombically stable at the instant they are created and that there exists a universal scaling law for the daughter droplets charge [57]. Alternatively, Gañán-Calvo *et al.* used the promising Volume of Fluid (VoF) method for tracking and locating the free surface (fluid-gas interface) [61]. They succeeded to simulate with high precision the first drop emitted from the

jet of an electrified parent droplet and give universal scaling laws for the diameter and electric charge of the first issued daughter droplet, that were validated both numerically and experimentally.

The main aim of this work is to study the shape deformation of a charged droplet as a function of the liquid properties. We propose thus to develop a numerical code, with the requirements that it simulates the whole deformation path of a critically charged droplet, from the onset of the Coulomb instability up to charge breakup and back to the initial sphere. This includes also the forced oscillations of a sub-critically ($X < 1$) charged droplet in the AC quadrupole electric field of the Paul trap (see Fig. 1.5) as well as the slow oblate deformation of super-critically ($X > 1$) charged droplets, (see Fig. 1.8). Below, we detail the theoretical approaches on which our numerical code is based.

1.4.1 Navier-Stokes equation for Newtonian incompressible fluids

We define the following quantities that will be used throughout the manuscript. Let Ω be the volume of droplet bounded by the interface $\partial\Omega$, and $\vec{s}$ a vector pointing at the surface. Let $\vec{n}(\vec{s})$ be the unit vector normal to the surface pointing outwards, and $\vec{\tau}(\vec{s})$ a vector in the corresponding tangent plane. Let $\phi(\vec{s})$ be an arbitrary scalar function defined on the closed surface $\partial\Omega$. We introduce the following surface operators, (where the dependence on $\vec{s}$ has been omitted) [43]

- $\vec{\nabla}_s \phi = \vec{\nabla}\phi - \vec{n}(\vec{n}\cdot\vec{\nabla})\phi$: tangential gradient $\qquad$ (1.7)
- $\vec{\nabla}_s(\phi\vec{\tau}) = \vec{n}\cdot(\vec{\nabla}\wedge(\vec{n}\wedge(\phi\vec{\tau})))$: surface divergence tangent vect. $\quad$ (1.8)
- $\vec{\nabla}_s(\phi\vec{n}) = -2H\phi$: surface divergence of normal vector. $\qquad$ (1.9)

The latter defines the local mean curvature H of the surface at the surface point $\vec{s}$. Further, we define the following quantities characterizing the liquid droplet:

- $\vec{u}$: velocity vector field [m/s] of the fluid.

- ρ : density of the fluid [kg/m^3], assumed constant ($\vec{\nabla}\rho = 0$).

- ε_r : dielectric constant of the fluid ($\vec{\nabla}\varepsilon_r = 0$).

- ε_0 : permittivity of the vacuum.

- γ : surface tension [N/m] of the fluid, assumed constant ($\vec{\nabla}_s\gamma = 0$).

- μ : dynamic viscosity [Pa.s] of the fluid.

- R : radius [m] of the spherical droplet.

28

- $\vec{E}$: electric field [V/m].

- V : electric potential [V].

- σ : surface charge density [C/m^2].

- κ : electric bulk conductivity [S/m] of the liquid.

- λ : charge mobility [m^2/s/V] of a charge carrier at the interface.

- X : fissility of the droplet.

We want to simulate the shape-deformation of an initially spherical charged drop in a gas g atmosphere. The liquid is supposed electrically conductive. As a result, the charges accumulate at the droplet surface and the electric field is divergence-free inside and outside the droplet volume,

$$\vec{\nabla} \cdot \vec{E} = 0 \quad \text{in} \quad \mathbb{R}^3 \tag{1.10}$$

This corresponds to the Taylor-Melcher leaky dielectric model [9]. In our particular case, the deformation is assumed axisymmetric and the liquid of the droplet incompressible. The density ρ of the liquid is thus constant. The latter condition implies that the velocity vector field of the fluid is divergence-free (solenoidal),

$$\vec{\nabla} \cdot \vec{u} = 0 \tag{1.11}$$

ensuring that the time evolution of the droplet occurs at constant volume. The Navier-Stokes equation for an incompressible (Newtonian) fluid in the volume Ω is expressed by the equation

$$\frac{d\vec{u}}{dt} = \frac{\partial \vec{u}}{\partial t} + \vec{u} \cdot \vec{\nabla}\vec{u} = \frac{1}{\rho}\vec{\nabla} \cdot T \tag{1.12}$$

where T is the stress tensor, defined by

$$T = -pI + 2\mu D + M \tag{1.13}$$

with I being the identity matrix, p the pressure in the liquid, $2\mu D$ the rate-of-strain tensor with

$$D = \frac{1}{2}\left(\vec{\nabla}\vec{u} + (\vec{\nabla}\vec{u})^t\right) \tag{1.14}$$

and M the Maxwell stress tensor

$$M_{i,j} = \varepsilon_0\varepsilon_r E_i E_j - \frac{\varepsilon_0\varepsilon_r}{2}\vec{E}^2\delta_{i,j} \quad . \tag{1.15}$$

Note that T is symmetric, $T = T^t$. As there are no volume charges, the electric force per unit volume is zero, $\vec{\nabla} \cdot M = 0$. Thus, in the leaky dielectric model, the Maxwell tensor is divergence-free.

Boundary conditions for viscous charged drops

The pressure p in the liquid is obtained via the boundary condition; the jump ($||$) of the normal stress across the liquid-gas interface of the droplet is balanced by the capillary (curvature) force per unit area P_s,

$$T_{nn}|| = \vec{n} \cdot (T^g - T) \cdot \vec{n} \; = \; T^g_{nn} - T_{nn} = P_s \qquad /\partial\Omega \qquad (1.16)$$

The latter is due to the phenomenon of surface tension γ, and is given by Young-Laplace equation,

$$P_s = \gamma(\vec{\nabla} \cdot \vec{n}) = \gamma(\vec{\nabla}_s \cdot \vec{n}) = -2\gamma H \quad . \qquad (1.17)$$

The right hand identity relates the mean curvature H to the surface divergence of the normal vector $\vec{n}$ at a surface point $\vec{s}$, according to (1.8). Having defined the normal vector at the drop interface pointing outward, the mean curvature of a sphere of radius R is negative, $H = -1/R$, so that $P_s > 0$. This definition ensures that the pressure of the liquid is higher than the pressure of the atmosphere! At room temperature, the dynamic viscosity of air is about 50 times lower than that of water. We suppose here that the viscosity of the outer gas atmosphere is negligible $\mu^g \ll \mu$ and that the pressure of the outer atmosphere p^g is constant (and set to zero[6]), so that at the drop interface $\partial\Omega$ one has:

$$\begin{aligned} P_s \; &= \; T^g_{nn} - T_{nn} & (1.18) \\ &= \; -(p^g - p) + 2(\mu^g - \mu)D_{nn} + M^g_{nn} - M_{nn} & (1.19) \\ &\simeq \; p - 2\mu D_{nn} + M^g_{nn} - M_{nn} & (1.20) \end{aligned}$$

We introduced the Coulomb pressure P_c, defined as the jump of the Maxwell tensor across the interface

$$P_c = M^g_{nn} - M_{nn} = \frac{\varepsilon_0}{2}\left((E^g_n)^2 - \varepsilon_r E^2_n + (\varepsilon_r - 1)E^2_\tau\right) \qquad (1.21)$$

Injecting the surface charge density $\sigma = \varepsilon_0(E^g_n - \varepsilon_r E_n)$ into (1.21) allows expressing the Coulomb pressure as a function of σ and the electric field (E_n, E_τ), evaluated at the liquid side of the liquid-gas interface of the droplet.

$$P_c = \frac{\varepsilon_0}{2}\left(\left(\frac{\sigma}{\varepsilon_0} + \varepsilon_r E_n\right)^2 - \varepsilon_r E^2_n + (\varepsilon_r - 1)E^2_\tau\right)$$

Finally rearranging (1.20) we obtain an equation for the pressure at the liquid interface,

$$-p = -P_s + P_c - \mu 2D_{nn} \quad , \qquad (1.22)$$

---

[6]As only the gradient of the pressure enters the dynamics, the pressure p^g can be chosen arbitrarily.

and the jump condition of the normal component of the stress tensor (1.16) may be expressed as

$$T_{nn} - M_{nn} \; = \; -P_s + P_c \quad . \tag{1.23}$$

In contrast, the shear stress $T_{\tau n}$ is continues across the free interface,

$$\begin{aligned} T_{\tau n}|| &= \vec{\tau} \cdot (T^g - T) \cdot \vec{n} = 0 \tag{1.24} \\ &= 2\mu^g D_{\tau n}^g + M_\tau^g - (2\mu D_{\tau n} + M_{\tau n}) = 0 \quad /\partial\Omega \quad . \tag{1.25} \end{aligned}$$

We deduce from (1.25), by neglecting the contribution of the viscous rate-of-strain tensor in the gas atmosphere, that the shear (tangent to the surface) component of the viscous rate-of-strain tensor in the liquid must be equal to the shear component of electric field E_τ at the surface times the surface charge density σ,

$$\mu 2 D_{\tau n} = (M_\tau^g - M_{\tau n}) = \sigma E_\tau \quad /\partial\Omega \quad . \tag{1.26}$$

Alternatively, boundary condition (1.25) may be expressed in the useful form,

$$T_{\tau n} - M_{\tau n} \; = \; \sigma E_\tau \quad . \tag{1.27}$$

where the latter equality is deduced from (1.15). Note that for a perfectly conducting liquid, $E_\tau = 0$, yielding the more usual condition that the shear strain rate must be zero at the liquid-gas interface. Equations (1.23) and (1.27) represent boundary conditions that must be fulfilled by a charged viscous drop in atmosphere. Finally the prohibition of mass transfer across the interface $\partial\Omega$ is guaranteed by the kinematic condition,

$$\vec{n} \cdot \left(\frac{d\vec{s}}{dt} - \vec{u} \right) = 0 \quad \text{on} \quad \partial\Omega \quad . \tag{1.28}$$

Equation (1.28) describes the time evolution of the shape deformation of the droplet[7]!

---

[7]In our code, the shape function $s(\theta, t)$ is defined on the collocation points θ_i, which are the zeros of a high order Legendre polynomial and thus given once for all. We propagate in time the shape function $s(\theta_i, t)$ for fixed angle θ_i using

$$\frac{\partial s}{\partial t} = u_r - \frac{\partial s}{\partial \theta} \frac{u_\theta}{s} \quad .$$

1.4.2 Charge dynamics at the interface

We suppose that all excess charges are located within a thin layer (skin) at the interface so that the surface charge approximation holds. The charge dynamics at the interface is thus governed by the *surface* charge transport equation on a closed deforming surface. The latter is moving because of the non-zero normal component of the fluid velocity evaluated at the surface (1.28). The charge dynamics at the interface is governed by the *surface* charge transport (continuity) equation on a closed deforming surface [60, 61].

$$\frac{D\sigma}{Dt} + u_n \vec{\nabla}_s \cdot \vec{n} + \vec{\nabla}_s \cdot \vec{j}_s = \kappa E_n \tag{1.29}$$

where the convective time derivative means the derivative when we follow the surface along a direction normal to itself, that is

$$\frac{D\sigma}{Dt} = \frac{\partial \sigma}{\partial t} + u_n \frac{\partial \sigma}{\partial n} \quad .$$

The term $u_n \vec{\nabla}_s \cdot \vec{n}$ accounts for the deforming surface. The term κE_n plays the role of a source term, that brings charges from the bulk to the surface or moves charges from the surface into the bulk. The surface charges are dragged by the liquid flow and pushed by the electric field. The surface current $\vec{j}_s$ has thus two contributions,

$$\vec{j}_s = \sigma(u_\tau + \lambda E_\tau)\vec{\tau} \quad . \tag{1.30}$$

The first is the velocity field of the fluid tangent to the surface u_τ and the second is the tangent component of the electric field E_τ times the charge mobility λ. We neglect the diffusion term which is usually 2 orders of magnitude smaller than the two former terms. Noting that $\vec{\nabla}_s \cdot \vec{n} = -2H\sigma$, (1.9), the surface charge evolution eventually reads

$$\frac{D\sigma}{Dt} \quad + \quad \vec{\nabla}_s \cdot (\vec{\tau}\sigma(u_\tau + \lambda E_\tau)) - 2H\sigma u_n = \kappa E_n \tag{1.31}$$

The surface divergence operator $\vec{\nabla}_s \cdot$ may not be well known to the reader, so we give a computationally useful expression of the second term in (1.31). Because the droplet deformation and charge dynamics have axis symmetry, $\partial_\phi \sigma = \partial_\phi u_\tau = \partial_\phi E_\tau = 0$, the surface divergence simplifies, using 1.8, to

$$\vec{\nabla}_s \cdot (\vec{\tau}\sigma(u_\tau + \lambda E_\tau)) = \vec{n} \cdot \left(\vec{\nabla} \wedge \sigma(u_\tau + \lambda E_\tau)\vec{e_\phi} \right) \tag{1.32}$$

In the general case of curvilinear orthogonal coordinates (ξ, η, ϕ) and for an axis symmetric function $F = \sigma(u_\tau + \lambda E_\tau)$ defined on the surface $(\xi_s(\eta), \eta)$, the expression (1.32) yields,

$$\vec{n} \cdot \left(\vec{\nabla} \wedge (F(\xi(\eta), \eta)\vec{e_\phi}) \right)\Big|_{\xi=\xi_s} \quad = \quad \vec{n} \cdot \vec{e_\xi} \frac{1}{h_\eta h_\phi} \frac{d}{d\eta} (h_\phi F(\xi_s(\eta), \eta)) \tag{1.33}$$

The latter expression can be used for the computation of the surface divergence of an axis symmetric tangent vector defined on the surface.

In spherical coordinates (r, θ, ϕ), with $h_r = 1$, $h_\theta = r$ and $h_\phi = r \sin \theta$, one has at the surface $(R(\theta), \theta)$

$$\vec{n} \cdot \left(\vec{\nabla} \wedge (F[r, \theta] \vec{e_\phi}) \right) = \vec{n} \cdot \vec{e_r} \frac{1}{h_\theta h_\phi} \frac{d}{d\theta} (h_\phi F[R(\theta), \theta]) \tag{1.34}$$

$$= \frac{1}{\sqrt{1 + k^2}} \frac{1}{R^2(\theta) \sin \theta} \frac{d}{d\theta} (\sin \theta \, R(\theta) F[R(\theta), \theta]) \tag{1.35}$$

with $k = \frac{1}{R(\theta)} \frac{dR}{d\theta}$.

1.4.3 Kinetic energy dissipation

It is interesting to look at the dissipation of the kinetic energy of a viscous fluid. Multiplying (1.12) by $\vec{u}$ and integrating over the droplet volume Ω yields the time evolution of the mechanical energy of the droplet. Using the identity,

$$\vec{\nabla} \cdot (\vec{u} \cdot T) = \vec{u}(\vec{\nabla} \cdot T) + T : \frac{1}{2} \left(\vec{\nabla} \vec{u} + (\vec{\nabla} \vec{u})^t \right) \quad , \tag{1.36}$$

which holds for a symmetric tensor T, the dissipation of the kinetic energy is given by

$$\frac{d}{dt} E_{\text{kin}} = \frac{d}{dt} \int_\Omega \frac{\rho u^2}{2} d\Omega \tag{1.37}$$

$$= \int_\Omega \vec{u}(\vec{\nabla} \cdot T) d\Omega \tag{1.38}$$

$$= \underbrace{\int_{\partial\Omega} \vec{u} \cdot (T - M) \cdot \vec{n} ds^2}_{\mathcal{T}} - \underbrace{2\mu \int_\Omega D : D d\Omega}_{\mathcal{D}} \tag{1.39}$$

where $\mathcal{T}$ stands for the power of traction (driving power) and $\mathcal{D}$ for the dissipation power. The operator : stands for the double dot product of tensors[8]. We used here the property that, in the leaky dielectric model, the symmetric Maxwell tensor M is divergence-free so that from the tensor identity 1.36 and divergence theorem one has

$$\int_\Omega D : M d\Omega = \int_\Omega \vec{\nabla} \cdot (\vec{u} \cdot M) d\Omega = \int_{\partial\Omega} \vec{u} \cdot M \cdot \vec{n} ds^2 \tag{1.40}$$

---

[8]Let h_{ij} and g_{ij} be two square matrices, then $h_{ij} : g_{ij} = \sum_{ij} m_{ij} g_{ij}$ is a scalar

We also note that for the identity matrix I times the pressure p one has

$$D : (-pI) = p\vec{\nabla} \cdot \vec{u} = 0 \tag{1.41}$$

Injecting the boundary conditions (1.23) and (1.27) into (1.39) yields

$$\frac{d}{dt}E_{\text{kin}} = \underbrace{\int_{\partial\Omega}(u_n(-P_s + P_c) + u_\tau\sigma E_\tau)ds^2}_{\mathcal{T}} - \underbrace{2\mu\int_\Omega D : Dd\Omega}_{\mathcal{D}} \tag{1.42}$$

The dissipation power $\mathcal{D}$ is proportional to the viscosity and involves only the viscous rate of strain tensor D. For rotational fluids the strain rate tensor is **not** divergence-free and dissipative forces exist inside the droplet as well as at the interface[9]. The traction power includes the capillary pressure, the Coulomb pressure but also the shear stress of the Maxwell tensor, all evaluated at the interface. Equation (1.42) is valid for all Newtonian viscous fluids satisfying the boundary condition ((1.23) and (1.27) at a free charged surface.

1.4.4 Potential Flow approximation: Case of a perfectly conducting inviscid liquid drop

Even by assuming an axisymmetric shape deformation, the numerical propagation of the fluid via the Navier-Stokes (NS) equation with moving boundaries is quite CPU expensive. Several authors [50, 57, 58, 59] used the finite element method (FEM) to solve the NS equation and propagate the droplet interface in time. While they successfully describe the drop deformation, the high CPU cost makes systematic studies challenging. We simplify the description of the fluid dynamics by assuming that the liquid is inviscid (zero viscosity) and the flow irrotational $\vec{\nabla} \wedge \vec{u} = 0$. The latter implies that the velocity field $\vec{u}$ of the fluid can be obtained as the gradient of the scalar velocity potential Ψ

$$\vec{u} = \vec{\nabla}\Psi \quad \text{in } \Omega \quad, \tag{1.43}$$

leading thus to the potential flow (PF) approximation[10]. Within these assumptions, the axis-symmetric Navier-Stokes equation simplifies to the 1D non-linear

---

[9]For irrotational fluids the strain rate tensor is divergence-free so that the last term in (1.42) involving a volume integration can be replaced by a surface integration.

[10]In flow regions where vorticity is known to be important, such as wakes and boundary layers, potential flow theory is not able to provide reasonable predictions of the flow. Fortunately, there are often large regions of a flow where the assumption of irrotationality is valid which is why potential flow is used for various applications. For instance in: flow around aircraft, groundwater flow, acoustics, water waves and macro-sized (cm range) water droplets.

time-dependent Bernoulli equation, giving the time-evolution of the velocity potential Ψ on the interface as a function of the interface pressure p.

$$\frac{\partial \Psi}{\partial t} + \frac{\vec{u}^2}{2} + \frac{p}{\rho} = 0 \quad \text{on} \quad \partial\Omega \tag{1.44}$$

Note that, unlike Betelú et al. [46] who studied the shape deformation using the Stokes equation, the inviscid liquid model ignores viscous properties of the fluid but includes the convection term $\rho\frac{\vec{u}^2}{2}$, accounting for time-independent acceleration of the flow with respect to space and thus accounting for some inertial effects.

In the limit of an inviscid fluid, $\eta = 0$, the boundary condition (1.27) can only by fulfilled for a perfect conductor, $-\vec{\nabla}_s V = E_\tau = 0$. The liquid is thus considered to be perfectly conducting so that the electric field is zero in the drop volume and the electric potential at the surface and equipotential. We obtain from (1.23) and (1.27) that the pressure at the liquid interface given by the difference of the surface tension pressure and the Coulomb pressure,

$$p = P_s - P_c = -2\gamma H - \frac{\sigma^2}{2\varepsilon_0} \quad \text{on } \partial\Omega \tag{1.45}$$

while the jump condition of the tangential component of the stress tensor (1.27) is automatically satisfied. As the velocity field is divergence-free, the velocity potential Φ satisfies the Laplace equation

$$\vec{\nabla}^2 \Psi = 0 \quad \text{in } \Omega \quad, \tag{1.46}$$

The boundary condition necessary to solve the above Laplace equation is given by (1.44). The velocity field of the fluid at the droplet interface is finally computed using (1.43) and the interface propagated using (1.28),

Surface charge distribution for a perfectly conducting liquid

The liquid being a perfect conductor, the charge distribution is always at equilibrium so that the electric potential is constant all over the surface. We use thus the latter condition to compute the surface charge density for a given droplet shape. The electric field inside a conductor is zero, it is sufficient to compute the electric field outside the droplet volume. As the electric field is divergence-free, the electric potential V satisfies the Laplace equation, with the boundary condition that V is constant at the interface,

$$\vec{\nabla}^2 V = 0 \quad \text{in} \quad \mathbb{R}^3\backslash\Omega \tag{1.47}$$

$$V = V_0 \quad \text{on } \partial\Omega \quad, \tag{1.48}$$

The potential V can now be readily computed for an arbitrary equipotential V_0 using, for example, the technique where V is projected onto harmonic functions, see appendix A.1. The surface charge density $\sigma = -\varepsilon_0 \partial V / \partial n$ is deduced from the normal derivative of the electric potential V, with V_0 being determined by the condition that the integration of the surface charge density over the droplet surface equals the total charge $Q = 8\pi\sqrt{X\gamma\varepsilon_0 R^3}$ of the droplet,

$$Q = \int_{\partial\Omega} \sigma(t, \vec{s}) \, ds^2 \quad . \tag{1.49}$$

Dimensionless equations:

In order to find the quantities that control the dynamics we put equation 1.44 into dimensionless form. We introduce the characteristic deformation time scale

$$\tau_0 = \sqrt{\frac{\rho R^3}{\gamma}} \tag{1.50}$$

and define the following dimensionless quantities

$$\tilde{t} = t/\tau_0 \tag{1.51}$$

$$\tilde{\Psi} = \Psi\frac{\tau_0}{R^2} \tag{1.52}$$

$$\sqrt{X}\tilde{\sigma} = \sigma\left(\frac{4\gamma\varepsilon_0}{R}\right)^{-1/2} \tag{1.53}$$

$$\tilde{H} = HR \tag{1.54}$$

$$\vec{\tilde{u}} = \vec{u}\frac{\tau_0}{R} \tag{1.55}$$

The dimensionless form of (1.44) redas then,

$$\frac{\partial\tilde{\Psi}}{\partial\tilde{t}} + \frac{\vec{\tilde{u}}^2}{2} - 2\tilde{H} - 2X\tilde{\sigma}^2 = 0 \quad \text{on} \quad \partial\Omega \tag{1.56}$$

We remind that $\tilde{H} < 0$ is a negative quantity. As we consider here a perfectly conducting, inviscid liquid, the fissility parameter X is the only free parameter of the model that influences the pathway. The quantities R, γ, ρ define merely the time scale τ_0 of the droplet deformation. The latter is therefore quite general within the given hypotheses. Details about the numerical resolution of the PF model are given in appendix A.1.
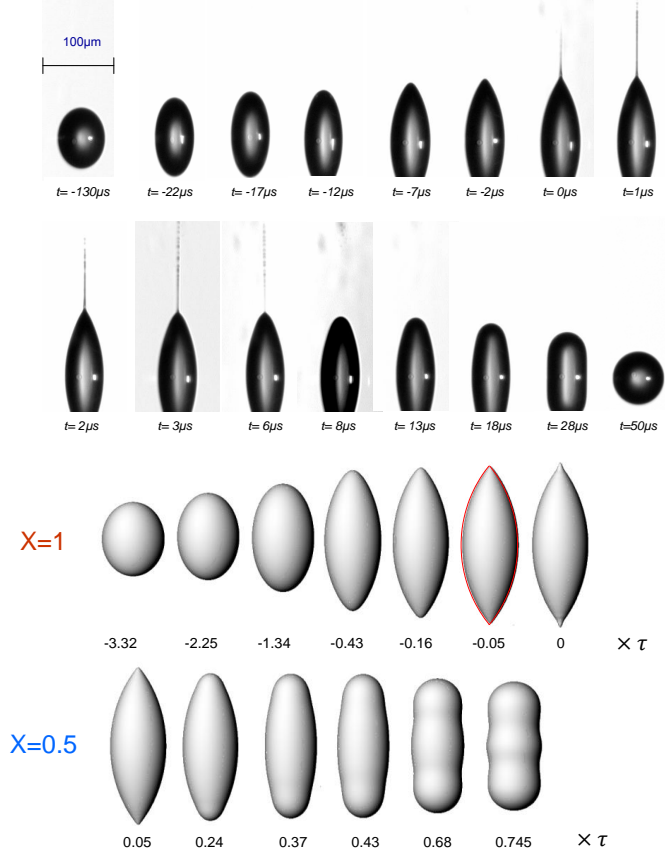
Figure 1.21: Bottom panel:Calculated shape sequence of an initially critically charged droplet $X = 1$, experiencing charge emission $X = 0.5$ at the moment a bulb appears at the tip. Physical times are obtained by multiplying dimensionless times t, shown under each shape, by the characteristic time τ of a given droplet. Fluid is nonviscous and perfectly con- ducting. Charge emission is chosen as origin of time. The red lemon-fit has been slightly shifted for better comparison. Top panel: Snapshots of a deforming glycol droplet for comparison.

Simulated results using the PF approach

In Fig. 1.21, we show snapshots of the simulation before $(X = 1)$ and after charge emission $(X = 0.5)$. The starting point is a critically charged prolate spheroid of small eccentricity (almost spherical drop)

$$e = \sqrt{1 - a^2/b^2} = 0.2 \quad ,$$

where a and b are defined in section 1.2.1. We see that the model is able to reproduce qualitatively the whole initial sequence of the non-linear deformation

dynamics of a critically charged droplet. In particular, for $X = 1$, we end up with the same spindle-like form as the glycol droplet. At the moment, when the droplet starts to form a jet at the tips (snapshot labeled by the dimensionless time 0), we reduce the charge by -30% by changing suddenly the fissility to $X = 0.5$. This allows us to emulate the charge emission and to describe the shape deformation after it, without stopping the calculation. After emission, the droplet retracts similarly to experimental data, adopting a capsule-like form, which, unlike the glycol droplet has a bulge in the middle. The model also shows some weaknesses. The lack of viscosity hinders the dissipation of the excess of potential energy obtained during charge emission. The model is therefore not able to describe the deformation back to equilibrium shape (sphere). Further, as viscosity slows down the flow, we expect that the deformation time we get from the simulation underestimates the experimentally observed one. Indeed, glycol droplets such as the one shown in Fig. 1.21 with $(\rho, \gamma, R) = (1.1 \text{ g/cm}^3$, 47 mN/m, 24 μm), (see Table 1.1), have a characteristic time scale of $\tau_0 = 18$ μs. From Fig.1.21 we note that the glycol droplet needs 22 μs to attain the spindle-like shape, starting from a prolate spheroid with a ratio $a/b = 2$. For the same deformation, the simulation needs $0.6 \times \tau_0 \simeq 11$ μs. Compared to the observed 22 μs, the inviscid drop deforms about 2 times faster.

For the supercooled water droplets shown in Fig. 1.10, the droplet needs 30 μs to deform from the prolate spheroid with a ratio $a/b = 1.6$ (15 μs) to the lemon-shaped drop (45 μs). Our water drop has a characteristic time of $\tau_0 = 24$ μs (using $(\rho, \gamma, R) = (1.0 \text{ g/cm}^3$, 76 mN/m, 35 μm) The simulation gives for the some deformation $0.9 \times \tau_0 \simeq 22$ μm, meaning the inviscid liquid deforms 1.4 times faster than the supercooled water drop. We assign the trend to the lower viscosity of supercooled water with respect to glycol.

The simulations describe the shape of the tips of the droplet just before surface breakup. It was an open question whether the jets are emitted from a Taylor cone [8] as assumed by de la Mora [48], likely to electrosprays [23], or rather from a hyperboloidal tip as was pointed out by Yarin *et al.* [37] in the case of sessile and pendant droplets in an electric field. When zooming on the tip, we note that the jets are not emitted from a conical tip, but at best from a hyperboloid which is tangent to a cone of 33°. Yarin et al. showed that the maximal electric potential at which a stationary infinite hyperboloid can exist, corresponds to a hyperboloid tangent to a cone of 33.5° [37]. This critical hyperboloid was the starting point from which jets are formed from pendant droplets for increasing electric fields. Interestingly, it is close to the hyperboloid that best fits the tip, hinting that the last one is close to break-up. Nevertheless, in our case, the hyperboloid is not a satisfying fit either, in the sense that it only fits the tip, instead of the whole droplet. We looked for a geometrical description of the whole shape, just before

charge emission, and found that the droplet is remarkably well fitted by a "lemon" of equation

$$z^2 = A^2 - (B + r)^2, \quad A = 3.02, \quad B = 2.25 \tag{1.57}$$

with $r = \sqrt{x^2 + y^2}$ being the distance from the symmetry axis. Note that the fit has only one free parameter as A and B are related by the volume constraint. The lemon is shown in the upper inset of Fig. 1.22 as a red contour. When zooming on the tip, we see only a small discrepancy close to the apex (lower inset of Fig. 1.22). We deduce that the tip is tangent to a cone of 39°, thus significantly narrower than the Taylor cone (49.3°) but larger than the one obtained by Betelú *et al.* (cone of 25° for a viscous droplet [46]. The experimentally observed tip's opening half-angle of 30° lies between both predictions. The lemon may be considered as the asymptotic shape of a critically charged droplet, if breaking up could be hindered.

For further analysis of the tip behavior, we introduce the local fissility $x(\theta)$ defined as the Coulomb pressure divided by the pressure due to the surface tension, $x(\theta) = X\sigma^2(\theta)/H(\theta)$. In order to be able to break up the surface, the Coulomb pressure must outbalance the stress due to the surface tension $x(\theta) > x_c \geq 1$, where the critical local fissility x_c still needs to be determined. For a spheroid, the Coulomb pressure can be expressed as a function of the Gaussian curvature K of the surface [25], yielding

$$x(\theta) = X\sqrt{K(\theta)}/H(\theta) \quad .$$

As for spheroids, one has always $H^2 \geq K$, independently of the eccentricity. Hence, the local fissility of critically charged spheroids ($X = 1$) cannot exceed the unit $x(\theta) \leq 1$ and jets cannot appear at their ends, even for large eccentricities. Critically charged lemons, however, behave differently as the local fissility is no longer bound and can exceed one at the tips. Indeed, for the lemon tip shape depicted in Fig. 1.22, the surface charge density diverges close to the apex as $\sigma(r \to 0) \propto r^{-0.59}$, while the mean curvature diverges as $H(r \to 0) \propto r^{-1}$ (not shown). Hence, the local fissility diverges at the apex as $x(r \to 0) \propto r^{-0.18}$. Such critically charged lemon shapes lead therefore inevitably towards surface break up of the tip. In Fig.1.22, we give the local fissility (upper panel) and charge distribution (lower panel) of the droplet at different times (shapes) before charge emission and compare them to the one calculated for the lemon shape. As soon as the shape deviates from a spheroid to become rugbyball-like (around $t_1 = -0.43$), the local fissility exceeds 1 at the tips $x(0) = 1.08$. This shows that the local fissility can reach values larger than 1 at nonsingular surface points. However, this also shows that $x > x_c = 1$ is not a sufficient criterion for surface break-up but indicates rather the less stable region. At time $t_0 = -0.05$, the charge distribution compares well to the charge distribution on the lemon surface except that it stays bounded at the apex. At that moment, the electric field at the tip is about 6 times larger
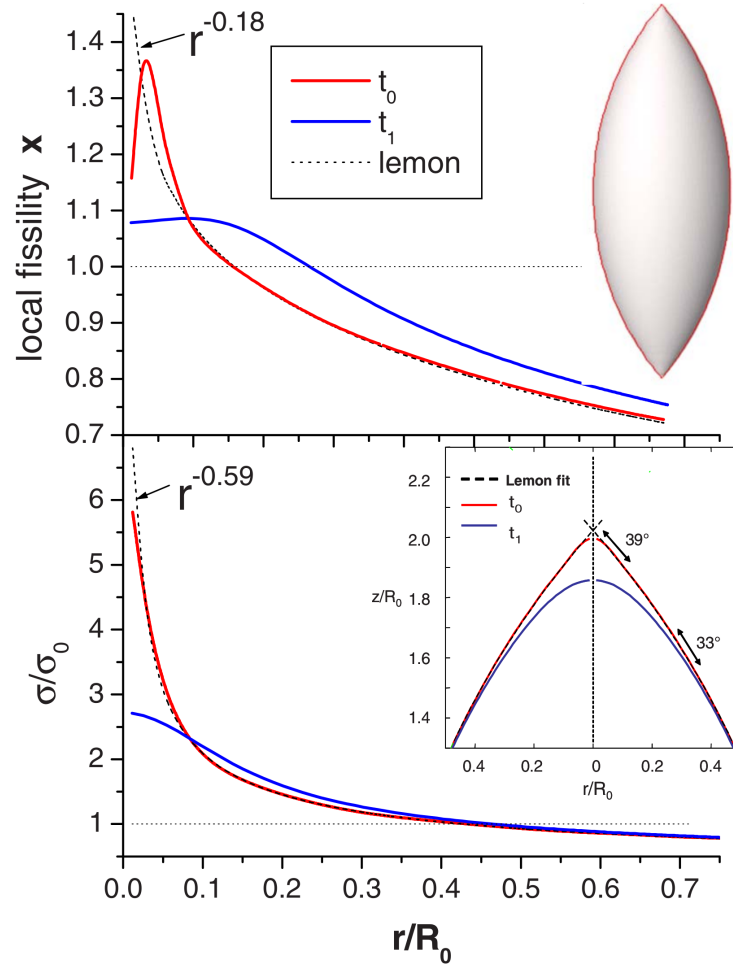
Figure 1.22: Local fissility and and tip formation

than initially. Finally, a bulb appears at the tip, which indicates the formation of a jet. The simulated sequence is quite general for inviscid perfectly conducting liquid droplets. However, properties of the fluid like viscosity and charge mobility may change the details of the deformation dynamics. For polar liquids like water and glycol, the Coulomb pressure on the droplet surface may significantly deviated such as the one of a perfectly conducting droplet.

We compare in Fig. 1.23 the simulated pathway to the experimental data. The simulation should well describe the deformation of a critically charged mercury droplet, which has low viscosity and is an excellent conductor. It predicts that the pointed ends are formed for a ratio $a/b = 2.6$, which is significantly lower than the values obtained for supercooled water ($a/b = 3.2$) and glycol ($a/b = 3.5$).
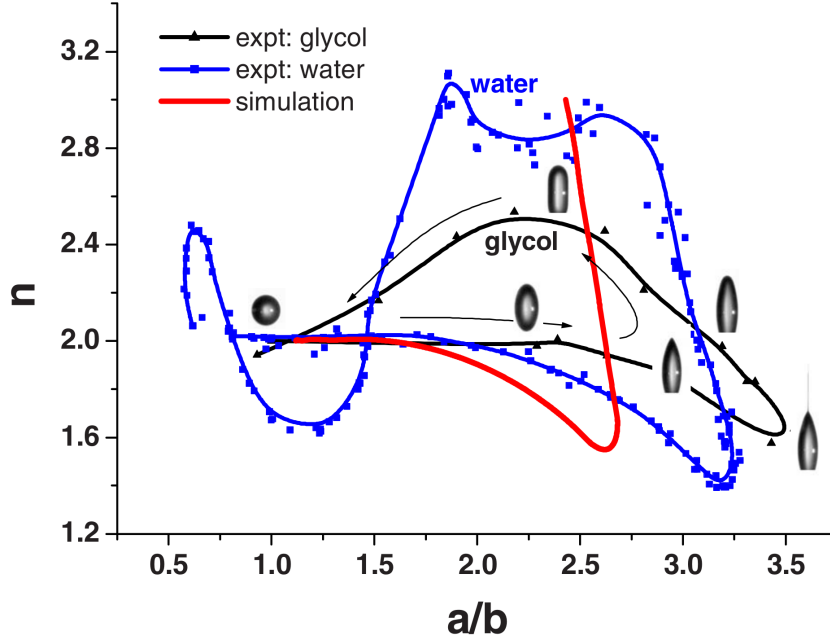
Figure 1.23: Pathway (red curve) of an inviscid perfectly conducting, compared to experimental data of a $\varnothing = 48\mu m$ glycol and supercooled $\varnothing = 70\mu m$ water droplet.

We expect that the difference is due to the viscosity and finite charge mobility of the polar liquids. Indeed, for even lower viscous drops, namely negatively and positively charged water droplets at room temperature, a lower ratio a/b between 2.7 and 2.8 was found (see Fig. 1.32). After charge emission, the deformation is mainly driven by the surface tension. The latter tends first to flatten the tips to form a capsule. The slope of the simulated curve after charge emission compares well to the experimental low-viscous water curve. As mentioned before, the model cannot describe the way back to the equilibrium shape and we stop the simulation when $n = 3.2$. However, the comparison with the experimental curve for glycol fails, highlighting the role of viscosity and charge mobility. We deduce that after charge emission, the details of the pathway are dominated by viscous properties of the fluid and, thus, poorly described by the present model. Nevertheless, the inviscid fluid simulations give the asymptotic ratio a/b and slope of the curve, after charge emission, that cannot be overcome by low-viscous fluids. The influence of the viscosity and charge mobility of real fluids on the deformation pathway will be studied in the following sections.

1.4.5 Viscous Potential Flow (VPF) approximation

The inviscid liquid model suffers clearly from the absence of a dissipation term in the fluid dynamics. While keeping the potential flow approximation, which has a clear CPU cost advantage over to the full Navier-Stokes equation, we relax the condition that the drop liquid is inviscid. This yields the viscous potential flow model (VPF) and the pressure at the liquid interface reads (1.22)

$$p = P_s - P_c + 2\mu D_{nn} \quad \partial\Omega \quad . \tag{1.58}$$

Compared to the inviscid liquid model, the pressure has now an additional term witch is proportional to the viscosity μ. The strain rate tensor D at the interface is computed using the irrotational velocity field $\vec{u}$. Note that, while for an irrotational flow the viscous force per unit volume is zero $\vec{\nabla} \cdot D = 0$ inside the drop, its contribution to the surface pressure is non-zero

$$D_{nn} \neq 0 \quad \text{and} \quad D_{\tau n} \neq 0 \quad \text{on} \quad \partial\Omega \tag{1.59}$$

As a result, the jump of the shear (tangential) stress $T_{\tau,n}$ across the interface violates the zero shear stress boundary condition at a free surface,

$$T_{\tau n} - M_{\tau n} = \mu 2 D_{\tau n} \neq \sigma E_\tau \quad \partial\Omega \quad . \tag{1.60}$$

Compared to (1.27) the last equality is not satisfied in VPF. Indeed, VPF has not enough degrees of freedom to enforce that the shear strain rate $D_{\tau n}$ equals the shear stress of the Maxwell tensor. In the particular case of a perfectly conducting liquid, where the shear stress of the Maxwell tensor is zero, the shear strain rate $D_{\tau n}$ should vanish at the interface, which is in contradiction with (1.59). The rotational part of the velocity field is missing here to fulfill the condition (1.60). Compared to a rotational flow where condition (1.60) can be enforces, VPF results in an incorrect dispersion relationship, i.e. the damping of a given surface mode is underestimated for low viscosities and overestimated for very large viscosities [51].

While the VPF model is certainly not perfect, it includes after all viscous forces at the free boundary and thus dissipation of the kinetic energy E_k. The power equation (1.42) is valid for rotational as well as for irrotational fluids. Using (1.58) and (1.60) and reminding that in the VPF approach the strain rate tensor D is also divergence-free, equation (1.42) leads to

$$\frac{d}{dt}E_{\text{kin}} = \underbrace{\int_{\partial\Omega} u_n(-P_s + P_c)ds^2}_{\mathcal{T}^{\text{VPF}}} - \underbrace{2\mu \int_{\partial\Omega} u_n D_{nn} ds^2}_{\mathcal{D}^{\text{VPF}}} \tag{1.61}$$

Compared to the inviscid liquid model, VCP adds the dissipation term $\mathcal{D}^{\text{VPF}}$ proportional to the viscosity μ. The added dissipation allows the fluid to relax to its equilibrium shape and thus to model the shape dynamics of the droplet after jet emission.

1.4.6 Viscous Corrected Viscous Potential Flow (VCVPF) approach

By ignoring the zero shear stress boundary condition at the free surface in VPF, we ignored also dissipative forces originating at the surface due to the zero shear stress boundary condition. In order to compensate for the lack of those viscous forces, Joseph and Wang [40, 45] derived a viscous correction formulation for the irrotational pressure. It expresses the idea that a viscous correction of the pressure at the gas-liquid interface is required to compensate for the non-vanishing irrotational shear stress. The accepted idea, is that the pressure correction is a real viscous pressure which varies from the pressure in the irrotational flow outside a narrow vorticity layer near the gas-liquid surface, to the required value at the interface. They called this solution the Viscous Correction of the VPF model (VC)VPF. They proposed thus to add a fictive viscous pressure p_μ to the normal stress,

$$T_{nn} - M_{nn} = -P_s + P_c - p_\mu \quad . \tag{1.62}$$

The viscous pressure p_μ is assumed to satisfies the Laplace equation in the drop volume[11] and is defined such as the power of the viscous pressure equals the dissipation power of the unbalanced shear stress at the boundary,

$$\int_{\partial\Omega} \vec{n} \cdot \vec{u} (-p_\mu) ds^2 = \int_{\partial\Omega} \vec{\tau} \cdot \vec{u} \underbrace{\left(-2\mu D_{\tau n} + \sigma E_\tau \right)}_{T^g_{\tau n} - T_{\tau n}} ds^2 \tag{1.63}$$

Expression (1.63) however does not uniquely define p_μ. We will further ask that the power of the viscous pressure balances the power of the jump of the shear stress across the boundary for each surface element ds^2,

$$u_n(-p_\mu) ds^2 = u_\tau(-2\mu D_{\tau n} + \sigma E_\tau) ds^2 \tag{1.64}$$

Loosely said, the elementary force $p_\mu ds^2$ accounts for the missing viscous forces at the free surface element that would originate if the zero shear stress boundary conditions was satisfied. A numerical method for the evaluation of p_μ is given in Appendix A.4. The power of traction in VCVPF becomes using (1.62) and (1.64),

$$
\begin{aligned}
\mathcal{T}^{\text{VCVPF}} &= \int_{\partial\Omega} \vec{u} \cdot (T - M) \cdot \vec{n} \, ds^2 \\
&= \int_{\partial\Omega} u_n(-P_s + P_c - p_\mu) \, ds^2 + 2\mu \int_{\partial\Omega} u_\tau D_{\tau n} \, ds^2 \tag{1.65} \\
&= \int_{\partial\Omega} (u_n(-P_s + P_c) + u_\tau \sigma E_\tau) ds^2 \simeq \mathcal{T}^{\text{VPF}} \tag{1.66}
\end{aligned}
$$

---

[11]ensuring that the correction is divergence-free

which is the same expression than for rotational fluids (1.42), apart that here $\vec{u}$ is purely irrotational. The power of traction $\mathcal{T}^{\mathrm{VCVPF}}$ differs from the one in VPF by the term $\int u_\tau \sigma E_\tau \, ds$, which is usually negligible for conducting liquids. So the traction power in VPF and VCVPF can be considered similar. Reminding that the strain rate tensor D is divergence-free, the dissipation power $\mathcal{D}$ reads

$$\mathcal{D}^{\mathrm{VCVPF}} = 2\mu \int_{\partial\Omega} (u_n D_{nn} + u_\tau D_{\tau n}) ds^2 \neq D^{\mathrm{VPF}} \tag{1.67}$$

The dissipation power $\mathcal{D}^{\mathrm{VCVPF}}$ has a contribution from the shear strain rate $\int u_\tau D_{\tau n} \, ds$, not found in VPF (1.61). However, while VCVPF allows to recover the correct expression of the power of traction, it only approaches the power of dissipation of the Navier-Stokes equation, mainly because the rotational part of the velocity field is still missing. Besides, the rotational part of the velocity field is also necessary to satisfy explicitly the jump condition of the shear stress at the free surface.

Dimensionless time evolution of the velocity potential Ψ and surface charge σ.

Following the lines of section 1.4.4, the time evolution of the dimensionless velocity potential $\tilde{\Psi}$ at the interface is given in VCVPF

$$\frac{\partial \tilde{\Psi}}{\partial \tilde{t}} + \frac{\vec{\tilde{u}}^2}{2} - 2\tilde{H} - 2X\tilde{P}_c + \mathrm{Oh}(2\tilde{D}_{nn} - \tilde{p}_\mu) = 0 \quad \text{on} \quad \partial\Omega \tag{1.68}$$

where we introduced the dimensionless Ohnesorge number,

$$\mathrm{Oh} = \frac{\mu}{\sqrt{\rho\gamma R}} \qquad \left(\frac{\text{viscosity}}{\sqrt{\text{inertia} \times \text{surface-tension}}} \right) \tag{1.69}$$

that relates the viscous forces to inertial and surface tension forces. Larger Ohnesorge numbers indicate a greater influence of the viscosity. If we omit the viscous pressure term, we recover indeed the time evolution of Ψ in the VPF model, where only the normal rate stress contributed to the dissipation. In VCVPF, the viscous pressure p_μ adds (viscous) forces at the surface that balances the non-zero power of the shear stress at the interface. If, because of finite conductivity, the tangential component of the electric field is non-zero, p_μ also adds traction originating from the non-vanishing shear stress of the Maxwell tensor σE_τ at the interface. The technicalities for the evaluation of the viscous pressure p_μ are detailed in appendix A.4.

The charge dynamics at the interface is governed by (1.31). Introducing the surface and bulk relaxation rates

$$\tau_s^{-1} = \lambda\sqrt{\frac{\gamma}{R^3\varepsilon_0}} \qquad \tau_b^{-1} = \frac{\kappa}{\varepsilon_0\varepsilon_r} \tag{1.70}$$

allows to define the dimensionless charge carrier mobility $\tilde{\lambda}$ and dimensionless bulk conductivity $\tilde{\kappa}$

$$\tilde{\lambda} = \frac{\tau_0}{\tau_s} = \lambda\sqrt{\frac{4X\rho}{\varepsilon_0}} \tag{1.71}$$

$$\tilde{\kappa} = \frac{\tau_0}{\tau_b} = \kappa\sqrt{\frac{\rho R^3}{\gamma\varepsilon_0^2\varepsilon_r^2}} \tag{1.72}$$

where the characteristic deformation time τ_0 is given by (1.50). Note that $\tilde{\lambda}$ depends on X. Further, defining the characteristic surface charge density

$$\sigma_0 = \sqrt{4\gamma\varepsilon_0/R} \quad ,$$

introducing the dimensionless quantities

$$\sigma = \sqrt{X}\tilde{\sigma}\,\sigma_0 \tag{1.73}$$

$$E_\tau = \sqrt{X}\tilde{E}_\tau\sigma_0/\varepsilon_0 \tag{1.74}$$

$$E_n = \sqrt{X}\tilde{E}_n\sigma_0/\varepsilon_0 \tag{1.75}$$

and using the definitions (1.51,1.54,1.55), allow us to put the surface charge transport with moving boundaries (1.31) into a dimensionless form,

$$\frac{D\tilde{\sigma}}{D\tilde{t}} + \vec{\nabla}_{\tilde{s}} \cdot (\vec{\tau}\tilde{\sigma}(\tilde{u}_\tau + \tilde{\lambda}\tilde{E}_\tau)) - 2\tilde{H}\tilde{\sigma}\tilde{u}_n = \tilde{\kappa}\varepsilon_r\tilde{E}_n \quad \text{on} \quad \partial\Omega \tag{1.76}$$

where all the quantities are now dimensionless. Note that the factor ε_r, found in the last term, simply comes from the factor ε_r^{-1} used in the definition[12] of the bulk relaxation rate (1.70). The charge dynamics at the interface is controlled by two parameters namely $\tilde{\lambda}$ and $\tilde{\kappa}$. If one of the latter has a value much larger than unit, the charge relaxation dominates the rate of motion of the fluid and the surface charge distribution is close to equilibrium, meaning that the electric potential at the surface is an equipotential. We recover thus the case of the perfect conductor. For $\tilde{\lambda} \simeq 1$ and $\tilde{\kappa} \simeq 1$, the charge at the surface may not be at equilibrium during the ultra-fast deformation (in the sense that the potential at the surface is no longer an equipotential), because the charges at the surface are now also driven by the flow of the liquid at the surface. As a result, the electric field inside the

---

[12]The inner field E_n, obtained via (A.26), includes the polarization charges that appear at the interface separating two dielectric media (here the liquid of dielectric constant ε_r and vacuum). As a result, the inner field is scaled by the factor ε_r^{-1}. That is why the bulk relaxation rate also scales like ε_r^{-1}. We show this explicitly, by using the factor ε_r^{-1} in the definition of the bulk relaxation rate.

drop is non-zero and the dimensionless Coulomb pressure $\tilde{P}_s$ found in (1.68) and defined by

$$\tilde{P}_c = P_c \left(\frac{\sigma_0^2}{2\varepsilon_0} \right)^{-1} \tag{1.77}$$

$$\tilde{P}_c = \left(\tilde{\sigma} + \varepsilon_r \tilde{E}_n \right)^2 - \varepsilon_r \tilde{E}_n^2 + (\varepsilon_r - 1)\tilde{E}_\tau \tag{1.78}$$

deviates from the one of the perfect conductor, $\tilde{P}_c = \tilde{\sigma}^2$. Hence, the shape deformation of the drop depends now also sensibly on the parameters $\tilde{\lambda}$ and $\tilde{\kappa}$. Note that, while $\tilde{\lambda}$ does not depend on the radius R of the drop, $\tilde{\lambda}$ scales linearly with R. For a given bulk conductivity κ of the liquid, larger droplets have thus a larger dimensionless bulk conductivity.

Decay rate: VPF vs VCVPF
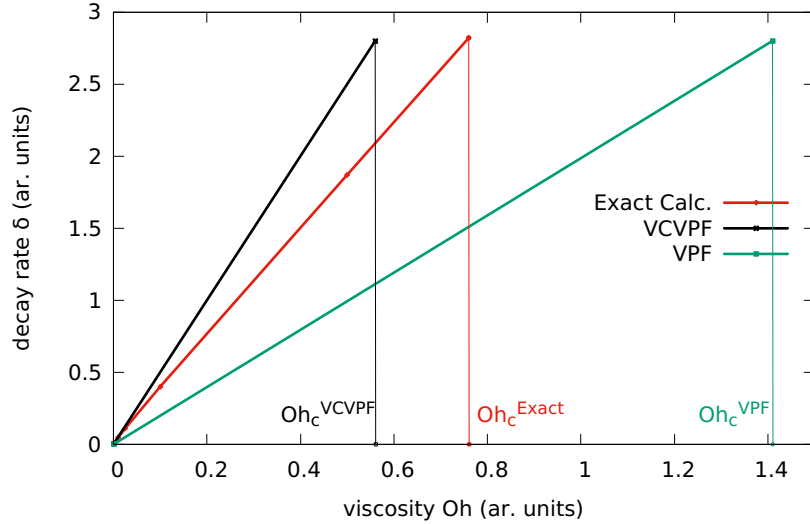
Figure 1.24: *Dimensionless decay rate δ of the quadrupole amplitude as a function of the dimensionless viscosity Oh for the VPF and VCVPF models and for the exact calculation. The values of Oh for which the decay is critical are shown by thin vertical lines and labeled accordingly, where $Oh_c^{VCVPF} \simeq 0.56$, $Oh_c^{VPF} \simeq 1.41$ and $Oh_c^{Exact} \simeq 0.76$.*

In the following section we will discuss briefly the differences between VPF and VCVPF regrading the dissipation. Using the small amplitude oscillation approximation, the dispersion relationship of a viscous (uncharged) drop was analysed by Padrino *et al.* [51] in the case of PF, VPF and VCVPF. The dispersion relationship links the complex frequency to the surface modes (quadrupole, hexapole,

octupole ...) of the surface. The dimensionless complex oscillation frequency $\tau_0 \Omega$ for the different approaches becomes

$$
\begin{aligned}
\tau_0 \Omega_m{}^{\text{PF}} &= \pm i\sqrt{(m+2)m(m-1)} = \pm i(\tau_0 \omega_m) && (1.79) \\
\tau_0 \Omega_m{}^{\text{VPF}} &= m(m-1)\text{Oh} \pm i\sqrt{(\tau_0 \omega_m)^2 - (m(m-1)\text{Oh})^2} \\
\tau_0 \Omega_m{}^{\text{VCVPF}} &= (2m+1)(m-1)\text{Oh} \pm i\sqrt{(\tau_0 \omega_m)^2 - ((2m+1)(m-1)\text{Oh})^2}
\end{aligned}
$$

where m stands for the mth deformation mode of the droplet surface. We note that for the quadrupole mode, the dimensionless decay rate $\delta_2 = \text{Real}(\tau\Omega_2)$ in VCVPF is $5/2$ time the one in VPF, making thus VCVPF noticeably different from VPF. For larger $m \gg 1$ the ratio tends toward 2. The decay rate of the quadrupole moment of the surface oscillations as a function of Oh are shown in figure 1.24 and compared to the exact calculation form [51]. Remarkably, it was found that in the low viscosities range, the VCVPF dispersion relationship tends to the exact one as was noted in [51]. Indeed as shown in Fig. 1.24, for Oh< 0.1, the VCVPF model gives a decay rate $\delta_{m=2}$ much closer to the exact one than the VPF model.

We label Oh$_c$ the critical value of the dimensionless viscosity, for which the imaginary part of the surface mode becomes zero. It is different for VPF and VCVPF:

$$
\text{Oh}_c^{\text{VPF}} = \sqrt{\frac{(m+2)}{m(m-1)}} \tag{1.80}
$$

$$
\text{Oh}_c^{\text{VCVPF}} = \sqrt{\frac{(m+2)m}{(2m+1)^2(m-1)}} = \frac{m}{2m+1}\text{Oh}_c^{\text{VPF}} \tag{1.81}
$$

In VCVPF, the critical value is shifted towards lower viscosities, compared to VPF. For the quadrupole moment $m = 2$, we get $\text{Oh}_c^{\text{VPF}} \simeq 1.41$ and $\text{Oh}_c^{\text{VCVPF}} \simeq 0.56$, where the latter is much closer to $\text{Oh}_c^{\text{Exact}} \simeq 0.76$ of the exact calculation. Now, our glycol micro-droplets have typically a (Oh$\simeq 0.4$) and are thus close to critically damping in VCVPF but not in VPF. So glycol droplets are expected to give sensibly different results in the VPF or VCVPF approach. While for low viscous water droplets, (Oh$\simeq 0.025$), VCVPF and VPF should give similar results, VCVPF is expected to come closer to the exact solutions. The VCVPF model seems thus preferable and we used for our simulations mainly the VCVPF model, keeping in mind that VCVPF calculations should be limited to Oh$< \text{Oh}_c^{\text{VCVPF}} \simeq 0.56$.

Charge break up

The ultra fast jet formation and emission are not simulated in this work as the underlying numerical method, based on harmonic function expansion in prolate

coordinate system, is not able to solve the Laplace equation for shapes with almost singular tips[13]. Successful simulations of the jet formation based on FEM aproaches and are given in [57, 61, 59]. Now, the jet not only removes charges from the drop's surface but removes also fast flowing matter. As a result, the jet reduces in several μs the charge and the kinetic energy of the droplet. We use two different methods to remove the charge and kinetic energy of the droplet.

1. In the first and simplest method, we simulate the jet emission by reducing suddenly the total charge and kinetic energy of the droplet, by applying a constant factor to the surface charge density σ and to the velocity potential Ψ.

$$\sigma(\vec{s}) \;\to\; \sqrt{1 - \frac{\Delta Q}{Q}}\, \sigma(\vec{s}) \tag{1.82}$$

$$\Psi(\vec{s}) \;\to\; \sqrt{1 - \frac{\Delta E_{\mathrm{kin}}}{E_{\mathrm{kin}}}}\, \Psi(\vec{s}) \tag{1.83}$$

where Q and E_{kin} are the charge and the kinetic energy of the droplet just before charge break up and ΔQ the emitted charge and ΔE_{kin} the loss of kinetic energy due to jet emission[14]. The deformation dynamics of the sub-critically charged drop $X < 1$ continues then using the same propagator but with reduced charge and kinetic energy. The pieces of information about the amount of emitted charge and lost kinetic energy are usually taken from experimental data.

2. In the second method, we simulate the charge emission by adding for a limited (dimensionless) time $\Delta \tilde{t}$ a source term $\tilde{\sigma}s$ to equation (1.76) that simulates the charge loss at the tip at the rate $\tilde{\tau}_{\mathrm{jet}}$,

$$\frac{D\tilde{\sigma}}{D\tilde{t}} + \vec{\nabla}_{\tilde{s}} \cdot (\vec{\tau}\tilde{\sigma}(\tilde{u}_{\tau} + \tilde{\lambda}\tilde{E}_{\tau})) - 2\tilde{H}\tilde{\sigma}\tilde{u}_n = \tilde{\kappa}\varepsilon_r \tilde{E}_n - s(\tilde{t}, \tilde{z})\frac{\tilde{\sigma}}{\tilde{\tau}_{\mathrm{jet}}} \tag{1.84}$$

where

$$s(z, t) = \frac{1}{\tau_{\mathrm{jet}}}\Theta(|z| - z_0)\Theta(t - t_0)\Theta(t_0 + \Delta t - t) \tag{1.85}$$

---

[13]We will present in section 1.5.4 a numerical method that does allow simulating the jet formation

[14]While the choice of ΔQ is suggested by direct measurements, the choice of ΔE_{kin} may be deduced indirectly from the thickness of the jet and from the deformation pathway of the subcritical drop. We expect ΔE_{kin} to decrease with thinner jets. Where the jet is clearly visible on the experimental snapshots, we remove usually as much as $\Delta E_{\mathrm{kin}}/E_{\mathrm{kin}} = 50\%$ of the kinetic energy. In the case where no observable jet is formed, like for negatively charged droplets, we expect the loss of kinetic energy during charge emission to be negligible so that $\Delta E_{\mathrm{kin}}/E_{\mathrm{kin}} = 0$.

is a window function that limits the source term in time and space, namely to the tip surface $|z| > z_0$ and to the time interval $\Delta \tilde{t}$, with $\Theta()$ being the step function.

The kinetic energy loss is simulated by adding a source term to the Cauchy momentum equation. The mass loss due to jet emission may be expressed by the continuity equation with the source term $\rho s > 0$

$$\partial_t \rho + \vec{\nabla} \cdot (\rho \vec{u}) + \rho s = 0 \qquad (1.86)$$

The Cauchy momentum equation describes the non-relativistic momentum transport in the droplet volume. In convective (or Lagrangian) form it is written:

$$\rho \left(\partial_t \vec{u} + \vec{u} \cdot \vec{\nabla} \vec{u} \right) = \vec{\nabla} \cdot T \qquad (1.87)$$

where the stress tensor T accounts for conservative and non-conservatives (viscous) contributions. We can always add a zero contribution $0\vec{u}$ to the momentum equation,

$$\rho \left(\partial_t \vec{u} + \vec{u} \cdot \vec{\nabla} \vec{u} \right) + \vec{u} \left(\underbrace{\partial_t \rho + \vec{\nabla} \cdot (\rho \vec{u}) + \rho s}_{0} \right) = \vec{\nabla} \cdot T \qquad (1.88)$$

which yields the Cauchy momentum equation (conservative form) with source term

$$\partial_t (\rho \vec{u}) + \vec{\nabla} \cdot (\rho \vec{u} \otimes \vec{u}) = \vec{\nabla} \cdot T - \rho s \vec{u} \qquad (1.89)$$

Usually Δt is chosen such that the loss of charge ΔQ due to equation (1.84) equals the requested charge loss. So with this method, the information of the charge loss ΔQ is still required and cannot be deduced from simulations because the charge loss is not done with the correct velocity field that would emerge when simulating explicitly the jet. In other words, the source term is active until the requested charge loss ΔQ is attained.

Simulations of charge loss and kinetic energy loss with the second method are underway, but and all the presented results where achieved using the first method.

1.5 Simulated Results with VCVPF

1.5.1 Influence of the dimensionless viscosity Oh on the deformation pathway

We first consider the case where the conductivity of the fluid is assumed sufficiently high so that, during the drop deformation, the electric potential remains
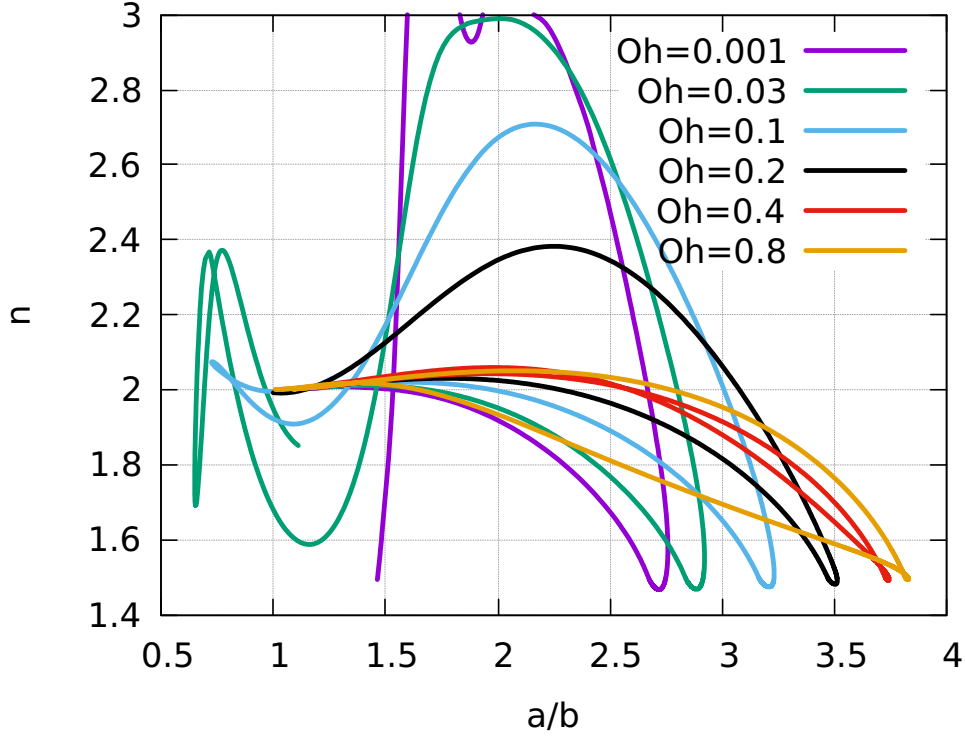
Figure 1.25: Deformation pathway of a critically charged droplet as a function of the Ohnesorge number Oh. At the tip appearance ($n = 1.5$), 20% of the initial charge is removed $X \to 0.64$ and kinetic energy reduced by 80%.

an equipotential $V(\vec{s}, t) = V(t)$ at the surface. As a result, at the boundary we have $E_\tau = 0$ and $\tilde{P}_c = \tilde{\sigma}^2$. We simulated for different Ohnersorge numbers Oh (eq. 1.69), ranging from 0.001 to 0.8, the deformation pathway on critically charged droplets ($X = 1$). The results are shown in Fig.1.25. The initial shape was a spheroid with a small eccentricity of $e = 0.1$ (almost spherical). We found that with increasing Oh and thus with increasing viscosity of the liquid, the droplet adopted a more and more elongated shape before pointed tips appeared at the ends, typically when $n \simeq 1.5$. For Oh=0.001, the maximal elongation was characterized by the ratio $a/b = 2.66$, close to the value of 2.6 found for inviscid fluids (see figure 1.23). At the other extremity, for Oh=0.8, the aspect ratio a/b was 3.82, close to the factor 3.86 found by Betelù *et al.* [46] in the case of the Stokes flow approximation (creeping flow with vanishing inertia forces). The latter is an approximation of the incompressible Navier-Stokes equation is the limit of large Oh $\gg 1$. The aspect ratio found for $n = 1.5$ as a function of Oh $\in [0, 1.4]$ is summarized in Fig. 1.26. The latter is compared to the VPF model, which shows

50

a different trend. In particular, VPF exceeds the asymptotic aspect ratio of 3.86 found in the Stokes flow approximation for larger Oh, confirming that VCVPF may be better suited for a larger range of viscosities.
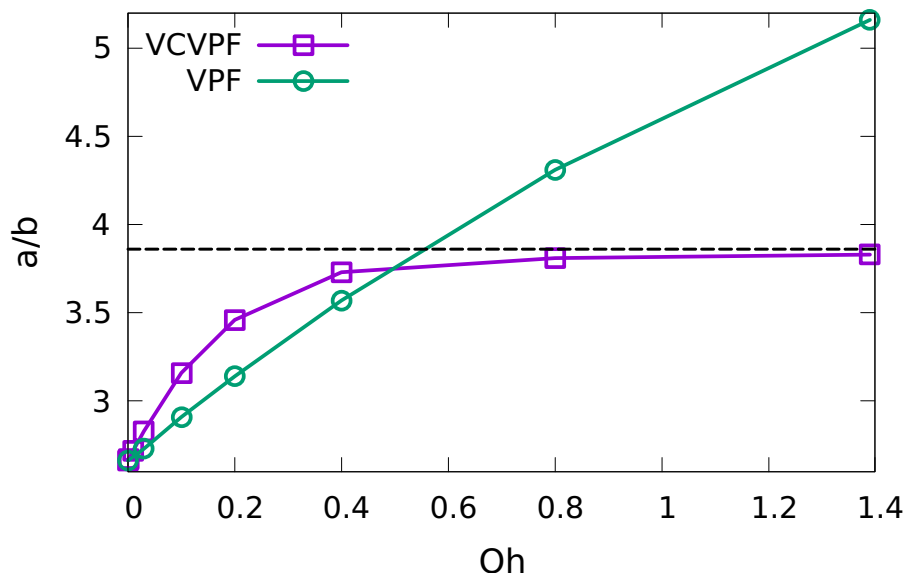
Figure 1.26: Aspect ratio a/b of the droplet at charge break-up, (taken at for $n = 1.5$) as a function of the dimensionless viscosity Oh. Pink empty boxes stand for the VCVPF model and green empty circles for the VPF model. The horizontal dotted black line is $a/b = 3.86$ and gives the maximal elongation of the drop in the case of Stokes flow approximation [46].

For the simulated pathways in Fig. 1.25, once the tip has formed, 20% of the initial charge are suddenly removed and the fissility parameter drops instantaneously to $X = 0.64$. At the same time, we reduced the kinetic energy by 80 % [15]. After charge emission, the pressure due to the surface tension dominates the Coulomb pressure at the surface and the tips relax. This is represented by the increase of the parameter n from 1.5 to up to 3.0 depending on the Oh number. Because of viscous forces, the accumulated kinetic energy is dissipated and the drops returns finally to the spherical shape, unlike the simulations done with the inviscid liquid (1.23). The shape deformation of viscous drops shows a similar behaviour than the damped forced oscillator. Oh $\simeq 0.2$ corresponds to the value were the droplet is critically damped, meaning that it does no longer overshoot into the

---

[15]This is an arbitrary choice and motivated here so as to allow simulating also very low viscous drops Oh= 0.001 for which the low energy dissipation could otherwise prevent the computation of the return path of the low-viscous drop.

oblate domain when returning to the asymptotic spherical shape. For lower Oh, the dynamics is underdamped and the return to the sphere goes through oblate shapes as indicated by the ratio $a/b < 1$. In the $(a/b, n)$ graph, the droplet oscillates, with decreasing amplitude, between the prolate and oblate shapes and between pointed and rounded tips. For Oh> 0.2, the motion is overdamped and the droplet returns slowly to steady state spherical shape. In the particular case of Oh=0.8, the return path is even characterized by $n \leq 2$, meaning that the tips stay pointed even after charge emission. As in this case, Oh= $0.8 > \mathrm{Oh}_c = 0.56$, the prediction may not be meaningful.

1.5.2 Comparison of VCVPF calculations with experimental results

Glycol and supercooled water droplets
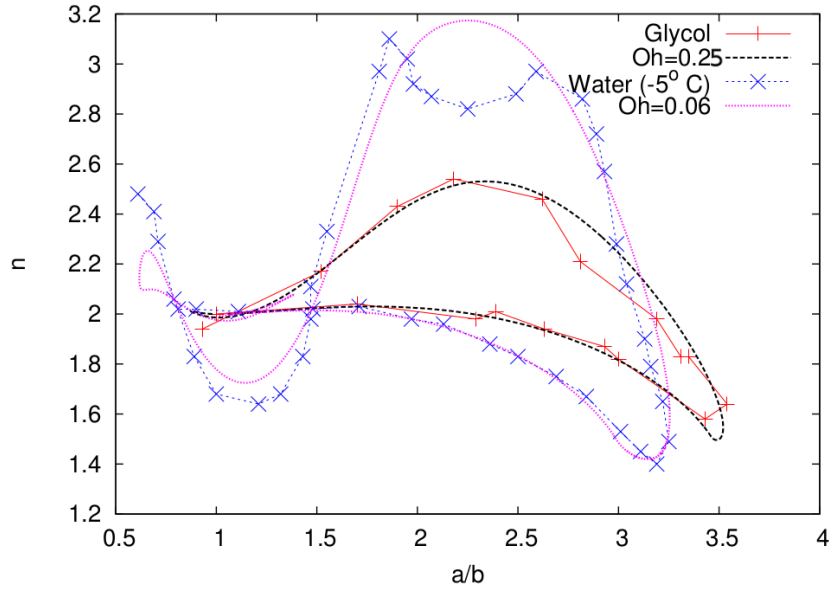
Figure 1.27: Simulated deformation pathway (dotted pink and dashed black lines) compared to experimental data (blue "x" and red"+" standing for supercooled water and glycol droplets respectively. At charge break-up, ($n = 1.5$ for Oh=0.06 and $n = 1.55$ for Oh=0.25), the charge was reduced by 20% ($X = 0.64$) while the kinetic energy was reduced by 20%.

We superpose in Fig.1.27 the VCVPF calculations with Oh=0.06 and Oh=0.2 to the experimental data already presented in the previous sections, namely glycol

droplets and supercooled pure water droplets. We found a remarkable agreement between Glycol and the Oh=0.25 VCVPF curve. For the supercooled water droplets, the VCVPF curve with Oh=0.06 seems to slightly overestimate the damping on the "way back" but gives a overall excellent agreement. Knowing the radius, surface tension and density of the glycol[16] and water droplets[17], we can deduce a viscosity of 9 cP for Glycol and 2.5 cP for supercooled water. In the case of glycol, the deduced viscosity is below the expected one by about 50%. The reason is that VCVPF tends to clearly overestimate the damping for Oh> 0.2. Also, in the case of the Glycol drop, the deformation may not have been observed at room temperature, but slightly above. Indeed, Glycol droplets were injected at about 80° C, then cooled down due to evaporation in the trap for about 3 minutes before reaching the critical fissility. The final temperature of the droplet for which the critical value is reached may thus be slightly above 25° C.
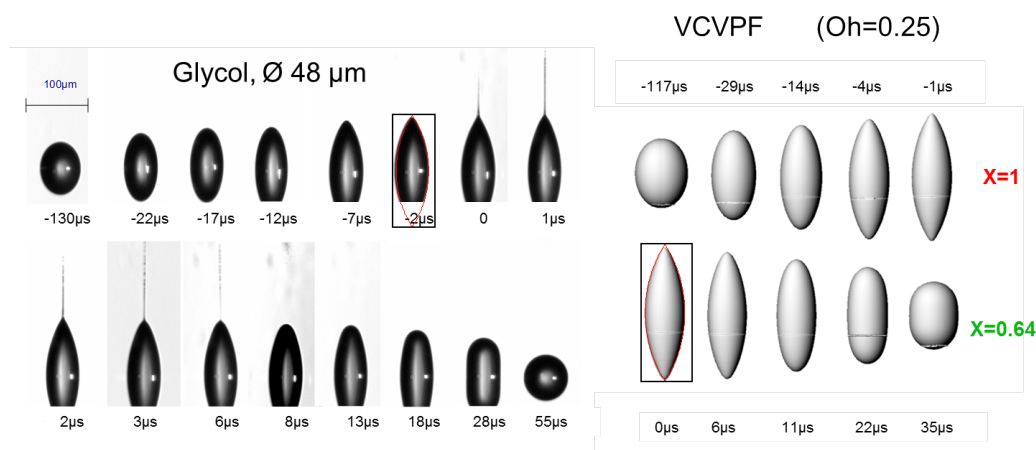
Figure 1.28: *Snapshots of critically charged droplet shapes at different times before and after charge emission simulated with the VCVPF model. We used here Oh=0.25 and the perfect conductor approximation. The same red lemon shape (same aspect ratio) was used for fitting the experimental snapshot and the simulated one.*

We took snaptshots of the simulated droplet deformation for Oh=0.25. The snapshots are compared in Fig.1.28 to the experimentally observed shapes of a critically charged glycol drop of same diameter, namely $\varnothing = 48\mu$m. We note the

---

[16]With $(\rho, \gamma, R) = (1.1 \text{ g/cm3 }, 48 \text{ mN/m}, 24 \text{ μm})$ for the glycol droplet, Oh=0.25 yields a viscosity of $\text{Oh}\sqrt{\gamma \rho R} \simeq 9$ cP, which is 1/2 of the expected value 18 cP of Glycol at room temperature.

[17]With $(\rho, \gamma, R) = (1.0 \text{ g/cm3 }, 78 \text{ mN/m}, 34 \text{ μm})$ for the water droplet, Oh=0.06 yields a viscosity of 2.5 cP, which is close to the expected viscosity of supercooled water droplets of 2.2 cP at -5° C.

excellent agreement. In particular the shapes after charge emission are now well reproduced by the VCVPF model, and the droplet returns to its initial spherical shape without overshooting. Both, the simulated and observed shape at $t = 0$ are compared to the same lemon profile 1.57 with $A = 4.97$ and $B = 4.27$ and shown by the red contour shapes in Fig.1.28. This indicates that the observed and simulated shapes, at the moment of charge emission, agree and that the VCVPF model is sufficient to reproduce the observed data. The "return path" to the sub-critical spherical shape is also well reproduced.

Glycol-Water mixture
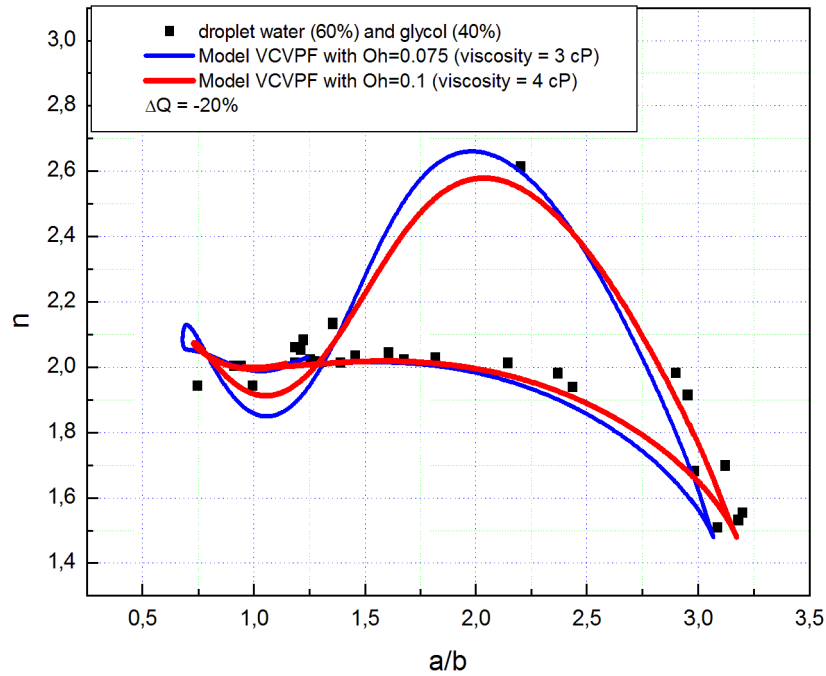
Figure 1.29: Simulated deformation pathway for two different viscosities. Black squares are correspond to observed glycol-water droplets and fitted by a superellipsoid. At charge break-up ($n = 1.52$), the kinetic energy was reduced by 30% and 25% of the initial charge was emitted.

We showed in Fig.1.18 and Fig.1.17 the experimental data of critically charged droplets made out of a mixture of 60% water and 40% of glycol. The viscosity of

those droplets at room temperature is expected to be around 3 cP. We simulated the deformation pathways of a droplet for various viscosities. We found that best agreement with the experimental data was obtained for droplets having an Ohnesorge number between 0.075 and 0.1, see Fig.1.29. Taking the same initial radius of the droplets than the experimental one ($\varnothing = 26\mu$m), and taking the viscosity and surface tension of the glycol-water mixture, $\gamma = 58$ N/m and $\rho = 1060$ kg/m^3, we get that Oh=0.075 and Oh =0.1 corresponds to fluids having a viscosity of 3 and 4 cP, respectively. Remarkably, the simulations corroborate the estimated viscosity of the mixture!

Pure water droplets
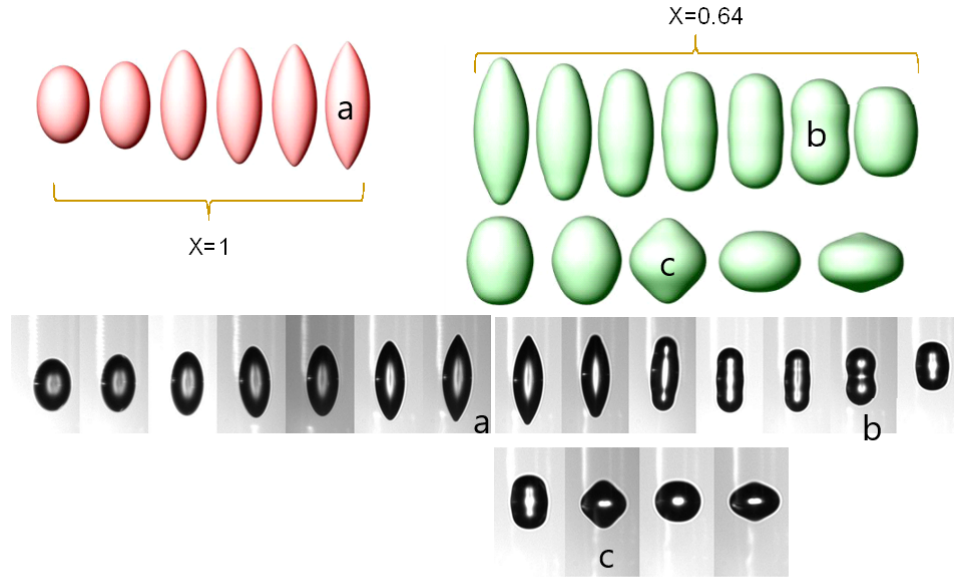
Figure 1.30: Comparison between simulated (top) and observed (bottom) snapshots of $\varnothing = 52\mu$m deionized water droplets at room temperature. Initially, the red droplets are charged at the Rayleigh limit $X = 1$. At charge break up, 20 % of the charge is removed and the fissility for the green drop is $X = 0.64$. Shape labels: (a) lemon, (b) peanut, (c) diamond.

Finally, we took snapshots of the ultrafast shape deformation of pure water droplets at the Rayleigh limit. At the onset of the instability, the trapped water

droplets have a $\varnothing = 52\mu$m. Assuming that water at room temperature has a viscosity of 1 cP, a density of 1000 kg/cm^3 and a surface tension of 0.072 N/m, the droplets are characterized by a low dimensionless viscosity of Oh=0.023 (see table 1.2), and are thus particularly good candidates for the simulation with our VCVPF code. As mentioned before, no jets were detected on the snapshots, neither for positively nor for negatively charged water droplets at room temperature. The lack of observed jets made us assume that the kinetic energy loss during charge emission should be negligible. We also assumed that the charge is emitted in an amount of time short enough to consider the droplet deformation frozen during charge emission. In our numerical code, the charge emission is simulated thus by simply removing instantaneously a fraction of the charge as soon as pointed tips are formed. The kinetic energy accumulated during the first part of the deformation is conserved during the charge emission. In the example showed in Fig. 1.30 the deionized water droplets were positively charged. The measurements in [52] indicate that positively charged pure water droplets emit at room temperature about 20 % of the initial charge at charge breakup.

We simulated with our numerical code, based on the VCVPF model, the complete shape deformation of an initially critically charged droplet, including the charge breakup and the "return" to the stable sub-critically charged spherical drop. We used in our simulations a bulk conductivity of $\kappa_b = 5.5 \times 10^{-6}$ S/m and a charge mobility of $\lambda = 37 \times 10^{-8}$ m^2/s/V (see table 1.2). We compare in Fig. 1.30 the simulated shapes to the observed ones. The red simulated shapes in Fig.1.30 are critically charged droplets ($X = 1$) and show the ultra-fast shape deformation after the onset of the instability. Once the pointed tips are formed, we removed, as suggested by [52], 20% of the charge and the fissility reduces instantaneously to $X = 0.64$. At that moment the shape fits remarkably well the experimentally found lemon-like shape. But even more remarkably is the agreement between simulated and observed shapes during the sub-critical shape deformation (green shapes). Especially, the *peanut* and *diamond* shape have been found by the simulation. The general agreement validates our approach for describing low-viscous liquid droplets.

1.5.3   Influence of the charge carrier mobility

In this section, we focus on the influence of the charge mobility of excess charge carrier on the deformation pathway. The mobility of the charge carriers in the liquid may be such that the surface τ_s and bulk τ_b charge relaxation times (eq.1.70) are comparable to the characteristic deformation time τ_0. In that case, the liquid cannot be considered as a perfect conductor and the charges at the surface may not be at equilibrium for a given shape (the Coulomb potential is not an equipotential at the surface). We consider the particular case where the dimensionless bulk
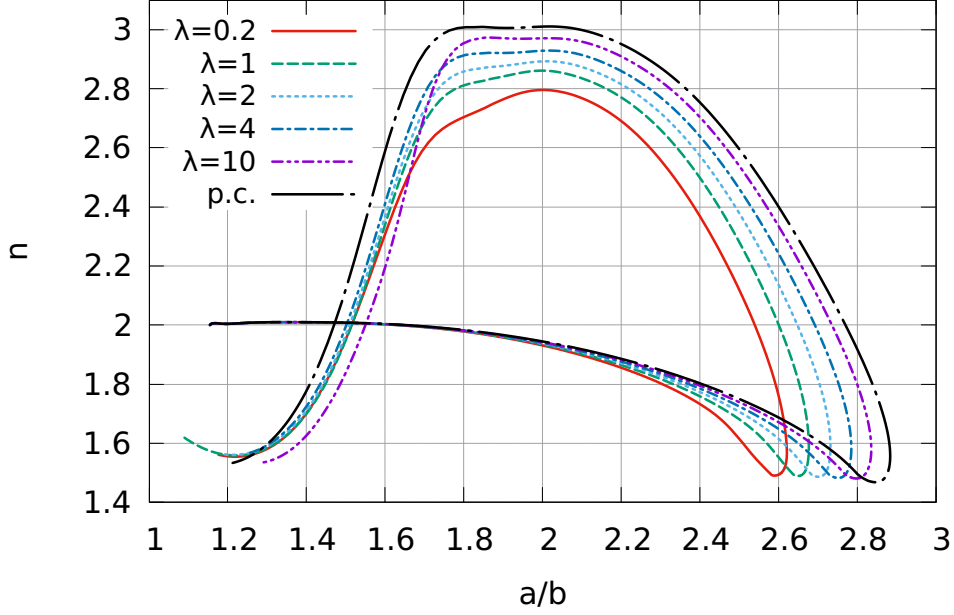
Figure 1.31: Deformation pathway of a droplet with Oh=0.023 (typically a 50 μm water droplet at room temperature) for various dimensionless charge carrier mobility $\tilde{\lambda}$, ranging from 0.1 to 10 and for the perfect conductor (p.c.). Except for the latter, we used the bulk conductivity of deionized water of 5.5 μS, leading to a dimensionless bulk conductivity of $\tilde{\kappa} = 0.1$. At charge break-up ($n = 1.5$) the charge was reduced by 20% ($X = 0.64$) while the kinetic energy was reduced by 80%.

conductivity $\tilde{\kappa} \ll 1$ is sufficiently small so that the charge dynamics is dominated by the surface current j_s and depends mainly on the dimensionless charge mobility $\tilde{\lambda}$ (1.71). The latter gives the ratio between the dimensionless velocity of the charges dragged by the liquid and the velocity of the charges pushed by the electric field at the interface. In figure 1.31, we show the pathway of a critically charged drop as a function of the charge mobility $\tilde{\lambda}$. The simulations were performed with $\tilde{\kappa} = 0.1$ and with a dimensionless viscosity of Oh=0.023 (corresponding to a $\varnothing = 52\mu m$ droplet of deionized water at room temperature, see table 1.2. We see that with decreasing mobility, the aspect ratio a/b of the droplet at tip formation ($n \sim 1.5$) decreases from 2.85 to 2.6. Taking $\tilde{\lambda} \gg 10$ gives a pathway with is indistinguishable from the perfect conductor (p.c) case. At $n = 1.5$ the charge was reduced by 20% ($X = 0.64$). The effect of the charge mobility on the return path was found negligible and will not be further discussed here.

The reason why smaller charge mobilities $\tilde{\lambda}$ tend to accelerate the tip formation is explained by the competition between the charged being dragged by the fluid

and the charges being pushed by the tangent component of the electric field at the surface. For low-viscous drops, Oh< 0.03, the velocity at the surface may be so high that the flow drags a large amount of charges to the tips. If the accumulated charge density at the tips exceeds the equilibrium charge density σ_{eq} (the equilibrium charge corresponds to the charge distribution that results in an equipotential at the surface) it generates an electric field directed from the tip to the equator of the droplet, acting against the drag of the flow. The larger the charge mobility, the larger the surface charge relaxation rate τ_s^{-1} and the closer the charge distribution stays to the equilibrium charge distribution σ_{eq}. That is why the deformation pathway tends to the p.c. case for $\tilde{\lambda} \gg 1$. On contrary, for $\tilde{\lambda} \ll 1$ the surface charges move mainly with the fluid to the ends, where they accumulate. The large concentration of charges at the tips tends to accelerate the formation of pointed ends[18]. The finite charge mobility has thus a non-negligible effect on the shape deformation and should be taken into account when looking at the pathway in detail. We will see below that the charge mobility allows to discriminate between positively and negatively charged pure water droplets.

Positive vs negative drops

In the last example of this section, we compare the simulated shape deformation of positively and negatively charged droplets to our experimental data. By changing the sign of the polarization ring of the injector, negatively or positively charged droplets can be injected and trapped. From the recorded snapshots, we reconstructed in Fig. 1.32 the deformation pathway of positively (green squares) and negatively (black circles) charged drops. Surprisingly, the pathways differ and the positively charged droplets show at jet emission a more elongated shape with an aspect ratio of $a/b = 2.9$ than the negatively ones ($a/b = 2.7$). As the radius was 26μm for both cases and as the viscosity and density are not expected to depend on the sign of the charge, we supposed that the different behaviour comes from the different mobility of the charge carriers in water. Indeed, protons H^+ and hydroxides OH^- in aqueous solution have both an anomalously large diffusion coefficients, but with the mobility of H^+ being almost twice as large as that of OH^- anions [54, 44].

We simulated the pathway with the VCVPF model, with the surface charge dynamics depending on the mobility of the charge carriers via the dimensionless factor $\tilde{\lambda}$ defined by (1.71) and on the bulk conductivity via the dimensionless factor $\tilde{\kappa}$. In table 1.2, we give the relevant parameters of a droplet of deionized water of radius $R = 26$μm at room temperature used in the simulations. We chose for the charge mobility of positive and negative drops respectively $\lambda^+ = 37 \times 10^{-8}$

---

[18]Pointed tips have a higher electric capacity C than rounded tips so that the Coulomb energy $\frac{1}{2}Q^2/C$ diminishes for pointed tips

and $\lambda^- = 20 \times 10^{-8}$ (m^2/s/V), corresponding to the charge mobility of H$^+$ and OH$^-$ [44] at room temperature. Positively and negatively charged droplets are distinguished only by the charge carrier mobility and, in both cases, the dimensionless charge mobility dominates the dimensionless bulk conductivity $\tilde{\lambda} \gg \tilde{\kappa}$. As a result, the deformation pathway is expected to depend sensibly on $\tilde{\lambda}$, with the bulk conductivity having merely a negligible effect on the deformation dynamics[19]. The two simulated paths are superposed in Fig.1.32 to the experimental data. We found a remarkable agreement between the simulated and observed pathway. In particular, the larger aspect ratio a/b at jet emission of positively charged drops compared to negatively charged drops is well reproduced by the simulation.

It seems thus that the reason to why positively charged pure water droplets have a aspect ratio a/b larger than negatively charged ones is because H$^+$ has a higher charge mobility than OH$^-$. For such low-viscous droplets, Oh= 0.023, the

---

[19]for see water, having a bulk conductivity of 5 S/m, one has $\tilde{\kappa} \gg \tilde{\lambda}$. As a result, positively and negatively charge droplets should yield the same deformation path, unlike deionized water
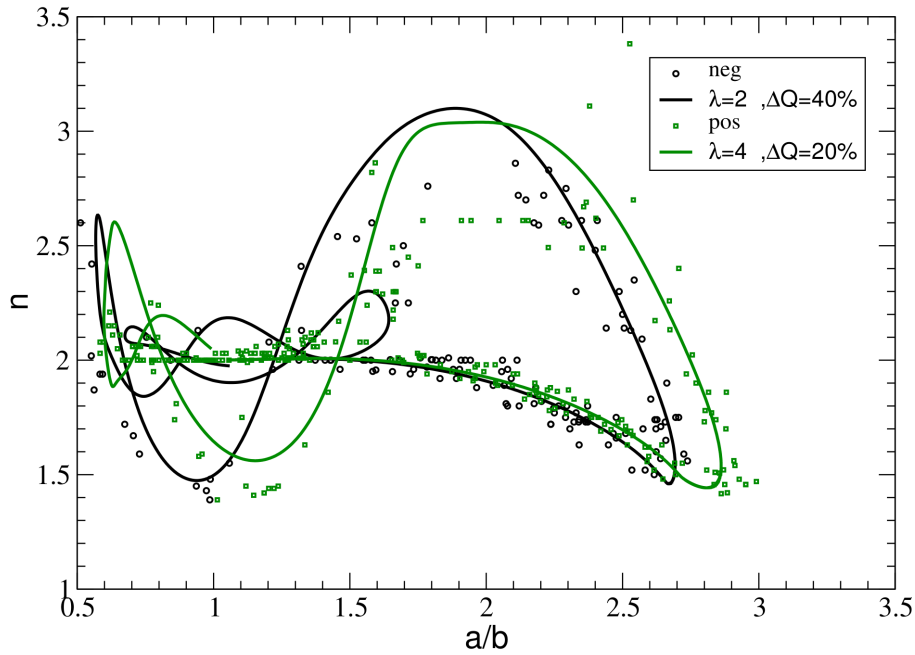
Figure 1.32: Deformation pathway for positively and negatively charged water droplets having a radius of 26 μm. Full lines are simulations with Oh=0.023. The green line used $\tilde{\lambda} = 4$ and the black used $\tilde{\lambda} = 2$. The emitted charge is given in the legend. Black circles and green squares are experimental results of negatively and positively charged deionized water droplets, respectively. As no jets were found on the snapshots, **no** kinetic energy was removed from the drop during charge emission.

Table 1.2: *Parameters of positively and negatively critically charged droplet of deionized (pure) water. Upper table: Parameters, common to positive and negative drops; Lower part: electrical properties depending on the sign of the critical charge Q.*

R (µm)	μ (cP)	ρ (kg/m^3)	γ (mN/m)	ε_r	Oh	τ_0 (µs)
26	1	1000	72	80	0.023	16

Sign(Q)	κ (µS/m)	λ (m^2/s/V)	$\tilde{\kappa}$	$\tilde{\lambda}$
pos	5.5	37×10^{-8}	0.1	4.0
neg	5.5	20×10^{-8}	0.1	2.1
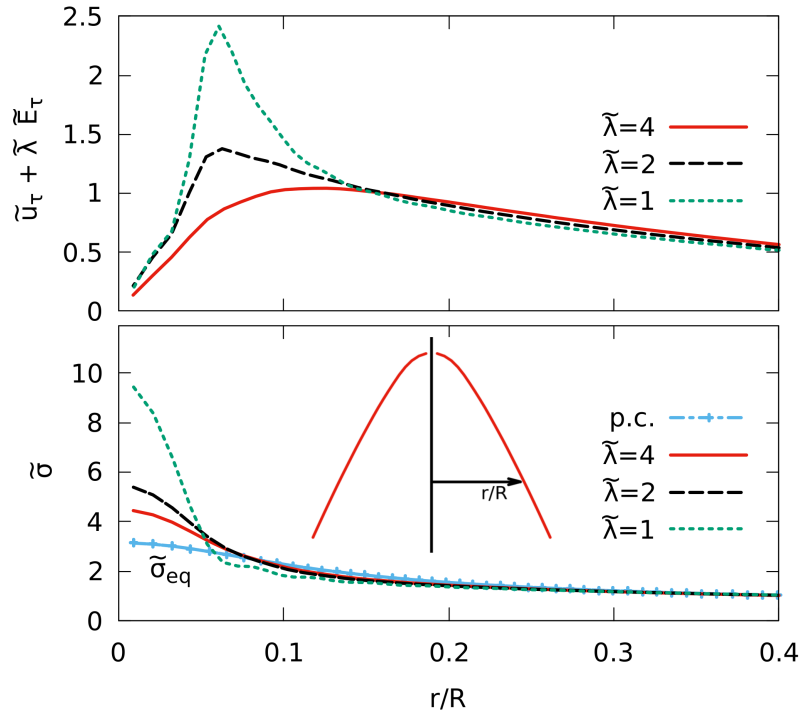
Figure 1.33: *Upper panel: dimensionless velocity of the charges tangent to the surface, $\tilde{u}_\tau + \tilde{\lambda}\tilde{E}_\tau$, as a function of the dimensionless distance r/R defined in the inset. Positive values indicate velocities directed towards the tips. Lower panel: Dimensionless surface charge density $\tilde{\sigma}$ as a function of r/R. The quantities are calculated for three different charge mobilities $\tilde{\lambda}$. The blue "+" symbol line gives the equilibrium surface charge density $\tilde{\sigma}_{eq}$ in the case of a perfectly conducting liquid (p.c.).*

drag of the charges by the fluid velocity is in competition with the push by the electric field. It happens that for OH^- the latter effect is less efficient so that more charges accumulate at the tips, accelerating the tip formation. The charge velocity tangent to the surface, given as the sum of the drag velocity $\tilde{u}_\tau$ and "electric field" velocity $\tilde{\lambda}\tilde{E}_\tau$ is illustrated in the upper panel of Fig.1.33 for three different values of $\tilde{\lambda}$. The quantities in Fig.1.33 are given as a function of the dimensionless distance r/R, corresponding to the distance from the symmetry axis to a surface point, such that $r/R \to 0$ corresponds to the tips (see inset). We note that close to the tips ($r/R \simeq 0.06$), the velocity of the charges is reduced by a factor 2 when increasing $\tilde{\lambda} = 1$ to $\tilde{\lambda} = 4$. The accumulated charge density at the tips (lower panel) for $\tilde{\lambda} = 1$ was also found to be larger about by a factor 2 than for $\tilde{\lambda} = 4$, accelerating thus the tip formation.

We found that, for negatively charged drops, removing only 20% of the charge, as we did for the positively charge drop, was not sufficient to reproduce the experimental *way back* pathway. We had to remove 40% in order to reproduce the amplitude of the *way back* path. This is corroborated by the observations reported by R. Müller in his thesis[20]. They found that negatively charged droplets with $R = 31$ µm emit about 40% of the initial charge at charge break up. The reason for the latter may be found in the higher accumulated surface charge at the tips with decreasing charge mobility.

What if instead of pure water we had used sea water? Sea water, having a bulk conductivity of 5 S/m yields a dimensionless conductivity $\tilde{\kappa} \simeq 10^4$ which is much larger than the typical dimensionless charge mobility $\tilde{\lambda} < 10$ of excess charge carrier. The charge dynamics would then be dominated by the bulk current $\tilde{\kappa}\tilde{E}_n$ and the liquid well approached by a perfect conductor. We expect thus positively and negatively charged droplets of sea water to yield the same deformation path and emit the same amount of charge at charge break-up. The latter prediction may be verified in future experiments.

Concluding remarks for VCVPF: We conclude this section by highlighting the remarkable results.

1. The VCVPF model predicts that the aspect ratio of the shape just before charge break-up is is increases with increasing dimensionless viscosity Oh. This is because the tip formation is retarded due to higher viscosity, whereas for lower dimensionless viscosities, the tips are formed earlier. We found that the ratio a/b lies between 2.5 for inviscid liquids to 3.86 for Stokes flows, $a/b \in [2.6, 3.86]$.

---

[20] *Stabilität und Zerfallsdynamik hochgeladener Flüssigkeitströpfchen*, Dissertation by René. Müller (2010), Fakultät für Mathematik und Naturwissenschaften der Technischen Universität Ilmenau. https://www.db-thueringen.de/receive/dbt_mods_00015683

2. The model can be used to predict the viscosity of a liquid (here mix of water and glycol) by fitting the experimental pathway in the $(a/b, n)$ graph. The predictions are more reliable for lower viscosities, Oh < 0.2.

3. In the particular case of critically charged pure (deionized) water drops at room temperature, the VCVPF model describes accurately all steps of the shape deformation. The pathway from the initial spherical shape to the lemon shape, the instantaneous charge emission with negligible kinetic energy loss and the pathway back to the sphere by going through exactly the same exotic shapes. The excellent agreement gives much confidence in the underlying model and numerical algorithms of the simulations.

4. We found that, if the dimensionless charge mobility $\tilde{\lambda}$ dominates the dimensionless bulk conductivity $\tilde{\kappa}$ of the liquid while being of the order of 1, the droplet deformation is sensitive to the mobility of the charge carriers. In the case of pure water droplets, the polarity of the charge can eventually be determined by comparing the aspect ratio a/b of positively and negatively droplets just before charge breakup.

1.5.4 Boundary element method

In VCVPF, the Laplace solver uses harmonic functions in the prolate coordinate system. While that algorithm is adapted for simulating the time evolution of a critically charged drop, from the initial spherical shape to the pointed lemon shape and back to the sphere, it breaks down at the jet formation. Indeed numerical errors increase exponentially when the ends become pointed and the simulation usually stops just before the Taylor cone and jet could be formed. The culprit is the loss of orthogonality of the harmonic basis functions ϕ_k when the shape of the drop deviates strongly from a prolate spheroid. Some eigenvalues of the overlap matrix $S_{k'k} = \int \phi_{k'} \frac{\partial \phi_k}{\partial n} \, ds$ tend then to zero which makes the matrix almost singular. Also, an increasingly large number of harmonic functions are necessary to represent finely the tip of the pointed drop shape. As a result, the numerical method based on the expansion of harmonic functions in prolate spheroidal coordinate system is no longer appropriate to solve the Laplace equation 1.46 inside the volume of a droplet near charge breakup. We proposed thus to solve the Laplace equation using the Boundary Element Method (BEM[21]). The advantage of BEM is that it can solve the Laplace equation for wherever regular closed surface enclosing a volume and is thus well adapted to describe for example the cone formation at the droplet tip.

---

[21]The Boundary Element Method is well documented on
http://www.boundaryelements.com) and
http://www.boundary-element-method.com by Stephen Kirkup.
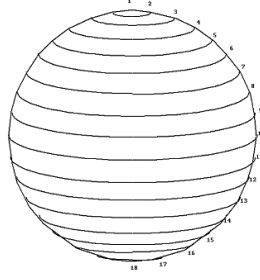
Figure 1.34: Representation of the sphere by truncated conical panels.

The disadvantage of BEM is that it converges slowly ($\propto N^{-1}$) to the exact solution with increasing number N of elements, increasing thus the CPU cost. To optimize the simulation, the numerical code switches thus from the harmonic expansion method to BEM once the overlap matrix $S_{k'k}$ is close to singular. In practice, we switched to BEM algorithm once the n parameter of the superellipsoid fit falls below 1.54. We discretized the axisymmetric droplet surface $\xi(\eta_i)$ using 400 points that clustered close to the apex, so that the density of points close to the apex was higher than close to the equator. Because of axisymmetrie, each BEM element is thus a truncated cone defined by two successive points at the surface (see Fig.1.34 for example). We used cubic splines[63] to interpolate the surface at any arbitrary point[22] and to calculate the mean curvature at the grid points.

Simulated Results

The BEM algorithm allowed us to simulate the tip formation and even the onset of the jet emission of a droplet. In Fig.1.35 we show the time evolution (black lines taken at successive time steps) of the tip of a critically charged droplet with Oh=0. Interestingly, we found that the half-opening angle of the tip just before break-up, approaches the Taylor angle of 49° [8], with an estimated angle of 48.3° near the tip, confirming Taylor's prediction of a conical tip. This result is a refinement of the one shown in Fig.1.22, where an estimated tip angle of 39° was found. Please note the dimensionless x-scale of Fig.1.35; The Taylor angle is measured within a distance of 0.03 from the symmetry axis and the angle drops quickly beyond that region. BEM succeeded also to simulate the onset of the jet formation. The latter is characterized by a kink around 0.01 from the symmetry axis and an exponentially fast increasing of the tip height. Unfortunately, the BEM methods also breaks down at this point as the curvature becomes near singular. The finite thinness of the jet seems to be spurious and limited by the numerical resolution

---

[22]We used zero first derivative at the end points

63
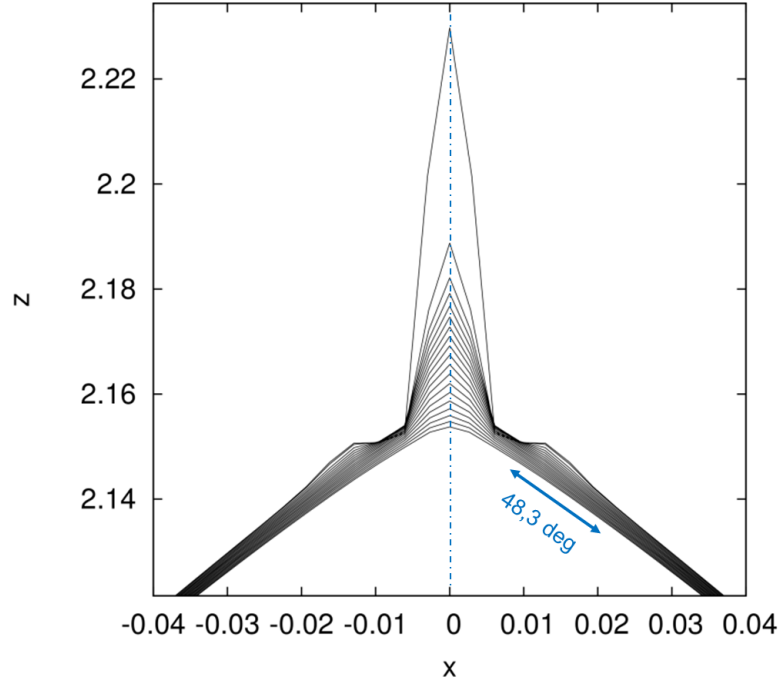
Figure 1.35: Simulated time-evolution of the tip shape. x and z are dimensionless, normalized to the initial droplet radius.

of BEM (the 400 points). In the case of Oh> 0, the jets are expected to have a finite thinness as was observed in the experiments. Simulations with Oh> 0 have not been done yet, as some numerical adjustments needed to be done.

1.5.5   Finite element method

BEM is a promising technique for solving the Laplace equation for arbitrary droplet shapes in irrotational flow approaches like VCVPF or Stokes flows like [46]. However, fluid dynamics of viscous droplets is best described by the full Navier-Stokes (NS) equation. The latter is usually solved using a Finite Element Method (FEM[23]), where the boundary conditions are imposed weakly. With Dr. Radcliff Allister, who occupied the 1-year post-doctoral position founded by the

---

[23]The Finite Element Method is introduced by:

Daryl L. Logan (2011). *A first course in the finite element method.* Cengage Learning. ISBN 978-0495668251.

Reddy, J. N. (2006). *An Introduction to the Finite Element Method* (Third ed.). McGraw-Hill. ISBN 9780071267618.

ANR DYNAMIC 2007, we proposed to describe the deformation dynamics and Coulomb explosions using a non-conforming, discontinuous Galerkin finite element procedure with moving meshes. Assuming xOy plane symmetry for the droplet deformation, the droplet is discretized in FEM by a mesh of triangles Fig.1.36. The simple equations that model these finite elements are then assembled into a larger system of equations that models the entire problem. FEM then uses variational methods from the calculus of variations to approximate a solution by minimizing an associated error function. Unlike the (VC)VPF models, FEM calculates explicitly the fluid dynamics in the volume. As a result, FEM is clearly more CPU expensive than the (VC)VPF models. However, it is not restricted to potential fluids and is indeed well appropriate for resolving the Navier-Stokes equation for a real (viscous Newtonian fluid). The full Navier-Stokes equations are discretized
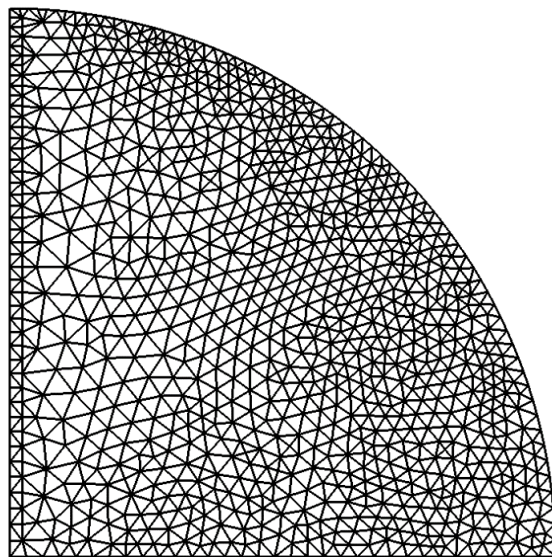
Figure 1.36: Discretization of the surface by triangles for FEM calculations. Initial mesh of 1908 finite elements used for the prolate deformations. Note the structured "zigzag diagonal" nature of the mesh elements abutting the axis of rotational symmetry. Extracted from [58].

and solved in an Eulerian manner with a simple predictor-corrector Lagrangian updating of the free boundary location coincident with the droplet surface at each solution iteration. We used linear Crouzeix-Raviart basis functions for the velocity and piece-wise constant pressures. The use of the original and ever popular $P_1^{NC} - P_0$ Crouzeix-Raviart non-conforming velocity-pressure finite element pair [12] was made in anticipation of future developments for flexible mesh - interpolation polynomial ("h-p") refinement about the droplet tip during jet formation

and to avoid introducing the additional high-order singularities that appear in the axisymmetric stabilization terms required for otherwise unstable $P_1 - P_0$ or equal-order $P_1 - P_1$ conforming velocity finite element schemes [31]. To avoid spurious mass build-up along inter-element edges and to impose the zero tangential traction applied by two different elements either side of such shared edges equal and opposite (see eq. 1.25), it is necessary to introduce extra terms to penalize any velocity and traction jumps across these internal edges. This is a usual requirement of non-conforming methods and is typically parameterized by a scalar penalty parameter β. The greater this parameters value, the more severe such jumps are punished, but also the more ill-conditioned the final system matrix becomes. A judicious choice of $\beta = 0.07$ was found to be appropriate for the given problem and its value is discussed in [58].

One of the principle difficulties encountered in the simulation of the droplet lay in the calculation of the mean curvature H (eq. A.14) of its surface. The fourth-order polynomial stencil fitting was in most instances found to be adequate. However, it should be noted that unless using very coarse meshes, the nodes on such stencils could sometimes become approximately collinear and the calculation of mean curvature become very ill-conditioned[24]. The numerical code is validated with the results, presented both for the simple (oscillatory) relaxation of elongated electrically (un)charged droplets to a sphere and for the deformation of super-critically charged initially slightly oblate spheroidal droplets.

Simulated Results

In a first step, we confirm that the underlying dynamics of the charged droplet are correct, validating the finite element numerical model used. This is performed by considering the relatively small viscous damped oscillations of a prolate elongated droplet after a deformation induced by a small initial irrotational quadrupole velocity field of dimensionless amplitude of $u_0 = 0.07$, $\vec{u} = u_0 \vec{\nabla}(r^2 P_2(\cos(\theta)))$. Figure 1.37 shows the computed results for just this initial perturbation using the non-conforming scheme described in [58], with blue and red vertical gridlines marking the expected semi-periods for each case respectively. The expected periods of the droplet oscillations with $X = 0.5$ and $X = 0$ were calculated using 1.2. The horizontal displacement for the gridlines was chosen so that the leftmost would correspond with the first peak in each case. We distinguish 3 subsets in Fig.1.37 , one with an "s" suffix, one with an asterisk, and one bare. For the "asterisk" subset, the zero shear stress boundary condition was weakly imposed by the penalty parameter $\beta = 0.007$ while the said boundary condition was not imposed

---

[24]This problem was avoided in the VCVPF approach, at least as long no singular tips are formed, as we used a spectral method based on Gauss-Legendre collocation points to interpolate the droplet surface allowing to compute accurately the mean curvature H.
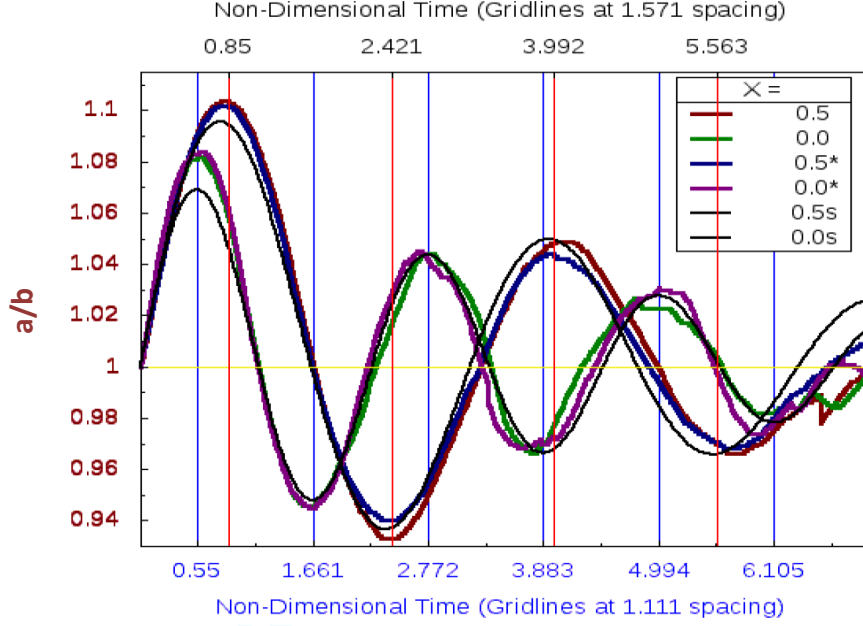
Figure 1.37: Oscillatory relaxation to a sphere after an initial launch with a initial quadrupole velocity of (dimensionless) amplitude of 0.07 for both a charged (X = 0.5) and uncharged (X = 0) liquid droplet with Oh = 0.04.

for the "bare" set. We see that in the low amplitude oscillatory regime, the zero shear stress boundary condition has little to no influence on the damping, as it it not severely violated when not imposed. This is corroborated by the "s" subset with stand for the VCVPF calculations (irrotational flow) and for which the zero shear stress boundary conditions is also not satisfied. The comparison between the VCVPF and FEM approach highlights rather the spurious damping of the FEM method at very low amplitudes due to the numerical errors in the evaluation of the mean curvature at the piece-wise constant discretized surface. We note here that a possible numerical improvement would be to use elliptic mesh generation[25], allowing a continuous boundary second derivative to be defined easing problems with the calculation of mean curvature and helping suppress surface irregularities.

---

[25]"Elliptic grid generation" signifies generation of generalized curvilinear coordinate grids through solution of elliptic partial differential equations (PDEs). Usually, such grids are fitted to bounding bodies. Such a grid is smooth and has continuous first and second derivatives, grid lines are appropriately stretched or clustered, and grid lines are orthogonal or nearly so over most of the grid domain.

FEM as presented here nevertheless reproduces nicely the damped oscillations of the viscous drop.
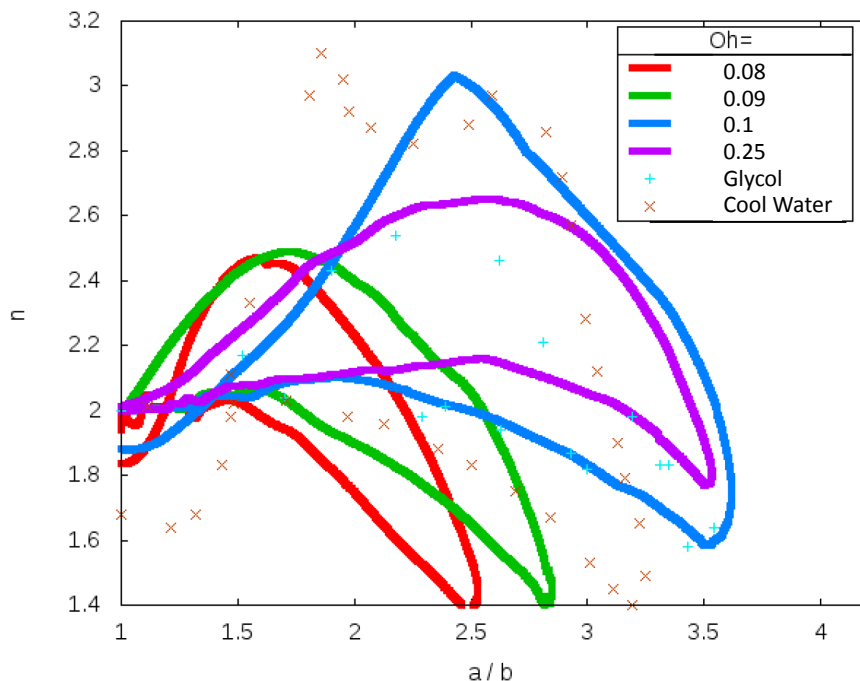
Figure 1.38: Simulated full deformation cycles for critically charged $(X = 1)$ prolate droplets of various viscosities (given by the Ohnesorge values) and compared against experimental results for Glycol (Oh$\simeq$ 0.2) and super-cooled water (Oh$\simeq$ 0.09). For the return, $X = 0.4$, meaning about 36% of the cahrge was removed.

Confident of our FEM approach, we simulated the deformation pathway of droplets of various dimensionless viscosities (Oh). Similar to VCVPF, the elongation (a/b) of the droplet before pointed ends were formed increased with Oh. Unfortunately, our attempts to simulate the jet formation, were not successful as we run into numerical problems, mainly for the evaluation of the mean curvature close to the tip, owing to significant displacements of the boundary nodes and to the appearance of slight surface kinks. Also the extreme sensitivity of the charge distribution to any surface irregularities worsened the numerical stability of the code. To cure partially the problem, a simple volume conserving re-positioning of boundary nodes was occasionally used to equalize local boundary node separation distances when these were significantly different and to remove surface indentations. The simulated deformation pathways (Fig.1.38) differ significantly form the VCVPF calculations (Fig.1.25), showing a much too strong influence of Oh on the

maximal elongation in FEM than in VCVPF. For example, the path for Oh=0.1 (blue curve) and Oh=0.09 (green curve) are quite different for only a 10 % variation of the dimensionless viscosity Oh. However, the simulations appear to capture the expected general deformation path. At this point, the simulations with the full NS approach solved via FEM must be considered as preliminary and the effect of the penalty parameter β on the pathway must be studied. Also the numerical errors arising in the evaluation of the mean curvature and surface charge distributions may have a non-negligible influence on the pathway.

1.6 Summary and Conclusion

In conclusion, we have studied the deformation dynamics of critically charged microdroplets from an experimental and theoretical point of view. The project was founded by the ANR 2007 and allowed us to acquire the necessary material to inject, trap and take snapshots of fast deforming droplets at the Rayleigh limit. We inherited a Paul trap of the first generation graciously given by the group of Prof. Thomas Leisner in Ilmenau and profited from their expertise to to set up quickly the whole experimental apparatus. Within 6 months (taking into account the incompressible time for purchasing the needed material), we had a functioning setup similar to the one used by the group of T. Leisner. After spending some unsuccessful time to inject mercury droplets, we succeed in injecting and trapping mixed water-glycol droplets. Our first snapshots taken in CIMAP and fitted to a superellipsoid allowed to compare in detail the effect of the viscosity of the deformation pathway. Compared to pure glycol droplets, our water-glycol droplets showed mainly a shorter elongation of the drop at charge emission, while the amount of emitted charge is comparable. We further injected positively and negatively charged pure water droplets. Their low viscosity confirmed the trend that with decreasing viscosity the droplets are less elongated at charge break-up. Moreover the study put into evidence the effect of the influence of the charge carriers mobility in the liquid on the deformation pathway. Remarkably, we observed no jet emission from pure water droplets at room temperature.

At the same time we started the development of our numerical codes based on a potential flow approximation. In a first step, we developed a numerical model based on the PF model, valid for inviscid liquids. This allowed us to validate (i) the time propagator of the surface vector and (ii) the evaluation of the Coulomb pressure and mean curvature at the surface. We checked for instance the conservation of the total energy and volume of the drop. It showed however quickly its limitations as the lack of viscosity did not allow to compute the deformation after charge emission. Also the numerical approach did not allow to compute the jet formation. In a second step, we improved our model by adding a dissipative term

69

proportional to the viscosity of the liquid. We based our code on the VCVPF approach, which is discussed in section 1.4.6. We presented an original numerical technique to include the effect of the shear stress in the pressure term, that is an improvement of the technique proposed by Joseph *et al.* [40] for small surface oscillations. Our VCVPF simulations corroborated the main results of the observed data and highlighted in particular a clear trend of the ratio a/b of the drop at charge emission as a function of the viscosity. We found that the ratio varies from $a/b = 2.6$ for an inviscid liquid to $a/b = 3.9$ for a high viscous liquid. The high viscous limit is in agreement with the calculation done for a Stokes flow (creeping liquid), giving confidence in our VCVPF model. The latter keeps the CPU advantage of the PF approach, where the velocity field is obtained from a scalar function defined on the axisymmetric surface (1D scalar function)[26]

Our study on pure water droplets as well as the PhD work by R. Müller [52], showed that, while no jet emission was observed for charged water droplets at room temperature, jet emission and daughter droplets were observed for cooled water droplets, but then only for positively charged drops, not for negatively charged ones. These observations motivated us to refine our numerical models. We lifted the perfect conductor assumption and added the dynamics of the surface charge distribution to the time evolution of the droplet surface. The charge dynamics was assumed to depend on the mobility of the charge carriers at the surface and on the bulk conductivity of the liquid. We demonstrated that the deformation pathway depends on the mobility of the charge carriers at the surface, but only in the cases where the charge relaxation rate of the bulk conductivity can be neglected (which is the case for pure water droplets). Our model succeeded thus to explains clearly why positively charged pure water droplets are more elongated than negatively charged droplets at charge emission.

While our VCVPF model was able to describe the whole deformation pathway for droplets with different viscosities and charge mobilities, we were still not able to simulate the jet emission. Even the tip formation, just before jet emission was badly described be our numerical technique. We added thus to our code a module that solves the Laplace equation with the BEM technique, where the surface is discretized by 400 points distributed non-uniformly, with a higher density of points close to the ends. BEM has a rather high CPU cost and was activated only when the shape approached the tip formation, that is, when the parameter n of the superellipsoid was below 1.54. We found the remarkable result that the jet is indeed emitted from a Taylor cone. The half-opening angle of the BEM simulated pointed tip, just before jet formation, was 48.3°, close to the predicted Taylor angle of 49°. Unfortunately we did not succeed to simulate also the jet, as we ran

---

[26]The Navier Stokes approach needs to propagate a 2D vector field, defined in the volume of the axisymmetric drop.

into numerical instabilities in the evaluation of the pressure terms, which became near singular near the tip. The development of an improved numerical algorithm is underway.

A. Radcliffe, who occupied a post-doc position in CIMAP for 15 months, developed a numerical code based on non-conforming finite elements to solve the 2D axisymmetric Navier-Stokes (NS) equations. Finite Element Method (FEM) have an even higher cost than BEM. For the FEM, we chose triangles which are implemented in standard libraries. First results showed that the chosen algorithmic succeeded to simulated grossly the surface oscillations on viscous drops. The code was particularly accurate for high viscosities, but less for lower viscosities. As such the NS-FEM approach is complementary with VCVPF, which is particularly accurate for low viscosities. We tried to simulate the jet emission with the NS-FEM approach but ran into the same problem than with VCVPF, that is, the pressure terms are evaluated with increasing numerical error close to the tip formation. A possible solution to this issue is to use the algorithm presented by Collins *et al.* [50], which uses FEM with elliptic mesh generation and adaptive implicit time integration to solve the NS equations. It allows unparalleled accuracy in the evaluation of the mean curvature as the technique is able to resolve in a single simulation length scales that differ by four orders of magnitude. Alternatively, Gañán-Calvo *et al.* used the promising Volume of Fluid (VoF) method for tracking and locating the free surface (fluid-gas interface) [61]. The VoF belongs to the class of Eulerian methods which are characterized by a mesh that is either stationary or is moving in a certain prescribed manner to accommodate the evolving shape of the interface.

This 5 year study, involving a small group in CIMAP, namely R. Rangama in charge of the experimental part, A Radcliffe in charge of the NS-FEM approach and myself, tackled the Coulomb instability of charged droplets and their amazing shape deformations. Using various numerical approaches, we succeeded in reproducing with our simulations the observed shape deformations of various liquids and highlighted trends of shape deformation as a function of the viscosity, charge mobility and amount of emitted charge. In the case of negatively charged pure water droplets, where no jets are observed, our simulations are in excellent agreement, giving high confidence in our numerical approach. In a future step, a new algorithm may allow to study also the jet emission as well as the amount of emitted charge, mass and lost kinetic energy.

Perspective

1.7 Rotationally Corrected Viscous Potential Flow (RCVPF)

While, in VCVPF, we recover the correct power of traction, the dissipation is still calculated using a purely irrotational velocity vector field. The viscous forces in the volume are still absent and the shear stress boundary condition is still not satisfied. We propose in this section to further refine the VCVPF approach by adding a rotational field to the potential velocity field that accommodates adiabatically so as to satisfy the zero shear stress boundary condition at each time step. We call this original approach the RCVPF approach. In the following we give some preliminary development of the RCVPF model.

In order to overcome the limitations of the previous potential flow models, we add a rotational axisymmetric velocity field to the irrotational velocity field $\vec{\nabla}\Psi(\xi,\eta)$. In a prolate spheroidal coordinate system (ξ,η,φ) it reads

$$\vec{u}(\xi,\eta) = \vec{v}(\xi,\eta) + \vec{w}(\xi,\eta) = \underbrace{\vec{\nabla}\,\Psi(\xi,\eta)}_{\vec{v}} + \underbrace{\vec{\nabla}\wedge(F(\xi,\eta)\hat{\mathbf{e}}_\varphi)}_{\vec{w}} \tag{1.90}$$

where $\Psi(\xi,\eta)$ and $F(\xi,\eta)$ is a scalar function. The decomposition (1.90) is known as the Helmholtz decomposition of an axisymmetric vector field. Because of the xOy plane symmetry, Ψ is an even function and F an odd function with respect to η. We remind that the incompressible liquid condition requires that $\vec{\nabla}\cdot\vec{u} = 0$, so that that $\vec{\nabla}^2\,\Psi = 0$. As was already shown in the previous sections, Ψ can be expanded on harmonic basis functions ψ_k. Limiting the expansion to the first L basis elements, the irrotational part of the vector field expands as

$$\vec{v} = \vec{\nabla}\Psi = \sum_{k=1}^{L} a_k\,\vec{\nabla}\psi_k = \sum_{k=1}^{L} a_k\,\vec{k} \quad, \tag{1.91}$$

where we introduced $\vec{k} = \vec{\nabla}\psi_k$ for simplicity. For the rotational vector field $\vec{w} = \vec{\nabla}\wedge F\hat{\mathbf{e}}_\varphi$, we expand the scalar function $F(\xi,\eta)$ onto the L basis functions $f_\lambda(\xi,\eta)$. The latter must satisfy $\Delta f_\lambda\hat{\mathbf{e}}_\varphi \neq 0$ in order to contribute to the rotational field. The rotational part of the axisymmetric vector field is thus expressed as

$$\vec{w} = \vec{\nabla}\wedge F\hat{\mathbf{e}}_\varphi \;=\; \sum_{\lambda=1}^{L} b_\lambda\vec{\nabla}\wedge(f_\lambda\hat{\mathbf{e}}_\varphi) = \sum_{\lambda=1}^{L} b_\lambda\vec{\lambda} \tag{1.92}$$

where we introduced $\vec{\lambda} = \vec{\nabla}\wedge(f_\lambda\hat{\mathbf{e}}_\varphi)$ to simplify the notation. We can further require the rotational basis elements $\vec{\lambda}$ to be orthogonal to the irrotational vector

basis $\vec{k}$. The orthogonality condition is satisfied if the basis function f_λ are zero on the droplet surface[27]. We define the symmetric tensors D and W, standing respectively for the irrotational and rotational contribution of the velocity vector field to the strain-rate tensor :

$$D = \frac{1}{2}\left(\vec{\nabla}\vec{v} + (\vec{\nabla}\vec{v})^t\right) \tag{1.93}$$

$$W = \frac{1}{2}\left(\vec{\nabla}\vec{w} + (\vec{\nabla}\vec{w})^t\right) \tag{1.94}$$

We remind that D is a divergence-free tensors, unlike W. The boundary conditions of the normal and tangential stress now write:

$$T_{nn} - M_{nn} = -p + 2\mu(D_{nn} + W_{nn}) = -P_s + P_c \tag{1.95}$$

$$T_{\tau n} - M_{\tau n} = 2\mu(D_{\tau n} + W_{\tau n}) = \sigma E_\tau \tag{1.96}$$

With the additional rotational field we have this times enough degrees of freedom to satisfy explicitly the zero shear stress boundary condition (1.96)! The *ad hoc* viscous pressure p_μ found in VCVPF is replaced here by the strain rate tensor W based on the rotational field $\vec{w}$. The power equation in RCVPF is obtained by projecting the Navier-Stokes equation 1.12 onto the (irrotational) vector $\vec{v}$.

$$\frac{dE_{\text{kin}}}{dt} = \rho\left(\vec{v}\cdot\frac{d\vec{u}}{dt}\right)_\Omega = \rho\left(\vec{v}\cdot(\vec{\nabla}\cdot T)\right)_\Omega \tag{1.97}$$

$$= -2\mu\left(V:(D+W)\right)_\Omega + \int_{\partial\Omega} \vec{v}\cdot(T-M)\cdot\vec{n}\,ds^2 \tag{1.98}$$

$$\tag{1.99}$$

where $()_\Omega$ means integration over the drop volume Ω. Injecting the boundary conditions (1.95) and (1.96) yields the power of traction and the power of dissipation

---

[27]The vectors $\vec{k}$ are orthogonal to $\vec{\lambda}$ in the droplet volume Ω if the functions $f_\lambda = 0$ on the droplet surface $\partial\Omega$,

$$\int_\Omega \vec{\lambda}\cdot\vec{k}\,d\Omega = \int_\Omega \vec{\nabla}\cdot(f_\lambda\hat{\mathbf{e}}_\varphi \wedge \vec{k})\,d\Omega + \int_\Omega f_\lambda\hat{\mathbf{e}}_\varphi\cdot\underbrace{(\vec{\nabla}\wedge\vec{k})}_{0}\,d\Omega$$

$$= \int_{\partial\Omega}(f_\lambda\hat{\mathbf{e}}_\varphi \wedge \vec{k})\cdot\vec{n}\,ds$$

$$= -\int_{\partial\Omega}\underbrace{f_\lambda}_{0} k_\tau\,ds = 0$$

for arbitrary $k_\tau = \vec{k}\cdot\vec{\tau}$. (Note that, as f_λ and k_τ are odd functions at the surface, the product $f_\lambda k_\tau$ is an even function on the surface.)

proportional to the viscosity μ,

$$
\frac{dE_{\text{kin}}}{dt} = \underbrace{\int_{\partial\Omega} \left(v_n\left(-P_s + P_c\right) + v_\tau(\sigma E_\tau)\right) ds^2}_{\mathcal{T}^{\text{RCVPF}} = \mathcal{T}^{\text{VCVPF}}}
$$

$$
\underbrace{-2\mu \int_{\partial\Omega} \left(v_n D_{nn} + v_\tau D_{\tau n} + w_n D_{nn} + w_\tau D_{\tau n}\right) ds^2}_{\mathcal{D}^{\text{RCVPF}}} \qquad (1.100)
$$

A more detailed derivation of the power equation (A.43) is given in the appendix A.5. We recognize the traction integral of the VCVPF model. However, compared to VCVPF, the RCVPF has additional terms in the power of dissipation integral, that involves the rotational vector field $\vec{w}$ evaluated at the boundary. We may further chose the basis function $f_\lambda(\vec{s})$ to be zero on the surface. As a result, the basis vectors $\vec{k}$ and $\vec{\lambda}$ are orthogonal in the drop volume and $\vec{n} \cdot \vec{\lambda}(\vec{s}) = 0$ at the surface, so that $w_n(\vec{s}) = \sum_\lambda \vec{n} \cdot \vec{\lambda}(\vec{s}) = 0$. In this case, the power of dissipation $\mathcal{D}^{\text{RCVPF}}$ reads,

$$
\mathcal{D}^{\text{RCVPF}} = \mathcal{D}^{\text{VCVPF}} - 2\mu \int_{\partial\Omega} \left(w_\tau D_{\tau n}\right) ds \quad . \qquad (1.101)
$$

Within the orthogonality assumption, RCVPF adds, with respect to VCVPF, a single term that involves only the tangential component of the rotational vector field w_τ. We will see in the next section that RCVPF allows to recover the correct decay rate of the surface oscillations of a viscous drop, even in the higher viscosity regime, where VCVPF overestimates the rate. RCVPF keeps the advantageous numerical CPU cost of the VCVPF model, where all the quantities are calculated on the interface.

The vector field $\vec{w}$ is activated by the boundary condition (1.96), which can now be satisfied using the additional degrees of freedom given by the set of expansion coefficients b_λ of $\vec{w}$. Defining the tensor $\Lambda = \frac{1}{2}\left(\vec{\nabla}\vec{\lambda} + (\vec{\nabla}\vec{\lambda})^t\right)$ so that

$$
W = \sum_\lambda^L b_\lambda \Lambda \qquad (1.102)
$$

and projecting (1.96) onto the irrotational basis $\{\vec{k}\}$, yields a set of L equations that must satisfy the L coefficients b_λ of the rotational basis $\{\vec{\lambda}\}$,

$$
\int k_\tau D_{\tau n}\, ds^2 + \sum_{\lambda=1}^L b_\lambda \underbrace{\int k_\tau \Lambda_{\tau n} ds^2}_{R_{\lambda k}} = \int k_\tau \sigma E_\tau\, ds^2 \quad , 1 \leq k \leq L \qquad (1.103)
$$

74

Solving the latter system of equations implies that the matrix $R_{\lambda k}$ must be non-singular so that $R_{\lambda k}$ can be inverted. As the rotational field $\vec{w}$ that enters the RCVPF model is defined only by the shear stress boundary condition (1.103), we have to restrict $\vec{w}$ to a subspace which yields a non-singular matrix in (1.103). The RCVPF model depends thus on the choice of the subspace of the rotational field that spans $\vec{w}$.

We also want to emphasize that if the rotational part of the velocity field vanishes, $\vec{\nabla} \wedge \vec{w} \to 0$, the RCVPF model tends toward the VPF model and not toward the VCVPF. This becomes clear, when looking at equation A.45 in the appendix. Indeed, if $W \to 0$, the shear stress condition of RCVPF cannot be satisfied any longer, similar to VPF, and is thus ignored. On the other hand, if the diffusion length of vorticity layer is negligible compared to the droplet radius, so that the vorticity layer is limited to the surface, RCVPF tends to the VCVPF model. This behaviour will be illustrated in section 1.7.

To summarize, the RCVPF model allows to add a dissipation term originating from the rotational part of the field, that is activated by enforcing the shear boundary condition at the free boundary. The numerical approach of the RCVPF model in detailed in the appendix A.6.

Choice of the rotational basis set

We suppose that the viscous force originating from the tangential shear stress acts inside a thin vorticity layer at the interface. In the case of small quadrupole surface oscillations, we can define the vorticity diffusion lengths l_μ [51]

$$l_\mu \simeq \sqrt{\frac{\mu}{\rho\omega(\lambda)}} = R\sqrt{\text{Oh}}(\lambda(\lambda+2)(\lambda-1))^{-1/4} \qquad (1.104)$$

where $\omega(\lambda) = \tau_0^{-1}\sqrt{\lambda(\lambda+2)(\lambda-1)}$ is the dispersion relation ship in the PF model[28]. The diffusion lengths corresponds to the thickness of the vorticity layer. For an axisymmetric problem expressed in an orthogonal coordinate system, the rotational part of the velocity field is expressed by (1.92). In prolate coordinate system we suggest the following expansion [29]

$$F(\xi,\eta) = \sqrt{(1-\eta^2)}\sum_\lambda b_\lambda \sqrt{(\xi^2-1)}P'_{\lambda+N}(\xi)\,P'_\lambda(\eta) \qquad (1.107)$$

---

[28]Alternatively, we could use the dispersion relationship of the VPF model:

$$\omega(\lambda) \equiv \text{Im}\left(\Omega^{\text{VPF}}\right) = \tau_0^{-1}\sqrt{\lambda(\lambda+2)(\lambda-1) - \lambda^2(\lambda-2)^2\text{Oh}^2} \qquad (1.105)$$

[29]The rotational field can be made orthogonal to the potential velocity field $\vec{v} = \vec{\nabla}\Phi$ by modifying the the basis functions such that they are zero at the axisymmetric surface defined by

with $N \geq 1$ being a positive integer. The choice of F is motivated by the fact that with larger N, the radial part of F is non-zero mainly close to the interfaces, meaning that the vorticity layer near the interface is narrower, or that the vorticity layer has a smaller diffusion length at the interface. We are looking thus for a relationship for N of the form

$$N(\text{Oh}, \lambda) \simeq \frac{R}{l_\mu} = \frac{(\lambda(\lambda + 2)(\lambda - 1))^{1/4}}{\sqrt{\text{Oh}}}. \tag{1.108}$$

We simulated small amplitude surface oscillation as a function of time with the RCVPF model and extracted the damping of the quadrupole mode, $\lambda = 2$. We tuned the free parameter N so as to match the decay time obtained from the exact dispersion relationship of the quadrupole of a viscous drop [51]. Figure 1.39 shows the matching N (black points) as a function of $\sqrt{\text{Oh}}$. We found that the points are well fitted by the a law $N(\text{Oh}) + 1 = 8^{1/4}\text{Oh}^{-1/2}$, in agreement with (1.108)
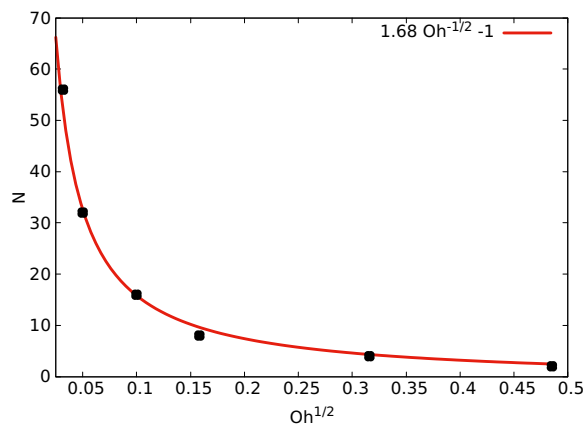
Figure 1.39: Integer N versus the dimensionless viscosity Oh

First simulations with RCVPF: Damped surface oscillations

We illustrate the RCVPF model in the case of small surface oscillations (mainly quadrupole moment) of a droplet. We compare the damped oscillations given by the RCVPF approach to the VCVPF one and to the exact damping given by

---

the function $\xi_s(\eta) > 1$,

$$F(\xi, \eta) = \sqrt{(1 - \eta^2)} \sum_\lambda b_\lambda \left(\sqrt{(\xi^2 - 1)} P'_{\lambda+N}(\xi) - \frac{(\xi_s^2(\eta) - 1)}{\sqrt{(\xi^2 - 1)}} P'_{\lambda+N}(\xi_s(\eta)) \right) P'_\lambda(\eta) \tag{1.106}$$

A. Prosperetti [15] and discussed in E. Becker [27] and O.A. Basaran [28] and A.N. Zharov *et al.* [41]. We show in Fig.1.40 the damping of quadrupole surface oscillation amplitude computed with the VCVPF and RCVPF model and compare it to the exact damping [15].
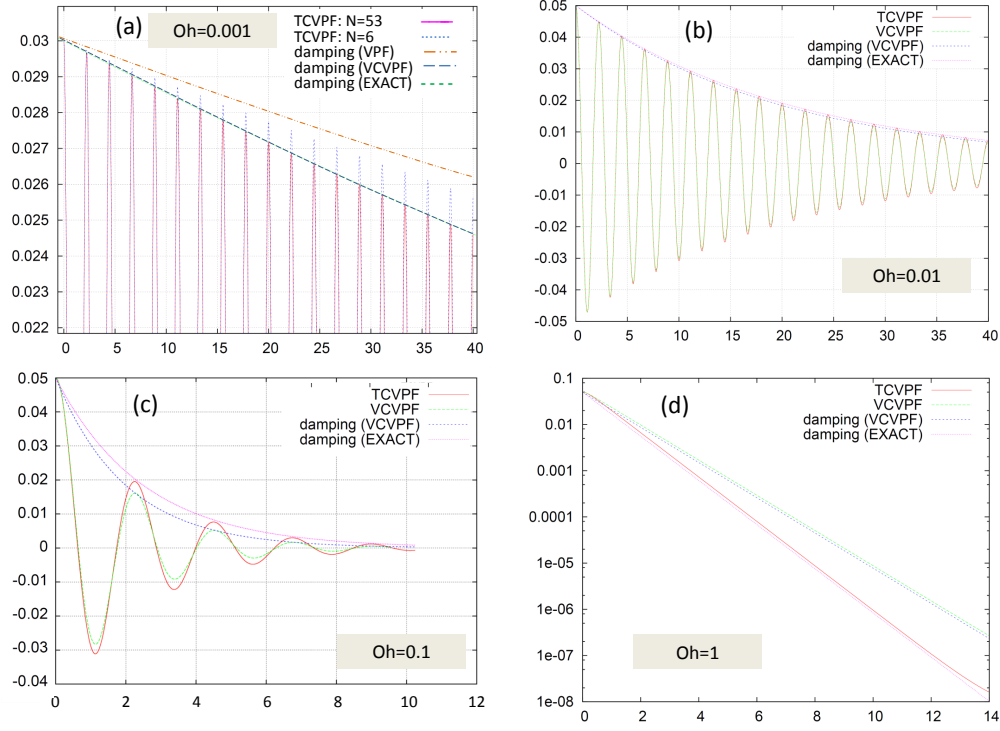
Figure 1.40: *For all panels, the x-axis is the dimension less time t/τ_0 and the y-axis is the dimensionless quadipole amplitude a_2/R. Panel (a): Quadupole surface oscillations with Oh=0.001. Pink full line used the RCVPF model with $N = 53$ while the blue doted line uses RCVPF with $N = 6$. Dashed-dotted orange line gives the damping is the VPF and the long-dashed blue line the damping in VCVPF approach. Green dashed line corresponds to the exact damping. Panel (b): Damping of quadupole oscillations with Oh=0.01. The RCVPF model with $N = 18$ (dashed blue) is in agreement with the 'exact' damping (dotted pink). For subcritical Oh values, the VCVPF overestimates the damping. Panel (c): Damping of quadupole moment with Oh=0.1. The RCVPF model with $N = 4$ (full red line). Again, the VCVPF overestimates the damping. Panel (d): Damping of quadupole moment with the supercritical value Oh=1. The RCVPF model with $N = 8$ (full red line) is in agreement with the 'exact' damping (dotted pink). VCVPF (green dashed line) underestimates now the damping.*

1. In panel (a) of Fig.1.40, we consider the low viscous limit with Oh=0.001.

First we note that the damping of the (VCVPF) and (EXACT) methods are indistinguishable on the presented time range, confirming the validity of VCVPF in this regime. Second, we see that the RCVPF model with $N = 53 \simeq 1.68/\sqrt{\text{Oh}}$ (pink full line) is in agreement with the *exact* damping. Comparing the latter to RCPVF with $N = 6$ shows the sensitivity of the damping with respect to N and thus with respect to the thickness of the boundary layer. Indeed, for $N = 6$, the damping is underestimated, as shown by the blue dotted oscillations, and closer to the damping of VPF model.

2. In panel (b) we considered Oh=0.01, which is still on the low viscous side and corresponds roughly to our water droplets at room temperature. The VCVPF model slightly overestimates the damping, as can be expected for sub-critical Oh<$\text{Oh}_c = 0.56$ values. On the other hand, the RCVPF model with $N = 18 \simeq 1.68/\sqrt{\text{Oh}}$ is in total agreement with the 'exact' damping.

3. In panel (c), we used Oh=0.1, which is still a sub-critical value. Damping of the quadupole moment in the RCVPF model with $N = 4 \sim 1.68/\sqrt{\text{Oh}}$ is in full agreement with the 'exact' damping. Again, the VCVPF overestimates the damping and the error is now significant.

4. Panel (d) shows the damping of the quadrupole moment with Oh=1. The RCVPF model with $N = 8$ is in agreement with the 'exact' damping implying that the "$N \sim 1.68/\sqrt{\text{Oh}}$" law may not apply for supercritical values of Oh. For **supercritical** values of Oh, the VCVPF now **underestimates** the damping.

We conclude this section by highlighting the excellent agreement of RCVPF with the exact damping in the case of small amplitude surface oscillations. Guided by the physical considerations, we proposed a simple function (1.106) for the rotational part of the velocity field which is parametrized by the integer N, accounting for the diffusion length of the vorticity layer of a viscous oscillating drop. At this time, the RCVPF model has not been used to calculated the whole deformation pathway of a critically charged drop but we are confident that RCVPF allows to go a step further than the VCVPF and simulate with even higher accuracy the flow o f viscous drops with Oh close to, or above the critical Oh_c. RCVPF has a comparable CPU cost advantage than VCVPF, but satisfies in addition the zero shear-stress boundary condition *adiabatically* by adding the necessary degrees of freedom in the form of a rotational velocity field. The latter adds a correction to the VCVPF dissipation term resulting in a damping rate that is indistinguishable from the exact one.

Appendices

Appendix A

A.1 Numerical method of the Potential Flow (PF) model

.

A Galikin approach has been used by Patzek *et al.* for the numerical resolution of Bernoulli's equation in the case of *Nonlinear oscillations of inviscid free drops* [26]. We propose here a different numerical approach, making use of the fact the velocity potential and Coulomb potential can both be expanded on harmonic functions in a prolate spheroidal coordinate system.

As the velocity potential satisfies the Laplace equation, Ψ can be written as a linear combination of harmonic functions, having the correct behaviour close to the origin. We choose to solve the Laplace equation in the prolate spheroidal coordinate system[1] (ξ, η, ϕ), which is well adapted to our boundary problem, while the harmonic functions f_{nm} are still separable

$$f_{nm}(\xi, \eta, \phi) = P_n^m(\xi) P_n^m(\eta) e^{im\phi} \quad \text{in} \quad \Omega \tag{A.1}$$

where P_n^m is a Legendre polynomial[2] of order n and degree m. As $\xi > 1$ we use here the The angular coordinate $-1 < \eta_i < 1$, is discretised over 400 points, corresponding to the zeros of Legendre polynomial of order 400, $P_{400}(\eta_i) = 0$. Because of axial symmetry, only $m = 0$ need to be considered. The expansion coefficients $\{a_n\}$ are chosen such as to satisfy the boundary condition

$$\Psi(\eta_i) = \sum_n a_n P_n(\xi(\eta_i)) P_n(\eta_i) \quad \forall i <= 600. \tag{A.2}$$

$$= \sum_n a_n f_{n0}(\vec{s}_i) \tag{A.3}$$

---

[1]https://en.wikipedia.org/wiki/Prolate_spheroidal_coordinates
[2]https://en.wikipedia.org/wiki/Legendre_polynomials
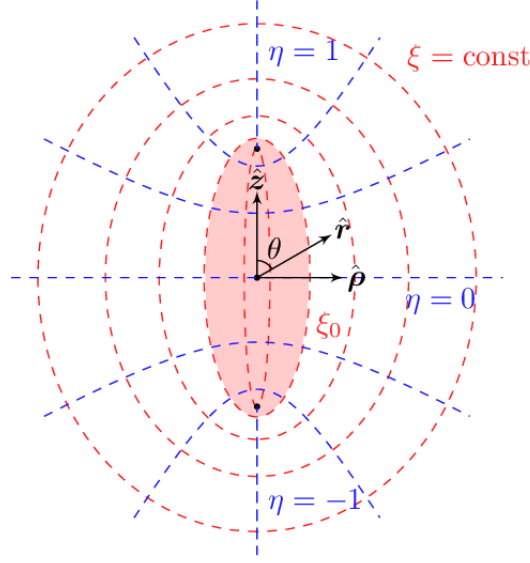
Figure A.1: Prolate coordinate system (ξ, η, ϕ). Domain of definition is ; $\xi \geq 1$, $-1 \leq \eta \leq 1$, $0 \leq \phi \leq 2\pi$. Shapes with constant ξ are prolate spheroids of eccentricity $e = (\xi^2 - 1)^{-1/2}$. The 2 black points represent the focii and their distance $2a$ defines the length scale of coordinate system.

The vector $\vec{s}_i = (\xi(\eta_i), \eta_i)$ describes the discretized droplet surface in the prolate coordinate system. As the boundary condition (1.68) evolves in time, the set of linear equations (A.2) must be solved at each time step. We use a singular value decomposition (SVD) of the matrix $f_n(\eta_i)$ to calculate the coefficients $\{a_n\}$. The velocity at the surface is finally obtained by taking the gradient of the velocity potential function Ψ (1.43);

$$u_\xi(\eta) = \frac{1}{h_\xi} \sum_n a_n \left. \frac{\partial P_n(\xi)}{\partial \xi} \right|_{\xi(\eta)} P_n(\eta) \qquad (A.4)$$

$$u_\eta(\eta) = \frac{1}{h_\eta} \sum_n a_n P_n(\xi(\eta)) \frac{\partial P_n(\eta)}{\partial \eta} \qquad (A.5)$$

where h_ξ, h_η and h_ϕ are scale functions of the prolate coordinate system [4]. A similar technique is used to calculate the Coulomb potential V outside the droplet. For the expansion of V, we chose harmonic functions having the correct behaviour in the the outer domain of the droplet,

$$g_{nm}(\xi, \eta, \phi) = Q_n^m(\xi) P_n^m(\eta) e^{im\phi} \quad \text{in} \quad \mathbb{R}^3 \backslash \Omega \qquad (A.6)$$

where Q_n^m is a Legendre polynomial of second type. For a perfect conductor, even in the presence of an external field V_{ext}, the potential at the surface is an equipo-

tential V_0. Assuming an axisymmetric external potential, $m = 0$, the expansion coefficients $\{b_n\}$ are obtained by satisfying the boundary condition

$$V_0 - V_{\text{ext}}(\eta_i) = \sum_n b_n Q_n(\xi(\eta_i)) P_n(\eta_i) \quad \forall i <= 600 \tag{A.7}$$

$$= \sum_n b_n g_{n0}(\vec{s}_i) \tag{A.8}$$

Knowing the initial charge of the droplet Q_0, the value of V_0 is readily found by the equation

$$Q_0 = \varepsilon_0 \int_{\partial\Omega} \vec{E}^g \cdot \vec{n} \, ds \tag{A.9}$$

where the electric field outside the droplet is computed using

$$\vec{E}^g = -\sum_n b_n \left(\frac{1}{h_\xi} \frac{\partial g_{n0}(\xi, \eta)}{\partial \xi} \vec{e}_\xi - \frac{1}{h_\eta} \frac{\partial g_{n0}(\xi, \eta)}{\partial \eta} \vec{e}_\eta \right) \tag{A.10}$$

In the case where V_{ext} is zero, the surface charge distribution at the equilibrium $\sigma = \varepsilon_0 \, \vec{n} \cdot \vec{E}^g$ depends thus only on the droplet shape $\vec{s} = (\xi(\eta), \eta)$. A schematic matrix representation of how to determine V_0 as a function of Q_0 is given in the footnote[3] It allows to compute the capacity $C = Q_0/V_0$ of the droplet. We used a maximum of $n \leq 200$ harmonic functions. Careful testing of the results convinced us that we were using a sufficient number of terms.

---

[3]V_0 is the unknown and is computed knowing Q_0. We define $g_{n0}(\vec{s}_i) = G_{ni}$ and $\varepsilon_0 \left(\frac{1}{h_\xi} \frac{\partial g_{n0}(\vec{s}_j)}{\partial \xi} \vec{e}_\xi - \frac{1}{h_\eta} \frac{\partial g_{n0}(\vec{s}_j)}{\partial \eta} \vec{e}_\eta \right) \vec{n} ds = M_{jn}$. The sum over j corresponds to the surface integration of (A.9). Relations (A.8) and (A.9) become respectively

$$\sum_n G_{in} b_n = V_i^0 + V_i^{\text{ext}} \tag{A.11}$$

$$\sum_{j,n} M_{jn} b_n = Q_0 \tag{A.12}$$

The b_n is eliminated in equation (A.12) by inverting equation (A.11).

$$\underbrace{\sum_{j,n,i} M_{jn} G_{ni}^{-1} V_i^0}_{C} = -\underbrace{\sum_{j,n,i} M_{jn} G_{ni}^{-1} V_i^{\text{ext}}}_{0} = Q_0 \tag{A.13}$$

The left hand term in equation (A.13) computes the capacity C and gives the potential $V_0 = Q_0/C$.

Another quantity that must be computed, is the mean curvature H, which depends only on the surface vector $\vec{s}$. For an axisymmetric surface $\vec{s}$ depending in curvilinear coordinates on (η, ϕ) (valid for prolate and spherical coordinate systems), the mean curvature is defined as

$$2H = \frac{eG + gE}{EG} \tag{A.14}$$

with

$$E = \left|\frac{\partial \vec{s}}{\partial \eta}\right|^2 = \left|h_\xi \frac{\partial \xi(\eta)}{\partial \eta}\vec{e}_\xi + h_\eta \vec{e}_\eta\right|^2 \tag{A.15}$$

$$G = \left|\frac{\partial \vec{s}}{\partial \phi}\right|^2 = |h_\phi \vec{e}_\phi|^2 \tag{A.16}$$

being the non-zero coefficients of the first fundamental form and

$$e = \vec{n} \cdot \frac{\partial^2 \vec{s}}{\partial \eta^2} \tag{A.17}$$

$$g = \vec{n} \cdot \frac{\partial^2 \vec{s}}{\partial \phi^2} \tag{A.18}$$

the non-zero coefficients of the second fundamental form[4]. The mean curvature depends thus on the first and second derivatives of $\xi(\eta)$ with respect to η and are computed using a Gauss-Legendre interpolation scheme [18], which is an extremely precise algorithm. (However, for pointed tips, H becomes near singular at the extremities, which is usually a source of numerical instabilities.)

---

[4]Using the relations for the unit vectors,

$$\frac{\partial \vec{e}_j}{\partial q_j} = -\vec{e}_k \frac{1}{h_k}\frac{\partial h_j}{\partial q_k} - \vec{e}_i \frac{1}{h_i}\frac{\partial h_j}{\partial q_i} \tag{A.19}$$

$$\frac{\partial \vec{e}_k}{\partial q_j} = \vec{e}_j \frac{1}{h_k}\frac{\partial h_j}{\partial q_k} \quad k \neq j \tag{A.20}$$

the coefficients of second fundamental form become,

$$e = \vec{n} \cdot \left(\frac{\partial}{\partial \eta}\left(g_\xi \frac{\partial \xi}{\partial \eta}\vec{e}_\xi + h_\eta \vec{e}_\eta\right)\right) \tag{A.21}$$

$$= \vec{n} \cdot \left(\left(\frac{\partial h_\xi}{\partial \eta}\frac{\partial \xi}{\partial \eta} + h_\xi \frac{\partial^2 \xi}{\partial \eta^2} - \frac{h_\eta}{h_\xi}\frac{\partial h_\eta}{\partial \xi}\right)\vec{e}_\xi + \left(\frac{\partial \xi}{\partial \eta}\frac{\partial h_\eta}{\partial \xi} + \frac{\partial h_\eta}{\partial \eta}\right)\vec{e}_\eta\right)$$

$$g = h_\phi \vec{n} \cdot \frac{\partial \vec{e}_\phi}{\partial \phi} \tag{A.22}$$

$$= h_\phi \vec{n} \cdot \left(-\frac{\vec{e}_\xi}{h_\xi}\frac{\partial h_\phi}{\partial \xi} - \frac{\vec{e}_\eta}{h_\eta}\frac{\partial h_\phi}{\partial \eta}\right)$$

A.2 Time propagator (valid also for VCVPF and RCVPF)

The axisymmetric shape of a perfectly conducting droplet is propagated in time by the following scheme. Knowing the shape $\vec{s}(t)$ and velocity potential $\Psi(t)$ at time t, we propagate the surface to $\vec{s'}(t + dt)$. This is the predictor step. Then, we compute the pressure and velocity at this new intermediate surface $\vec{s'}(t + dt)$. Finally, taking the mean value of the pressure computed at $\vec{s}(t)$ and $\vec{s'}(t + dt)$, the corrector step calculates the new surface $\vec{s}(t + dt)$ and velocity potential $\Psi(t + dt)$. The 9 computing steps are summarized below:

1. $\vec{u}(t) = \vec{\nabla}_{\vec{s}(t)} \Psi_n(t)$

2. $H(t) \equiv H(\vec{s}(t)), \ \sigma(t) \equiv \sigma(\vec{s}(t))$

3. $\dot{\psi}(t) = 2H(t) + 2\sigma^2(t) - \vec{u}^2(t)/2$ (c.f. 1.68)

4. $\vec{s'}(t + dt) = \vec{s}(t) + dt\vec{u}(t)$ (c.f. 1.28)

5. $\Psi'(t + dt) = \Psi(t) + dt\dot{\psi}(t)$

6. $\vec{u'}(t + dt) = \vec{\nabla}_{\vec{s}(t+dt)} \Psi_n(t + dt)$

7. $\dot{\psi}'(t + dt) = 2H'(t + dt) + 2\sigma'^2(t + dt) - \vec{u'}^2(t + dt)/2$

8. $\Psi(t + dt) = dt(\dot{\psi}(t) + \dot{\psi}'(t + dt))/2$

9. $\vec{s}(t + dt) = \vec{s}(t) + dt(\vec{u}(t) + \vec{u'}(t + dt))/2$

The dimensionless velocity increases exponentially in time during the first step of the deformation. We used thus also a time adaptive scheme, where the time step is reduced by a factor two as soon as $|\vec{u}|dt > \epsilon$, where $\epsilon \simeq 10^{-5}$ is a small arbitrary number. This second order time adaptive predictor-corrector-like scheme allows to propagate the shape of the droplet, while conserving the volume and energy of the droplet (inviscid liquid). Typically, the volume and energy are conserved within a relative error of less then 10^{-9} and 10^{-5} respectively during the whole deformation pathway, except for the moments where pointed tips (singularities) are formed and where the numerical method accumulated larger errors or simply fails. The accumulation of numerical errors is significant when pointed ends develop at the tip as the harmonic basis, used for solving the Laplace equation, is no longer adapted, meaning that a large number of basis functions are necessary to capture the near singular velocity potential at the tips mainly because the harmonic basis functions are not necessarily orthogonal on the droplet surface. The jet emission is modelled

by reducing instantaneously the drop charge. Usually,the charge is reduced by a given fraction just before the singularities develop, making the droplet sub-critically charged. At that point, the pressure due to the surface tension dominates again and the tip formation is stopped and reversed (tips become flattened) and the calculation can continue.

A.3 Electric field in the case of a non-equilibrium charge distribution

In the case the potential V at the surface in not an equipotential, the technique based on A.8 is not applicable and the evaluation of the electric field needs to be adapted. The potential V^- inside the drop and V^+ outside the drop are assumed to satisfy the Laplace equation and can therefore be expanded on harmonic functions f_n and g_n having the appropriate behaviour at the origin and at infinity.

$$V^-(\xi, \eta) \;=\; \sum_n^N a_n f_n(\xi, \eta) \quad \text{in } \Omega \tag{A.23}$$

$$V^+(\xi, \eta) \;=\; \sum_n^N b_n g_n(\xi, \eta) \quad \text{in } \mathbb{R}^3 \backslash \Omega \tag{A.24}$$

The functions f_n and g_n were introduced in (A.1) (A.6) respectively. The expansion coefficients $\{a_n\}$ and $\{b_n\}$ are obtained by solving the boundary conditions equations at the $i \in [1, N_i]$ grid points $\vec{s}_i$ of the droplet interface.

$$V^-(\vec{s}_i) - V^+(\vec{s}_i) \;=\; 0 \quad \text{on } \partial\Omega \tag{A.25}$$

$$\vec{n}_i \cdot (\varepsilon_r \vec{\nabla} V^-(\vec{s}_i) - \vec{\nabla} V^+(\vec{s}_i) \;=\; \frac{\sigma}{\varepsilon_0} \quad \text{on } \partial\Omega \tag{A.26}$$

Injecting (A.23, A.24) into the above boundary equations yields a $N_i \times N$ system of equations for the coefficients. Once the system is solved using a matrix inversion techniques like SVD[5] and the coefficients determined, the electric field inside and outside the drop are readily computed. Note that for $n \leq N = 150$ and $i \leq N_i = 200$, this technique is CPU efficient compared to the cost of the other functions in the numerical code. The method however loses its precision as soon as the matrices $f_{ni} \equiv f_n(\vec{s}_i)$ or $g_{ni} \equiv g_n(\vec{s}_i)$ become singular and a more robust technique like BEM[6], introduced in section 1.5.4, should be used.

---

[5] Sigular Value Decomposition, for over-determined system of equations with more equations than unknows $N_i \geq N$, gives the solution is the sens of a least square method.

[6] Boundary element method

A.4 Numerical method for the evaluation of p_μ in VCVPF

The VCVPF model is only useful if one can compute the viscous pressure p_μ, which enters the normal stress term. We propose here a numerical method to compute the viscous pressure in VCVPF. Making use of the fact that the Laplace operator is separable in prolate spheroid coordinate system ($\xi \geq 1, -1 \leq \eta \leq 1, 0 \leq \varphi \leq 2\pi$), we get a simple expression for the harmonic functions f_m that satisfy the Laplace equation $\vec{\nabla}^2 f_m = 0$. As we want $f_m(\xi, \eta) = f_m(\xi, -\eta)$ to be axisymmetric and even and defined at the origin $f(1, 0) < \infty$, we have

$$f_m(\xi, \eta) = P_{2m}(\xi) P_{2m}(\eta) \tag{A.27}$$

where $P_m()$ are Legendre polynomials of order m. Let $\{f_m\}$ be a basis of harmonic function. We may now expand the viscous pressure on the harmonic basis f_m,

$$p_\mu(\xi, \eta) = \sum_{m=1}^{M} b_m f_m(\xi, \eta) \tag{A.28}$$

The expansion coefficients $\{b_m\}$ are deduced using the boundary condition (1.64),

$$\sum_{m=1}^{M} b_m \underbrace{f_m(\vec{s}_i) u_n(\vec{s}_i) ds_i}_{F_{mi}} = \underbrace{u_\tau(\vec{s}_i)(2\mu D_{\tau n}(\vec{s}_i) ds_i}_{d_i} \\ - \underbrace{u_\tau(\vec{s}_i)\sigma_i(\vec{s}_i) E_\tau(\vec{s}_i)) ds_i}_{e_i} \tag{A.29}$$

where $\vec{s}_{i \leq N}$ is an ensemble of N points at the surface. Equation (A.29) is a system of N equations and M unknowns of the form

$$\sum_{m=1}^{M} b_m F_{mi} = d_i - e_i \quad , \quad 1 \leq i \leq N \tag{A.30}$$

If $N \geq M$ the system is overdetermined and can be solved using a singular value decomposition (SVD), which finds the coefficient $\{b_m\}$ as least squares solutions.

A.5   Derivation of the RCVPF model

We define the symmetric tensors K and Λ, standing respectively for the irrotational and rotational contribution of the basis vectors to the strain-rate tensor :

$$K \quad = \quad \frac{1}{2}\left(\vec{\nabla}\vec{\kappa} + (\vec{\nabla}\vec{\kappa})^t\right) \tag{A.31}$$

$$\Lambda \quad = \quad \frac{1}{2}\left(\vec{\nabla}\vec{\lambda} + (\vec{\nabla}\vec{\lambda})^t\right) \tag{A.32}$$

$$D \quad = \quad \sum_{k=1}^{L} a_k K \tag{A.33}$$

$$W \quad = \quad \sum_{\lambda=1}^{L} b_\lambda \Lambda \tag{A.34}$$

$$\tag{A.35}$$

We remind that K and D are divergence-free tensors, unlike Λ and W.

The time evolution of the irrotational velocity field $\vec{v}$ in the RCVPF model is obtained by projecting the Navier-Stokes equation 1.12 on the (irrotational) basis vector $\vec{k}$.

$$\rho\left(\vec{k}\cdot\frac{d\vec{u}}{dt}\right)_\Omega \quad = \quad \left(\vec{k}\cdot(\vec{\nabla}\cdot T)\right)_\Omega \tag{A.36}$$

$$= \quad -(K:T)_\Omega + \int_{\partial\Omega} \kappa_n T_{nn} + \kappa_\tau T_{\tau n} ds$$

$$= \quad -2\mu\left(K:(D+W)\right)_\Omega + \int_{\partial\Omega} \kappa_n(T_{nn} - M_{nn})\,ds$$

$$+ \int_{\partial\Omega} \kappa_\tau(T_{\tau n} - M_{\tau n})\,ds \quad ,$$

where $()_\Omega$ means integration over the drop volume Ω. Injecting the boundary conditions (1.95) and (1.96) and noting that [7]

$$(K:D)_\Omega \quad = \quad \int_{\partial\Omega}(\kappa_n D_{nn} + \kappa_\tau D_{\tau n})\,ds \tag{A.37}$$

$$(K:W)_\Omega \quad = \quad \int_{\partial\Omega}(w_n K_{nn} + w_\tau K_{\tau n})\,ds \tag{A.38}$$

$$\left(\vec{\kappa}\cdot\frac{d\vec{u}}{dt}\right)_\Omega \quad = \quad \int_{\partial\Omega}\psi_k\frac{d\vec{u}}{dt}\cdot\vec{n}\,ds \tag{A.39}$$

---

[7]Equation A.38 results form the commutativity of the double dot product $K:W = W:K$. The latter property yields also $(\vec{v}(\vec{\nabla}\cdot W))_\Omega = (\vec{v}\cdot\nabla^2\vec{w})_\Omega = \int_{\partial\Omega}(\vec{v}\cdot W - \vec{w}\cdot D)\vec{n}ds$, where we recognize the Greens vector identity.

one has

$$\rho \int_{\partial\Omega} \psi_k \frac{d\vec{u}}{dt} \cdot \vec{n}\, ds = \int_{\partial\Omega} \left(\kappa_n \left(-P_s + P_c \right) + \kappa_\tau (\sigma E_\tau) \right) ds$$
$$-2\mu \int_{\partial\Omega} \left(\kappa_n D_{nn} + \kappa_\tau D_{\tau n} \right) ds$$
$$-2\mu \int_{\partial\Omega} \left(w_n K_{nn} + w_\tau K_{\tau n} \right) ds \qquad (A.40)$$

We deduce from (A.40) the traction and dissipation power of the RCVPF model, by summing over k,

$$\frac{dE_{\text{kin}}}{dt} = \rho \sum_k^L a_k \int_{\partial\Omega} \psi_k \frac{d\vec{u}}{dt} \cdot \vec{n}\, ds \qquad (A.41)$$
$$= \rho \int_{\partial\Omega} \Psi \frac{d\vec{u}}{dt} \cdot \vec{n}\, ds \qquad (A.42)$$
$$= \int_{\partial\Omega} \left(v_n \left(-P_s + P_c \right) + v_\tau (\sigma E_\tau) \right) ds$$
$$-2\mu \int_{\partial\Omega} \left(v_n D_{nn} + v_\tau D_{\tau n} \right) ds$$
$$-2\mu \int_{\partial\Omega} \left(w_n D_{nn} + w_\tau D_{\tau n} \right) ds \qquad (A.43)$$

A.6   Numerical method of RCVPF

We propose the following scheme to solve numerically the RCVPF equations. We assumes that the basis function $f_l(\vec{s}) = 0$ on the boundary so that the vectors $\vec{\kappa}$ and $\vec{\lambda}$ are orthogonal in the drop volume. The surface integrals (A.6) and equations (A.40) and (A.43) involving λ_n and w_n thus vanish and the coefficients $b(t+\Delta t)$ are found by satisfying *adiabatically* by the shear stress boundary condition. Using the expansion of the velocity field (1.90), we can re-write equation(A.40) and (1.103) in a matrix form, ,

$$\begin{pmatrix} \int \phi_{k'}\, \kappa_n\, ds & \overbrace{\int \phi_{k'} \lambda_n ds}^{=0} \\ \int \kappa'_\tau K_{\tau n}\, ds & \int \kappa'_\tau \Lambda_{\tau n}\, ds \end{pmatrix} \begin{pmatrix} a_k(t+\Delta t) \\ b_\lambda(t+\Delta t) \end{pmatrix} = \begin{pmatrix} \int_{\partial\Omega} \phi_{k'}\, u_n ds + \Delta t\, f_{k'} \\ \int \kappa'_\tau \sigma E_\tau\, ds/2\mu \end{pmatrix} \qquad (A.44)$$

which is resolved using a matrix inversion technique like SVD. The computed $a_k(t+ \Delta t)$ and $b_l(t+\Delta t)$ give the velocity vector $\vec{u} = \vec{v}+\vec{w}$ at the surface at time $t+\Delta t$.

Using the predictor-corrector propagation scheme (A.2), the surface deformation is computed. Here we assumed that λ_n is zero at the surface (Orthogonal Helmholtz decomposition). The right hand terms are all taken at time t, with f_k containing the traction and the dissipation power as well as the non-linear advection term of the rotational and irrotational field,

$$f_{k'} = \int_{\partial\Omega} \kappa'_n \left(P_s + P_c - \frac{v^2}{2} \right) ds - 2\mu \int_{\partial\Omega} (\kappa'_n D_{nn} + \underbrace{w_n K'_{nn}}_{0}) ds$$

$$+ 2\mu \int_{\partial\Omega} (\kappa'_\tau W_{\tau n} - w_\tau K'_{\tau n}) ds + (\vec{\kappa'} \cdot (\vec{v} \wedge (\vec{\nabla} \wedge \vec{w})))_{\Omega} \qquad (\text{A.45})$$

We will in the following neglect the last (advection) term containing the rotation field $\vec{w}$, which is usually small compared to the irrotational vector field $\vec{v}$. The term f_k differs from the right hand term of (A.40). Indeed, the shear stress boundary condition was not used in f_k because it is expressed by the system of equations (A.44) and thus automatically fulfilled by the solution. So equations (A.40) and (A.44) are equivalent. Note that the coefficients $b_l(t)$ are not actually propagated in time. They satisfy adiabatically the boundary condition while itself propagates in time.

Bibliography

[1] C. B. Richardson, A.L. Pigg, L.R. Hightower, Proceedings of The Royal Society A 422 p 319 (1863)

[2] "On the Equilibrium of Liquid Conducting Masses Charged with Electricity", Lord Rayleigh, Philosophical Magazine, Vol. **14**, No. 87, 1882, pp. 184-186

[3] "Instability of Electrified Liquid Surfaces", John Zeleny, Phys. Rev. 10, 1 (1917)

[4] Morse PM, Feshbach H (1953). Methods of Theoretical Physics, Part I. New York: McGraw-Hill. p. 661

[5] "Deformation Energy of a Charged Drop. II. Symmetric Saddle Point Shapes" W.J. Swiatecki, Physical Review **104** p 993 (1956)

[6] "Charged droplet experiments", C.D. Jr. Hendricks, J. Colloid Sci. **17** 249 (1962)

[7] A. Doyle, D.R. Moffett, B. Vonnegut, J. Colloid Sci. **19** 136 (1964)

[8] "Disintegration of water drops in an electric field", Sir G. Taylor, Proc. R. Soc. London, Ser. A 280, 383 (1964).

[9] "Electrohydrodynamics: a review of the role of interfacial shear stresses", J. R. Melcher and G. I. Taylor, Annu. Rev. Fluid Mech. 1, p 111. (1969)

[10] "Stability limit of charged drops", J.W. Schweizer and D.N. Hanson J. Colloid Interface **35** 471 (1971)

[11] "Study of Evaporation and Instability of Charged Water Droplets", M. Roulleau and M. Desbois Journal of Atmospheric Sciences, vol. 29, Issue 3, pp.565-569 (1972)

[12] "Conforming and nonconforming finite element methods for solving the stationary stokes equations", M. Crouzeix M, P.A. Raviart, R.A.I.R.O Sér. Rouge (1973); 7:33-75

[13] Brazier-Smith PR, Jennings SG, Latham J (1973) "Increased rates of rainfall production in electrified clouds". Q J R Meteorol Soc 99(422):776-786

[14] "Inertia, friction, and angular momentum of an oscillating viscous charged liquid drop under surface tension", R.W. Hasse, Ann Phys. (N.Y.) **93** 68 (1975)

[15] "Normal-mode analysis for the oscillations of a Viscous liquid drop immersed in another liquid", A. Prosperetti, J. Méc, **19** p 149 (1980)

[16] "An experimental study of small-amplitude drop oscillations in immiscible liquid systems", E. Trinh, A. Zwern and T.G. Wang, J. Fluid Mech. vol 115, p 453 (1982)

[17] "Optical properties of interplanetary dust - Comparison with light scattering by larger meteoritic and terrestrial grains", K. Weiss-Wrana, Astron. Astrophys. **126** 240 (1983)

[18] Milton Abramowitz and Irene Ann Stegun, *Handbook of Mathematical Functions*, Dover Books on Mathematics, (Gauss Legendre) p 887 , eds. (1983)

[19] A.G. Bailey, *Atomisation Spray Technol.* **2**, 95 (1986)

[20] W.K. Rhim *et al.* Mater. Res. Soc. Symp. Proc. 329 87 (1987)

[21] E. J. Davis, T.L. Ward, D.G. Rodenhizer, R.W. Jenkins and D.D. McRae, Part. Sci. Technol. **6** 68 (1988)

[22] D.C. Taflin, T.L. Ward and E.J. Davis, *Langmuir*, **5** 376 (1989)

[23] J. B. Fenn, M. Mann, C. K. Meng, S.F. Wong and C. M. Whitehouse, "Electrospray ionization for mass spectrometry of large biomolecules", Science **246** 64 (1989)p 113

[24] M. Cloupeau and B. Prunet-Foch, J. Electrost. 22, 135 (1989).

[25] "Conductor curvature and surface charge density", IW McAllister, J. Phys. D **23** 359 (1990)

[26] "Nonlinear Oscillations of Inviscid Free Drops", T.W Patzek, R.E Benner Jr, O.A. Basaran, L.E Scriven, JOURNAL OF COMPUTATIONAL PHYSICS, 97, 489-5 15 (1991)

[27] "Experimental and theoretical investigation of large-amplitude oscillations of liquid droplets", E. Becker, W.J. Hiller and T.A. Kowalewski, J. Fluid. Mech vol 231 p 189 (1991)

[28] O.A. Basaran, "Non-linear oscillations of viscous liquid drops" ,J. Fluid. Mech. vol 241, p 169 (1992)

[29] "Charge and fission of droplets in electrostatic sprays ", A. Gomez and K. Tang, Phys. Fluids **6** 404 (1994)

[30] C. Pantano, A. M. Gañán-Calvo, and A. Barrero, J. Aerosol Sci. 25, 1065 (1994).

[31] Tabata M. Finite element analysis of axisymmetric flow problems. ICIAM/GAMM 95 - Numerical Analysis, Scientific Computing, Computer Science, Hamburg, (1995)

[32] A. Anderko and M.M. Lencka, "Computation of Electrical Conductivity of Multicomponent Aqueous Systems in Wide Concentration and Temperature Ranges" Ind. Eng. Chem. Res. 36, p 1932-1943 (1997)

[33] A. M. Gañán-Calvo, Phys. Rev. Lett. **79** p 217 (1997)

[34] J. Eggers, Reviews of modern physics **69** p 865 (1997)

[35] D.A. Saville "The Taylor-Melcher Leaky Dielectric Model", Annual Review of Fluid Mechanics, Vol. 29, p 27-64 (1997) https://doi.org/10.1146/annurev. fluid.29.1.27

[36] A. Castellanos "Electrohydrodynamics", section 1.4, p 13, Springer

[37] A. L. Yarin, S. Koombhongse and D. H. Reneker, J. Appl. Phys. **90**, 4836 (2001)

[38] D.Duft, H. Lebius, B.A. Huber, C. Guet, T. Leisner, Phys. Rev. Lett. **89** 0845031 (2002)

[39] D.Duft, T. Achtzehn, R. Müller, B.A. Huber, and T. Leisner, Nature (London) **421**, 128 (2003).

[40] D.D. Joseph and J. Wang, J. Fluid. Mech. vol 505, p 365 (2004)

[41] A. N. Zharov, A. I. Grigor'ev, S. O. Shiryaeva, *Properties of expansions in Legendre polynomial derivatives that show up in analysis of nonlinear vibrations of a viscous liquid drop*, Gases and Liquids, Volume 50, Issue 9, p 1124 (2005)

[42] T. Achtzehn, R. Müller, D. Duft and T. Leisner, Eur. Phys. J. D **34** p 311 (2005)

[43] Henk F. Arnoldus, Optics Communications **265** (2006) p 52

[44] P. W. Atkins and Julio De Paula, Publisher: Oxford ; New York : Oxford University Press, (2006) ISBN 0198700725 (table 21.5 page 763)

[45] J. Wang and D.D. Joseph, J. Fluid. Mech. vol 559, p 461 (2006)

[46] S.I. Betelu, M.A. Fontelos, U. Kindelan and O. Vantzos, Phys. Fluids **18** 051706 (2006)

[47] Lee D, Shin Y, Yu T, Hwang J (2007) "Electrohydrodynamic printing of silver nanoparticles by using a focused nanocolloid jet". Appl Phys Lett 90(8), 081905

[48] J. F. de la Mora, Annu. Rev. Fluid Mech. **39**, 217 (2007).

[49] "Shape deformations of surface-charged microdroplets", E. Giglio, B. Gervais, J. Rangama, B. Manil, B.A. Huber, D. Duft, R. Müller, T. Leisner, C. Guet Phys Rev E **77** p 036319 (2008) https://doi.org/10.1103/PhysRevE.77.036319

[50] "Electrohydrodynamic tip streaming and emission of charged drops from liquid cones" R.T. Collins, J.J. Jones,M.T. Harris and O.A. Basaran, Nature Physics Vol 4, Issue 2, 149 (2008) https://doi.org/10.1038/nphys807

[51] J.C.Padrino T.Funada D.D.Joseph "Purely irrotational theories for the viscous effects on the oscillations of drops and bubbles", International Journal of Multiphase Flow, Volume 34, Issue 1, p 61-75 (2008) https://doi.org/10.1016/j.ijmultiphaseflow.2007.06.008

[52] Dissertation by René. Müller (2010), *Stabilität und Zerfallsdynamik hochgeladener Flüssigkeitströpfchen*, Fakultät für Mathematik und Naturwissenschaften der Technischen Universität Ilmenau. https://www.db-thueringen.de/receive/dbt_mods_00015683

[53] S. Hi Lee and J. C. Rasaiah, Journal of Chem. Phys. **135**, 124505 (2011)

[54] Song Hi Lee and Jayendran C. Rasaiah, J. Chem. Phys. 135, 124505 (2011)

[55] J. C. Burton and P. Taborek, Phys. Rev. Lett. **106** p 144501 (2011)

[56] B. Harsh *et al.*, IEEE TRANSACTIONS ON VISUALIZATION AND COMPUTER GRAPHICS, VOL. 19, NO. 8, (2013)

[57] R.T. Collins, K. Sambath, M.T. Harris and O.A. Basaran, PNAS March 26, (2013) 110 (13) 4905-4910; https://doi.org/10.1073/pnas.1213708110

[58] A. Radcliffe "Non-conforming finite elements for axisymmetric charged droplet deformation dynamics and Coulomb explosions", International Journal for Numerical Methods in Fluids 71, Issue 2, p 249-268 (2013)

[59] A. Radcliffe, Int J Model Simul., Vol. 7 No. 3 (2016) 1650016

[60] H. Nganguia, Y.-N. Young, A. T. Layton, M.-C. Lai, W.-F. Hu "Electrohydrodynamics of a viscous drop with inertia", Phys Rev E 93, 053114 (2016)

[61] A. M. Gañán-Calvo , J. M. López-Herrera , N. Rebollo-Muñoz and J. M. Montanero, "The onset of electrospray: the universal scaling laws of the first ejection", Scientific Reports, 6:32357 (2016), https://doi.org/10.1038/srep32357

[62] Neha Gawande, Y. S. Mayya, and Rochish Thaokar, Phys. Rev. Fluids 2, 113603 (2017)

[63] Numerical Recipes; The Art of Scientific Computing *Section: Cubic Splines Interpolation* http://numerical.recipes/

Chapter 2

Guiding and focusing power of insulating capillaries

Introduction

When low energetic ions hit an insulating surface, charge carriers are injected at the impact points and trapped by defects. As a result, charge accumulates in the dielectric, generating an electric field that, if sufficiently strong, deviates the following beam particles, preventing them to hit the insulator surface. This basic property led to the discovery that slow ions can pass through insulator capillaries (having an aspect ratio, length over diameter, larger than 50) without any change, neither in the ion charge state nor in the ion kinetic energy, even when the geometrical conditions do not allow it. The phenomenon is called charged particle guiding by insulating capillaries and it has become an intensively studied field since its discovery by the pioniering work by N. Stoltherfoht for polyethylene terephthalate (PET or Mylar) nano-capillaries [17] and T. Ikeda for glass macro-capillaries [22], more than 10 years ago. The first simulations showing the guiding effect were
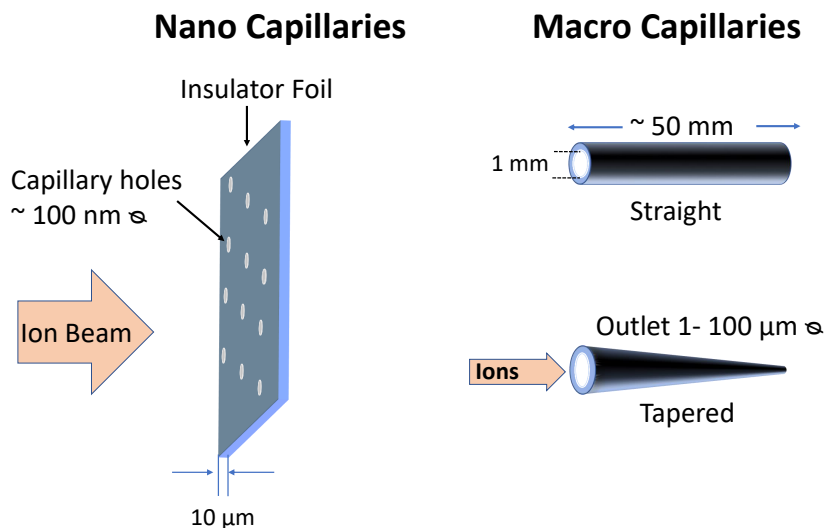
Figure 2.1: Examples of nano and macro-capillaries

developed by K. Schiessl *et al.* [24, 25]. They developed a classical trajectory transport theory of this self-organized guiding process. The guiding electric field was deduced from the accumulated charge in the capillary and the induced image charge. For the charge relaxation channel, they mainly considered surface and bulk diffusion. Despite ignoring the charge relaxation channel due to electrical conductivity, they found a relative good agreement of the simulated transmission coefficients with experimental data.

M. B. Sahana *et al.* observed Ne^{+7} ions being transmitted through well-ordered,
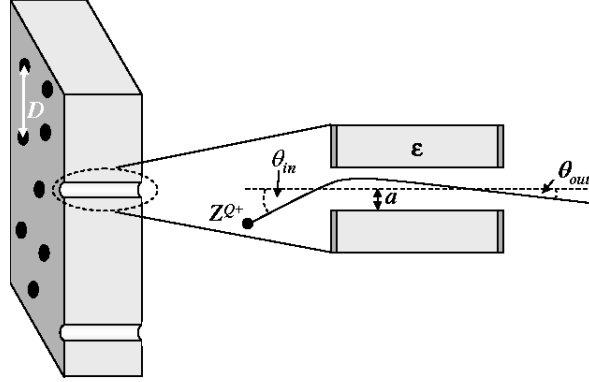
Figure 2.2: Scheme of the transmission of an ion beam, tilted with respect to the capillary axis, through insulating nano-capillaries. Extracted from [24]

parallel SiO_2 nanocapillaries with a decreasing transmitted intensity up to a factor 100, when increasing the capillary tilt angles up to 4°. In particular, they found narrower angular distribution in comparison to PET nano-capillaries [17].

In 2007, A.R. Milosavljevic *et al.* reported the guiding of low-energy electrons by highly ordered Al_2O_3 nanocapillaries with large aspect ratio (140 nm diameter and 15 μm length). The guiding of the electron beam was observed for tilt angles up to 12°. The experimental results clearly showed the existence of the guiding effect, as found for highly charged ions. The energy losses suggest that electrons undergo multiple elastic and inelastic scattering within the capillaries before being transmitted or lost inside the capillary. Despite the considerable energy losses, it has been found that the inelastically as well as the elastically scattered electrons are guided through the capillaries.

P. Skog *et al.* gave evidence that 7 keV Ne^{+7} ions are guided through nanocapillaries by sequentially formed charge patches [32]. A. Cassimi *et al.* showed that 230 keV Xe^{23+} ions are guided through glass macro-capillaries, in agreement with the picture of charge patches created sequentially along the capillary and thus deflecting the beam until a stationary state is reached [37]. Later it was shown that the Xe^{23+} ions show no evidence of energy loss or change in the charge state of the ion, changing except for the production of a small neutral fraction. The latter was determined to be due to ions that had become neutralized at the interface to form atoms rather than due to photon emission [44].

N. Stolterfoht presented in 2013 simulations that indicate that non-linear conductivity to transport the deposited charges along the capillary surface must be taken into account to describe properly the observed transmission in nano-capillaries [48, 49]. Remarkably, he found that if the ion beam is tilted with respect to the capillary axis, ion trajectories are found to be focused, enhanc-

ing the ion guiding, a phenomenon that will be discussed in more detail in the manuscript. Later the same model was used to simulate the guiding of 4.5-keV Ar^{7+} ion guiding through a conical glass macrocapillary. For the latter, the surface conductivity was ignored and the charge dynamics modeled by assuming that the injected charges fade away at a rate depending on the bulk conductivity and thus temperature of the insulator [53]. Recently, evidence of a 1 MeV proton microbeam guided through insulating macrocapillary was given by Nagy *et al.* in [68]. Other advances in the field are described in this non-exhaustive list [31, 33, 34, 35, 36, 37, 38, 40, 41, 42, 43, 46, 47, 51, 62, 64, 67], where the guiding power of insulating nano-capillaries as well as straight, curved and tapered macro-capillaries in various conditions is demonstrated. Detailed reviews about guiding properties of macro- and nano-capillaries are given in [50] and [59]. A recent review including curved teflon macro-capillaries is presented bi T. M. Kojima in [63].
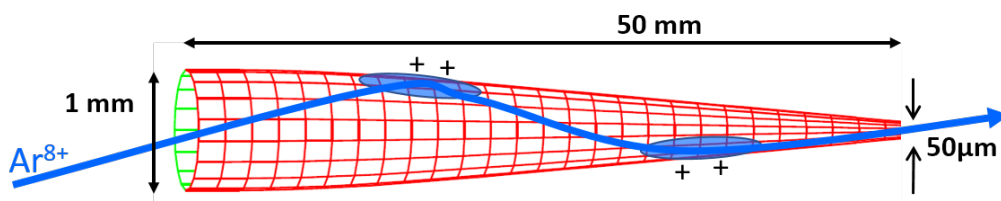
Figure 2.3: Scheme of the transmission of an ion beam, tilted with respect to the capillary axis, through an insulating tapered (conical) macro-capillaries, by sequentially formed charge patches.

While the guiding of ions through glass-capillaries due to charged patches is qualitatively understood, the complex nature of the electric conduction in such insulators makes quantitative theoretical predictions still a challenging task. Indeed, for a given ion beam, the guiding is entirely controlled by the dynamics of the charge patches in the dielectric, which in turn depends (a) on the electrical properties of insulator, (b) on the possible presence of electrodes that affect the electric field inside the capillary and (c) on the charge transfer at the interfaces. Some theoretical studies, simulating the ion trajectories through capillaries have already been presented in [24, 25, 48, 49, 50]. But they suffer mainly by a simplified description of the charge dynamics of the patches and are limited to a relative low number of trajectories due to relatively inefficient algorithms. As a result, they may not have access to the long time (asymptotic) behaviour of the transmission, mainly dominated by the typical long relaxation time of the charge patches in insulators. Also, they do not account for near-laying grounded or floating electrodes that might modify the electric field inside the insulators with low dielectric constant, affecting the trajectories of the ions and thus the charge patch

formation.

In order to get some insights into the relaxation dynamics in glass capillaries, the author developed a numerical code, labelled *InCa4D*, that simulates the ion transport through insulating capillaries. The code is based on the explicit description of the charge accumulation and charge dynamics at the insulator interfaces. Much work was put into developing a CPU efficient numerical code for the calculation of the ion trajectories and charge dynamics in the capillary wall, so that the asymptotic behaviour could be analysed. The model can simulate capillaries having rotational symmetry, such as tubes and conical shaped capillaries. The development of the model started in 2013 and was since developed incrementally to include more and more features, that will be addressed in later sections. One original motivation for studying the transport of ions through insulating capillaries, was to prove that conical glass capillaries can focus an injected beam, similar to electrostatic lenses (Einzel Lenz). While some authors imagined such process, it was not jet demonstrated neither experimentally nor theoretically. Another motivation for the development of *InCa4D* was the rich amount of experimental data available in the literature, awaiting for more detailed theoretical support. In return, the experimental data provided constraints to the model that the simulations had to fulfil. Using a feedback-loop, the model was refined in order to reproduce the experimental data. We foresee to make *InCa4D* freely available, for simulating with high accuracy the ion transport in insulating capillaries, in the spirit of SIMION ®

Regarding the history of capillaries in CIMAP: Capillaries were already studies experimentally in CIMAP since 2005 using a setup developed by A. Cassimi and L. Maunoury. Several collegues collaborated since on the setup and their findings were published in [31, 37, 44]. In 2016, S. Guillous and E. Giglio, started to develop a capillary holder specially designed to allow the observation of the radial focusing effect in conical capillaries. The development of the capillary holder is discussed in the manuscript in section 2.7. The symmetry constraints on the capillary holder as well as the additional features integrated in the design, were suggested by simulations. Indeed, the holder and the numerical code were development hand in hand so as to make comparison between simulated and measured results as meaningful as possible.

2.1 Electric conductivity in glasses

In a first step, the author will discuss in some detail the electrical conductivity in insulating material (mainly ionic glasses) and at the insulator-vacuum and insulator-conductor interfaces. This will allow to introduce the assumptions used in the theoretical model underlying the numerical code *IncA4D*.

2.1.1 Bulk conductivity
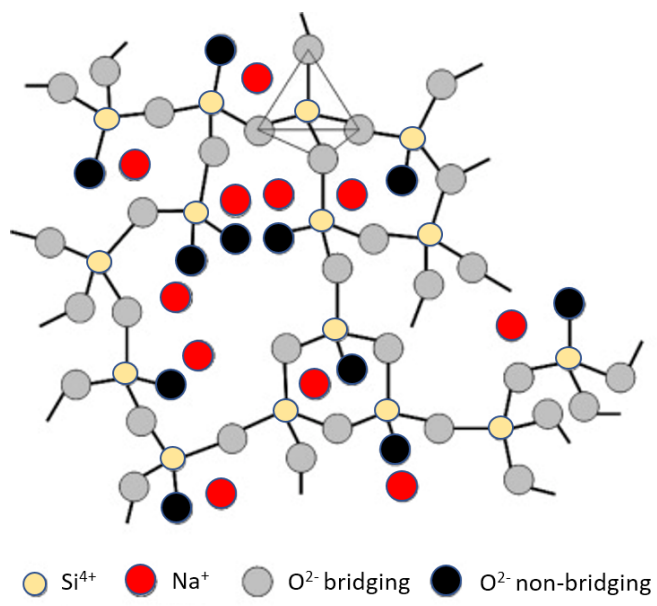
Figure 2.4: Borosilicate glassy network structure

In amorphous insulators with a large band gap, the electrical conductivity is entirely due to extrinsic charge carriers. In glasses, the electric conductivity is mainly based on the transport of impurity ions through the glassy network. The mobility of electrons and holes in those glasses is usually too small to contribute significantly to the electric conductivity [6] and will be neglected in this study. For example, for ®PYREX borosilicate glass, the dominating charge carriers are alkali ions, mostly Na^+ ions. The following discussion however should hold for most ionic glasses. In borosilicate glass, the sodium cation is mainly trapped in the vicinity of a negatively charged non-bridging oxygen (NBO) or tetrahedral BO_4 (B^4) unit and migrates via a thermally activated hopping mechanisms from one trap to another [2, 4, 5, 7, 8, 9, 13, 39, 52]. The NBO and B^4 anions however are firmly linked to the glassy network and are considered immobile. The conductivity

in borosilicate glass follows the Arrhenius law, where E_a is the activation energy of the alkali cation, k_B the Boltzmann constant, and T the temperature,

$$\kappa = A \exp\left(\frac{-E_a}{k_B T}\right) \tag{2.1}$$

For ®Pyrex 7740, we have typically $A = 10^{-3.24}$ S/m and $E_a = 0.42$ eV.

Weak electrolyte: In a material, whose electrical conduction results from the migration of a unique charge carrier species, the electric bulk conductivity κ_b may be expressed as

$$\kappa_b = qn\mu \tag{2.2}$$

with q being the charge for the charge species, n the *effective* charge carrier concentration and μ its mobility. The latter is related to the ion diffusivity D through Einstein's relation

$$D = \frac{\mu k_B T}{q} \quad . \tag{2.3}$$

Expression 2.2 allows for two different interpretations, assuming that either all the ions move with the same low mobility (strong electrolytes), or only a small fraction of impurity ions move with a higher mobility (weak electrolytes). According to J.J. Muray [5] and J.L. Souquet [9, 13, 39], alkali glasses behave like a weak electrolyte[1]. Only those Na^+ ions that are thermally excited from a regular deep trap to a week interstitial trap, where two ions share the same NBO or B^4 unit, can be considered mobile, with a non-negligible mobility μ^+. Let n^+ be the density of thermally activated Na^+, the conductivity of a weak electrolyte with one dominant charge carrier may thus be written as,

$$\kappa_b = e\,\mu^+\,n^+ \quad . \tag{2.4}$$

Assuming a typical sodium ion density for borosilicate of about $n_0^+ \simeq 3 \times 10^{22}$ Na^+ ions/cm^3, a bulk conductivity of $\kappa_b \simeq 10^{-15}$ S/cm and a charge carrier mobility

---

[1] At room temperature and higher, the electrical conduction of electrically neutral borosilicate glasses is based on the transport of Na^+ ions through the glassy network. In its regular site, the cation is bond by a Coulomb interaction preferably to a negatively charged BO_4^- borate group. With enough thermal energy, the cation can leave the regular site and occupy for a short time an interstitial site formed by two alkali cations sharing the same counter-ion. Such a defect has a higher mobility and is responsible for the alkali transport in silicates, as the lower activation energy of the weakly bound Na^+ allows it more easily to jump to a nearby regular site. The density of defect pairs depends on the concentration of Na^+ ions, their bond strength to the network in their regular cationic site and the thermal energy. The short lifetime of about 10^{-10} s of these defects indicates that only a small number of alkali ions participate to the conductivity at a given time, making borosilicate a weak electrolyte.

of about $\mu^+ \simeq 4 \times 10^{-10}$ cm$^2 V^{-1} s^{-1}$ at room temperature [6, 5], about $n^+ = \kappa_b/(q\mu) \simeq 5 \times 10^{13}$ ions/cm^3 are thermally activated at given time and contribute to the conductivity Compared to a typical density in borosilicate, mobile ions account for a fraction of $n^+/n_0^+ \simeq 10^{-9}$ at room temperature, making borosilicate indeed a weak electrolyte.

Enhanced conductivity due to excess charge carriers:

In the case where a glass is positively charged, such that there are less negative counter-ions n_0^- than alkali ions n_0^+, the ionic conductivity of the charged glass may be enhanced with respect to a neutral glass. As mentioned before, in borosilicate, the mobile ions are mainly those which share the same NBO or B^4 unit. Now the excess density $\rho = e(n_0^+ - n_0^-)$ stands for those alkali ions that have lost their counter ion, and have to share a negative unit with another alkali, exactly like the thermally activated ones. Little data exists in the literature that describes such phenomenon in glass, mainly because it is negligible in most cases. For charged capillaries however, the charge stored in the glass may be high enough to enhance sensibly the bulk conductivity. Indeed, for glass-capillaries we are interested in, we typically store about 2 nC of charge in a volume of glass of 10^{-2} cm^3. This gives a density of 10^{12} ions/cm^3 that are activated by the excess charge. This is to be compared to the thermally activated sodium density of $\simeq 5 \times 10^{13}$ ions/cm^3 at room temperature[2]. Thus, for a weak electrolyte like glasses, the density of thermally activated ions does not necessarily dominates the density of excess alkali ions and the latter may contribute significantly to the conductivity. Especially, below room temperature. In the absence of any data regarding their mobility, we assume in the following that the mobility of the sodium ions having lost their counter ion equals the mobility μ^+ of the thermally activated alkali. Within this hypothesis, the density of mobile ions is locally enhanced by the excess charge carriers and the ionic conductivity eventually reads

$$\kappa = e\mu^+(n^+ + (n_0^+ - n_0^-)) \qquad (2.5)$$
$$= \kappa_b + \mu^+\rho \qquad (2.6)$$

While at higher temperature, the last term of equation (2.6) is certainly negligible compared to the bulk conductivity, it may no longer be dominated at low temperature and for high space charge in the insulator. For completeness, the enhancement of the conductivity by positive space charge is taken into account in this model.

---

[2]In contrast, in strong aqueous electrolytes, containing for example HCl (hydrochloric acid) or (NaOH (sodium hydroxide), where all the ions are active, the density of active ions would only marginally increase $(n_0^+ - n_0^-) \ll n_0^+$, so that the contribution of excess charges to the conductivity may be safely ignored.

2.1.2 Surface conductivity

Usually, the surface conductivity of insulating surfaces, labelled κ_s, stands for the conductivity along the insulator-gas interface due to adsorbed impurities. The surface conductivity is expressed in Siemens (S). In the atmosphere for example, the surface conductivity of glass samples depends strongly on the humidity in the atmosphere, meaning that the adsorbed water ions are the main contributors to the anomalous large surface conductivity for glasses in the atmosphere. In near vacuum, the humidity is clearly low and the surface conductivity decreases be several orders of magnitude with respect to the humide atmosphere. It was found by Gruber *et al.* [43] that the surface conductivity in Borosilicate glass follows an Arrhenius type law, with a typical value of $\kappa_s = 10^{-16}$ S at room temperature.

2.1.3 Non-linear conductivity

The conductivity may be written $\kappa_b = qn\mu$, where the separation of carrier density n and mobility μ is artificial; carrier density and mobility are strongly correlated and may depend on the spatial and energy distribution of the charge carriers. One distinguishes shallow and deep (regular) traps. In its regular site, the cation is bond by a Coulomb interaction preferably to a negatively charged BO_4^- borate group. With enough thermal energy, the cation can leave the regular site and occupy for a short time an interstitial site formed by two alkali cations sharing the same counter-ion [9, 13, 39]. Such a interstitial defect has a higher mobility and is responsible for the alkali transport in silicates, as the lower activation energy of the weakly bound Na^+ allows it more easily to jump to a nearby regular site. The ability for a carrier to escape the regular site are influenced by the temperature and by the applied electric field E. In the thermally assisted hopping model, the rate of escape

$$\Omega_0(T) = \nu \exp\left(-\frac{\Delta H}{k_B T}\right)$$

depends on the attempts frequency ν and the average trap depth ΔH. In the presence of an electric field, the probability of escape is the sum of the probability in both directions, with the field and against the field.

$$\Omega(E,T) = \Omega_0 2 \sinh\left(\frac{eEa}{2k_B T}\right) \quad ,$$

with $a \simeq 8$ nm being the average anomalously large distance between interstitial traps [9]. Ω can be linked to the carrier mobility through the drift velocity,

$$a\Omega = \mu E$$

From the definition of the current density $j = \kappa_b E = n\mu E = na\Omega$ one deduces the carrier mobility,

$$\mu = \frac{qa^2\nu}{k_bT} \exp\left(-\frac{\Delta H}{k_BT}\right) \mathrm{sinhc}\left(\frac{qEa}{2k_BT}\right) \tag{2.7}$$

$$= \mu_0 \,\mathrm{sinhc}\,(E/E_c) \tag{2.8}$$

where sinhc() the hyperbolic sinus cardinal and $E_c = \frac{2k_BT}{qa} \simeq 8\,\mathrm{kV/mm}$, the critical field well below the dielectric strength field of 14 kV/mm in pyrex. For

$$E \ll E_c \tag{2.9}$$

we recover the field independent mobility μ_0. For ionic conductivity, the thermally assisted hopping model (TAHM) is here preferred to the Poole-Frenkel model, $\mu \propto \exp(\sqrt{E/E_c^{\mathrm{PF}}})$ [1], which rather describes the electronic conduction of holes and electrons in polymers like Teflon or Mylar [48]. For macro-capillaries, like the one we studied here, the condition 2.9 is usually fulfilled and we will consider thus in the following that the conductivity is field independent, except if stated otherwise.

2.1.4 Interface charge carrier injection

Inner surface

When an insulating surface is irradiated by a positively charged beam, the ions may be implanted into, and/or electrons are removed from the surface, depending on the nature, impact angle and energy of the ions. For grazing impact angles, like the one considered here, cations preferably injects holes into the solid in the vicinity of the impact. We consider the case where a low energy ion beam is injected into a borosilicate capillary. When slow grazing Ar^{q+} ion hit the inner surface of the dielectric, electrons are ejected from (or holes injected into) the surface at the impact point. These holes are quickly trapped near the impact point, mostly by NBO's, which act as hole traps. While usually q ejected electron are captured by the Ar^+ ion, the others will fall back on the surface and trapped by electron traps at the interface and eventually recombine with the holes. As a result, the net deposited charge per impact is q holes captured by q NBO units. This analyses can be generalized to others simply or multiply charged ions. Indeed, in the case of a Xe^{23+} ion beam at 10 keV, Cassimi *et al.* [31] found only neutrals and ions of charge state of +23 in the transmitted beam, giving the indirect evidence that the ions hitting the surface have all been neutralized, by capturing 23 electrons. Of course, the number of electrons ejected from the impact point generally exceed the charge state of the ion. But those electrons, which are not captured by the ion,

fall back on the surface. **We assume in the following that the non-captured electrons fall back to the impact point from where they were emitted**[3]. As a result, the deposited charge per ion at the impact point is equal to the ion charge, independent of the charge state of the surface and energy of the ion. The number of injected holes N_h per unit surface ds and unit time dt at an inner surface point $\vec{r}$, namely $\gamma^h(\vec{r})$, is thus given by

$$e\frac{d^2 N_h}{ds\,dt} \equiv \gamma^h(\vec{r}) = \vec{\eta}(\vec{r}) \cdot \vec{\gamma}(\vec{r}) \quad , \tag{2.10}$$

where $\vec{\gamma}$ is the incoming beam current density, $\vec{\eta}$ the vector normal to the surface and e the elementary charge. For the NBO units that have captured a hole, the charge of the near lying Na^+ ion is no longer compensated. The alkali ions will start to repel each other and move away, driven by the electric field, which is generated by the uncompensated Na^+ ions. This way, in alkali glasses like borosilicate, the positive charge injected by beam ions are not removed because of the migration of electrons or holes, but rather because of the migration of uncompensated alkali ions away from the impact point. Possibly, the migration of electrons and holes in those glasses may happen on a much longer time scale.

Outer surface

Stray electrons: At the outer glass-vacuum interface, no ionic charge transfer takes place. However, potential low energetic stray electrons, that are attracted by the positive charge stored in the capillary walls, may be injected at the outer interface, where they are quickly trapped by electron centres. A reliable expression for the injection rate of stray electron per unit surface may be taken from [62], where a detailed study on the injection rate of stray electrons was proposed. The authors assumed that the stray electrons are mostly produced by the beam ions that hit metal parts in the chamber. The intensity of stray electrons is thus taken proportional to the injected ion beam current I. This proportionality factor, $\lambda_s \geq 0$, depends on the shielding of the capillary's outer surface from secondary electron sources and on the potential of the capillary. Naturally, a positively charged capillary attracts more electrons than a neutral one. The injection rate must thus also depend on the charge of the capillary, or alternatively on its Coulomb potential U. In the study presented in [62], the authors found that, for a given beam current I and a given shielding quantified by the value λ_s, the injection rate increases linearly for low capillary potentials but tends asymptotically to $I\lambda_s$ above a threshold potential U_c, where all the stray electrons, that bypass the shielding, are injected

---

[3]This assumption will be relaxed in a later development of the model and numerical code so that secondary electrons emitted from the impact point are transported through the capillary and injected at new impact point, redistributing the injected charge in the capillary.

into the outer surface. The rate of injected stray electron per unit surface at an outer surface point $\vec{r}$ is thus simply given by

$$\gamma_{\mathrm{str}}^e(\vec{r}) = I \, \lambda_s \, \mathrm{erf}\left(\frac{U(\vec{r})}{U_c}\right) \quad . \tag{2.11}$$

Note that stray electrons may represent a major neutralizing channel, if the capillary is not sufficiently shielded from secondary electrons sources. Indeed, in the setup presented in [62], the shielding was obviously incomplete and λ_s was measured to be about 0.95. The study showed that the neutralization channel due to stray electrons was so strong in that setup that the asymptotic potential of the capillary stayed well below the extraction potential of the ion source for all injected beam intensities.

Interface conductivity: In the presence of an electric field, mobile cations are field driven until they reach an interface. If the interface is blocking for the ionic charge carrier so that no exchange of ions can take place, they accumulate near the interface. This is certainly true for the glass-vacuum interface but also for many electrode-glass interfaces. Typically, electrodes consisting of a silver or carbon paste layer, as has been used in many capillary setups [43, 37], can be considered as quasi blocking for the Na^+ cations. As a result, there is accumulation or depletion of ions near the interfaces, leading to the formation of space-charge layers. The voltage drops rapidly in these layers, which implies a huge electrical interface polarization of the material and a drop of electric field in the bulk. For completely blocking glass-electrode interfaces, the charge migration would vanishes asymptotically. That it does however not vanish but tends instead towards a steady-state current, as is observed in metal-insulator-metal resistivity measurements, is due to a surface process that removes sodium ions from the interface to provide for continuity of the current [15]. A possible mechanism, proposed by Rohatgi [3], is some sort of surface recombination of Na^+ ions with surface electron traps, replenished by dawning electrons from the metal electrode to the surface of the glass. The latter phenomenon may explain the observed glass-conductor interface conductivity. Interface conductivity may differ by several orders of magnitude from the bulk conductivity of glass and depends mainly on the type of contact. If the interface conductivity is higher than the bulk conductivity of the dielectric, than the discharge current is controlled by the bulk conductivity. Otherwise the discharge current is dominated by the interface conductivity. A detailed description of the insulator-metal interface conductivity may be found in [19]. For each charge carrier, one distinguishes at the glass-conductor interface between ohmic and blocking type of contact.

Let us assume that the glass-electrode interface is blocking for the ionic charge carriers and only electrons are allowed to pass the interface. This is certainly

106

the case if the electrode is a graphite layer, which cannot supply or receive alkali ions. If the inner surface is positively charged by ion beam impacts, the outer surface is negatively biased (cathode), favouring electron injection through the conductor-glass interface into the insulator, with the injection rate depending again on the type of contact. In the extreme case where the contact is also blocking for electrons, the interface conductivity would be zero. On the other extreme, for an ohmic contact, electrons flow readily from the electrode into the insulator where they are quickly trapped by electron traps at the glass interface. As the mobility of trapped excess electrons is negligibly low, they accumulate there. The electron flow through the interface stops once the thermodynamic equilibrium at the interface is attained. There is thus a reservoir of filled electron centres at the interface that re-trap the Na^+ cations that reach the interface, giving rise to a neutral pair. The recombining rate of a sodium ion with an electron centre (NBO, B^4 ...) at the interface corresponds thus, in the case of an ohmic contact, to the rate at which the ions approach the interface and is thus controlled by the bulk conductivity.

For simplicity, we will in the following assume that the interface contact is ohmic. Within this assumption, the interface current density γ_{int} is proportional to the normal component of the electric field $E_n(\vec{r})$ at the glass-conductor interface, with the proportionality factor κ_b standing for the ionic bulk conductivity.

$$\gamma_{int}(\vec{r}) = \kappa_b E_n(\vec{r}) \quad . \tag{2.12}$$

If the type of contact is known at the interface, κ_b in equation 2.12 may be replaced by the corresponding expression.

2.2 Charge dynamics in the capillary walls

In the capillary field, several groups have developed a numerical code in order to support theoretically the observed guiding power in insulating capillaries [24, 25, 48, 49, 53]. In all cases, the classical trajectory of the projectiles are deduced from the electric field generated by the accumulated charges in the capillary wall. The time-dependent ion transmission depends of course on the time evolution of the guiding electric field and thus on the charge dynamics of the excess charge carriers in the insulating capillary. Thus much attention must be paid to the description of the charge dynamics in capillaries in order to obtain reliable simulations that are accurate and predictive. In the previous works, in order to keep the CPU cost viable, simplified models for the charge dynamics were proposed. The relaxation channels that were considered in the description of the charge dynamics in [24, 25, 53] were usually described phenomenologically, by retaining mainly the characteristic time related to the considered channels. While this approach captures the main effect of the channel on the charge dynamics, it

lacks the refinement of an explicit field dependent charge dynamics. In [48, 49], N. Stolterfoht included a relaxation channel where the injected charges migrate along the surface with a velocity that depends non-linearly on the electric field. This was a refinement over the previous approach, which allowed him to explain the guiding power in nano-capillaries. In this work, the author will go a step further and give a detailed description of the charge dynamics in insulating capillaries by considering explicitly the charge current associated with each relaxation channel. The resulting model is assumed to be applicable in most situation, may it be for nano- or macro capillaries, even if here, the description mainly emphasizes on glass macro-capillaries.

2.2.1 Excess charge carrier density

The time-evolution of the density of the charge carriers in the insulator is described by the continuity equation. Although the mobility of negatively charged point defects like NBO, B^4 or other filled electron centres is negligible low, the density n_0^- of those negative units varies in time due to hole injection at the inner surface and possible electron injection at the outer surface,

$$e\frac{\partial n_0^-}{\partial t} = \vec{\nabla} \cdot (\gamma^h - \gamma_{\text{str}}^e - \gamma_{\text{int}}^e)\vec{\eta} \quad . \tag{2.13}$$

Here e stands for the elementary charge. The density n_0^+ of Na$^+$ ions , on contrary, varies because a part of them have a mobility high enough to be field driven,

$$e\frac{\partial n_0^+}{\partial t} + \vec{\nabla} \cdot \vec{j} = 0 \quad , \tag{2.14}$$

where $\vec{j}$ stands for the ionic current density. As we assumed that no ionic charge transfer takes place at the interfaces, no source term is added. Eventually, the excess charge density, which is defined as

$$\rho = e(n_0^+ - n_0^-) \quad , \tag{2.15}$$

evolves in time accordingly and reads

$$\frac{\partial \rho}{\partial t} + \vec{\nabla} \cdot \vec{j} = -\vec{\nabla} \cdot (\gamma^h - \gamma_{\text{str}}^e - \gamma_{\text{int}}^e)\vec{\eta} \quad . \tag{2.16}$$

Inside the dielectric, $\vec{j}$ has two main contributions, one proportional to the electric field, $\vec{E} = -\vec{\nabla}V$, and one proportional to the charge density concentration gradient $\vec{\nabla}\rho$.

$$\vec{j} = \kappa\vec{E} + D\vec{\nabla}\rho \quad , \tag{2.17}$$

108

with κ and D being respectively the alkali conductivity and diffusivity. The diffusion term may be neglected here as it is quickly dominated by the electric field term[4]. As discussed before, in weak electrolyte like glasses, the density of thermally activated ions does not necessarily dominates the density of excess alkali ions and the latter may contribute significantly to the conductivity. As a result, the ionic bulk conductivity $\kappa_b = e\mu n^+$ is locally enhanced by the excess charge carriers and the current density eventually reads

$$\vec{j} = \kappa\vec{E} = e\mu(n^+ + (n_0^+ - n_0^-))\vec{E} \tag{2.18}$$
$$= (\kappa_b + \mu\rho)\vec{E} \quad . \tag{2.19}$$

In a sense, this is similar to adding salt into deionized water.

2.2.2 Surface charge approximation

In alkali glasses like borosilicate and soda lime glasses, the mobility of holes, electrons and anions is negligible compared to the mobility of alkali cations and the bulk conductivity κ in those glasses is dominated by the mobile alkali cations. Also, electrons and holes that are injected at the interfaces are quickly trapped by electron traps or hole traps at the interface. We assume thus that the rate τ_h^{-1} at which the injected holes migrate into the bulk is negligible compared to the charge relaxation rate due to bulk conductivity, $\tau_h^{-1} \ll \tau_b^{-1} = \dfrac{\kappa}{\varepsilon_0\varepsilon_r}$. This implies that the electrons and holes that are injected at the interfaces accumulates only at the inner and outer surface and not in the bulk. For example, if a hole migrates into the bulk, the mobile alkali ions will rearrange around the hole at the rate τ_b^{-1}, so that the hole is balanced ("neutralized") by a deficit of mobile ions. As a result, for each hole that migrates into the bulk, an alkali ion will migrate " rapidly" to the interface, leaving a zero net charge in the bulk. The injected charge can thus be represented by a surface charge density. Consequently, the mobile charge carriers in the insulator are driven by a divergence-free electric field $\vec{\nabla} \cdot \vec{E} = 0$ through the glass bulk. If the electric field is directed from the inner to the outer surface, field-driven Na^+ cations tend to deplete the inner interface and accumulate at the blocking outer interfaces S_2, so that the excess charge density ρ is mainly non-zero at the interfaces. Further away from the interfaces, the excess charge density ρ tends to zero. These trends are depicted in figure 2.6. Because the excess charge density ρ is mainly non-zero at the interfaces, we propose to replace the charge

---

[4]Using the Einstein relation, linking the diffusivity to the charge carrier mobility, $D = \dfrac{\mu k_B T}{e}$, we deduce from the dimensionless analysis that the diffusion term is negligible if $k_B T \ll eU$ where U is the potential in the capillary. At room temperature, $T = 300$ K, this condition is fulfilled for $U \gg 0.24$ V.
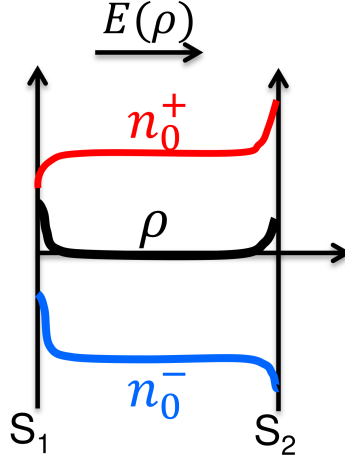
Figure 2.5: *Negative n_0^-, positive n_0^+ and excess charge carrier distribution ρ in the glass wall following charge injection at the interface. Because the mobile alkali ions are field driven from the inner S_1 to the outer S_2 interface by the electric field E, they deplete at the inner and accumulate at the outer interface. The negative immobile anion charge density n_0^- depletes at the inner interface because of hole injections by the projectiles at the inner surface. At the outer interface the accumulation of negative charges accounts for a possible injection of electrons by either stray electrons or by a grounded electrode. The excess charge density ρ is simply the sum of the positive and negative charge densities and is mainly non-zero at the interfaces.*

distribution ρ by surface charge densities σ_1 and σ_2 at the inner and outer surface respectively. Using the cylindrical coordinates system (r, θ, z), the inner and outer surface of an axisymmetric capillary are given by the function $R_1(z)$ and $R_2(z)$, respectively. The surface charge densities at the two interfaces may then be defined by

$$\int_{R_1(z)}^{R_2(z)} r\rho(r, \theta, z)\,dr \simeq \sigma_1(\theta, z)\frac{ds_1}{dz} + \sigma_2(\theta, z)\frac{ds_2}{dz} \tag{2.20}$$

where $ds_i = \sqrt{R_i^2(z) + R_i'^2(z)}dz$ is the surface element at the interface i.

2.2.3 Surface charge dynamics at the interfaces

Motivated by the above discussion, we assume here that no excess charges are stored inside the bulk $\rho = 0$ and that the electric field is therefore divergence-free inside the capillary walls

$$\vec{\nabla} \cdot \vec{E} = 0 \quad . \tag{2.21}$$

110

The time evolution of the charge density in the capillary (2.16) is replaced by the time evolution of the surface charge density at the interfaces (S_1) and (S_2) and best described by the surface continuity equation [60, 61]. At the inner interface (S_1), the time evolution of σ_1 is given by

$$\frac{\partial \sigma_1}{\partial t} + \vec{\nabla}_s \cdot ((\kappa_s + \mu \sigma_1)\vec{E}_1) = -\kappa E_{n,1}^+ + \gamma^h \tag{2.22}$$

where the operators

$$\vec{\nabla}_s = \vec{\nabla} - \vec{n}\left(\vec{n}\cdot\vec{\nabla}\right) , \quad \vec{\nabla}_s \cdot \vec{T} = \vec{n}\cdot\left(\vec{\nabla}\wedge(\vec{n}\wedge\vec{T})\right)$$

are respectively the surface gradient and the surface divergence, with $\vec{T}$ being an arbitrary vector tangent to the surface. The source term γ^h stands for the injected holes by ion impacts and $\kappa E_{n,1}^+$ for the current density of mobile charge carriers that are field-driven from the inner interface into the bulk. The term $\kappa E_{n,1}^-$ is not present because no mobile charge carriers are injected from the vacuum at the inner surface. On the outer interface (S_2) the dynamics of the surface charge σ_2 becomes,

$$\frac{\partial \sigma_2}{\partial t} + \vec{\nabla}_s \cdot ((\kappa_s + \mu \sigma_2)\vec{E}_2) = \kappa E_{n,2}^- + \gamma_{\text{str}}^e + \gamma_{\text{int}}^e \tag{2.23}$$

The source terms $\gamma_{\text{str}}^e + \gamma_{\text{int}}^e$ stand for the injected electrons at the outer surface and $\kappa E_{n,2}^-$ for the mobile charge carriers that are field driven typically from the bulk to the outer interface where they accumulate. The second left hand term in both equations gives the flow of mobile charges along the respective interface.

Limiting the charge dynamics in the capillary to both interfaces allows reducing by one (spatial) dimension the charge dynamics equation (2.16) and thus the CPU cost without sacrificing the scope of the model presented above. The coupling is due the electric field $\vec{E}$, which is a functional of two excess surface charge distribution $\sigma_{1,2}$. That the electric field needs to be evaluated only at the two interfaces helps to reduce even more the CPU cost for the charge dynamics in the dielectric.

2.2.4 Evaluation of the electric field at the interfaces

Polarization charges in dielectrics

We consider the general case where the capillary of relative dielectric constant ε_r is surrounded by an axisymmetric conducting (metal) surface (S_3), sharing the same symmetry axis then the capillary. The profile of the (S_3) metal-vacuum interface is defined by $R_3(z)$ with $R_3(z) > R_2(z)$. If no conducting surface is present for a given z, then $R_3(z)$ is pushed to infinity. We have eventually to
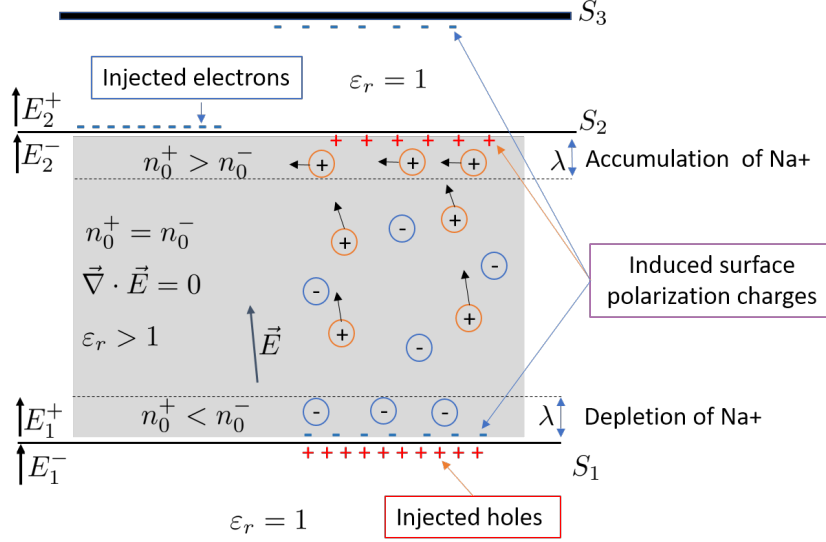
Figure 2.6: Scheme of the capillary wall with the 3 interfaces, namely S_1 and S_2 standing for the inner and outer capillary glass-vacuum interfaces and S_3 for the metal-vacuum interface of the metal layer surrounding the capillary. The red charges are the polarization charges appearing around the positive charges in the bulk and at the glass-vacuum interfaces. The blue surface charges at the vacuum-metal interface S_3 are free charges that accommodate to satisfy the Dirichlet condition of a constant potential V_3 at the surface of metal layer.

deal with three interfaces, two vacuum-dielectric interfaces, (S_1) and (S_2) and one metal-vacuum interface (S_3). In the presence of dielectrics and metal surfaces, some attention must be paid to the evaluation of the electric field $\vec{E}$ generated by the deposited charges in the capillary wall. Indeed, polarization surface charges induced at the glass-vacuum interfaces as well as free surface charges induced at the metal-vacuum interface affect the electric field generated by the deposited charges. A systematic error in the evaluation of the field induces discrepancies in the trajectories of the injected ions and consequently on the source term γ^h, which in turn controls the dynamics of the deposited charges in the capillary walls. Induced surface charges need thus to be computed accurately in order to avoid a systematic and accumulative errors in the simulations.

Let $\vec{r}_1$, $\vec{r}_2$ and $\vec{r}_3$ be the position vectors pointing respectively at the inner S_1, outer surface S_2 and metal surface S_3. Following the discussion in section 2.2.2, the accumulated charge is represented by the surface charge densities $\sigma_{1,2}$ defined on the interfaces S_1 and S_2. At both vacuum-glass interfaces S_1 and S_2 appear polarization surface charges $\widetilde{\sigma}_{1,2}$. At the metal-vacuum interface, S_3, free surface charges $\widetilde{\sigma}_3$ appear so as to maintain an equipotential on S_3. A schematic

representation of the interfaces in given in 2.6. Note that in the literature, these surface polarization charges are often referred to as image charges. The electric potential V at arbitrary point $\vec{r}$, due to the accumulated charge distributions $\sigma_{1,2}$ and the three induced surface charge densities $\widetilde{\sigma}_{i=1,2,3}$ at the three interfaces $S_{i=1,2,3}$, is eventually given by

$$V(\vec{r}) = \int_{S_1} \frac{\sigma_1 \, ds_1}{4\pi\varepsilon_0 |\vec{r} - \vec{r}_1|} + \int_{S_2} \frac{\sigma_2 \, ds_2}{4\pi\varepsilon_0 |\vec{r} - \vec{r}_2|} + \sum_{i=1}^{3} \int_{S_i} \frac{\widetilde{\sigma}_i d^2 s_i}{4\pi\varepsilon_0 |\vec{r} - \vec{r}_i|} \qquad (2.24)$$

with ds_i being the surface element. The polarization charges $\widetilde{\sigma}_1$ and $\widetilde{\sigma}_2$ at the inner and outer surface of the dielectric are deduced from the boundary conditions of the normal component of the electric field across both interfaces. In the presence of free surface charges $\sigma_{1,2}$, one has,

$$(\text{S}_1): \qquad -\varepsilon_r \frac{\partial V}{\partial \vec{n}}\bigg|_{r=r_1^+} + \frac{\partial V}{\partial \vec{n}}\bigg|_{r=r_1^-} = \frac{\sigma_1}{\varepsilon_0} \qquad (2.25)$$

$$(\text{S}_2): \qquad -\frac{\partial V}{\partial \vec{n}}\bigg|_{r=r_2^+} + \varepsilon_r \frac{\partial V}{\partial \vec{n}}\bigg|_{r=r_2^-} = \frac{\sigma_2}{\varepsilon_0} \qquad . \qquad (2.26)$$

The surface density $\widetilde{\sigma}_3$ of free charges at the metal layer is deduced from a Dirichlet boundary condition, i.e. the potential is an equipotential at the metal interface.

$$(\text{S}_3): \quad V(\vec{r}_3) = V_3 \qquad . \qquad (2.27)$$

In the case where the value of the equipotential V_3 of the electrode is not imposed but floating, we use the constraint that the total initial charge of a floating isolated electrode does not vary in time,

$$\int \sigma_3 ds_3 = Q_3 \qquad .$$

If for example the electrode was initially neutral, then $Q_3 = 0$. With this supplementary condition, the value of the equipotential V_3 is found.

Matrix representation of the surface integrals

In order to compute the surface densities $\widetilde{\sigma}_i$, one needs to evaluate the electric potential and the normal component of the electric field at the interfaces. It is convenient, for the sake of a compact notation, to cast the surface integrals, found in (2.24), into matrix forms,

$$\int_{S_i} \frac{\widetilde{\sigma}_i ds_i}{4\pi\varepsilon_0 |\vec{r}_j - \vec{r}_i|} \equiv K_{ji}\widetilde{\sigma}_i \qquad , \qquad (2.28)$$

where the indexes $i = \{1, 2, 3\}$ and $j = \{1, 2, 3\}$ stand for the three interfaces. Similar, the normal derivatives of the surface integrals taken at the interfaces may be expressed in matrix form,

$$\frac{\partial}{\partial \vec{n}} \int_{S_i} \left. \frac{\widetilde{\sigma}_i ds_i}{4\pi\varepsilon_0 |\vec{r} - \vec{r}_i|} \right|_{r=r_j} \equiv N_{ji} \widetilde{\sigma}_i \quad . \tag{2.29}$$

Details about K_{ji} and N_{ji} are given in the appendix. Because of the discontinuity of the normal component of the electric field through an interface, we must distinguish between the inner (-) and outer (+) field in the case where $i = j$. Eventually, we obtain for each boundary condition (2.25),(2.26) and (2.27) a matrix equation. These equations are coupled by the induced surface charges $\widetilde{\sigma}_{1,2,3}$ at the interfaces, yielding a system of matrix equations of the form,

$$\begin{bmatrix} N_{11}^- - \varepsilon_r N_{11}^+ & \beta N_{12} & \beta N_{13} \\ -\beta N_{21} & \varepsilon_r N_{22}^- - N_{22}^+ & -\beta N_{23} \\ K_{31} & K_{32} & K_{33} \end{bmatrix} \times \begin{bmatrix} \widetilde{\sigma}_1 \\ \widetilde{\sigma}_2 \\ \widetilde{\sigma}_3 \end{bmatrix} = \begin{bmatrix} (\mathrm{RHT}_1) \\ (\mathrm{RHT}_2) \\ V_3 - V_\rho \end{bmatrix} \tag{2.30}$$

with $\beta = (1 - \varepsilon_r)$. The right hand terms (RHT_1) and (RTH_2) stand for the electric field at the interfaces S_1 and S_2 evaluated using the known quantities $\sigma_{1,2}$

$$\begin{aligned} (\mathrm{RHT}_1) &= (\varepsilon_0^{-1} + \varepsilon_r N_{11}^+ - N_{11}^-)\sigma_1 - \beta N_{12}\sigma_2 \\ (\mathrm{RHT}_2) &= \beta N_{21}\sigma_1 + (\varepsilon_0^{-1} - \varepsilon_r N_{22}^- + N_{22}^+)\sigma_2 \end{aligned} \tag{2.31}$$

At the interface S_3, the known quantity at the right hand side of the matrix system is given by the difference between the equipotential V_3 of the metal layer and the Coulomb potential $V_\rho(\vec{r}_3)$,

$$(S_3) \quad : \quad V_3 - V_\rho(\vec{r}_3) \quad . \tag{2.32}$$

The polarization charges $\widetilde{\sigma}_{1,2}$ as well as the free charges on the metal layer $\widetilde{\sigma}_3$ are readily computed by solving the system by matrix inversion. Finally, the potential at an arbitrary point is now evaluated using equation (2.24), from which the electric field $\vec{E} = -\vec{\nabla}V$ is deduced. More detail about the evaluation of the electric field and potential are given in appendix 2.11.3. The influence of the polarization charge on the electric field is illustrated by an example in appendix 2.11.4.

2.2.5 Image charge potential of projectile

The image charge potential of projectile of charge q becomes non-negligibly when the projectile approaches the inner glass-vacuum interface within a nanometer scale

distance, so that the ion can induce enough polarization charges at the interface S_1 to affect its trajectory. In order to avoid that the image charge force diverges, the projectile's charge q is screened below a distance $d_{\text{scr}} = 10^{-9}$ m from the surface. For micro-capillaries with an inner radius much larger the the screening distance d_{scr}, we preferably use the analytic expression of the image charge potential, in the adiabatic approximation, obtained in the case of a infinite plane interface between a dielectric of dielectric constant ε_r and the vacuum.

$$V_{\text{im}}(r, \theta, z) = \frac{q}{8\pi\varepsilon_0} \frac{\varepsilon_r - 1}{\varepsilon_r + 1} \frac{1}{R_1(z) - r} \text{erf}\left(\frac{R_1(z) - r}{d_{\text{scr}}}\right) \qquad (2.33)$$

However for a cylindrical surface with a radius in the nano-meter range, this expression may over-estimate the image charge force. The image force for a cylindrical interface may then be expressed more accurately by a (slowly converging) series of Bessel terms [21, 54].

2.3 Equation of motion of the projectile

For low enough ion beams intensities $I < 1$ pA, the coulomb interaction between the ions of the beam can be neglected and the trajectories regarded as independent one from another. The equation of motion (EOM) of a particle of charge q and mass m at the position $\vec{r}_p$ interacting with a charged capillary of dielectric constant ε_r may be written

$$\frac{d^2\vec{r}_p}{dt^2} = -\frac{q}{m} \left.\vec{\nabla}\left(V[\rho, \widetilde{\sigma}_{1,2,3}] + V_{\text{im}}[d(\vec{r}_p, S_1)]\right)\right|_{\vec{r}=\vec{r}_p}, \qquad (2.34)$$

where the potential $V[\rho, \widetilde{\sigma}_{1,2,3}]$ is given by (2.24) and where V_{im} stands for the non-dissipative part of the image charge potential of the projectile. Eventually, the trajectory of the ion is computed on the fly by evaluating the electric field $-\vec{\nabla}(V + V_{\text{im}})$ at the projectile position using equation (2.24). The propagation is based on a 4th order time adaptive Predictor-Corrector scheme [29].

2.4 Charge relaxation rates

In the following section, we will show how to extract the charge relaxation rate for insulating capillaries like those used in [43, 51, 53]. A detailed study of the charge relaxation dynamics of charge patches and their associated relaxation time scales is given in Giglio *et al.* [67]. I will give here a short summary of the main ideas presented in the paper. We consider a cylindrically shaped glass capillary (tube) of length H, with an inner radius R_1, an outer radius of R_2 and which has

a dielectric constant ε_r (see Fig. 2.7). The insulating capillary tube of symmetry axis Oz has the outer surface, entrance and exit grounded. We assume that the electric charge is injected by the ion beam at the inner interface and that the charges accumulate only at the interface but not in the bulk. As a result, the electric field is divergence-free and the electric potential V satisfies the Laplace equation everywhere. The underlying model considers thus merely two interfaces namely the inner glass-vacuum interface S_1 of the capillary and the outer glass-metal interface S_2. The charge dynamics taking place at the inner interface S_1 is expressed in the cylindrical coordinate system by the equation,

$$\frac{\partial \sigma}{\partial t} = -\kappa_b E_r - \frac{\partial}{\partial z}\left(\kappa_s E_z\right) - \frac{1}{R}\frac{\partial}{\partial \theta}\left(\kappa_s E_\theta\right) + \gamma I_{\mathrm{inj}} \qquad (2.35)$$

The first right hand term, which is proportional to the bulk conductivity κ_b, stands for the mobile charge carriers that are driven from the inner to the grounded outer surface by the radial component E_r of the electric field. The second and third right hand terms stand for the charge carriers that are field driven at the inner interface respectively along the symmetry axis by the tangential field E_z and along the angular direction by the tangential field E_θ. The surface current is proportional
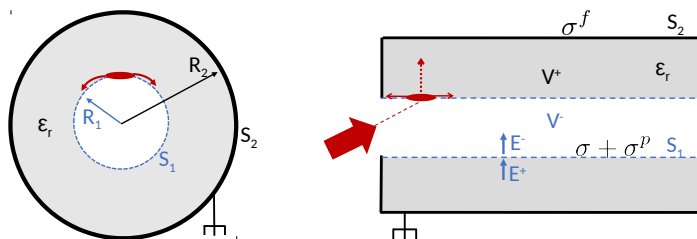
Figure 2.7: *Scheme of the surface current in the capillary. The outer surface S_2 is grounded. The insulating inner surface S_1 carries the accumulated surface charge density . The induced polarization charges p and free charges f are also shown. The tilted injected beam (large red arrow) deposits a charge patch near the entrance, which will relax in time due to a surface current along the angular direction (red arrows in left figure) a surface current along the axial direction and a current through the bulk to the outer grounded surface (red arrows in right figure).*

116

to the surface conductivity κ_s. The last term represents the injected charge per unit time and unit area, with I_{inj} being the beam current and γ the hole-injection cross-section. To keep the math simple, we omitted here the part of the surface conductivity due to the excess charges $\mu\sigma$. The latter can however be added without larger difficulties in principle. Extracting the charge relaxation rate of the injected patch via a dimensionless analysis of (2.35) is not straightforward as it would yield three different characteristic relaxation rates related to the three independent relaxation channels,

$$\tau_b^{-1} = \frac{\kappa_b}{\varepsilon_0 \varepsilon_r} \tag{2.36}$$

$$\tau_s^{-1} = \frac{\kappa_s}{\varepsilon_0 R_1} \tag{2.37}$$

$$\tau_z^{-1} = \frac{\kappa_s}{\varepsilon_0 H} \tag{2.38}$$

and we have no clear way to combine them to get the total relaxation rate. Here, we present a simple method that allows us to extract the total charge relaxation rate of an injected charge patch located at the S_1 interface. The charge relaxation dynamics will be obtained in the case where the capillary potential satisfies the following boundary and symmetry conditions:

1. The outer surface is grounded: $V(S_2) = 0$

2. The entrance and exit are grounded: $V(z=0) = V(z=H) = 0$

3. The potential is assumed having the xOz plane symmetry so that: $V(\theta) = V(-\theta)$

4. If we label V^- the potential in the inner domain $r \leq R_1$ and V^+ the potential in the bulk domain $R_1 \leq r \leq R_2$, then the continuity of the potential implies $V^-(R_1, \theta, z) = V^+(R_1, \theta, z)$

Equation (2.35) is solved by using the multipole expansion technique. The potentials are expanded on a harmonic basis which satisfying the Laplace equation as well as the imposed symmetry and boundary conditions:

$$V^-(r, \theta, z, t) = \sum_{mn} v_{mn}(t) \frac{I_m(k_n r)}{I_m(k_n R_1)} \cos(m\theta) \sin(k_n z), \quad r \leq R_1 \tag{2.39}$$

$$V^+(r, \theta, z, t) = \sum_{mn} v_{mn}(t) h_{mn}(r) \cos(m\theta) \sin(k_n z), \quad R_1 < r \leq R_2$$

$$\tag{2.40}$$

117

where we introduced the auxiliary function $h_{mn}(r)$ defined as

$$h_{mn}(r) = \frac{I_m(k_n r)K_m(k_n R_2) - I_m(k_n R_2)K_m(k_n r)}{I_m(k_n R_1)K_m(k_n R_2) - I_m(k_n R_2)K_m(k_n R_1)} \tag{2.41}$$

in order to simplify the notations, with $I_m(k_n r)$ and $K_m(k_n r)$ being modified Bessel functions of the first and second kind of order m. Here $m \geq 0$ gives the angular moment of the distribution and $k_n = \frac{n\pi}{H}$ the wave number of the mode $n \geq 1$. Note that $h_{mn}(R_1) = 1$ and $h_{mn}(R_2) = 0$ satisfy the imposed boundary conditions (5) and (1). Similar, we expand the surface charge density and injection cross section defined on the interface S_1 onto a basis set that satisfies also the xOy plane symmetry and zero boundary conditions at the endpoints. The latter is justified by the fact that the grounded inlet and outlet imposes that the free surface density and source term are also zero at $z = 0$ and $z = H$,

$$\sigma(\theta, z, t) = \sum_{mn} \sigma_{mn}(t)\cos(m\theta)\sin(k_n z) \tag{2.42}$$

$$\gamma(\theta, z, t) = \sum_{mn} \gamma_{mn}(t)\cos(m\theta)\sin(k_n z) \tag{2.43}$$

Using the jump condition of the electric field through an interface separating to dielectrics, which relates the free surface charge density σ to the electric potentials V^+ and V^-

$$\varepsilon_r \left.\frac{\partial V^+}{\partial r}\right|_{(S_1)} - \left.\frac{\partial V^-}{\partial r}\right|_{(S_1)} = \frac{\sigma}{\varepsilon_0} \tag{2.44}$$

allows to express $v_{mn}(t)$ as a function of $\sigma_{mn}(t)$,

$$v_{mn}(t) = \frac{\sigma_{mn}(t)}{\varepsilon_0}\left(\varepsilon_r h'_{mn}(R_1) - h'_{mn}(R_2)\right) \tag{2.45}$$

The prime symbol stands for the partial derivatives with respect to the radial coordinate r. Injecting (2.45) into the expansions (2.39 - 2.43) into 2.35 yields a differential equation (uncoupled) for each surface charge moment σ_{mn} of the form,

$$\frac{\partial \sigma_{mn}(t)}{\partial t} = -\frac{1}{\tau_{mn}}\sigma_{mn}(t) + \gamma_{mn}(t)I_{\text{inj}} \tag{2.46}$$

where τ_{mn}^{-1} is the charge relaxation rate associated with the mode (m, n). The rate τ_{mn}^{-1} is given as the weighted sum of the surface $\tau_s^{-1} = \dfrac{\kappa_s}{\varepsilon_0 R_1}$ and bulk rate $\tau_b^{-1} = \dfrac{\kappa_b}{\varepsilon_0 \varepsilon_r}$,

$$\frac{1}{\tau_{m,n}} = \frac{b_{m,n}}{\tau_b} + \frac{c_{m,n}}{\tau_s} \quad , \tag{2.47}$$

118
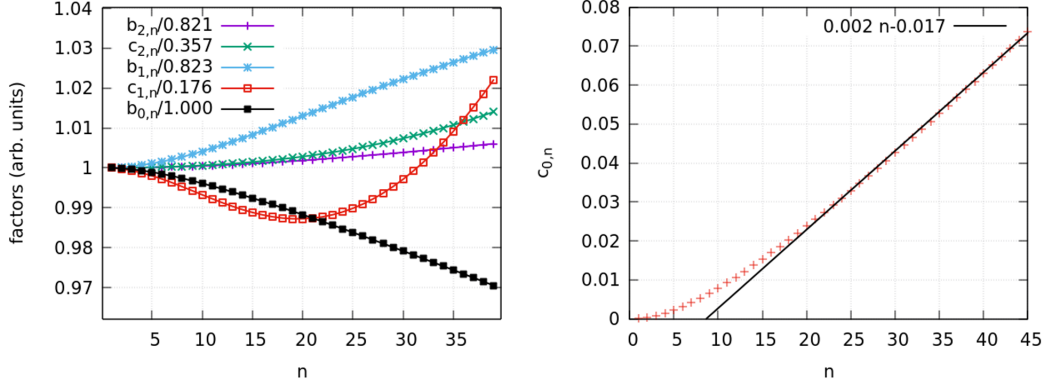
Figure 2.8: *Weight factors b_{mn} and c_{mn} for $m \leq 2$ and $1 \leq n \leq 40$. Left: all but c_{0n} vary by less than 4 % with n, so that they can be considered constant over the range $n < 40$. Right: c_{0n} varies asymptotically linear with n, starting from $c_{01} \simeq 10^{-3}$.*

where the positive coefficients $b_{m,n}$ and $c_{m,n}$ give the strength of the bulk and surface rate respectively,

$$b_{mn} = \frac{h'_{mn}(R_1)}{h'_{mn}(R_1) + \varepsilon_r^{-1} \frac{I'_{mn}(R_1)}{I_{mn}(R_2)}} \quad , \quad c_{mn} = \frac{(m^2 + k_n^2 R_1^2)/(\varepsilon_r R_1)}{h'_{mn}(R_1) - \varepsilon_r^{-1} \frac{I'_{mn}(R_1)}{I_{mn}(R_2)}} \quad .$$

The coefficients are time independent and need to be calculated only once for all. Equation (2.47) is a remarkable result as it shows that each relaxation rate $(\tau_{m,n})^{-1}$ includes contributions of the three possible relaxation channels, namely through the bulk, along the angular and along the axial direction at the surface and that the weight of each contribution varies with (m, n). Both coefficients b_{mn} and c_{mn} depend on the dimensions of the capillary and more precisely on the ratios R_1/H and R_2/H as well as the dielectric constant ε_r of the insulator. Usually, b_{mn} is close to unit, while c_{mn} scales as $(m^2/(k_n R_1) + k_n R_1)$ with m and n. The trends of both coefficients with m and n are shown in Fig. 2.8 and discussed in detail in [67]. From (2.46) we deduce the time evolution of the accumulated charge distribution and the interface as well as the important result that each surface charge moment $\sigma_{mn}(t)$ decays exponentially with the relaxation rate $(\tau_{mn})^{-1}$

$$\sigma_{mn}(t) = \underbrace{\sigma_{mn}(0) \exp\left(-\frac{t}{\tau_{mn}}\right)}_{\text{discharge}} + \underbrace{I_{\text{inj}} \int_0^t \gamma_{mn}(t') \exp\left(\frac{t' - t}{\tau_{mn}}\right) dt'}_{\text{charge}} \quad . \tag{2.48}$$

119

Eventually, the analytical solution of (2.35) is given as a linear combination of surface charge moments that satisfy the given boundary conditions.

$$\sigma(\theta, z, t) \;=\; \sum_{m,n} \sigma_{mn}(t)\cos(m\theta)\sin(k_n, z) \quad. \tag{2.49}$$

Let us consider now the interesting case where the accumulated charge is stationary, $\partial_t\sigma_{mn}(t) = 0$. In that case we have that the accumulated charge varies adiabatically as

$$\sigma_{mn}(t) = I_{\text{inj}}\tau_{mn}\gamma_{mn}(t) \quad. \tag{2.50}$$

Using (2.45) and (2.39) the guiding electric potential can be evaluated. This may be a helpful tool to estimate if the guiding electric field is sufficient or not to guide the injected ion beam through the capillary. In conclusion, the advantage of the above multipole analyses is that we obtain an excellent estimate of the accumulated charge at the inner interface of the capillary as a function of the dimensions of the capillary beam parameters. Note that the method can be easily extended to account for an insulator-vacuum interface at S_2 instead and a grounded interface at S_3 surrounding S_2. Work for this more general case is underway. We give below a quick example of how to use equation (2.47) for the interpretation of experimental data.

Examples

Consider for example a borosilicate glass tube with a length of 43 mm, an inner radius of $R_1 = 0.29$ mm and outer radius of $R_2 = 0.275$ mm, with the outer surface electrically grounded, like the one used in a therory-experiment comparison found in [69]. The values of the coefficients $b_{m,n}$ and $c_{m,n}$ for this particular capillary are published in [69]. For borosilicate at room temperature, one has typically $\kappa_b = 10^{-13}$ S/m and $\varepsilon_r = 4.6$, yielding $\tau_b^{-1} = 2.4$ mHz. The surface conductivity κ_s is not a well known quantity as it depends strongly on the adsorbed ions at the surface. We assume here a value of $\kappa_s = 10^{-16}$ S as measured by [43], yielding $\tau_s^{-1} \simeq 40$ mHz. Let us consider a small charge patch of lengths $d = 4$ mm located several mm behind the entrance of the capillary, that has been injected by a tilted ion beam. We are interested in its charge relaxation rate of the accumulated charge once the ion beam stops, $\gamma_{mn} = 0$. As suggested by (2.47), the rate is given as a weighted mean value with the weights depending on the geometry of the capillary and the considered angular moment of the charge patch. Here, we limit our expansion (2.49) to the first two angular moments, namely $m = 0$ and $m = 1$. The dipole part ($m = 1$) of the accumulated charge distribution is the first non-zero angular moment and is mainly responsible for the deflection of the ion beam by the charge patch, so it is interesting to consider its relaxation rate. The

monopole moment $m = 0$ characterizes rather the charge relaxation of the total charge. Noting that the first $n \leq 10$ are sufficient to describe the $d = 4$ mm charge patch, $(d \cdot k_{n=10} \simeq \pi)$, we limit our expansion to the modes $n \leq 10$. As shown in Fig. 2.8, the coefficients b_{mn} and c_{mn} depend only weakly on n. We may thus get an excellent guess of the monopole and dipole relaxation considering only $n = 10$.

$$
\begin{aligned}
\tau_{0,10}^{-1} &\simeq \frac{0.99}{\tau_b} + \frac{0.008}{\tau_s} \\
&\simeq 0.99 \times 2.4 + 0.008 \times 40 \simeq 2.8 \text{ mHz}
\end{aligned}
$$

$$
\begin{aligned}
\tau_{1,10}^{-1} &\simeq \frac{0.826}{\tau_b} + \frac{0.176}{\tau_s} \\
&\simeq 0.826 \times 2.4 + 0.176 \times 40 \simeq 7 \text{ mHz}
\end{aligned}
$$

First, we note that the relaxation rate of the dipole is 2.5 times higher than the monopole one. Unsurprisingly, for the monopole part, the contribution of the surface channels are negligible with respect to the bulk channel. Indeed, only the surface channel along the symmetry axis contributes slightly, but most of the charges relax via the bulk channel. The dipole part on the other hand activates an additional surface channel, namely the one along the angular direction, which also becomes the dominant one. Measuring the relaxation of the total charge $\tau_{0,n}^{-1}$ in a capillary and the relaxation of the dipole part $\tau_{1,n}^{-1}$ of a charge patch yields thus complementary pieces of information that allows to determine unambiguously the inner surface and bulk conductivity of the insulating capillary!

Dimensionless analysis

Instead of performing a dimensionless analysis of (2.35), we use instead (2.46) which is equivalent to (2.35) but has the advantage to define clearly the characteristic relaxation times τ_{mn}^{-1}. Introducing the extraction potential U_s of the ion source and the characteristic surface $S = 2\pi H R_1$, and capacity $C = 2\pi \varepsilon_0 \varepsilon_r H / \log(R_2/R_1)$ of the capillary, we can define the characteristic charging time

$$
\tau_c = \frac{C U_s}{I_{\text{inj}}} \tag{2.51}
$$

and the following dimensionless quantities

$$
\tilde{t} = t/\tau_c \tag{2.52}
$$

$$
\tilde{\sigma}_{mn} = \frac{S_0}{C U_s} \sigma_{mn} \tag{2.53}
$$

$$
\tilde{\gamma}_{mn} = S \gamma_{mn} \tag{2.54}
$$

We can now re-write equation (2.46) in a dimensionless form,

$$\frac{\partial \tilde{\sigma}_{mn}(t)}{\partial \tilde{t}} = -\frac{\tau_c}{\tau_{mn}} \tilde{\sigma}_{mn}(t) + \tilde{\gamma}_{mn}(t) \tag{2.55}$$

The charge dynamics at the inner capillary surface is thus entirely controlled by the ratio

$$\frac{\tau_c}{\tau_{mn}} = \underbrace{\frac{U_s}{I_{\text{inj}}}}_{\text{beam}} \times \underbrace{\frac{2\pi H}{\log\left(\frac{R_2}{R_1}\right)}}_{\text{length scale}} \times \underbrace{\left(b_{mn}\,\kappa_b + \frac{c_{mn}}{R_1}\kappa_s\right)}_{\text{conduct. \& B.C}} \tag{2.56}$$

The latter can by decomposed into a product of three terms. The first tells us that the charge dynamics scales with the fraction U_s/I_{inj}, that characterizes the injected beam. Thus doubling the injected intensity and the extraction potential simultaneously will lead to the same charge dynamics, with the same asymptotic dimensionless charge distribution, and thus ion transmission. The second term is merely a scale factor depending on the dimensions of the capillary. The third term regroups all the properties of the capillary, including the conductivities κ_b and κ_s, the dielectric constant ε_r and boundary conditions (B.C.) imposed to the electric field. Finally the ratio depends on the considered mode (m, n). For our capillary in the above example, we may calculate the monopole $m = 0$ and dipole term $m = 1$ for $n = N = 10$

$$m = 0: \quad \frac{\tau_c}{\tau_{0N}} = \frac{U_s}{I_{\text{inj}}} \times 0.73[\text{m}] \times \left(0.99\kappa_b + \frac{52}{[\text{m}]}\kappa_s\right) \tag{2.57}$$

$$m = 1: \quad \frac{\tau_c}{\tau_{1N}} = \frac{U_s}{I_{\text{inj}}} \times 0.73[\text{m}] \times \left(0.826\,\kappa_b + \frac{926}{[\text{m}]}\kappa_s\right) \tag{2.58}$$

where κ_s is expressed in Siemens (S), κ_b in (S/m) and the length in (m). For this particular capillary, we conclude that if $\kappa_s[S] \ll 10^{-3}\kappa_b[\text{S/m}]$, the surface conductivity does not affect the charge dynamics of both the dipole and the monopole angular distribution of the charge patch. If $\kappa_s[S] \sim 10^{-3}\kappa_b[\text{S/m}]$, then the surface conductivity does affect the dipole but still not the monopole distribution. For borosilicate glass (Pyrex), we are in the latter case, meaning that the surface conductivity affects the charge relaxation of the dipole part of the patch and thus the guiding properties of the capillary and may not be ignored in the modelling. The surface channel however affects only marginally the monopole part.

2.5 Simulations

2.5.1 Numerical model: *InCa4D*

The numerical model *InCa4D*[5] is based on the model presented in section 2.2.2. The surface charge dynamics at the inner and outer interfaces S_1 and S_2 of the capillary are evaluated using the surface continuity equations,

$$\frac{\partial \sigma_1}{\partial t} = -\kappa_b E_n^+ - \vec{\nabla}_s \cdot \left((\kappa_s + \mu \sigma_1) \vec{E}_\tau \right) + \gamma^h \quad \text{, on } S_1 \qquad (2.59)$$

$$\frac{\partial \sigma_2}{\partial t} = \kappa_b E_n^- - \vec{\nabla}_s \cdot \left((\kappa_s + \mu \sigma_2) \vec{E}_\tau \right) + \gamma_{\text{str}}^e + \gamma_{\text{int}}^e \quad \text{, on } S_2 \quad . \qquad (2.60)$$

The sources terms γ^h stands for the injected holes at the inner surface due to the ion beam and γ_{str}^e for the injected electrons at the outer surface. In our simulations, γ_{str}^e was set to zero, as the capillary holder in our setup screens the capillary from stray electrons. The entrance of the capillary is usually covered by a conducting layer and grounded. In our simulations, the conducting layer covered the first 11 mm of the outer surface S_2 [6], allowing electrons to be injected through the glass-conductor interface and neutralize the charge accumulated within the covered area. This is the only charge depletion channel we considered. The electron injection through the glass-conductor interface is described by the term $\gamma_{\text{int}}^e = -\kappa_b E_n(R_2^+) H(z_g - z)$, where H is the Heaviside step function and z_g the length of the outer conducting layer. The current density along the interface is proportional to the *enhanced* surface conductivity $\kappa_s + \mu \sigma$, while the current density through the bulk is proportional to the bulk conductivity κ_b of the capillary. The diffusion term was always ignored. The model has thus three free parameter, κ_b, κ_s and μ which need to be provided. Usually the charge mobility μ of the injected charged defects at the surface was set equal to the charge mobility of thermaly activated "labile" Na$^+$ ions in borosilicate, $\mu = 4 \times 10^{-14}$ m^2/V/s [5], if not said otherwise. For such low mobilities, contribution of excess charge carriers to the surface conductivity κ_s is negligible [7].

---

[5]Label "InCa4D" stands for "Ions through Capillaries" and the 4D stands for the 3 dimensions xyz and time.

[6]Our capillary holder has an 11 mm long cylindrical hole matching the outer diameter of about 1.5 mm of the the capillary. The capillary was inserted into that hole in order to keep it in place.

[7]The charge mobility of the injected charges at the surface is not a well know quantity. We assume that it is similar to mobility of interstitial pair defects (two alkali ions share one non-bridging oxygen anion NBO). The simulated insulators in this work are usually borosilicate (Pyrex) capillaries and the voltage of the source typically $U_s < 3$ kV. For borosilicate, a mobility of $\mu = 4 \times 10^{-14}$ m^2/V/s at room temperature was found by [5, 6]. Assuming a typical value for $\sigma_0 = \frac{\varepsilon_0 \varepsilon_r U_s}{R_2 - R_1} < 2.5 \times 10^{-4}$ C/m^2, the additional surface conductivity $\mu \sigma_0 < 10^{-17}$ S, is sufficiently

Additionally to the two glass-vacuum interfaces of the capillary, the code accounts for a third interface S_3, namely the interface of a metal cylinder surrounding the capillary. The electric potential of the latter is floating or kept at a fix potential and stands for the inner cylindrical electrode of the capacitor found in the the experimental setup, see Fig. 2.19. This way, the boundary conditions of the electric potential in the model are the same than those in the experimental setup. The dielectric constant $\epsilon_r = 4.6$ of the borosilicate glass is also taken into account by computing explicitly the polarisation charges $\tilde{\sigma}_1$ and $\tilde{\sigma}_2$ at the inner and outer glass-vacuum interfaces. The induced surface charges $\tilde{\sigma}_3$ at the metal cylinder interface are calculated using (2.30) which satisfies the appropriate boundary conditions at S_3. Finally, the divergence-free electric field is deduced from the electric potential V (2.24). Because the charges are computed only at the three interfaces, our approach is CPU cost efficient while keeping a realistic description of the charge transport in capillaries. In addition, as the boundary conditions at the 3 interfaces match the experimental ones, the numerical code is expected to reproduce with high accuracy the experimental electric field in the capillary and make reliable quantitative predictions. For example, long simulations, indented to study the radial focusing effect (typical 10^7 trajectories), as presented in this manuscript, take about 36 hours on a modern (2018) CPU core.

2.5.2 Features of the Numerical model InCa4D

The numerical code simulates the 3D classical trajectories though an insulating capillary, where the guiding electric field is computed from the time-depending surface charges at the interfaces. The code has been developed over several years while adding small incremental improvements. By 2019, the code has the following remarkable features:

1. **Transmission of neutrals:** Slow ions that hit the inner insulating surface are generally neutralized by the ejected electrons. A fraction of the scattered neutrals are transmitted through the capillary and can be detected for example by a micro channel plate (MCP) coupled to Position Sensitive Detector (PSD). The distribution of neutrals on the PSD is particularly useful for aligning the ion beam with the capillary axis, as shown in the upper panel of figure 2.9a. Indeed, when both are aligned, the distribution of neutrals yields a perfectly uniform circle on the PSD. We implemented a function in the code that follows the neutralized ions allowing to compute the energy loss of the neutrals as well as their distribution on the PSD. The function

small that the enhanced surface conductivity $\kappa_s + \mu\sigma$ is well approximated by $\kappa_s \sim 10^{-16}$ for the capillary we use
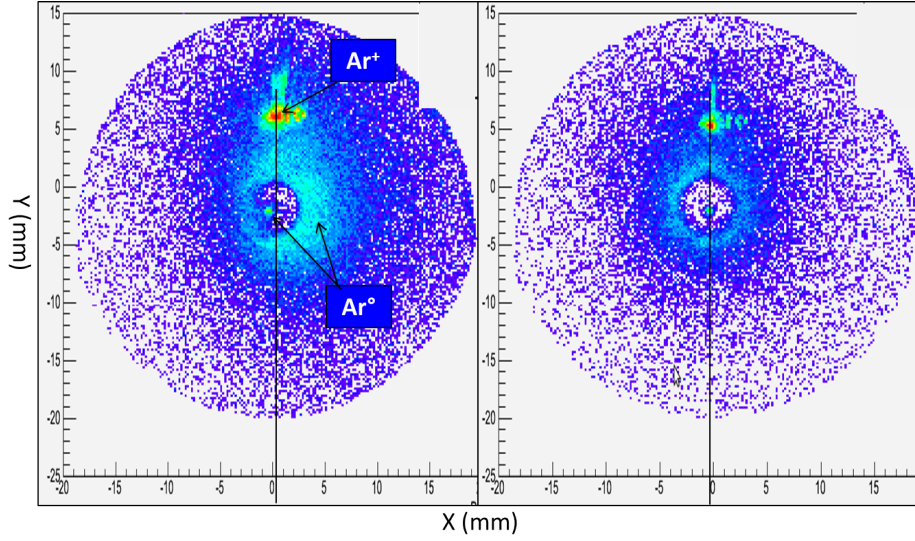
(a) Left: Ring of Ar neutrals on the PSD, 270 mm behind the capillary outlet, before fine-tuning the alignment of the capillary axis with the beam axis. Spot of neutrals is off-centered and the ring is not uniformly intense. The transmitted ions Ar^+ were deflected upwards. Right: Uniformly intense ring of neutral with centered spot after rotating the capillary by the 0.12 degree (azimuthal angle). The vertical black line shows the alignment of the ion beam spot with the neutral spot before and after fine-tuning. Beam intensity was below 100 fA and the capillary was heated to $70°$ C to avoid charge accumulaton and guiding.
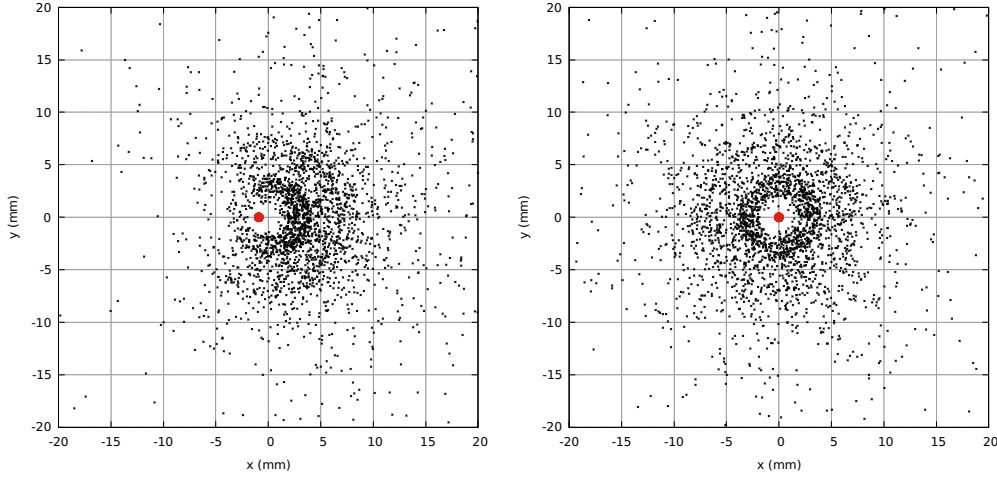
(b) Black points give the simulated distribution of transmitted neutral Ar atoms on the PSD. Red spot gives the transmitted Ar ions. Bulk conductivity was put to 10^{-11} S/m to avoid charge accumulation at the interface. In the right panel, the tilt angle is $0°$ and the ion spot lies on the origin of the PSD. The neutral distribution is a cercle, with a notable absence of neutrals for a radius of less then 2 mm, due to the tappered shape of the capillary[a]. In the left panel, the tilt angle is $-0.15°$. The distribution of neutral is no longer symmetric, with a higher intensity opposite to the tilted direction of the capillary. This property allows to align the capillary with the beam axis within an uncertainty of about $0.05°$.

---

[a] $R/H \times 270$ mm $\simeq 2$ mm, with $R = 0.4$ mm and $H = 50$ mm being the inner radius and length of the conical part of the capillary

is based on the following algorithm: At the impact point, a scattering velocity vector is chosen randomly from a data base that was generated in advance using SRIM[8]. The latter software was diverted to recorded in a file the backscattering velocity vector of a large number of impacting ions. We recorded the scattering velocities, for example in the case of 3 keV Ar atoms[9] impacting a fused quartz surface at grazing angle, but also for a 1 Mev H (or proton) colliding with a Teflon and fused quartz surface. We recorded files for grazing angles varying between 0.2° and 2°, allowing for a dependency of the backscattered velocity vectors on the impact angles. With this additional feature, we could compute the transmitted neutrals as a function of the tilt angle of the capillary. We give in the lower part of figure 2.9b the simulated distribution of transmitted neutral atoms through a conical capillary, projected on the PSD. For small tilt angles around zero, we found that usually 1 neutral Ar is transmitted for 10 ions. The nice agreement between observed and simulated distributions on the PSD, gives confidence in the chosen algorithm. It also shows that aligning the capillary using neutrals is relevant [64].

2. **Non-linear electrical conductivity:** In general, the de-trapping rate and thus the charge mobility $\mu \equiv \mu(E)$ depends on the local electric field E. As a result, the bulk conductivity $\kappa_b(E) = \rho\mu(E)$ depends on the electric field too. Same for the surface conductivity $\kappa_s \equiv \kappa_s(E)$. We implemented two models that take both into account the enhanced de-trapping rate of the charge carriers by the electric field. The first (2.8) is the thermally activated hopping model (TAHM) that is preferred for the ionic conductors and the second is the Poole-Frenkel model [1] which is preferred for electronic conduction in polymers, although it was also used for silicates [28]. Field depended non-linear conductivities have been shown crucial for explaining the guiding power of nano-capillaries [49]. Here, we limited our study to glass macrocapillaries in which case the electric field stays usually well below the critical electric field of 10 kV/mm. The latter is the typical value for which the transition from ohmic to non-ohmic conduction happens in materials like fused silica, HDPE polymer and low alkali glasses [66].

3. **Secondary electrons generated inside the capillary:** We recently added the tracking of the secondary electrons (SE) that are produced by the impaction ions at the insulating surface. Until then, electrons that were not

---

[8]SRIM - The Stopping and Range of Ions in Matter. SRIM includes quick calculations which produce tables of stopping powers, range and straggling distributions for any ion at any energy in any elemental target. We used the TRIM module to generate the backscattering velocities with the "Monolayer Collision Step/ Surface sputtering" option.

[9]The TRIM results may be less precise for ions below 10keV

captured by the ion, were assumed to fall back to the impact point. Now we propagate the emitted secondary electrons by the electric field in the capillary until they hit again the inner surface of the capillary or escape the capillary through the inlet and outlet. The emitted electrons have a cosine angular distribution and the energy follows a Poisson-like distribution peaked around 2 eV. The number of emitted electrons N_{SE} per impact is an adjustable parameter, taking integer values typically $N_{SE} \leq 3$. The CPU cost only increases marginally because usually not more than 3 electrons are propagated for a short path (typically the inner diameter of the capillary) per ion impact. In figure 2.10 we show the trajectories of SE (in blue) in a charged glass capillary. It was found that, initially, the ejected electrons are re-absorbed at the opposite side. But with increasing accumulated charge in patch, the electric field makes the ejected SE u-turn, so that the SE are re-absorbed some mm away from the original emission point. The SE channel thus contribute significantly to redistribute the accumulated charge at the interface. Mainly, the accumulated charge is smeared out by SE, resulting in a modified generated electric field and ion trajectories.
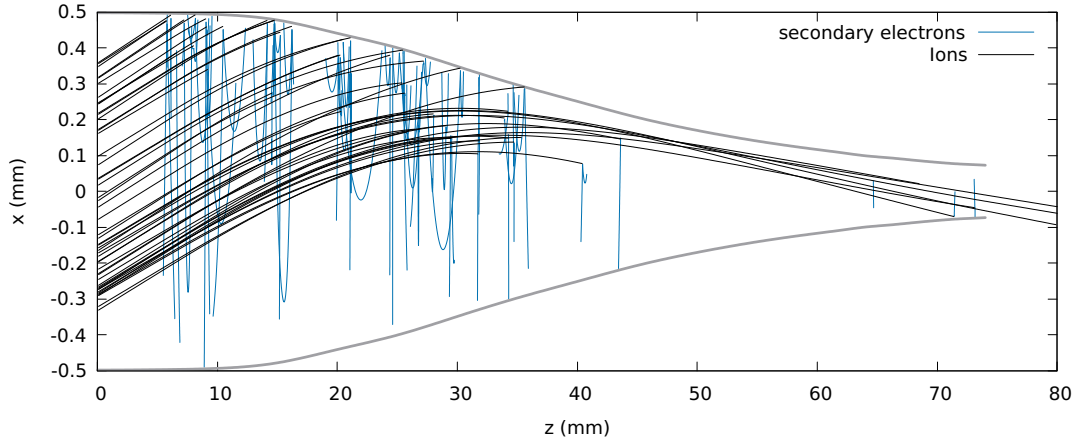
Figure 2.10: Secondary electrons (SE) emitted by impacting 2.5 keV Ar^+ ions at the insulator interface. The capillary is tilted by $1.2°$ with respect to the beam axis. The electrons are propagated via the electric field until they hit again the interface, where they are re-absorbed. Note that a large fraction of the SE fall back some mm away from the the original emission point, contributing to smear out the accumulated charge at the interface.

4. **S_3 interface electrode:** The potential of the cylindrical interface S_3 surrounding the capillary can kept floating or fixed to an arbitrary potential V_3 (see section 2.2.4). When kept for example grounded $V_3 = 0$, the electrode

can play the role of the cylindrically symmetric capillary holder. When kept floating but neutral (no accumulated charge) the electrode can measure by influence the charge stored in the capillary. The latter feature will be discussed in the following section. In the case where the potential is fixed to a non-zero value, the S_3 electrode can be used to simulated the behaviour of an Einzel lens, as was discussed in our collaboration with Ikeda Tokido. Here, the entrance and the exit of a conical insulating capillary are painted by a conducting paint and grounded (black layer in Fig. 2.11). The S_3 conical interface (red layer) was connected to a signal generator and a time-tependent potential V_{bc} was imposed. An Ar^+ ion beam, extracted by a potential $V_s = 2.5$ keV, was injected into the capillary. By increasing V_{bc} from $V_{\mathrm{bc}}/V_s = 0$ to 0.6, the focusing point of the ion beam was brought from infinity to the outlet of the capillary. At that point, the transmitted fraction was maximal. For an even larger ratio $V_{\mathrm{bc}}/V_s = 0.8$, the focusing point was located inside the capillary, reducing the transmitted fraction. We concluded that with this electrode configuration, the capillary setup behaves like an Einzel lens and is able to focus the injected beam. However it is crucial that the electrode setup has axisymmetry in order to avoid the appearance of dipole moments in the electric field, that would otherwise deflect the beam into the capillary wall. Note that the focusing of the injected beam by the electrode S_3 is to be distinguished from the self-organized radial focusing described in section 2.6.2.

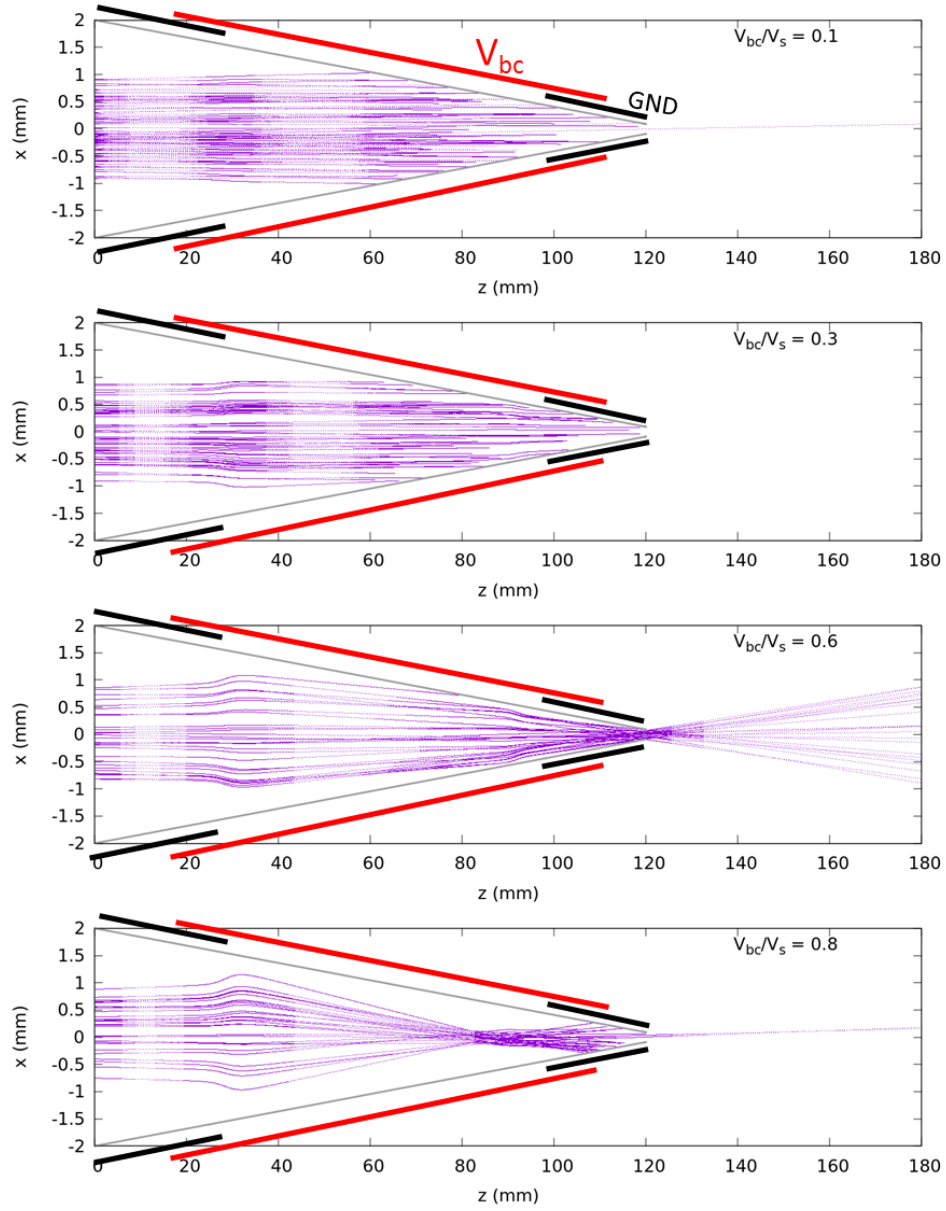Figure 2.11: The S_3 conducting interface (full red line) is connected to an external time dependent potential V_{bc}. The outer capillary surface is grounded near the entrance and near the outlet (black full lines). The inner surface (thin gray line) is the insulating glass-vacuum interface. The electrodes generate a field inside the capillary that focuses the trajectories like an Einzel lens

129

2.6 Most significant simulated results

We will present in this section merely the three most significant results obtained with our InCa4D code. The first one explains why the transmitted intensity increases when the capillary glass tube is tilted with respect to the beam axis. The second one shows that it is possible to focus an injected ion beam through a tapered glass capillary, similar to an Einzel lens. The third shows the influence of secondary electrons (SE) on the guiding power in cylindrical glass capillaries.

2.6.1 Transverse self-organized focusing

The mechanism

One has to distinguish between two mechanisms responsible for the enhanced transmitted current density. They differ by the symmetry of the accumulated charged distribution in the capillary wall. The first is due to a *non* axis symmetric charge deposition. For example, an injected ion beam, tilted with respect to the symmetry axis of the capillary, creates one or more local charge patches that guide the ions. The patches generate an electric field, which is stronger the closer it is to the charge patches. As a result, trajectories close to the charge patches are more deviated than trajectories farther away, resulting into a compression of the beam in one dimension. This compression mechanism is illustrated in Fig.2.12. The injected current is 30 pA. After only 300 pC have been stored at the inner capillary surface, the transmitted beam is compressed by a factor $j_{\text{out}}/j_{\text{in}} \simeq 4$ by the x-component of the electric field, as highlighted by the two red transmitted trajectories. The beam compression takes place rather quickly after beam injection (see inset of Fig.2.12), as *transverse* fields become efficient to deflect the beam after only a relatively small amount of charge has been accumulated in those patches. Indeed, in our simulation (Fig.2.12), the beam compression takes place for a potential inside the capillary as low as 14 V, which is well below the extraction potential of the ion source of 3 kV. In the following, we refer to this mechanism as the transverse field compression. Compression of an ion beam, injected into a straight capillary tilted with respect to the beam axis, was already noted by N. Stolterfoht in 2013 [48, 49], but not further analysed. A detailed discussion of the transverse focusing/compression is given in [64]. A nice example of transverse focusing is illustrated in Fig. 2.16 where a tilted beam is compressed in one direction due to sequential reflection by multiple charge patches in a straight capillary.

Explaining experimental results

The transverse self-organized focusing effect explains the enhancement of the transmitted intensity for non-zero tilt angles in the experimental data shown by Gruber
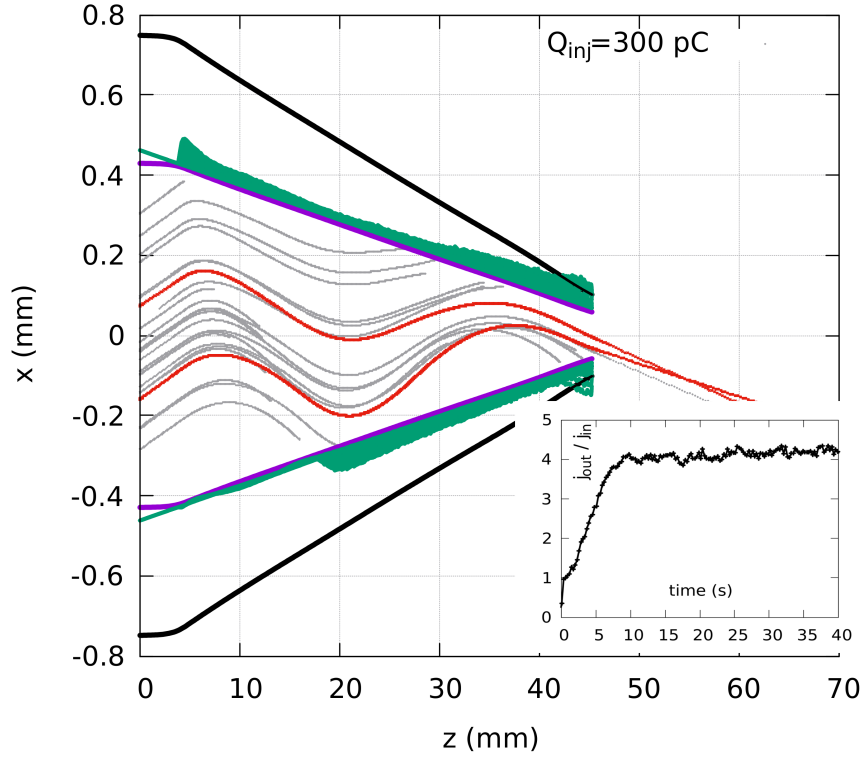
Figure 2.12: Illustration of the transverse field compression of an injected ion beam by non axis symmetric deposited charge patches in a tapered capillary of large aspect ratio: Full violet curve stands for the inner surface of an insulating capillary, black curve for its outer metallized and grounded surface. The green areas (darkk gray) give the accumulated charge at opposite sides at the inner surface in arbitrary units. Gray curves represent simulated trajectories of an Ar^+ beam at 3 keV and tilted by $0.8°$ with respect to the capillary axis. The inset shows the time-evolution of the transmitted current density j_{out} normalized with respect to the injected current density j_{in}.

et al. for tapered (conical) glass capillaries [51]. N. Stolterfoht *et al.* [53] succeeded to simulate the trend observed in [51], but gave no further convincing explanation as to why there was an enhancement. Note that an enhancement of the transmitted fraction for non-zero tilt angles can only be observed for tapered capillaries, which is coroborated by the data in [43] for a strait capillary.

During his visit in CIMAP, H. Zhang of the School of Nuclear Science and Technology, Lanzhou, China, repeated the measurements of the transmission of an ion beam through tapered capillaries as a function of the tilt angle. Injecting an Ar^+ at 3 keV into a tapered borosilicate glass capillary at room temperature, he found that at $0.75°$ tilt angle, the transmission was maximal and about twice
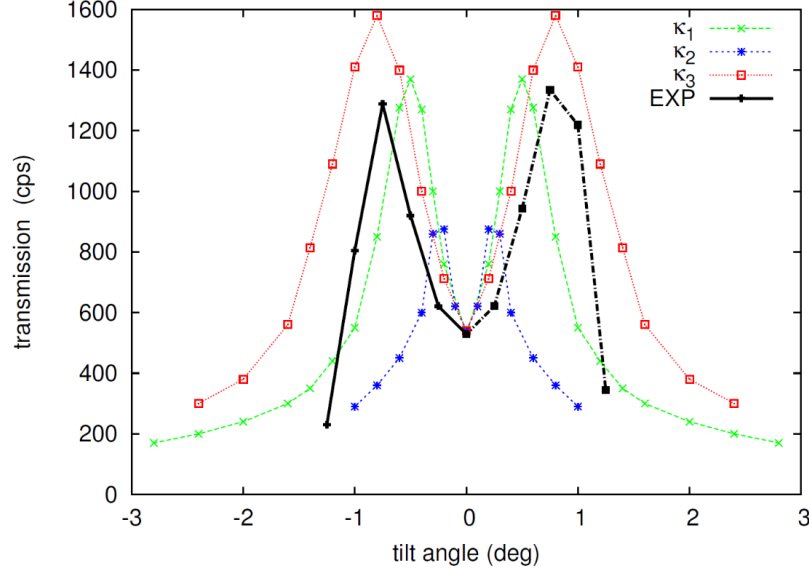
Figure 2.13: Transmission of a 3 keV Ar$^+$ ion beam of $I_{inj} = 0.5$ pA through a conical glass capillary with outer grounded surface as a function of tilt angle. The black points are experimental data. The blue stars, the green crosses and read boxes are simulations with respectively $\kappa_1 = 10^{-14}$ S/cm, $\kappa_2 = 3 \times 10^{-14}$ S/cm and $\kappa_3 = 5 \times 10^{-15}$ S/cm

as high as when the beam was aligned with the capillary axis (zero tilt angle). The observed results are reported in Fig. 2.13 (black points). Our simulations confirmed the result that a maximal transmitted fraction is obtained for non-zero tilt angle. They also confirmed the trend that the angle, for which the maximum transmission is observed, is shifted towards lower angles with increasing bulk conductivity, as was observed in [51]. On the other hand, the highest value of the transmission increases with decreasing conductivity, because more charge patches are formed in the capillary, multiplying the deflections and thus the transverse focusing.

2.6.2 Radial self organized Focusing

The other focusing mechanism is due to an axisymmetric charge accumulation, generating an axisymmetric potential in the capillary, which focuses the injected beam through the capillary outlet. The beam is compressed by the radial component of the electric field, similar to an electrostatic Einzel lens. We found in a preliminary numerical investigation, presented in [67], that the potential has to approach 70% of the extraction potential of the ion source in order to focus the

injected beam through the outlet of an insulating conical shaped capillary. The radial focusing and the transverse compression differ thus not only by the symmetry of the charge accumulation in the capillary wall, but also on the value of the self organized potential which is needed to became efficient. Summarizing: for radial focusing to be observable, two conditions must be fulfilled. The potential inside the capillary must (i) approach at least 70% of the extraction potential of the injected ions and (ii) have axial symmetry. In the following, we refer to this mechanism as the radial self-organized focusing.

The self-organized focusing power of a tapered glass capillaries is shown in Fig. 2.14. The injected Ar^+ ions have an intensity of $I_{in} = 210$ fA and the beam is aligned with the capillary's symmetry axis (zero tilt angle). The initial phase-space distribution of the injected ions are chosen such as to match the experimental divergence and emittance of the beam used in section 2.8.2 and measured in Fig. 2.22, namely a divergence of $0.1°$ half opening angle and a rms emittance of about 0.1 mm.mrad. The simulations were performed using a bulk conductivity of 1.8×10^{-13} S/m and a surface conductivity of 2.6×10^{-17} S. The snapshots give the trajectories of the injected ions for different amounts of charge stored in the capillary. Below each snapshot we show the corresponding potential at the inner surface. For the initially discharged capillary, only 5.3% of the injected ions are transmitted, corresponding to the geometrical transmission, corrected by the divergence of the beam. Most ions hit the inner surface and charge the capillary inner wall. With increasing charge stored in the capillary, $Q = 900$ pC, the trajectories are slightly focused by the electric potential in the capillary and the transmission doubles to 10%. The potential U in the capillary attains, at his highest value, already 1100 V, which corresponds roughly to half of the extraction potential $U_s = 2300$ V of the ion source. Once about $Q = 1600$ pC are stored in the capillary, the electric potential inside the capillary is strong enough to focus the beam at the outlet. The transmission fraction I_{out}/I_{in} reaches a maximum of 60% (which corresponds to a focusing factor of 11), resulting in a transmitted maximum current I_{out}^{max} of 124 fA. The latter is obtained for a potential U inside the capillary of about $0.75 \times U_s = 1725$ V at its apex. Without surprise, the potential has its maximum where most of the charges are deposited, in the region where the inner diameter of the capillary equals the diameter of the inlet aperture. From the relation $\vec{\nabla} \cdot \vec{E} = 0$, it results that the focusing radial field E_r is strong there, where the negative curvature (second derivative) of the potential along the z-axis is large,

$$E_r(R(z), z) = \frac{1}{R(z)} \int_0^{R(z)} r \frac{\partial^2 V}{\partial z^2} dr \quad . \qquad (2.61)$$

In the middle panel of Fig. 2.14, the maximum of the focusing radial field is thus located around $z = 30$ mm. The accumulated charges in the capillary is

depleted at a rate dominated by the bulk conductivity, $\tau^{-1} \simeq \frac{\kappa_b}{\varepsilon_0 \varepsilon_r}$ yielding a charge relaxation rate τ^{-1} of 4.4 mHz (2.47) for the monopole mode, which is the only non-zero mode. Now, the ratio, injected current over relaxation rate, I_{in}/τ^{-1},
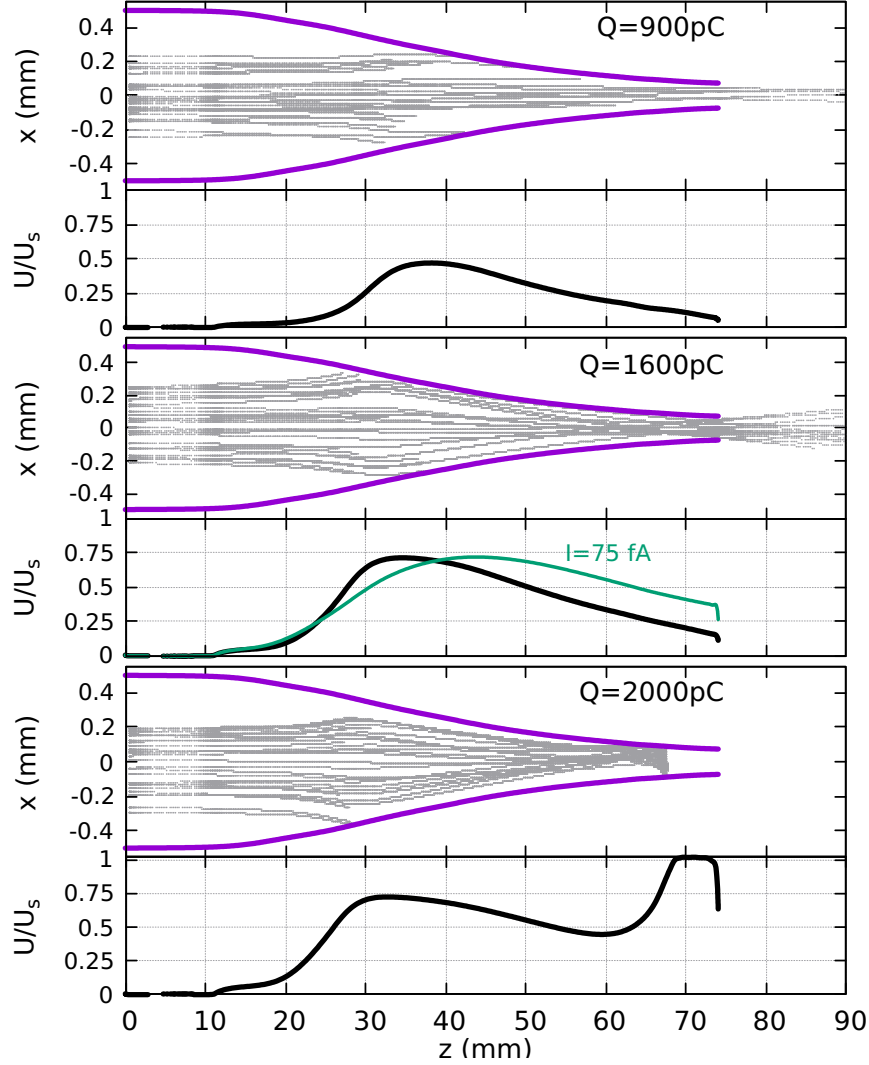
Figure 2.14: *Each snapshot, identified by the amount of charge Q stored in the capillary wall, is divided into two panels. The upper panel shows the ion trajectories (gray lines) through the capillary. The radius R(z) of the inner surface of the capillary is represented by a violet (dark grey) full line. The lower panel show the Coulomb potential U(z) at the inner capillary surface. The potential U(z) is normalized with respect to the extraction potential $U_s = 2300V$ of the ions source. The green curve (labelled I = 75 fA), obtained for an injected current of 75 fA, has been added for comparison. For all the other curves, the injected current was 210 fA.*

134

directly controls the steepness of the self-organized potential along the z-axis and thus its curvatures. The higher the value of $I_{in}\tau$, the steeper the variation of the potential along the z-axis and consequently the stronger its focusing power. This trend is illustrated by the flatter but not necessarily lower green curve, which is obtained for an injected current of only 75 fA and yields a transmission factor of barely 24%. The trend will be discussed more in details in the text section. Note that the capillary behaves similar to an Einzel lens, where the focal point is moved from infinity towards the outlet of the lens with increasing potential of the central electrode and with decreasing distance between the central and outer grounded electrodes [16].

The charge depletion rate τ_{leak}^{-1} is the rate at which the capillary evacuates the accumulated charge and is not to be confused with the charge relaxation rate τ^{-1} defined in the paragraph above. The charge depletion rate τ_{leak}^{-1} was simulated in section 2.8.1. With our particular setup and capillary, we found a depletion rate of $\tau_{leak}^{-1} = 0.01$ mHz for the given conductivities. At maximum transmission ($Q = 1600$ pC), the leakage current is estimated to be about $Q/\tau_{leak} \simeq 16$ fA. The deposited charge per time unit, $I_{in} - I_{out} = 85$ fA, still dominates the leakage current and the capillary continues to charge. As a result, the focusing distance continues to shorten and the focusing point enters the capillary tip. Part of the trajectories emerging from the focus point inside the capillary are now intercepted by the capillary walls and the potential rises quickly near the outlet. If the potential inside the capillary exceeds the potential of the ion source, the transmission blocks. In the lower panel of Fig.2.14 ($Q = 2000$ pC), the potential at the last 5 mm exceeds the source potential U_s of 2300 V and the ions u-turn at this point. This Coulomb blocking is inevitable, except of course if the deposited current is balanced by the leakage current before the potential in the capillary exceeds the source potential. Only then, can a stable transmission be expected. Nevertheless, this theoretical study clearly shows that insulating tapered capillaries can be used to focus a low energetic ion beam.

Short tapered capillaries are another class of capillaries for which focusing was observed experimentally, as was reported by Chen *et al.* [45]. They observed that the transmitted fraction of a 90 keV O^{6+} ion beam was enhanced by a factor 4 with respect to the geometrical transmission in a tapered glass capillary that was only 14 mm long (see profile of the capillary in Fig. 2.15). Our simulation confirm that even such capillaries, having an extremely short tapered part, allow radial focusing as is shown by the blue trajectories in Fig. 2.15. Our simulations predicted that the transmitted fraction increases from the initially 10% to 35%, which is close to the 40% observed in [45]. This is a promising result as it shows that focusing can also been observed in short tapered capillaries which are not near conical, opening self-organized radial focusing to a new class of macro-capillaries.
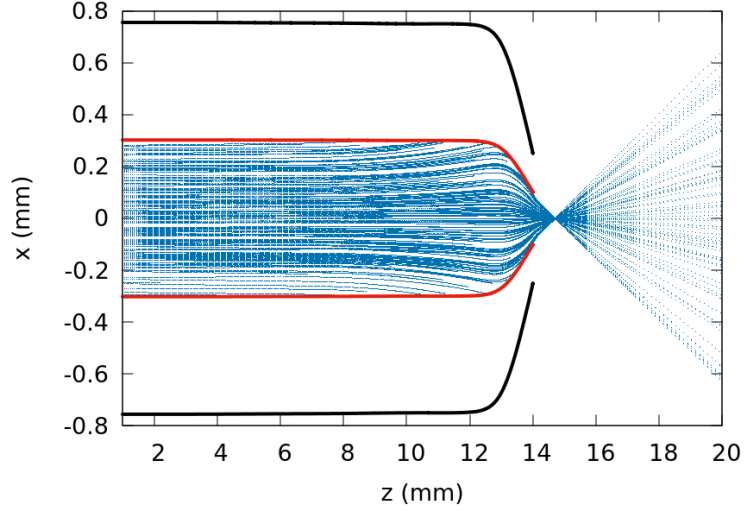
Figure 2.15: Simulated trajectorioes of 90 keV O^{6+} ions showing radial focusing through the short glass capillary similar to that used in [45]. The red and the black curve give the profile of the inner and outer interface of the capillary. In our simulations, the outer surface was grounded.

Recently, Maurya *et al.* [65] measured self-focusing in high current density ion beam transport through 7.5 mm short insulating glass capillaries having an outlet diameter ranging from 200 to 20 μm. For the 20 μ they found a focusing factor of more than 1000. Those studies indicate that focusing of beam ions by short tapered capillaries is seen as a promising tool for the producing of micro- and nano-beams.

2.6.3 Influence of Secondary Electrons on high intensity beam transmission

In an experimental study presented in [69], it was shown that a 1 keV Ar^+ beam, tilted by 5° deg, was transmitted through a cylindrical glass capillary for injected intensities as high as 50 pA. The borosilicate glass ($\varepsilon_r = 4.6$) capillary used in the experiment was $H = 43$ mm long, with an inner radius of $R_1 = 0.29$ mm and outer radius of $R_2 = 2.75$ mm. The outer surface of the capillary was grounded. We performed simulations for a capillary having the exact above dimensions and properties. In the simulation, the initial positions and velocities of the Ar^+ ions are sampled such as to produce a spatially uniform beam with a divergence of 0.15° half opening angle and a root mean square (rms) emittance of 0.3 mm.mrad, so as to reproduce the estimated experimental beam parameters. At that time,

Figure 2.16: Ion trajectories through straight capillary tilted by 5° with respect to the ion beam axis after 480 pC have be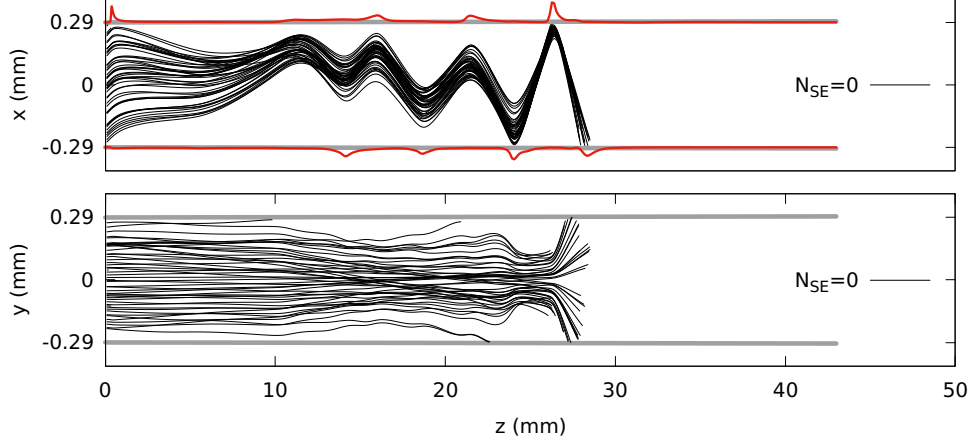en injected by a 12 pA, 1 keV Ar⁺ ion beam. Top : projection on the xOz plane; bottom : projection on the yOz plane. Note the compression of the current density in the x direction. After 40 s of beam time, the injected beam is deflected multiple times by at least 7 charge patches (illustrated by the red curve) but without escaping the capillary. The SE channel was inactivated, $N_{SE} = 0$.

our numerical code did not track the secondary electron that are emitted when an Ar⁺ projectile hits the inner insulating surface of the capillary. We naively thought that its influence would be negligible anyway. So, this former version of *InCa4D* had two free parameters[10], namely the bulk and surface conductivities. We took for the bulk conductivity of borosilicate at room temperature the typical value of $\kappa_b = 1.5 \times 10^{-13}$ S/m. The surface conductivity in borosilicate is not a well-known quantity and depends strongly on adsorbed impurities. At room temperature and in vacuum, it is typically less than $\kappa_s < 10^{-15}$ S. Experimentally, it was found that ion beams having an intensity as low as 0.28 pA, had a transmitted fraction of about 1%. We found from our simulations, by varying the surface conductivity, that κ_s must be smaller than 5×10^{-16} S if a 1% transmission should be observed for $I_{\text{inj}} = 0.28$ pA. Indeed, if $\kappa_s > 5 \times 10^{-16}$, no transmission is observed in our simulations. Simulations also showed that taking $\kappa_s = 3 \times 10^{-16}$ S, yields a transmission fraction of about 5%, which is too high compared to the observed one. Thus we deduce from our simulation that $3 \times 10^{-16} < \kappa_s < 5 \times 10^{-16}$ S. Consequently, we used $\kappa_s = 5 \times 10^{-16}$ S, which is in approximate agreement with the measured surface conductivities of Pyrex borosilicate glass [43]. We simulated the time-evolution of the transmitted beam fraction for I_{inj} ranging from 0.28 to 50 pA. With the secondary electron production, ($N_{\text{SE}} = 0$) ignored, no stable

---

[10]The charge mobility of the injected charge carriers are set to $\mu = 4 \times 10^{-14}$ m²/V/s

transmission could be simulated for beam intensities $I_{\text{inj}} > 8$ pA. For example, we found that up to 8 patches are formed inside the capillary by a 12-pA beam (see Fig. 2.16), which results in a fluctuating transmission (see green curve labeled $N_{\text{SE}} = 0$ in figure 2.17). The latter finally stops because, with increasing Coulomb potential in the capillary, deflections are so strong that the beam is stuck in the capillary. The simulated results however conflicts with the experimental data shown in Fig. 7 of [69], where a stable transmitted fraction, for $I_{\text{inj}} = 12$ pA, is observed for at least 500 s
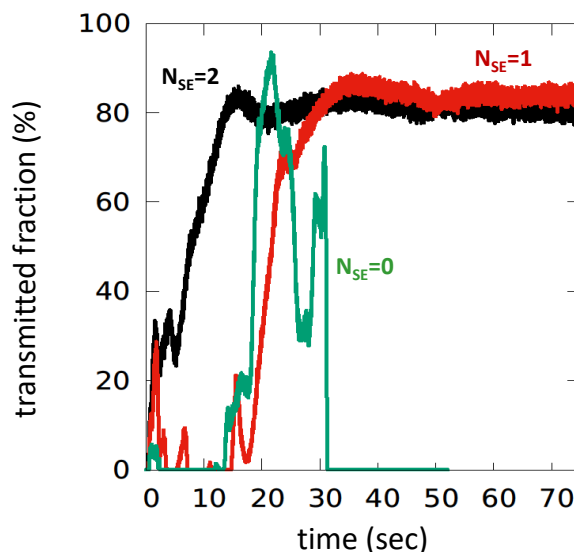
Figure 2.17: *Simulated transmitted fraction of a 12 pA, 1 keV Ar^+ beam through the 5° tilted capillary tube as a function of time. The green curve stands for the simulation without secondary electrons ($N_{SE} = 0$). The red and black curves stand for the simulations with respectively 1 and 2 secondary electrons emitted per ion impact.*

To address this conflict, we updated our numerical model to track secondary electrons (SE) generated by ion impacts at the inner surface, see section 3 for more details. We expected the SE emission to smear out the charge patches and possibly avoid blocking of the transmission at higher intensities. Most SE were found to fall back to the surface some hundreds of µm away from the point they were emitted, see Fig. 2.18. This helped indeed to redistribute the charge of the injected patch in a way that weakens the deflecting force of the patch, giving rise to a lower number of patches (~ 4) and eventually to a stable transmission as seen in Fig. 2.17. The case $N_{\text{SE}} = 2$, gave the best agreement with our experimental data. Based on the measurments of SE yields for low energetic He^+ and Ar^+ projectiles

on SiO_2 films by [18], we estimate that $N_{SE} = 2$ is a reasonable value for the SE yield in the case of grazing 1 keV Ar^+ ions on borosilicate glass capillary. And indeed, with $N_{SE} = 2$, we were able to simulate a stable transmission for injected current ranging from 0.26 to 50 pA.
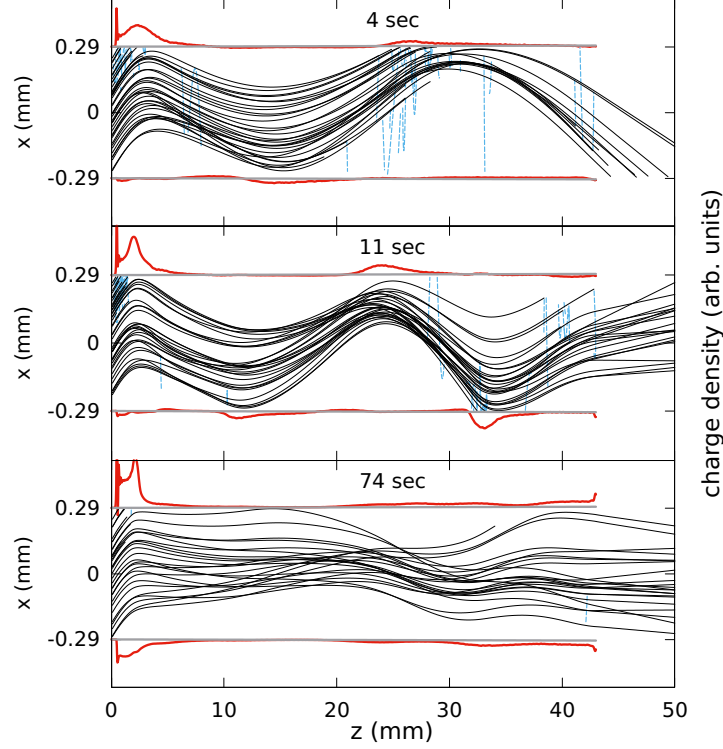
Figure 2.18: Snapshots of Ar^+ trajectories (black lines), projected on the x-axis, through the glass capillary at 4, 11 and 74 seconds after the beam is injected. The injected intensity was 12 pA and beam was tilted by $5°$ with respect to the capillary axis. The horizontal black lines at $x = \pm0.29$ mm show the inner capillary surfaces. Above and below the surface lines, the red curves show the intensity (arbitrary units) of the positive charge patches at the inner surfaces. Note that for $t = 74$ seconds, the amount of charge on the lower surface at the entrance is due to surface charge relaxation along the angular direction. The blue dashed lines are the trajectories of secondary electrons emitted from the impact point. Here we used $N_{SE} = 2$.

Figure 2.18 shows snapshots of the charge distribution and trajectories at various times for a 12 pA injected beam. The simulation shows that a few seconds after beam injection, (upper panel of Fig. 2.18) three charge patches have formed, two on the upper surface and one on the lower surface. The electric fields from these patches are sufficient to deflect the incoming beam and already a transmitted

fraction of 30% through the entire capillary is observed. There is also an indication that an additional charge patch will soon be formed on the lower surface near the exit of the capillary. The middle panel shows that at a later time (11 seconds) the "guiding electric fields" have caused the beam to interact closer the capillary entrance, thus producing a new charge patch further downstream. Now, about 60% of the injected beam is transmitted. After additional time, (bottom panel) except for the charge patch closer to the capillary entrance, the previously formed patches are now weaker while a fairly uniform charge layer has formed along the last quarter of the capillary. This leads to a significant portion (80%) of the injected beam being transmitted. The simulations provide new valuable insight into the guiding process, since they also model and track the redistribution of the charge deposited on the capillary surface. This redistribution is seen by the intensities opposite the charge patches formed where the beam impacts the surface. For example, in the upper panel of figure 2.18, the beam interacts with the upper surface at horizontal positions of approximately 2 and 30 mm and with the lower surface at 15 mm. However, in the last panel of Fig. 2.18, our simulations show that some of the charge patch produced on the upper or lower surface during the first few seconds has moved along the circumference with the result being less intense patches of charge on the opposite surface at the same horizontal distances. This redistribution of charge is most obvious near the capillary entrance. Thus, our simulations imply that a portion of the deposited (or created) charge rather quickly moves away from its original location with much of it moving to the opposite side. This weakens the electric field precisely in the regions which contribute to the guiding process. The combined theoretical and experimental study put into evidence that SE must be taken into account for the description of the guiding power of insulating capillaries. Without the SE channel, simulations cannot reproduce accurately the experimental results.

2.7   Experimental Setup

We designed a new capillary holder with the aim to put into evidence the radial focusing of the injected beam by a conical capillary and to perform precise measurements of the charge relaxation in capillaries. From the simulations (Fig 2.14), it became clear that the total charge in the capillary must approach 1600 pC in order to expect focusing. It is thus crucial that the charged capillary is well screened from stray electrons which would otherwise neutralize the capillary, as was demonstrated in Giglio *et al.* [62]. Simulations also suggested that the emittance of the beam must be low enough so that a major part of the injected beam can be focused to a diameter lower or equal to the diameter of the capillary's outlet. Also, in order to evaluate precisely the transmitted fraction I_{out}/I_{inj}, we

need to know accurately the injected intensity I_{inj}. Finally, the electric field in the capillary must have axial symmetry for focusing to be observable. The capillary holder should thus have the following features:

- Measure the charge stored in the capillary as a function of time.

- Measure the intensity of the injected beam.

- Measure the emittance of the injected beam.

- Screen the capillary from stray electrons.

- Allow heating the capillary up to 70°C on demand for faster discharge.

- Ensure axial symmetry around the capillary allowing for radial focusing.

- Allow alignment of the beam axis with the capillary symmetry axis.
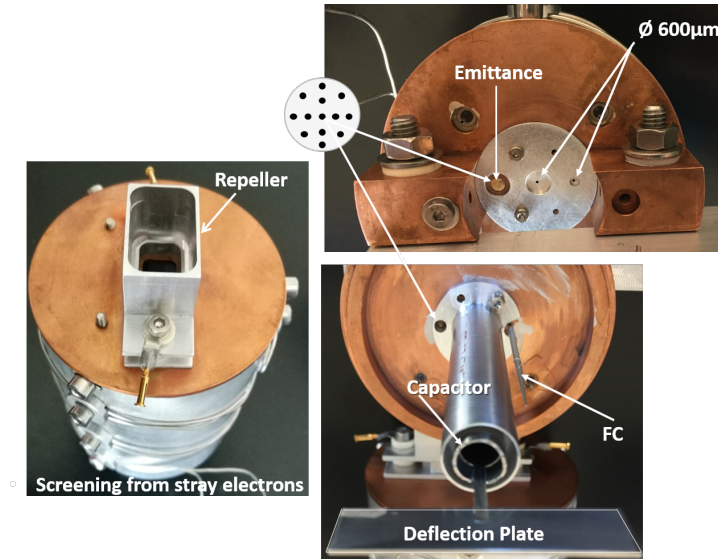
Figure 2.19: Left: cylindrical box with "repeller". Top: front of the box with 3 inlets for the ion beam. Bottom: Inside the box showing the Faraday-Cup (FC), Capacitor surrounding the capillary (not visible) and deflection plate.

In order to monitor the time-evolution of the total electric charge stored in the capillary, the capillary is surrounded by a cylindrical capacitor (Fig. 2.19 and Fig. 2.20). The latter imposes axisymmetric boundary conditions to the electric potential, as required. The inner cylinder of the capacitor is electrically connected to the upper plate facing a grounded plate. The outer cylinder of the capacitor

is grounded. In this configuration, the capacity of the inner cylinder is $C = 13 \pm 0.2$ pF. Due to total influence, the potential V of the floating inner cylinder of the capacitor and upper plate rises with the charge stored in the capillary, $V = Q/C$. An electric field builds up between the two plates with increasing potential V, deflecting the transmitted beam that passes through the plates. For low angles, the deflection ΔY, measured on a position sensitive detector (PSD) located 270 mm downstream, is thus proportional to the charge stored in the capillary. The proportionality factor is deduced from calibration measurements and is equal to 88 ± 3 pC/mm for this setup. The whole acts as a perfect Coulomb-meter. Assuming an initially neutral capillary, the charge stored in the capillary is eventually given by $Q[\text{pC}] = 88 \times \Delta Y[\text{mm}]$. Monitoring the accumulated charge in the capillary allows to indicate if and when an equilibrium has been reached for which the leakage current balances the deposited current such that the charge stored in the capillary is stationary. It also indicates if and when the charge stored in the capillary approaches the critical charge for which the capillary focuses efficiently the beam through the outlet. Last but not least, it tells if a blocking of the transmission is due to Coulomb-blocking or due to a charge patch that deviates the beam into the capillary walls.
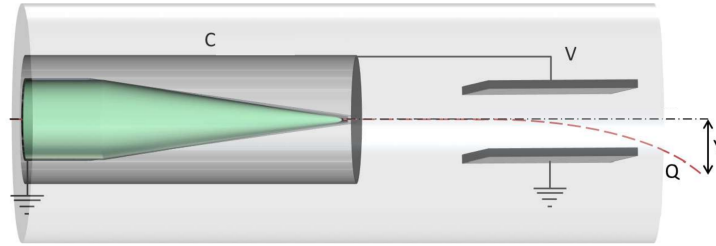
Figure 2.20: *A tapered glass capillary (green surface) is surrounded by a cylindrical capacitor C, which is electrically connected to the upper plate of a pair of deflection plates. The lower deflection plate is grounded. Due to total influence, the potential $V = Q/C$ of the upper plate rises with the charge Q in the capillary. The transmitted beam is deflected by the electric field between the plates and the deflection Y monitored on a position sensitive detector. The whole is inserted in a grounded metal box that screens the capillary and deflection plates from stray electrons. The entrance of the capillary is grounded (generally behind a grounded collimator having a slightly lower diameter than the capillary to avoid the charge up of the entrance).*

Particular attention has been paid to screen the capillary, capacitor and the deflection plates from stray electrons. The latter would otherwise be attracted by the positive potential of the capillary and limit the rise of the potential in the
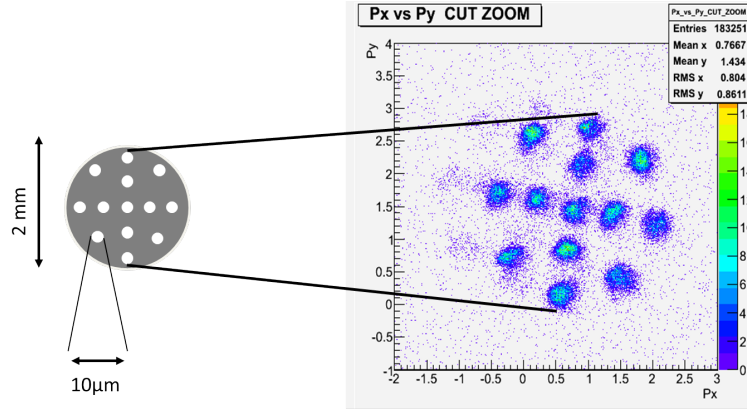
Figure 2.21: With a Focused Ion Beam (FIB) a grid of $\varnothing = 10\,\mu m$ holes were "digged" into a $\varnothing = 2mm$ inox disc having a thickness of 14 μm. The disc was placed in the left inlet of the holder. The injected beam produced on the PSD located 270 mm downstream a grid figure from which we can deduce the divergence of the injected beam and its rms emittance. Here, the divergence has a half-opening angle of $0.1°$ deg and a rms emittance of 0.1 mm.mrad.

capillary [62]. The capillary, capacitor and the deflection plates are therefore put into a larger grounded cylindrical box that screens them from outer stray electrons (Fig. 2.19). The cylindrical metal box has three circular inlet holes, one for the capillary (located on the symmetry axis), one for the Faraday cup (1 cm right) and one with a grid pattern (1 cm left) that together with the PSD allows measuring the emittance of the beam. It has also a 30×10 mm^2 large outlet to let pass the transmitted beam. Behind the outlet, we added a grid-less negatively biased electrode "repeller", to avoid that low energetic stray electrons can enter the box. The holder can be heated by a THERMOCOAX cable in order to increase the conductivity of the capillary, for example, to speed up the discharge of capillaries. The temperature is monitored inside the box by a thermocouple attached to the capacitor surrounding the capillary. The holder is mounted on a high precision rotatable and translational plate, allowing for an alignment of the capillary axis with the beam axis by less than $0.05°$, by adjusting the elevation and azimuthal angles. Upstream, the beam is collimated by a plate with a 2 mm hole. The plate is connected to an ammeter and the intensity recorded, allowing in the later analysis to account for the fluctuation of the intensity of the source.
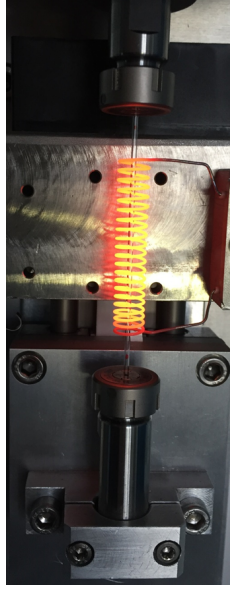
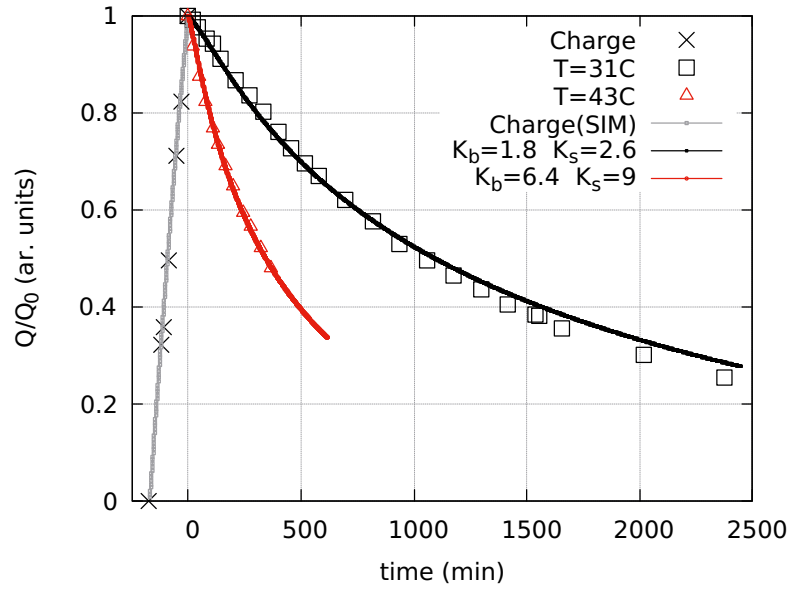Figure 2.22: Photo of the home-made capillary puller

Figure 2.23: Comparison between the experimental and simulated charge-discharge curve of our capillary for two different temperatures, as indicated in the legend. The bulk and surface conductivity which were used in the simulations are given.

144

2.8 Remarkable experimental results

2.8.1 Depletion (discharge) rate

We want to determine the surface and bulk conductivity of a borosilicate (®Pyrex 7740) glass capillary we used in our experiments. Our capillary is home-made by pulling a locally heated borosilicate glass tube (Fig 2.21). Much attention was paid to get a axis symmetric straight capillary so as to ensure an axis symmetric charge deposition at zero tilt angle [11]. The profile of the tapered capillary is given by the pink curve in Fig.2.14. Once mounted in the holder, only the 11 first mm of the outer surface of the capillary were grounded. As our setup allows measuring the accumulated charge as a function of time, we performed charge-discharge measurements of our capillary at different temperatures. In a first step, the capillary is charged by a 2.3 keV 0.1 pA-beam until a charge Q_0 of $\sim$ 1.5 nC has been accumulated in the capillary. Then, the holder is shifted by 1 cm, so as to present a 20µm hole to the beam. The transmitted beam passes through the deflector plates and monitors, via the ΔY deflection, the charge stored in the capillary. This way, we follow the discharge of the capillary in time. In Fig. 2.23, we show the observed charge-discharge curves for T =31° and 43° C. With this particular setup, an experimental depletion (leakage) rate of about $\tau_{\text{leak}}^{-1} \simeq 0.01$ mHz was found for T =31° C. For a higher temperature T =43° C, we found $\tau_{\text{leak}}^{-1} \simeq$ 0.03 mHz. We want to emphasize that the observed depletion rates[12] depend on the capacity C of the cylindrical capacitor that surrounds the capillary and are thus setup dependent. In our setup, we had $C = 13 \pm 0.2$ pF. The charge-discharge curves were simulated with our code and compared to the experimental data. To ensure a one to one comparison between the simulations and the experiments, a cylindrical electrode of 13 pF, and with floating potential, surrounded also the capillary in the simulations. Simulations with a surface conductivity $\kappa_s = 2.6 \times 10^{-17}$ S and bulk conductivity $\kappa_b = 1.8 \times 10^{-15}$ S/cm, in agreement with the measurements in [43], were found to reproduce the experimental discharge curve for T =31° C. In the case of T =43° C, an agreement was found for $\kappa_s = 9 \times 10^{-17}$ S and bulk conductivity $\kappa_b = 6.4 \times 10^{-15}$ S/cm. The depletion rate is a function of the surface and bulk conductivity, $\tau_{\text{leak}}^{-1} = f(\kappa_b, \kappa_s)$. For an experimental discharge curve at given temperature, we found that several couples (κ_b, κ_s) yield simulated discharge curves that fit all nicely with the experimental data. In figure 2.24 we

---

[11]Analyzing the shape of our pulled capillaries, we noticed that the symmetry axis of the tapered part of the pulled capillary was systematically rotated by a small arbitrary angle < 0.3 deg with respect to the symmetry axis of cylindrical part of the capillary. After fine tuning the capillary puller, we succeeded in forming a capillary whose tapered part deviated by less than 0.1 deg.

[12]They are not to be mistaken with the charge relaxation rates defined by (2.47).
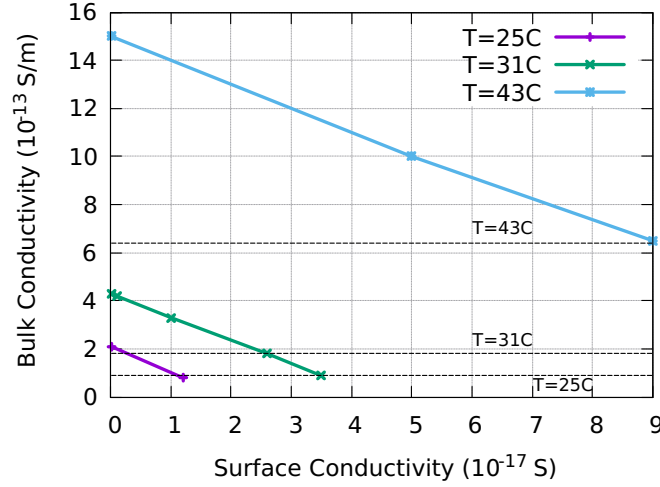
Figure 2.24: For the three indicated temperature, the set of (κ_b, κ_s) that give a good agreement with the measured discharge rates are plotted in the graph. The black dashed lines indicates the bulk conductivity of Pyrex at given temperatures.

give for $T = 25°$ C, $T = 31°$ C and $T = 43°$ C the couples of (κ_b, κ_s) that yield discharge curves that are in agreement with the respective observed data. For each temperature, the solutions lay on a line, as could be expected by analogy from (2.47). The horizontal black dashed lines in Fig.2.24 give the value of κ_b of Pyrex for the three indicated temperatures, as provided by the manufacturer[13]. From the intersection of the dashed line with the simulated data for each respective temperature, we deduce a non-zero surface conductivity that agrees well with the measured surface conductivity in [43]. On the other hand, taking $\kappa_s = 0$ yields a bulk conductivity that is systematically twice as large as the expected bulk conductivity for the given temperature. We deduce thus from this experiment that the surface conductivity plays a non-negligible role in the charge depletion in our glass capillary, and cannot be ignored in the modeling. Finally, we note that for capillaries mounted in the newly designed holder, *InCa4D* allows making accurate predictions, giving much confidence in the simulations.

2.8.2 Experimental evidence of self-organized focusing

Our original setup allows monitoring the transmitted beam (intensity and shape of the spot via the PSD) and accumulated charge in the capillary simultaneously. We take advantage of those features to give experimental evidence of the self

---

[13]http://valleydesign.com/Datasheets/Corning-Pyrex-7740.pdf

Figure 2.25: Y-projection of the transmitted beam on the PSD as a function of time. Colours indicate the normalized counts per second per area of the beam spot. The full green curve gives the simulated time-evolution of the charge Q stored in th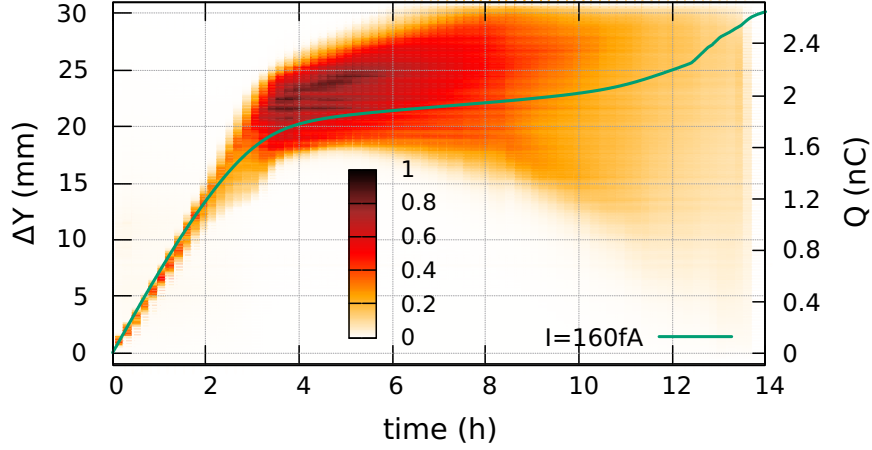e capillary for an input current of 160 fA. The right scale is the accumulated charge, using the relation $Q[nC] = 0.088 \times \Delta Y[mm]$, defined in the text.

organized radial focusing of an injected beam by a tapered insulating capillary. We used our home-made borosilicate capillary, with the profile given by the pink curve in Fig. 2.14. The capillary is aligned with beam axis using the technique involving the neutrals (see Fig. 2.9a), ensuring that the capillary is aligned with an error lower than 0.1°. We injected a low intensity Ar^+ ion beam at 2.3 keV and the transmitted fraction is monitored on the PSD. Figure 2.25, shows the y-projection of the transmitted beam spot on the PSD as a function of time for an injected intensity of 160 ± 7 fA, measured with a Faraday cup. The colors indicate the normalized counts per second (cps) of the spot. The deflection of the transmitted beam translates into the charge stored in the capillary using the relation $Q(t)[pC] = 88 \times \Delta Y(t)[mm]$. Initially, the spot on the detector has a size of less than 1 mm and is deflected vertically with increasing accumulated charge. After 2 hours of charging, the beam spot starts to spread, indicating that the focusing point approaches the outlet of the capillary. Two hours later, the electric field in the capillary is strong enough to focus the beam at the outlet, resulting into a high transmitted fraction of 50%, which is indicated by the darker colors. The spot has now a size of 7 mm corresponding to a full opening angle of 1.5 degree, close to the full opening angle of the capillary of around $\tan(1.05/45) = 1.4$ degree. At this point, the total deflection of 21 mm indicates that the capillary accumulated a total charge of about 1.8 nC. A high transmission of more than 80 fA is kept for about 4 hours before the transmission slowly fades away. During the high transmission, the beam spot continues to spread, while its center rises only slowly. The
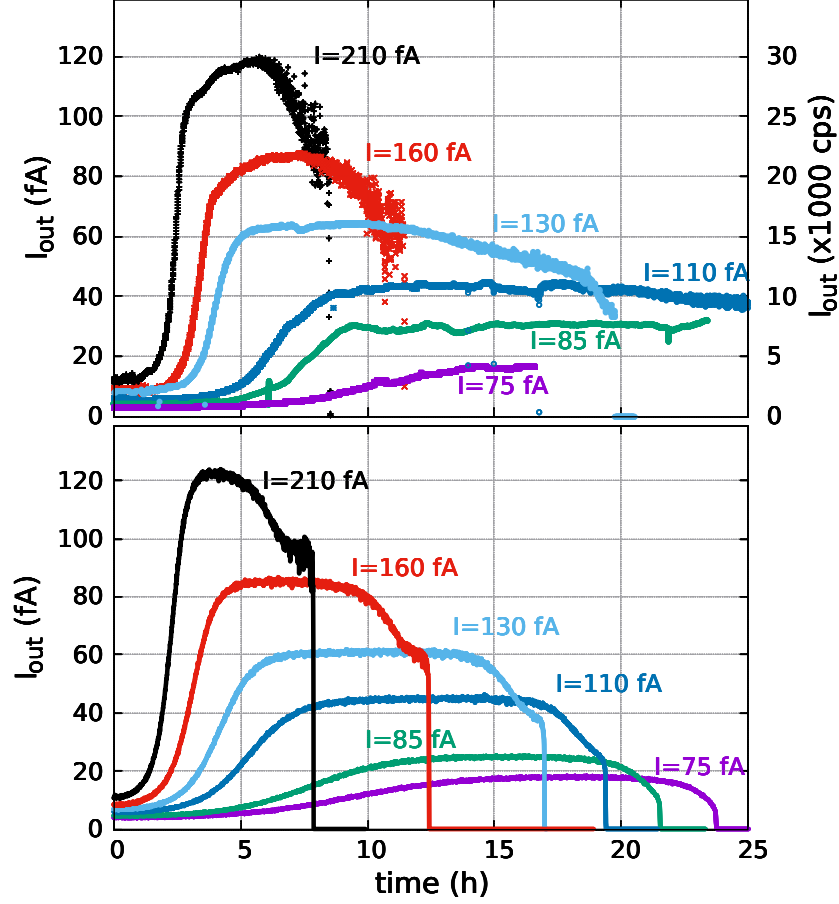
Figure 2.26: The transmitted intensity I_{out} through the glass capillary as a function of time, for 6 different injected intensities ranging from 75 to 210 fA. Top panel: Experimental data. The transmitted intensity passing through a transmission grid of 10% is measured on the PSD and expressed in counts per second (cps), as indicated by the right vertical scale. Assuming an efficiency of the detector of 40%, the left vertical scale gives the transmitted intensity in fA. Bottom panel: Theoretical transmitted current, simulated with our numerical code InCa4D using the parameters defined in section 2.7.

latter indicates that a quasi balance between the deposited and leakage current is attained. We add in Fig. 2.25 the simulated time-evolution of the accumulated charge $Q(t)$ in the capillary (full green curve) for a same input current of 160 fA. From the slope of the curve between 4h and 8h, we deduce that the capillary continues to accumulate charge at a rate of 15 fA. This low accumulation rate explains the long stable transmission for over 4 hours. Still, after 13 hours, a charge of 2100 pC has been accumulated and the transmission stops, because of Coulomb block-

ing. Monitoring the accumulated charge in the capillary is crucial for analysing and clearly identifying the different stages of the transmission dynamics, especially from the perspective to stabilize the transmission.

In a second step, we studied the transmitted beam intensity I_{out} for six different injected beam intensities I_{in}, ranging from 75 to 210 fA. The experimental results are given in the upper panel of Fig.2.26. Note the typical time-evolution of the transmitted fraction in the case of radial focusing, which differs strongly from the one in the case of transverse focusing (see inset of Fig.2.12). Only after at least 800 pC have been stored in the capillary walls, does the transmission increases rapidly from the initial geometrical fraction. We found that the focusing factor increases from 4 to 10, or alternatively, the transmission fraction $I_{\text{out}}/I_{\text{in}}$ increased from 20% to 50% with increasing beam intensity. For injected beam intensities less than 120 fA, the beam was transmitted for more than 24 hours and no Coulomb blocking was observed for the time of the experiment. In these cases, we know from the ΔY deviation of the spot on the PSD that the charge in the capillary never exceeded 2100 pC, which corresponds to the critical value for which the potential in the capillary is expected to exceed the source potential. For currents above 120 fA, the charge accumulated in the capillary during the time of the experiment was sufficient to generate a potential that exceeds the source potential and the transmissions faded slowly away. In these cases, the leakage current was too small to compensate for the deposited charge per time unit. Increasing the conductivity of the capillary (for example by heating) will certainly allow for higher input currents without experiencing Coulomb blocking.

We simulated for the same intensity range the transmission and compared it to the experimental data (lower panel of Fig.2.26). Simulations corroborate the experimental findings that the transmission fraction increased with the intensity. The quantitative agreement is remarkable, giving great confidence in the predictions that can be calculated by our model. This was made possible by developing the capillary holder, while keeping in mind that the boundary conditions imposed on the electric field in the capillary and its holder must be matched by our the numerical code. The simulations also corroborate that, with our particular experimental setup, the injected current always dominates the leakage current, so that the high transmission cannot be maintained and the Coulomb blocking not avoided. The numerical code offers thus a valuable tool to test the effect of different beam or capillary parameters on the stability of the transmission. For example, preliminary simulated results show that a lower beam emittance allow for higher focusing factors $j_{\text{out}}/j_{\text{in}}$ and for stable transmissions. Detailed studies about the influence of the beam emittance on the transmission are underway.

The simulations also confirm the trend that the Coulomb potential along the z-axis varies steeper for higher injected intensities. The profile of the potential along
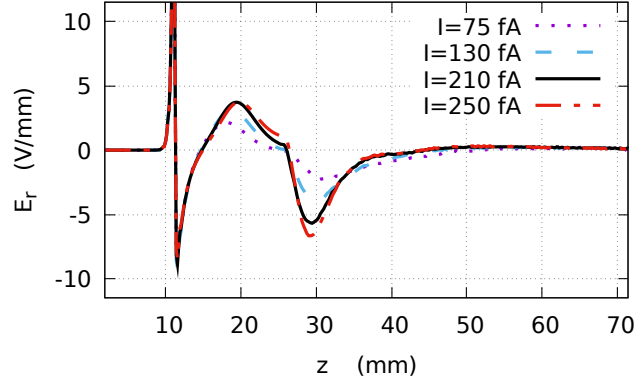
Figure 2.27: color online: Radial electric field $E_r(r = R(z), z)$ at the inner surface inside the capillary, taken at the apex of the transmission, for different injected current intensities. Negative values have a radial focusing effect while positive values have a defocusing radial effect. Note that the fast fluctuation of the field around 11 mm is due to the negative charge accumulation at the grounded outer electrode, which covers the first 11 mm of the outer capillary surface. It has only a negligible effect on the ion trajectories and is irrelevant here.

the z-axis exhibits thus a larger negative curvature, which yields a stronger focusing radial electric field (see eq. 2.61). Now, for axis symmetric charge distributions at the capillary interfaces, the radial component of the electric field E_r is strong mainly outside of the capillary interfaces and should be very weak inside, even if non-zero. It is thus interesting to show E_r inside the capillary at the moment the transmission is maximal. In figure 2.27, the axisymmetric radial field E_r, taken at the inner surface $R(z)$ of the capillary, is given for different injected current intensities. Negative values have a radial focusing effect while positive values have a defocusing effect. The focusing part of the field between 26 and 40 mm always dominates the preceding defocusing part and increases with increasing current intensity. This explains why focusing power and thus transmission fractions increases with higher injected currents. While the intensity of the focusing part of the fields are indeed relatively weak, (< 10 V/mm), they are sufficient to focus a 2300 keV Ar$^+$ beam through the capillary outlet.

2.9   Conclusion

In a first step, we discussed the electric conductivity in ionic glasses and motivated in detail the surface charge approximation used in our description of the accumulated charge at the interfaces. We then presented the theoretical model (and its

assumptions) that describes the surface charge dynamics at the capillary interface. We detailed the evaluation of the electric field that guides the ions through the capillary and drives the charge dynamics at the interfaces. We considered the general case where a third metal electrode surrounding the capillary is present, as the latter allows for a better comparison with experimental data. We presented an original analysis of the charge relaxation rates of the charge patches at the inner surface of an insulating capillary tube with the outer surface grounded. We showed that the relaxation rate is a weighted sum of the bulk and surface relaxation rate, with the weights depending on the dimensions of the capillary as well as the imposed boundary conditions. We gave an example where we used the theoretical predictions to analyse experimental relaxation rates.

We presented our numerical code *InCA4D* and highlighted its features. *InCA4D* takes into account secondary electrons, neutralized projectiles, induced polarization charges at the three interfaces and non-linear conductivity. In the second part of the chapter, we presented simulated results. We showed that one must distinguish between transverse and radial self-organized focusing. The transverse focusing explains the enhanced transmission in tapered capillaries for non-zero tilt angles. We showed that tapered capillaries can focus an ion beam similar to an Einzel lens. Simulations showed that the injected beam is efficiently focused through the outlet if the self-organized potential of our capillary approaches 75% of the extraction potential of the ion source. For a given electrical conductivity of the capillary, the self-organized potential is steeper with increasing injected intensity, resulting in a higher focusing radial electric field. We could thus explain the observed trend that the transmitted fraction increases with the injected beam intensity.

We presented an original capillary holder, that allows monitoring the accumulated charge in the capillary. The holder also screens the capillary from stray electrons and allows measuring the intensity and emittance of the injected beam with the integrated Faraday-Cup and micro-hole grid, respectively. We gave for the first time clear experimental evidence of the radial self-organized focusing by a tapered glass capillary, for intensities ranging between 70 to 200 fA. We found that the apex of the transmission could not be sustained for long times (days). By monitoring the accumulated charge, we could deduce the leakage current at the apex of the transmitted fraction and found that it was too low, compared to the deposited current, to maintain a stable transmission. Nevertheless, for intensities below 120 fA, the transmission was found stable for almost 24 hours. We expect that our simulations will be of immense help to improve and stabilize the transmission by identifying the bottlenecks and test original solutions. Indeed, simulations confirmed recently (not further discussed in the manuscript) that the emittance of the injected beam plays a crucial role on the stability of the trans-

mitted beam and that the high transmission could be maintained by grounding for example the tip of the capillary. Reliable simulations could be achieved by developing hand in hand the capillary holder and the numerical code, ensuring a one to one comparison between experimental and simulated results. Finally, fitting the experimental charge-discharge curves for our glass capillary, allowed to extract the surface and bulk conductivity of our Pyrex glass capillary and showed that surface conductivity should not be ignored in the description of the charge dynamics at the interface.

2.10 Perspectives

Three topics linked to the transmission of charged particles through insulating capillaries are presented below. Some may may give rise to Phd works with a mixed theoretical and experimental profile.

2.10.1 Stabilization of the focused ion beam
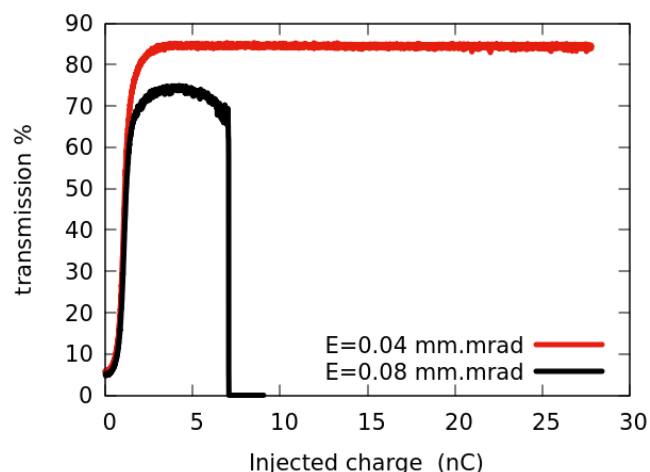
Figure 2.28: *Influence of the emittance E on the stability of the transmission of a focused beam.*

In the manuscript, we have highlighted the focusing power of a conical insulating capillary. Preliminary simulations indicated that if the injected beam has a low emittance, the transmission is maintained for a long time, at least well beyond the simulated time, see red curve in Fig. 2.28. In the extreme case of a zero emittance beam, the simulations predict even a 100% transmittance with a long time stability. In reality, the emittance of the injected beam is never zero and the focusing "point" has a non-zero spatial extension. If the diameter of the focusing area is larger than the diameter of the capillary outlet, a part of the injected beam is always intercepted by the capillary wall near the outlet. As a result the potential of the capillary continues to rise and eventually exceeds the extraction potential of the ion source (black curve in Fig. 2.28). Indeed, the leakage current, ie the current flowing to ground, is usually too small to compensate for the charge deposited per unit of time. The goal here is to optimize the leakage current in order to stabilize the charge in the capillary and therefore the transmission. The charge transport in the dielectric can be controlled by the following parameters:

1. The conductivity of the capillary (by varying the composition of the glass and / or its temperature);

2. Profile and dimensions of the capillary

3. Adding grounded electrodes on the outer tip surface of the capillary.

We privilege the latter and estimate that a grounded electrode surrounding the exit of the capillary should stabilize the transmission as the deposited charge is now faster removed, keeping the exit at low (near ground) potential. The beneficial effect of adding electrodes on the capillary was tested with the InCa4D code. As shown in Fig. 2.29, the idea is validated by the numerical code. We used the
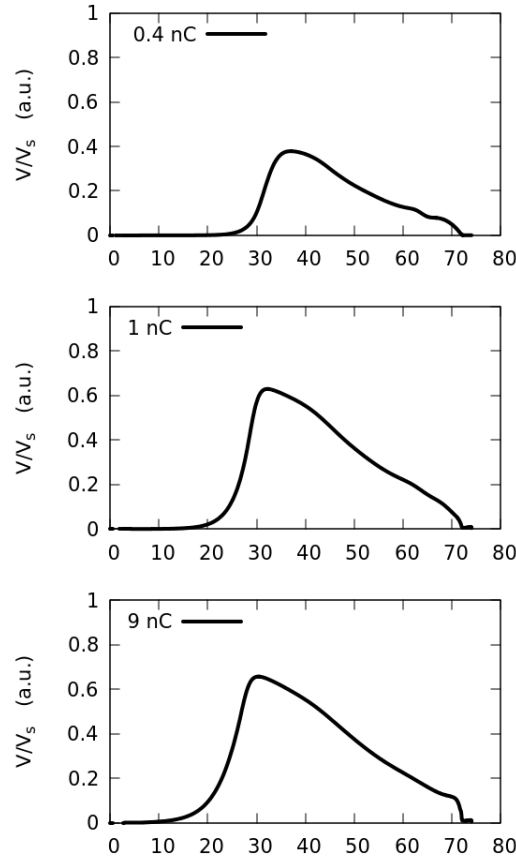
Figure 2.29: *Electric potential in the capillary, in the presence of a grounded electrode surrounding the last 3 mm of the capillary tip. Legend of the panels indicates the injected charge. Beam parameters were those used in Fig. 2.14 for better comparison. The abscissa coordinates are given in mm.*

same parameters for the injected beam as in Fig. 2.14. The potential near the outlet stays now near zero, even after 9 nC have been injected. The Coulomb blocking is avoided, contrary to what has been observed in the last panel of Fig. 2.14. Comparing the potential curve in middle and last panel, we see that the potential in the capillary stays almost constant, meaning that an equilibrium between the leakage and injected current has been found. In a near future, we want to bring the experimental evidence that such a setup stabilized the transmission. In a second step we want to reduce the outlet diameter of the capillary in order to reach stable beams of nanometre size. Capillaries with nano-sized outlets diameter can be be achieved with our capillary puller. The profile and dimensions of the tapered capillary are then measured with a microscope and the profile injected into the numerical code. A theoretical study will then evaluate its potential to stabilize transmission. In addition to the theoretical interest, Focused Ion Beams (FIB) have a great practical interest. Stable beams of nanometre size could find an application in the future European IMPLATION project for single ion implantation. Thus the focusing of ion beams by micrometre capillaries also responds to technological and societal issues.

2.10.2 Transmission through curved insulating capillaries

Figure 2.30: Curved capillary. Extracted from [63]

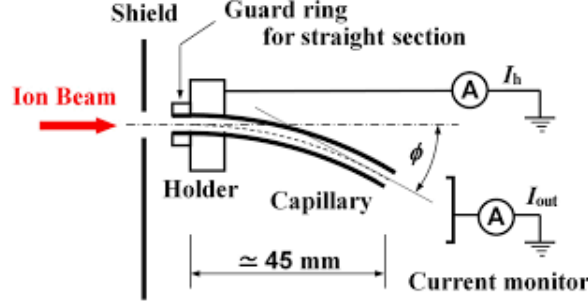The guiding power of insulating capillaries has also been tested for curved capillaries. It has been shown experimentally by T. M. Kojima *et. al.* [42] that ions can pass through a 5 cm long Teflon capillary arc, curved by 27°. The transmission was found to be about 20%. A review is given in [63]. Improvements are certainly possible and a theoretical study of the problem could identify the bottlenecks that have to be lifted and propose workarounds. I propose thus to simulate ion transmission through curved insulating capillaries. The goal is to find the necessary conditions for a capillary to transmit with a transmittance of more than 50% an ion beam through a curved 90° capillary. We would like to demonstrate that such a tube can effectively guide low energy (< 1000 V/q) multi-charged ions, keeping their energy and initial charge and without applying an external electric or magnetic field. To date, we have a numerical code, written in cylindrical coordinates, capable of simulating the transmission through axially symmetric capillaries. This code is however not suitable for describing curved capillaries. I propose here to modify the existing code in order to describe a curved tube up to 90 degrees for a given radius of curvature. Part of the work therefore consists of writing a function capable of solving the Laplace equation of the electrical potential in toroidal coordinates system (η, ξ, φ), (see Fig. 2.31). The success of the method is ensured by the fact that the Laplace equation is separable in the toroidal coordinate system,

$$\Phi(\eta, \xi, \phi) = \sqrt{\xi - \cos(\eta)} \sum_{n,m} a_{mn} P_{n-1/2}^m(\xi) e^{\pm in\eta} e^{\pm im\varphi} \rightarrow \nabla^2 \Phi = 0 \qquad (2.62)$$

allowing for a fast computation of the electric potential and field, with a cost similar to the model in cylindrical coordinates. For the inner surface, the Neumann conditions will be imposed, in order to satisfy the discontinuity of the normal field through an interface separating two different dielectrics. For the outer surface, the Dirichlet conditions will be imposed (the potential of the outer surface is

156
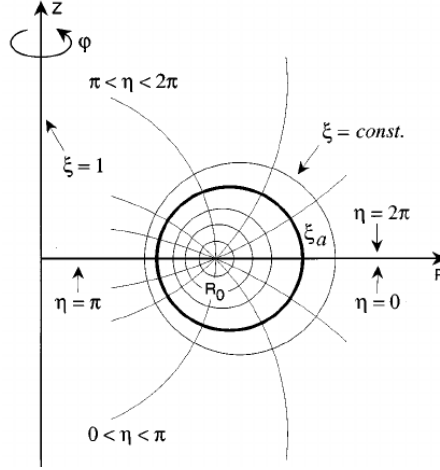
Figure 2.31: Toroidal coordinate system. Surfaces with constant $\xi > 1$ are toroids and φ the polar angle in the xOy plane.

grounded). The goal is to understand through simulations how the transmittance varies according to the radius of curvature and the length of the capillary. We will try to predict and optimize with our simulations the transmittance, with the goal to increase the length of the arc up to 90°, if possible. Then we will experimentally test the theoretical predictions with our experimental setup. Again, we manage to create a feedback loop between simulations and experimental data that might allow us to quickly converge towards the desired solution.

2.10.3 Transmission of injected electron beam

Transmission of electrons through insulating capillaries has been observed more than a decade ago in the pioneering work of Milosavljevic *et al.* [30]. Recently, the capillary community has renewed interest in electron transmission through insulating capillaries [57, 58]. Today, a relatively large experimental database is available. These data suggest that electron transmission through capillaries might be similar to that of ions. As with ions, electrons are guided through the capillary even if no geometric transmission is possible. And indeed, 500 eV electron transmission through nano-capillaries in PET has recently been observed. However a more detailed comparison shows divergences that are related to interaction mechanisms with insulators, which are different between ions and electrons. While the ions always deposit a positive charge at the point of impact, the sign of the charge deposited by the electrons depends on their velocity and their incident angle. Thus, the impact of a 500 eV electron on a Teflon or PET surface emits on average 4 secondary electrons, thus depositing on average 3 elementary positive charges at the point of impact, whereas for an electron of 20 eV, the charge deposited is negative [14]. This raises the question of how exactly an electric field, capable of guiding 500 eV electrons through a capillary, emerges with positive charge deposition at the point of impact. Of course, it should be noted that overall the charge deposited in the capillary is negative. Electrons can also penetrate the surface for a few nm before being backscattered by losing a fraction of their incident energy. The ion on the other hand is neutralized on the surface and is no longer guided by the electric field. Finally, electrons scattered near the surface are always subject to image charge and can be attracted back to the surface. It follows that the electron charge deposition mechanism differs greatly from that of the ions.

I propose to develop a model with a realistic description of the electron-dielectric interaction. The goal is to improve our understanding of the behavioural differences between ion and electron transmission. The focus will be on the description of the charge deposition and charge dynamics at the dielectric interfaces. It involves reconstructing the electric field map inside the capillary via simulations to explain the transmission of electrons through the insulating capillaries. The comparison between the theoretical predictions and the experimental data will make it possible to validate or not the initial hypotheses of the mechanisms of electron-insulating interaction as well as the dynamics of the electrons in the insulator.

2.11   Appendix : Numerical methods

2.11.1   Injected charge at the inner surface

When an ion hits an insulating surface, electrons are ejected from the impact point. Some are captured by the projectile ion while the other, if we consider a closed surface, are re-injected into the surface. We suppose here that the projectile is neutralized by the ejected electrons and that the remaining electrons fall back onto the impact point, meaning that the deposited charge is equal to the initial charge of the ion. We ignore hereby the possible capture of electrons by the insulator farer away from the impact point, avoiding the description of the dynamics of the ejected electrons.

The deposited surface charge density per unit time is computed using the following scheme. Let the inner surface of the capillary be mapped onto a two-dimensional grid (θ_i, z_j) of dimension $N_\theta \times N_z$ (see figure 2.32). Along θ we chose an uniform grid path $\Delta\theta = 2\pi/N_\theta$ and $\theta_i = (i-1)\Delta\theta$. Along the z axis the points $z_j = L\frac{(1+x_j)}{2}$ are distributed according to the Gauss collocation points x_j, where L is the length of the capillary and $\{x_j\}$ the N_z zeros of the Legendre polynomial of order N_z+1. For an impact point at the inner surface coordinate $((R_1(z), \theta, z))$, the
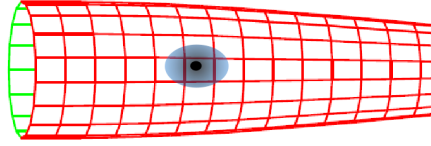
Figure 2.32: *Deposited charge on the 2d-grid, mapping the inner surface of the capillary. The charge is distributed on the grid using the 2d normalized gaussian function given in Eq. 2.63 (blue transparent ellipse), with the impact point (black circle) being the center of the gaussian distribution*

deposited charge q_d is distributed over the grid points (θ_i, z_j) using the normalized 2d gaussian function

$$f(\theta_i, z_j, \theta, z) = \frac{\exp\left(-\frac{(\theta-\theta_i)^2}{\gamma\Delta\theta^2}\right) \exp\left(-\frac{(z-z_j)^2}{\Delta z^2}\right)}{\Delta\theta\,\Delta z\, R_1(z)\,\pi\sqrt{1+R_1'(z)^2}\sqrt{\gamma}} \quad . \tag{2.63}$$

Choosing $\gamma = 1/\ln(2)$ and $\Delta z = L/N_z$, assures that the convolution function f is well integrated over the grid to unit with a relative error less then 10^{-6}. As the surface element $\Delta\theta\,\Delta z\, R_1(z)\sqrt{1+R_1'(z)^2}$ varies with z, the deposited charge is smeared over an area which depends on the impact abscissa z. In the case of

tapered capillaries, this may vary over one order of magnitude. It does however not affect the charging up as long as the surface element is small compared to the size of the beam spot projected on the inner surface. Our micro-capillaries being about 60 mm long with an inlet diameter of about 1 mm, we typically use in our simulations $N_\theta = 64$ and $N_z = 500$, yielding a grid mesh which is about 100μm $\times$ 120μm at its loosest point. This grid size satisfies the above condition and gives a good compromise between the precision with which the density is represented on the grid and CPU cost for computing the Coulomb potential and forces. Eventually, the deposited surface charge distribution at the grid points (θ_i, z_j) during the time interval Δt is given by

$$\gamma^h(\theta_i, z_j)\Delta t = q_d \sum_\alpha f(\theta_i, z_j, \theta_\alpha, z_\alpha) \quad , \tag{2.64}$$

where the sum runs over all the particles α that hit the surface during the time interval Δt.

2.11.2 Accelerating the charging up

The code is aimed at describing not only the guiding power of weakly charged insulating capillaries, but also to explore the possible focusing effect of highly charged tapered capillaries and even the Coulomb blocking. Coulomb blocking of the ion beam by the potential of the capillary happens only if the potential V of the capillary equals the extraction potential U_0, while the focusing effect may appear for potentials above 60% of U_0. Consequently, $Q_0 = \varepsilon_0 L_0 U_0$, gives the order of magnitude of the total charge, distributed on the capillary, necessary to block the beam. Taking typical values for $U_0 = 3$ keV and $L_0 = 0.001$ m, gives a characteristic charge Q_0 of the order of 3×10^{-11} C. One needs thus to simulate of about Q_0/q trajectories in order to deposit a charge that generates a potential field strong enough to Coulomb block the ions. In the case of singly charged ions, this means $Q_0/q = 10^8$ trajectories. This huge number would push the CPU time for 1 simulation to several weeks, making it unreasonable for systematic studies. Let us now assume that each simulated trajectory accounts for an ensemble of n particles where each particle deposits q charges. If the deposited charge per impact $q_d = nq$ is small enough as to influence the Coulomb potential V_c only in a negligible way, n can be adjusted in order to accelerate the charging up. For $n > 2000$, we found that the first trajectories were affected by the poorer sampling, that is, the coarse graining of the deposited charge per trajectory, which spuriously over-deflected the subsequent ions. No significant difference however was found for $n = 10, n = 100, n = 500$. To stay on the safe side, we used in all our simulations an acceleration factor of less then 500, $n \leq 500$. This leads to

about 10^6 trajectories per simulation, which is a feasible number of trajectories that one modern CPU can simulate in 24 hours.

We found in the above paragraph that the number of trajectories increases with the extraction potential. To avoid this, we may fix $N_t = 10^6$ and calculate the appropriate accelerating factor n. By choosing for n the particular value $n = Q_0/(N_t q)$, the deposited charge per ion impact becomes $q_d = nq = Q_0/N_t$. Note that the latter is independent of the ion charge q. For example in the case of Ar$^+$ extracted by a potential of 3000 V, we get an acceleration factor $n = Q_0/(N_t q) \simeq 160$. The latter is small enough as not to alter in a significant way the charging up with respect to $n = 1$. We found indeed no difference in the computed observables for $n = 160$ or $n = 16$, validating the assumption. By adjusting n so as to keep a reasonable number N_t of trajectories, allows to keep the same CPU cost per simulation independent on the extraction potential.

2.11.3 Evaluation of the potential and electric field inside the capillary

Even with a time step adaptive predictor corrector scheme, which is conservative on the evaluation of the force along the trajectory, an average of 100 evaluation of the electric potential / field are necessary for each trajectory. It is therefore vital to have a efficient numerical scheme to evaluate the electric potential and field at an arbitrary point inside the capillary. We give here an overview of the numerical scheme used in our code. We assume that the shape of the capillary has cylindrical symmetry. Let us decompose the angular part of the surface charge density and the Coulomb potential on the first M moments. We consider the case where the capillary axis may be tilted with respect to the beam axis. The two axis define then a plane of symmetry, fixing the xOz plane and the origin of the θ angle. The deposited surface charge density $\sigma(s(z), \phi, z) \equiv \sigma(\phi, z)$ is thus symmetric with respect to the xOz plane $\sigma(-\phi, z) = \sigma(\phi, z)$. Consequently, only the cosines moments are non-zero in the angular decomposition so that,

$$\sigma(\theta, z, t) = \sum_{m=0}^{M} = \sigma_m(z, t) \cos(m\theta) \tag{2.65}$$

$$V(r, \theta, z, t) = \sum_{m=0}^{M} = V_m(r, z, t) \cos(m\theta) \quad . \tag{2.66}$$

Note that if the capillary axis and the beam axis are aligned, only the moment $m = 0$ need to be considered, reducing by a factor M the CPU cost. The components V_m are defined in the rOz plane. Instead of calculating V_m for an arbitrary point of the rOz plane, we limit the evaluation of V_m on the grid points
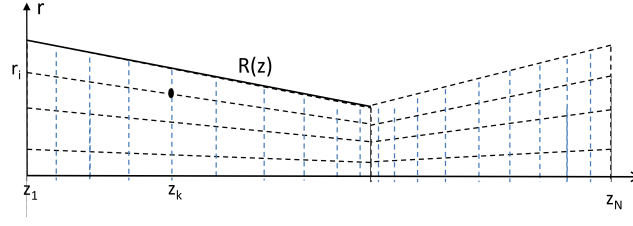
Figure 2.33: 2d grid of the rOz plane mapping the interior of the capillary as well as the space behind the outlet of the capillary so that the trajectories can be computed until the multipoles of the electric field become negligible.

of the 2d mesh that maps the inner region of the capillary as well as the space behind the outlet of the capillary so that the trajectories can be computed until the multipoles of the electric field become negligible (see figure 2.33). The grid has $N_i = 6$ points in the Or direction and $N_j = 2000$ points in the Oz direction, labelled z_j. Because the inner radius of the capillary $s(z)$ is varying with z, the interval between the radial points depends on z and is proportional to $s(z)$. The radial distribution depends thus explicitly on the coordinate z of the symmetry axis Oz and the radial points r_{ij} of the mesh read,

$$r_{ij} = x_i s(z_j) , \qquad (2.67)$$

where x_i are the collocation points of a N_i order Gauss Legendre interpolation scheme. In the Oz direction the $N_j = 2000$ points are distributed uniformly except at the capillary outlet where the density is increased in order to cope with the strong variation of the field. We chose to represent the surface charge moments $\sigma_m(z_k)$ on $N_k = 500$ collocation points. For a capillary of 70 mm length, this is in average 1 point every 0.14 mm, much smaller than the typical spatial variation of the surface charge density and Coulomb potential along the z axis.

The surface densities are evaluated on the interface grid as discussed in the previous section. The $m \leq M$ moment of the potential, V_m are efficiently computed by a simple algebraic equation

$$V_m(r_i, z_k, t) = \sum_q S^m_{i,k,q} \sigma_m(z_q, t) \qquad (2.68)$$

where the matrix S^m is the Coulomb kernel for the moment m and depends only on the shape of the capillary. As a result, $S^m_{i,k,q}$ is independent of time and can be computed once for all at the beginning of the simulation or read from disk if stored before. Only the moments $\sigma_m(z, t)$ depend on time and need to be undated regularly. Eventually, the potential at an arbitrary point inside the capillary is

162

obtained, first by interpolating $V_m(\rho, z, t)$ on the 2D grid using $V_m(\rho_i, z_k, t)$ and then by summing over the moments (2.66).

The same method is used for the electric field. As the amount of deposited charge per hit is small, it is sufficient to update the potential moments $V_m(\rho_i, z_k, t)$ on the 2D grid, via equation (2.68), only every $n_{\rm up}$ trajectories, reducing even more the CPU costs. In our simulation we took $M = 6$, limiting the decomposition of σ and V to the duodecapole moment. We found that $M = 6$ is indeed sufficient for most simulated cases, as long as the beam size is of the same order than the inner capillary diameter. The frequency with which V was updated depends on the characteristic dimensionless ratio $\tau_c/\tau_r = \kappa_b L_0 U_0 / I$. We typically take values for $N_k = 2000$, $N_i = 6$ and $n_{\rm up}$ about 300, meaning that the potential is only updated every 300 trajectories, making this scheme efficient if $N_i \times N_k \ll 100 \times n_{\rm up}$.

The S matrix

The Coulomb potential in cylindrical coordinates is given by

$$V(r, \phi, z, t) = \frac{1}{4\pi\varepsilon_0} \int_0^L \frac{\mathrm{d}\Sigma'}{\sqrt{(r + s(z'))^2 + (z - z')^2}} \times$$
$$\int_{-\pi}^{\pi} \frac{\sigma(s(z), \phi, z, t)\mathrm{d}\phi'}{\sqrt{1 - w\cos^2\left(\frac{\phi' - \phi}{2}\right)}} \tag{2.69}$$

with $w = \frac{4\rho s(z')}{(r + s(z'))^2 + (z - z')^2}$ and where $s(z)$ defines the inner capillary surface, $\mathrm{d}\Sigma' = s(z')\sqrt{1 + \left(\frac{ds}{dz'}\right)^2}dz'$ the surface element and L the length of the axisymmetric capillary. Injecting (2.65) into (2.69) allows to define the moments of the potential as defined in Eq. 2.66,

$$V(r, \phi, z, t) = \sum_{m=0}^M \frac{1}{4\pi\varepsilon_0} \int_0^L \frac{\sigma_m(z', t)\mathrm{d}\Sigma'}{\sqrt{(r + s(z'))^2 + (z - z')^2}}$$
$$\times \underbrace{\int_{-\pi}^{\pi} \frac{\cos(m\phi')\mathrm{d}\phi'}{\sqrt{1 - w\cos^2\left(\frac{\phi' - \phi}{2}\right)}}}_{F_m(w)\cos(m\phi)} \tag{2.70}$$
$$= \sum_{m=0}^M \frac{1}{4\pi\varepsilon_0} \underbrace{\int_0^L \frac{\sigma_m(z', t)F_m(w)\,\mathrm{d}\Sigma'}{\sqrt{(r + s(z'))^2 + (z - z')^2}}}_{V_m(\rho, z, t)} \cos(m\phi)$$
$$= \sum_{m=0}^M V_m(r, z, t)\cos(m\phi) \tag{2.71}$$

The integrating over ϕ' in eq. (2.70) is done analytically. As examples, the first 3 terms, calculated with Mathematica [20], are given below,

$$
\begin{align}
F_0(w) &= 4\mathrm{K}(w) \tag{2.72}\\
F_1(w) &= \frac{4(2\mathrm{E}(w) + (w-2)\mathrm{K}(w))}{w} \tag{2.73}\\
F_2(w) &= \frac{4(8(w-2)\mathrm{E}(w) + (w-4)(3w-4)\mathrm{K}(w))}{3w^2}
\end{align}
$$

$$\tag{2.74}$$

where $K()$ and $E()$ are complete elliptic function of type 1 and 2. In a second step, the surface charge density moment $\sigma_m(z,t)$ is interpolated by a sum of cardinal functions, $g_k(z)$, based on Legendre polynomials [23, 12]

$$
\sigma_m(z,t) \simeq \sum_k^{N_k} \sigma_m(z_k,t)g_k(z) \quad , \tag{2.75}
$$

where z_k are the N_k collocation points of the Legendre polynomial of order $N_k + 1$. Injecting (2.75) into (2.71) yields

$$
\begin{align}
V_m(r,z,t) &= \sum_k^{N_k} \sigma_m(z_k,t) \times \tag{2.76}\\
&\quad \int_0^L \frac{g_k(z')F_m(w)\,\mathrm{d}\Sigma'}{4\pi\varepsilon_0\sqrt{(r+s(z'))^2 + (z-z')^2}}\\
&= \sum_k^{N_k} \sigma_m(z_k,t)S_{m,k}(r,z) \tag{2.77}
\end{align}
$$

The matrix $S_{m,k}$ links the moment m of the surface charge distribution to the moment m of Coulomb potential. Indeed, because of the cylindrical symmetry of the capillary, the moments do not mix. The moments $V_m(r,z)$ as well as S are defined in the xOz plane. Finally the potential is recomposed by summing over all the moments,

$$
V(r,\theta,z,t) = \sum_{m=0}^M = V_m(r,z,t)\cos(m\theta) \quad . \tag{2.78}
$$

yielding the potential at an arbitrary point inside the capillary. Both interpolation schemes can be differentiated with respect to r or z to calculate the electric field at arbitrary points. Alternatively, similar to the S matrices for potential, the S matrices for the r and z components of the electric field can be pre-calculated. The electric field can then be interpolate using the same scheme than for the

164

potential. The letter scheme is used in our simulation to calculate the force at an arbitrary point inside the capillary to propagate the projectiles until they hit the inner surface or until they pass though the outlet. It is also used the calculate the electric field at the interfaces S_1, S_2 and S_3.

2.11.4   Induced surface charges

In order to illustrate the importance of accurately computing the induced surface charges at the interfaces, we propose to compute the electric field in the case of a single charge patch in a glass tube of dielectric constant $\varepsilon_r = 4.8$. The tube is 55 mm long and the inner and outer radii are respectively 0.43 mm (S_1) and 0.75 mm (S_2). The tube is surrounded by a grounded metal tube of 3 mm inner radius (S_3). We start with given free surface charge distributions σ_1 and σ_2 at the inner and outer surface of the glass tube, respectively. The latter were created by injecting a low intensity ion beam of 0.6 mm diameter into the glass tube. The beam was tilted by 0.8 deg with respect to the tube axis, until the beam was deviated by the electric field due to the charge patches. The right hand terms (2.31) of the matrices system 2.30 are evaluated and the induced surface charges at the 3 interfaces computed. Finally the normal and tangential components of the electric field at the inner and outer part of the S_1 and S_2 interfaces are evaluated. The symmetry axis of the tube and of the beam define a symmetry plane. Cuts, containing the symmetry plane, of the induced surface charge distributions at the 3 interfaces are given in the left panel of figure 2.34. As shown in the top left panel, the surface polarization charges $\widetilde{\sigma}_1$ an $\widetilde{\sigma}_2$ are clearly not negligible with respect to deposited screened charges σ_1/ε_r and σ_2/ε_r in the dielectric. The surface charges $\widetilde{\sigma}_3$ at the S_3 interface ensure that the equipotential of the metal tube equals zero. All three induced surface charges contribute sensibly to the Coulomb field in the dielectric.

We compare the computed screened surface charges to an alternative method, where the deposited charges are simply screened by the factor $2/(1+\varepsilon_r)$. The latter corresponds to the screening of a charge lying at the glass-vacuum interface of an infinite dielectric plane. Similarly, in this alternative approach, the grounded metal tube is taken into account via image charges in the spirit of an infinite grounded metal plane. This approach has been used by several authors in their simulations [48, 49]. While the latter method is easily implemented in numerical codes, it lakes the self-consistent nature of the above described matrix method. The right top panel compares the screened charges obtained by both methods. The pink color stands for the surface charges at the inner surface. We note that using a the factor $2/(1+\varepsilon_r)$ to screen the surface charges is indeed a viable approximation. However, for the outer screened surface charges (green full and dotted line) the difference is dramatic and it is clear that the factor $2/(1+\varepsilon_r)$ approach is failing.
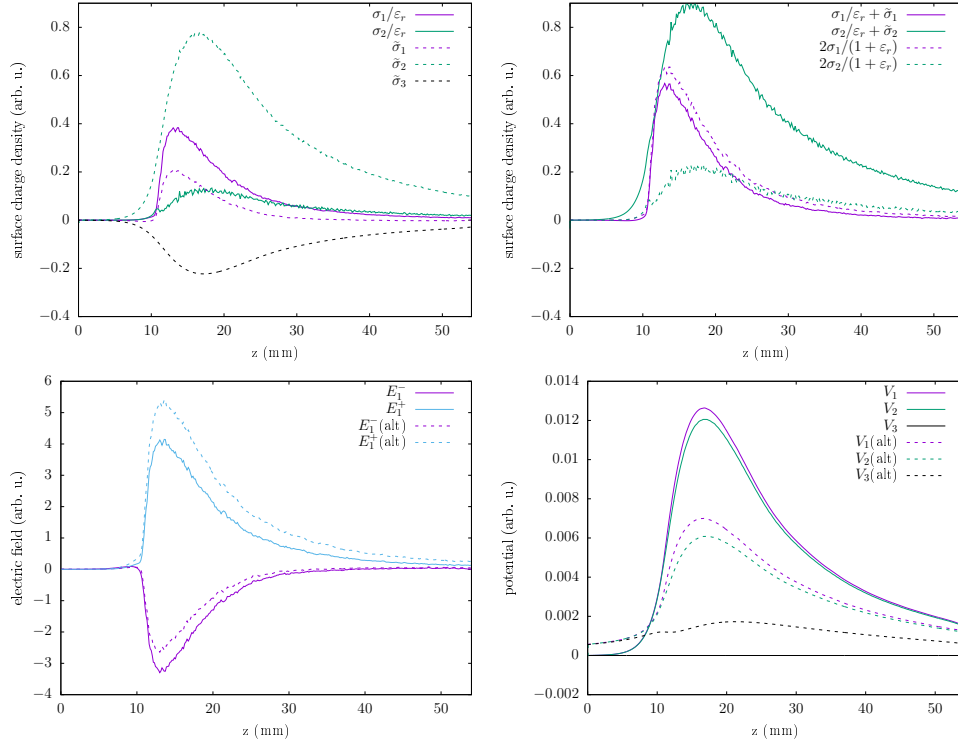
Figure 2.34: Full line; Force acting on the projectile due to the induced polarization charges on a cylindrical glass-vacuum interface as a function of the distance separating the projectile from the interface. Dotted line: plane interface. The dielectric constant of the glass was set to $\varepsilon_r = 4.8$

The left bottom panel shows the inner E_1^- and outer E_1^+ part of the electric field at the interface S_1. They control respectively the deflection of the beam ions at the inner surface and the migration of the charge carriers in the dielectric from the inner to the outer surface. Again, we compare the computed electric fields to an alternative method, where the deposited charges are screened by the factor $2/(1 + \varepsilon_r)$. We found in both cases a discrepancy of about 30% in the electric fields between both approaches for the same deposited charge distributions. The reason for the discrepancy is that the boundary conditions (2.27) and (2.25, 2.26) are not satisfied at the 3 interfaces in that simple alternative approach. Indeed, in the right bottom panel, we note that V_3(alt) is non-zero and does not meet the required boundary condition of $V_3 = 0$. Of course the discrepancy between the simple screening of the form $2/(1 + \varepsilon_r)$ and the exact method depends on the geometry of the interfaces $S_{1,2,3}$. The above example however clearly illustrates the sensitivity of the electric field on the induced polarization charges at the interfaces

166

and demonstrates the numerical advantages of the precise self-consistent matrix approach.

Bibliography

[1] J. Frenkel, "On pre-breakdown phenomena in insulators and electronic semiconductors", Phys. Rev., vol. 54, pp. 647-648, (1938)

[2] "Calculation of Activation Energy of Ionic Conductivity in Silica Glasses by Classical Methods", O. L. Anderson and D. A. Stuart, J. Am. Ceram. Soc., **37** (1954) 573

[3] "Photoelectric effect from borosilicate glass", V.K. Rohatigin J. App. Phys. **28** (1957) 951

[4] "Polarization and diffusion in a silicate glass", R.J. Charles, J. Appl. Phys. **32** (1961) 1115

[5] "Volume Conductivity of Borosilicate Glass", J.J.Muray, J. Appl. Phys. **33** (1962) 1517

[6] "Surface Conductivity of Borosilicate Glass ", J.J.Muray, J. Appl. Phys. **33** (1962) 1525

[7] "IONIC CONDUCTIVITY IN OXIDE GLASSES: PART I", D. Ravaine, J.L. Souquet. Physics and chemistry of glasses 18 (1977) 27

[8] "IONIC CONDUCTIVITY IN OXIDE GLASSES: PART II", D. Ravaine, J.L. Souquet. Physics and chemistry of glasses 19 (1977) 115

[9] "Ionic conductivity and the weak electrolyte theory of glass", M.D.Ingram, C.T.Moynihan, A.V.Lesikar, Journal of Non-Crystalline Solids, Vol 38-39, Part 1, (1980), Pages 371-376

[10] "Ionic conductivity in glass: A NEW LOOK AT THE WEAK ELECTROLYTE THEORY", J. A. Bruce et al. Solid State Ionics 18-19 (1986) 410414

[11] "Space-charge relaxation in ionicly conducting oxide glasses. I. Model and frequency response", H.J. Schütt, E. Gerdes, Journal of Non-Crystalline Solids, Vol. 144, (1992) 14-20

[12] "Polynomial Approximation of Differential Equations", D. Funaro, Springer Verlag, New York (1992)

[13] "A single microscopic approach for ionic transport in glassy and polymer electrolytes", J.L. Souquet, M. Levy, M. Duclot, Solid State Ionics **70** (1994) 337

[14] Sanju Hiro, Haruhisa Fujii and Alexandre Palov, "Theoretical Investigation of Total Secondary Electron Yield for Teflon", Japanese Journal of Applied Physics, Volume 37, Part 1, Number 7 (1998) https://doi.org/10.1143/JJAP.37.4162

[15] "dc Polarisation: An experimental tool in the study of ionic conductors", Rakesh Chandra Agrawal, Indian Journal of Pure and Applied Physics, Vol. 37 (1999) 294-301

[16] Heddle, D W O, Electrostatic Lens Systems, Bristol and Philadelphia: IOP Publishing Ldt (2000)

[17] "Transmission of 3 keV Ne^{7+} Ions through Nanocapillaries Etched in Polymer Foils: Evidence for Capillary Guiding", N. Stolterfoht, J.-H. Bremer, V. Hoffmann, R. Hellhammer, D. Fink, A. Petrov, and B. Sulik, Phys. Rev. Lett. **88** (2002) 133201

[18] "Measurement of ion-induced secondary electron emission yield of MgO films by pulsed ion beam method", Sang Kook Lee, Jae Hong Kim, Ji Hwa Lee and Ki Woong Whang, Journal of Information Display, 3:1, 17-21, DOI: 10.1080/15980316.2002.9651886

[19] "DIELECTRIC PHENOMENA IN SOLIDS", Kwan Chi Kao, Elsevier Academic Press (2004)

[20] Wolfram Research, Inc., Mathematica, Version 5.1, Champaign, IL (2004).

[21] "Electric potential due to an infinite conducting cylinder with internal or external point charge", J.A. Hernandes, A.K.T. Assis, Journal of Electrostatics 63 (2005) 1115-1131

[22] "Production of a microbeam of slow highly charged ions with a tapered glass capillary", T. Ikeda, Y. Kanai, T. M. Kojima, Y. Iwai, T. Kambara, and Y

Yamazaki, M. Hoshino, T. Nebiki and T. Narusawa, Appl. Phys. Lett. **89** (2006) 163502.

[23] B. Gervais, E. Giglio, A. Ipatov and J. Douady, Comp. Mat. Sci. **35** (2006) 359

[24] K. Schiessl, W. Palfinger, K. Tők´si, H. Nowotny, C. Lemell, and J. Burgdörfer,"Simulation of guiding of multiply charged projectiles through insulating capillaries", Phys. Rev. A. **72** (2005) 062902.

[25] K. Schiessl, W. Palfinger, K. Tők´si, H. Nowotny, C. Lemell, and J. Burgdörfer, "Simulation of ion guiding through insulating capillaries: Effects of inter-capillary interaction", NIMB, Vol. 258, Issue 1, (2007), p 150-154 https://doi.org/10.1016/j.nimb.2006.12.135

[26] M.B. Sahana, P. Skog, Gy. Vikor, R.T. Rajendar Kumar, and R. Schuch, Phys. Rev. A. **73** (2006) 040901(R).

[27] Cui ST. Electrostatic potential in cylindrical dielectric media using the image charge method. Mol. Phys. (2006) 104, p 2993-3001

[28] "Poole-Frenkel conduction in Al/ZrO2 /SiO$_2$/Si structures", P. V. Aleskandrova, V. K. Gueorguiev, Tz. E. Ivanov, J. B. Koprinarova The European Physical Journal B, (2006), Volume 52, Issue 4, pp 453-457,

[29] Numerical Recipes 3rd Edition: The Art of Scientific Computing 3, Cambridge University Press New York, NY, USA (2007)

[30] "Guiding of low-energy electrons by highly ordered Al2O3 nanocapillaries", A.R. Milosavljevic, Gy. Víkor, Z. D. Pesic, P. Kolarz, D. Sevic, and B. P. Marinkovic, S. Mátéfi-Tempfli, M. Mátéfi-Tempfli, and L. Piraux, Phys. Rev. A **75** (2007) 030901(R).

[31] "Multiply-charged ion nanobeams", A. Cassimi, T. Muranaka, L. Maunoury, H. Lebius, B. Manil, B.A. Huber, T. Ikeda, Y. Kanai, T.M. Kojima, Y. Iwai, T. Kambara, Y. Yamazaki, T. Nebiki, and T. Narusawa , Int. J. Nanotechnol. **5** (2008) 809.

[32] "Evidence of sequentially formed charge patches guiding ions through nanocapillaries", P. Skog, H. Q. Zhang, and R. Schuch, Phys. Rev. Lett. **101** (2008) 223202.

[33] "Electron guiding through insulating nanocapillaries", K. Schiessl, K. Tőkési, B. Solleder, C. Lemell, and J. Burgdörfer, Phys. Rev. Lett. **102** (2009) 163201.

170

[34] R.J. "Transmission of 4.5 keV Ar9 + ions through a single glass macro-capillary", Bereczky, G. Kowarik, F. Aumayr, and K. Tőkési, Nucl. Instr. and Meth. Phys. **B267** (2009) 317

[35] R G. Kowarik, R.J. Bereczky, F. Aumayr, and K. Tőkési, Nucl. Instr. and Meth. Phys. Res. B**267** (2009) 2277.

[36] Y. Kanai, M. Hoshino, T. Kambara, T. Ikeda, R. Hellhammer, N. Stolterfoht, and Y. Yamazaki, Phys. Rev. A **79** (2009) 012711.

[37] A.Cassimi, L.Maunoury, T.Muranaka, B.Huber, K.R.Dey, H.Lebius, D.Lelievre, J.M.Ramillon, T.Been, T.Ikeda, Y.Kanai, T.M.Kojima, Y.Iwai, Y.Yamazaki, H.Khemliche, N.Bundaleski, P.Roncin, Nucl.Instrum.Meth.in Phys.Res.B **267** (2009) 674.

[38] N Bundaleski, H. Khemliche, P. Rousseau, A. Cassimi, L. Maunoury and P. Roncin, J. Phys.: Conf. Ser. 163 (2009) 012091

[39] "Charge carrier concentration and mobility in alkali silicates.", Souquet JL, Nascimento ML, Rodrigues AC. J. Chem. Phys. 132, (2010) 034704 https://doi.org/10.1063/1.3271154

[40] "Energy dependence of electron transmission through a single glass macro-capillary", B. S. Dassanayake, S. Das, R. J. Bereczky, K. Tőkési, and J. A. Tanis, c

[41] "Guiding of argon ions through a tapered glass capillary", M. Kreller, G. Zschornack, and U. Kentsch, Nucl. Instr. and Meth. Phys. Res. B **269** (2011) 1032

[42] T. Kojima, T.Ikeda, Y. Kanai, Y Yamazaki and V. A. Esaulov, "Ion beam guiding with straight and curved Teflon tubes", Journal of Physics D: Applied Physics, Volume 44, Number 35 (2011)

[43] "Temperature control of ion guiding through insulating capillaries", E. Gruber, G. Kowarik, F. Ladening, J. P. Waclawek, F. Aumayr, R. J. Bereczky, K. Tőkési, P. Gunacker, T. Schweigler, C. Lemell and J. Burgdörfer, Phys. Rev. A **86** (2012) 062901.

[44] A. Cassimi, T. Ikeda, L. Maunoury, C. L. Zhou, S. Guillous, A. Mery, H. Lebius, A. Benyagoub, C. Grygiel, H. Khemliche, P. Roncin, H. Merabet, and J. A. Tanis, Phys. Rev. A **86** (2012) 062902.

[45] J. Chen et al. "Focusing of 90 keV O6+ ions through a single tapered glass macrocapillary", Nucl. Inst. Meth. Phys. Res. B 281, 26 (2012) https://doi.org/10.1016/j.nimb.2012.04.004

[46] R.D. Dubois, "Can positrons be guided by insulating capillaries", K. Tőkési, Nucl. Instr. and Meth. Phys. Res. B **279** (2012) 186.

[47] G.U.L. Nagy , I. Rajta, R.J. Bereczky, and K. Tőkési AIP Conference Proceedings 1525 (2013) 40.

[48] "Simulation and analysis of ion guiding through a nanocapillary in insulating polymers", N. Stolterfoht, Phys. Rev. A **87** (2013) 012902.

[49] "Simulations and analytic models of ion guiding through a nanocapillary in insulating polymers", N. Stolterfoht, Phys. Rev. A **87** (2013) 032901.

[50] "Interaction of charged particles with insulating capillary targets - The guiding effect", C. Lemell, J. Burgdörfer, F. Aumayr, Progress in Surface Science **88** (2013) 237

[51] "Temperature control of ion guiding through tapered capillaries" E. Gruber, N. Stolterfoht, P. Allinger, S. Wampl, Y. Wang, M. J. Simon, F. Aumayr, Nuclear Instruments and Methods in Physics Research B 340 (2014) 1-4: https://doi.org/10.1016/j.nimb.2014.06.023

[52] "Ionic transport of alkali in borosilicate glass. Role of alkali nature on glass structure and on ionic conductivity at the glassy state", M. Neyret, M. Lenoir, A. Grandjean, N. Massoni, B. Penelon, M. Malki, Journal of Non-Crystalline Solids, Volume 410, (2015) Pages 74-81

[53] N. Stolterfoht *et al.*, "Experiments and simulations of 4.5-keV Ar^{7+} ion guiding through a conical glass macrocapillary", Phys. Rev. A 91, 032705 (2015)

[54] "Solutions for the electric potential and field distribution in cylindrical core-shell nanoparticles using the image charge method", N. Daneshfara and N. Moradbeigi, AIP Advances 5, 127214 (2015); https://doi.org/10.1063/1.4938255

[55] "Low energy ion transmission through a conical insulating capillary with macroscopic dimensions", E. Giglio, R.D. Dubois, A. Cassimi, K. Tőkési, NIM B Vol 354, page 82 (2015)

[56] "Discharge properties of macroscopic glass capillaries after irradiation by low intensity low energy single charged Ar ions" E. Giglio , R. D. DuBois , and K. Tőkési NIM B, Journal of Physics: Conference Series 635 042010 (2015)

[57] Darshika Keerthisinghe *et al.* "Elastic and inelastic transmission of electrons through insulating polyethylene terephthalate nanocapillaries", Phys. Rev . A, **92** (2015) p 012703, DOI: 10.1103/PhysRevA.92.012703

[58] Samanthi Wickramarachchi, "Electron Transmission through Micrometer Sized Funnelshaped Tapered Glass Capillaries and Electron Micro-Beam Production" (2015). Dissertations. 598. https://scholarworks.wmich.edu/dissertations/598

[59] "Guiding of charged particles through capillaries in insulating materials", N. Stolterfoht and Y. Yamazaki, Physics Reports **629**, (2016) page 1-107

[60] D.A. Saville "The Taylor-Melcher Leaky Dielectric Model", Annual Review of Fluid Mechanics, Vol. 29, p 27-64 (1997) https://doi.org/10.1146/annurev.fluid.29.1.27

[61] A. Castellanos "Electrohydrodynamics", section 1.4, p 13, Springer

[62] "Evolution of the electric potential of an insulator under charged particle impact", E. Giglio, S. Guillous, A. Cassimi, H. Q. Zhang, G. U. L. Nagy, and K. Tőkési, Phys. Rev. A 95, 030702(R) (2017)

[63] Takao. M. Kojima, "Ion guiding in macro-size insulating capillaries: straight, tapered, and curved shapes", Journal of Physics B Atomic Molecular and Optical Physics, 51(4), 042001, 2018 https://doi.org/10.1088/1361-6455/aa9eaf

[64] "Self-organized focusing power in insulating capillaries" E. Giglio, S. Guillous, A. Cassimi, Phys. Rev. A 98, 052704 (2018)

[65] Sanjeev Kumar Maurya, Sushanta Barman, Samit Paul and Sudeep Bhattacharjee, "Charge dissipation and self focusing limit in high current density ion beam transport through a micro glass capillary", Journal of Physics D: Applied Physics, Volume 52, Number 5 (2018)

[66] Priyanka Dash, Mengxue Yuan, Jun Gao, Eugene Furman and Michael T Lanagan,"High electric field conduction in low-alkali boroaluminosilicate glass", JOURNAL OF APPLIED PHYSICS 123, 054102 (2018)

[67] "Relaxation dynamics of charge patches formed inside an insulating capillary by ion impact", E. Giglio, K. Tőkési, R D Dubois, Nuc. Inst. Meth. B (2019) accepted, in press, DOI: 10.1016/j.nimb.2018.12.027

[68] "Transmission dynamics of 1 MeV H+ microbeam guided through an insulating macrocapillary", G. Nagy, E. Giglio, I. Rajta and K. Tőkési, Nuc. Inst. Meth. B (2019) accepted, in press, DOI: 10.1016/j.nimb.2018.11.045

[69] "Guiding of Low-Energy Ions through an Insulating Capillary: A Study of the Charge Deposition, Redistribution and Decay capillaries", R D Dubois K. Tőkési, E. Giglio, submitted to PRA

List of publications: All my papers are fully available on ResearchGate, in preprints format with identical content as the published ones. A list of publications over the last decade as well as this HDR thesis in pdf format can be found on my CIMAP webpage.

ABSTRACT

Charged droplets at the Rayleigh limit. We model and simulate the shape evolution of critically charged droplets, from the initial spherical shape to the charge emission and back to the spherical shape. The shape deformation is described using the viscous correction for viscous potential flow model, which is a potential flow approximation of the Navier-Stokes equation for incompressible Newtonian fluids. The simulated shapes are compared to snapshots of experimentally observed drop deformations. We highlight the influence of the viscosity and charge carrier mobility of the liquid on the shape evolution of droplets and discuss the observed trends. We give an explanation as to why the observed deformation pathways of positively and negatively charged pure water droplets differ.

Ion transport through insulating capillaries. Self-organized charged particle guiding by insulating capillaries is modeled and simulated by our code InCa4D. Additionally, an original experimental setup is presented that allows us to monitor the accumulated total charge in the capillary and to link the charge to the transmitted fraction of the beam. In a combined theoretical and experimental study, we give evidence that the self-organized electric potential in tapered glass capillaries has the strength to focus a low energy ion beam, similar to Einzel lenses. The experimental data are corroborated by our simulations, which allows a valuable and comprehensive insight into the dynamics of the self-organized Coulomb potential in irradiated insulating capillaries.

RESUMÉ

Gouttelettes à la limite de Rayleigh. Lorsqu'une gouttelette chargée atteint une charge critique, elle devient instable et se déforme spontanément. Initialement sphérique, la gouttelette s'allonge, puis émet 2 jets de matières chargés. Ici, nous modélisons et simulons l'évolution de la forme d'une gouttelette chargées et comparons nos simulations aux résultats expérimentaux. La déformation de la gouttelette est décrite en utilisant le modèle d'écoulement potentiel visqueux avec correction visqueuse (VCVPF), qui est une approximation de l'équation de Navier-Stokes pour les fluides newtoniens incompressibles et faiblement visqueux. Nos simulations mettent en évidence l'influence de la viscosité et mobilité des charges du liquide sur l'évolution de la forme des gouttelettes. Nous explications ainsi pourquoi la déformation observée pour des gouttelettes d'eau pure chargée positivement et négativement, est différente.

Transport d'ions à travers les capillaires isolants. Le guidage auto-organisé des particules chargées par des capillaires isolants est modélisé, puis simulé par notre code InCa4D. Un dispositif expérimentale original, qui permet de mesurer la charge totale dans le capillaire et de relier cette dernière à la fraction transmise du faisceau, est présenté. Dans une étude théorique et expérimentale combinée, nous montrons que le potentiel électrique auto-organisé dans les capillaires coniques peuvent focaliser un faisceau d'ions de basse énergie, semblable à une lentille d'Einzel. Les données expérimentales sont corroborées par nos simulations, permettant ainsi une compréhension complete de la dynamique de charge à l'interface des isolants.